Inaugural dissertation

for

obtaining the doctoral degree

of the

Combined Faculty of Mathematics, Engineering and Natural Sciences

of the

Ruprecht - Karls - University

Heidelberg

Presented by

M. Sc. Marvin Hering

born in: Tübingen, Germany

Oral examination: September 20th, 2023

Sptlc2-derived sphinganine is indispensable for inflammatory TLR4 signaling in macrophages

Referees:

Prof. Dr. Viktor Umansky

Dr. Guoliang Cui

"Float like a butterfly, sting like a bee. You can't hit what your eyes don't see."
(Muhammed Ali, 1964)

"Your worst enemy could be your best friend, and your best friend could be your worst enemy."
(Bob Marley, 1976)

Bob Marley died in 1981 from **metastatic melanoma**. Muhammed Ali died in 2016 from **septic shock**. In the quotes above, neither the music icon nor the sports icon spoke of their immune systems. Yet, these are perfectly fitting descriptions of what, some years later, has happened in their bodies, causing both of their deaths. Their immune systems, their best friends to protect them from disease, could not adequately "see" the danger and efficiently fight for their health anymore and have, in turn, even become their worst enemies. What exactly has happened?

Disclosure

Some of the herein-presented data are included in the manuscript “Sphinganine membrane-anchors TLR4 adaptors in macrophages to promote inflammation” by Hering, M., Madi, A., Sandhoff, R., Ma, S., Wu, J., Mieg, A., Richter, K., Mohr, K., ten Bosch, N., Stichling, D., Poschet, G., Umansky, V., and Cui, G., which is currently submitted for publication (indicated in the respective figure legends).

Collaborations

Results from collaborative efforts are named in the respective figure legends and text sections.

Acknowledgements

First, I want to thank my supervisors, Dr. Guoliang Cui and Prof. Dr. Viktor Umansky, for giving me the opportunity to do this shared PhD as part of the RTG2099 program between their two labs. I am extremely thankful to Dr. Guoliang Cui for having me in his T cell metabolism lab at the German Cancer Research Center (DKFZ) Heidelberg, for constantly supporting me, and for giving me the chance to learn from his great scientific and personal experiences. I thank Prof. Dr. Viktor Umansky for his impressive scientific advice in the past years and for being willing to help in every situation.

Additionally, I would like to thank my thesis advisory committee member, Dr. Roger Sandhoff, for his constructive input during my TAC meetings and the scientific collaborative effort. In addition, I am also very grateful to Prof. Dr. Nina Papavasiliou and Prof. Dr. Ralf Bartenschlager for their participation in my examination committee.

Further thanks to members of the Umansky lab at the University Medical Center Mannheim (UMM) and at the DKFZ for the stimulating discussions.

Many thanks to former and current members of the Cui lab at the DKFZ: Dr. Jingxia Wu, Dr. Sicong Ma, Dr. Nina Weißhaar, Dr. Alaa Madi, Dr. Alessa Mieg, Dr. Jannis Wißfeld, Dr. Anke Werner, Kerstin Mohr, Nora ten Bosch, Tilo Schlimbach, Ferdinand Zettl, Xin Yan, Gesa Durniock-Thierschmann, Helena Borgers, Franziska Hertel, and Diana Stichling. Special thanks go to Alaa for her (almost daily) support in the office as well as in the lab; there is not enough chocolate in all stores to repay my gratitude. Further, I want to thank Kerstin and Nora for their patience in discussing the mouse genotyping with me and their support on “the big days”. About 3.5 years of daily interactions have come to an end. It was an exciting journey with many nerve-wracking and shocking stories but also many nice moments, and I have a lot of memories from our time together. I wish all of you only the best, and I hope we can see each other again one day.

I want to also thank Dr. Damir Krunic and Manuela Brom at the DKFZ Microscopy Core Facility, people at the DKFZ Animal Housing and DKFZ Flow Cytometry Core Facilities,

Jennifer Schwarz, Mandy Rettl, and Frank Stein at the Proteomics Core Facility (PCF) at the European Molecular Biology Laboratory (EMBL) Heidelberg, Martina Volz at the DKFZ Lipid Pathobiochemistry Group, Dr. Karsten Richter at the DKFZ Electron Microscopy Core Facility, Tobias Strobel at the DKFZ Molecular Therapy of Virus-associated Cancers group, and Dr. Gernot Poschet and his team at the Centre for Organismal Studies (COS) Heidelberg for the collaborative efforts. Further, I am thankful for the responsible people at my graduate schools, HBIGS, HIGS, and RTG2099. Some of the illustrations were created in BioRender.com.

I am also thankful to many more people I met at DKFZ and UMM in daily encounters, retreats, summer schools, and conferences; some became friends, and some I do not want to meet ever again. I learned a lot from all of you.

My deepest thanks and apologies go to the many mice that, in the course of this project, had to sacrifice their precious lives. Besides, my thoughts are with all the failed experiments and ideas and all the side projects that took lots of time and effort but are not further mentioned anywhere.

Lastly, my biggest thanks go to my friends and especially to my family and my love. Without your endless help, advice in all aspects of life, and limitless patience and support, I would not have been able to survive this intense time and do this work.

Hanne, Thorsten, Gianna, Mady, Anita, and Hanna, I am infinitely grateful for having you.

Abstract

Macrophages are key players in initiating, regulating, and driving inflammation, which, depending on the intensity and duration, can be extremely helpful or harmful during immune responses. A major pathway in macrophages driving inflammatory signaling is mediated through activation of the pattern recognition receptor Toll-like receptor (TLR) 4. After recognizing its ligand, lipopolysaccharide (LPS), TLR4 recruits adaptor proteins to the cell membrane, thereby initiating downstream signal transduction and triggering inflammation. Whether this recruitment is dependent solely on protein-protein interactions between TLR4 and adaptor proteins is unknown. Bioactive sphingolipids are regulators of multiple (patho-) physiological processes and have been associated with inflammatory macrophage signaling, with the underlying mechanisms remaining uncertain.

Here, I report that the sphingolipid sphinganine physically interacted with the adaptor proteins MyD88, TIRAP, and Tollip and promoted the recruitment of MyD88 to the cell membrane. LPS induced the expression and activity of Sptlc2, which is the key enzyme of sphingolipid metabolism, catalyzing sphinganine production and subsequent sphingolipid biosynthesis. Myeloid cell-specific deficiency in *Sptlc2* was found to decrease the membrane recruitment of MyD88 and to inhibit LPS-induced M1-like macrophage growth, marker expression, metabolic activity, and cytokine production. Overexpression of membrane-anchored MyD88 in *Sptlc2*-deficient macrophages restored cell growth, M1-like macrophage marker expression, and inflammatory cytokine production. In an LPS-induced sepsis mouse model, Sptlc2 was upregulated in macrophages, while *Sptlc2* deficiency attenuated inflammation and ameliorated symptoms of sepsis. In a melanoma mouse model in which LPS was detectable in the tumor microenvironment, Sptlc2 was upregulated in tumor macrophages, and *Sptlc2* deficiency decreased anti-tumor myeloid cell responses and increased tumor growth. Therefore, sphinganine biosynthesis is required for the initiation of TLR4 signal transduction and serves as a checkpoint involved in pattern recognition by macrophages. In summary, this work sheds new light on the multifaceted role of sphingolipids as signaling molecules and underlines the huge potential of sphingolipid modulation to treat disease-associated inflammation.

Zusammenfassung

Makrophagen haben eine entscheidende Funktion bei der Auslösung, Regulation und Förderung von Entzündungen, die je nach Intensität und Dauer äußerst hilfreich oder schädlich für Immunantworten sein können. Ein Hauptsignalweg, der die Entzündungssignale in Makrophagen antreibt, wird durch die Aktivierung des Mustererkennungsrezeptors Toll-like-Rezeptor (TLR) 4 vermittelt. Nach Erkennung seines Liganden Lipopolysaccharid (LPS) rekrutiert TLR4 Adapterproteine zur Zellmembran, um die nachgeschalteten Signalwege zu initiieren und Entzündungen auszulösen. Bislang ist nicht bekannt, ob diese Rekrutierung ausschließlich von Protein-Protein-Wechselwirkungen zwischen TLR4 und Adapterproteinen abhängt. Bioaktive Sphingolipide sind Regulatoren mehrerer (patho-) physiologischer Prozesse und wurden mit der Signalübertragung in inflammatorischen Makrophagen in Verbindung gebracht, wobei die zugrunde liegenden Mechanismen noch unklar sind.

In dieser Arbeit berichte ich, dass das Sphingolipid Sphinganin direkt mit den Adapterproteinen MyD88, TIRAP und Tollip interagierte und die Rekrutierung von MyD88 an die Zellmembran förderte. LPS induzierte die Expression und Aktivität von Sptlc2, dem Schlüsselenzym im Sphingolipid-Metabolismus, das die Produktion von Sphinganin und die anschließende Sphingolipid-Biosynthese katalysiert. Ein Mangel von *Sptlc2*, spezifisch in myeloiden Zellen, reduzierte die Membranrekrutierung von MyD88 und hemmte das LPS-induzierte Wachstum, die M1-ähnliche Marker-Expression, die Stoffwechselaktivität und die Zytokin-Produktion der Makrophagen. Überexpression von membranständigem MyD88 stellte das Zellwachstum, die Expression von M1-ähnlichen Markern und die Produktion entzündlicher Zytokine in *Sptlc2*-defizienten Makrophagen wieder her. In einem LPS-induzierten Sepsis-Mausmodell wurde Sptlc2 in Makrophagen hochreguliert, wohingegen ein *Sptlc2*-Mangel die Entzündung abschwächte und die Symptome der Sepsis verbesserte. In einem Melanom-Mausmodell, in dem LPS im Tumormikromilieu nachweisbar war, war Sptlc2 in Tumormakrophagen hochreguliert, und ein *Sptlc2*-Mangel verringerte die anti-tumoralen Reaktionen der myeloiden Zellen und erhöhte das Tumorwachstum. Zusammenfassend lässt sich daraus festhalten, dass die Sphinganin-Biosynthese für die Initiierung der TLR4-Signaltransduktion erforderlich ist und als Kontrollpunkt für die Mustererkennung durch Makrophagen dient.

Zusammenfassend wirft diese Arbeit ein neues Licht auf die vielfältige Rolle von Sphingolipiden als Signalmoleküle und unterstreicht das enorme Potenzial der Sphingolipid-Modulation bei der Behandlung krankheitsbedingter Entzündungen.

Table of contents

List of Figures

List of Tables

1. Introduction

"When the oracle of Delphi prophesies to Oedipus' parents that their son will murder his father and marry his mother, they choose to give him up for adoption. As an adult, while traveling, Oedipus unwittingly slays his father. When he arrives at the city of Thebes, the sphinx, a hybrid of a winged lion and a woman, stands guard on a rock and gives him the following riddle, which he has to solve or he will get eaten by the sphinx: "What is four-footed in the morning, two-footed at noon, and three-footed in the evening?" By answering "man", Oedipus solves the riddle and liberates the city. The sphinx falls into the abyss, and Oedipus marries the queen of Thebes, his mother."

(Greek mythology)

Its hybrid appearance and unknown origin give the sphinx an enigmatic figure. Today, the list of things named after the sphinx includes, for example, ships, asteroids, insects, mountains, and sphingolipids. The latter goes back to the 1870s, when the son of the Sophokles-translator G. Thudichum, named J. L. W. Thudichum, a German pathologist and physiologist, studied substances in ox brains by fractional crystallization of ethanolic brain extracts. In his work "A Treatise on the Chemical Constitution of the Brain" (*1*) from 1884, he named a group of these substances, in commemoration of their enigmatic (sphinx-like) properties, "sphingosines" (*2*). Later, from this, the term "sphingolipids" was derived. For his discovery of a large number of novel chemicals, Thudichum faced a lot of criticism in the scientific community (*3*). He was accused of using "new words for old facts" and that science had gained nothing from his research. This even led to Thudichum's exclusion from publishing in certain journals (*4*). Nowadays, Thudichum is seen as a neglected "father of neurochemistry", and the specialized nasal speculum he invented ("Thudichum's speculum") is still in use today. In honor of his work, since 1974, the "Thudichum Medal Lecture" has been awarded for outstanding contributions to neurochemistry. While the Egyptian sphinx is described as a guard for the pyramids, in Greek mythology, the sphinx is seen as a demon of destruction. In addition to the name, this contrary role is also reflected by sphingolipids, which are increasingly being deciphered to have health-promoting but also pathogenic properties. In Greek mythology, deciphering the riddles of the sphinx determined life or death. Deciphering the enigmas of sphingolipids potentially does so as well in modern medicine.

1.1 Our immune system and inflammation

Despite being continually exposed to disease-causing microorganisms, we only become ill in rare cases (*5*). This is due to our immune system, a complex network of organs, cells, and proteins that has evolved to defend our bodies against infection caused by pathogenic microbes, which themselves are constantly evolving (*6*). Simplified, our immune system can be divided into two major parts: the innate and the adaptive immune system. The innate part is the body's first line of defense, acting against all foreign substances, and is often called a "non-specific" immune system. It is initiated within minutes after infection, lasts for a few days, and can be subdivided into protection through physical barriers and protection through innate immune cells and their products. As an initial defense against infection, the anatomic and chemical barriers, such as the skin, tear fluid, and mucosal membranes, produce antimicrobial proteins, protecting the body from external harm. Once these barriers are evaded, innate immune cells are the next defense mediators. These cells include macrophages, granulocytes, mast cells, and dendritic cells, which all originate from the myeloid lineage. As another part of innate immunity, the complement system is involved in opsonization (recognizing and targeting pathogens for phagocytosis), lysis of pathogens, and promoting inflammation (*7*). Through their many innate recognition receptors, innate immune cells serve as sensor cells for inflammatory inducers such as bacterial products, and upon activation, some of them can digest pathogens through the process of phagocytosis and/or produce various inflammatory mediators, which either act directly on the pathogens or on other cells to propagate the immune response (*5*). The activation and recruitment of more immune cells from the bloodstream to the infected tissue is called inflammation. This is enabled by inflammatory mediators, which make blood vessels dilated and more permeable, causing the site of infection to swell, heat up, and redden. When innate immunity cannot clear the infection, adaptive immune responses set in hours to days after the infection and last for weeks. Adaptive immune cells include B and T lymphocytes, and the selection and amplification of unique B and T cell clones with receptors that specifically recognize foreign antigens allow for a more specific immune response. Moreover, in comparison to innate immunity, adaptive immunity can form a lifelong immunological memory, which allows for faster defense against recurring infections. Activation of adaptive immune cells requires contact with activated antigen-presenting cells in lymphoid tissues, typically dendritic cells with

major histocompatibility complex (MHC) molecules and co-stimulatory receptors. In this way, activated B cells can become antibody-producing plasma cells, and activated cluster of differentiation (CD) 8+ or CD4+ T cells exert cytotoxic activity or secrete mediators that activate other effector functions, respectively. Simultaneously, lymphocytes activate innate immune cells such as macrophages through interferon-gamma (IFN-γ) (*8*). Additionally, natural killer (NK) cells act at the interface between innate and adaptive immunity against viruses and in the immune surveillance of tumors (*9*). Once the infection-causing pathogen is successfully cleared, regulatory immune cells such as regulatory T cells (Tregs) and anti-inflammatory macrophages stop the inflammation and promote wound healing. When functioning correctly, our immune response represents a fascinating system to secure our health against a variety of infection-causing agents. However, misdirected immune responses and uncontrolled inflammation can damage host tissues and cause or promote diseases. Two different diseases driven and aggravated by malfunctioning inflammation and uncontrolled immune responses are sepsis and cancer.

1.1.1 Immune responses in sepsis

Sepsis is a life-threatening organ dysfunction caused by the dysregulated host response to an uncontrolled infection (*10*). Worldwide, sepsis affects around 50 million people each year, among whom at least 11 million die. That is one death every 2.8 seconds, making it a global health crisis (*11*). Sepsis is mostly caused by infection with gram-negative and gram-positive bacteria but also by fungi, viruses, and parasites (*12*). The key players in sepsis pathogenesis are dysfunctional macrophages, but other defense mechanisms such as neutrophils and complement factors are also involved (*13*). As a first line of defense, macrophages are typically activated through pattern recognition receptors (PRRs) like Toll-like receptors (TLR), which recognize danger-associated molecular patterns (DAMPs) and bacterial pathogen-associated molecular patterns (PAMPs), such as lipopolysaccharides (LPS) or lipoteichoic acid (LTA) of gram-negative or gram-positive bacteria, respectively (*14*). This causes their polarization towards a pro-inflammatory phenotype, promoting host defense through pathogen elimination and cytokine production in the early stages of sepsis (*15, 16*). However, if macrophage-mediated inflammatory responses cannot be quickly controlled, macrophages get over-activated, and excessive,

unregulated inflammatory signaling can cause a harmful cytokine storm, which can result in sepsis and associated organ dysfunction (*17-20*) (Figure 1). In addition, excessive pro-inflammatory signaling causes M2-like macrophage polarization and apoptosis of macrophages and drives immunosuppression in the later stages of sepsis (*21, 22*).

Clinical sepsis treatment mostly focuses on early antibiotic therapy and maintaining blood flow to organs through the administration of intravenous fluids. Severe infections or late treatment can progress to septic shock (a sepsis-associated drop in blood pressure), which requires therapy with vasopressors to guarantee organ perfusion. Such patients are typically located in intensive care units (ICU) for monitoring and stabilizing their breathing and heart action. Usually, first broad-spectrum antibiotics are used, and after identification of the sepsis-causing bacteria from blood tests, more specific antibiotics are applied. However, such therapies may not always be very specific, cause side effects, and contribute to increasing antibiotic resistance, which makes follow-up infections more difficult to treat. Accordingly, recent exposure to antibiotics has been linked to a higher incidence of hospital mortality in cases of severe sepsis caused by gram-negative bacteria (*23*). Together with the many long-term complications of sepsis, such as decreased cognitive functioning, post-traumatic stress disorder (PTSD), or joint and muscle pain (*24*), and the higher risk of developing sepsis again, this shows a better understanding of the drivers of inflammatory macrophage signaling pathways is required to develop urgently needed new therapeutic approaches against sepsis.

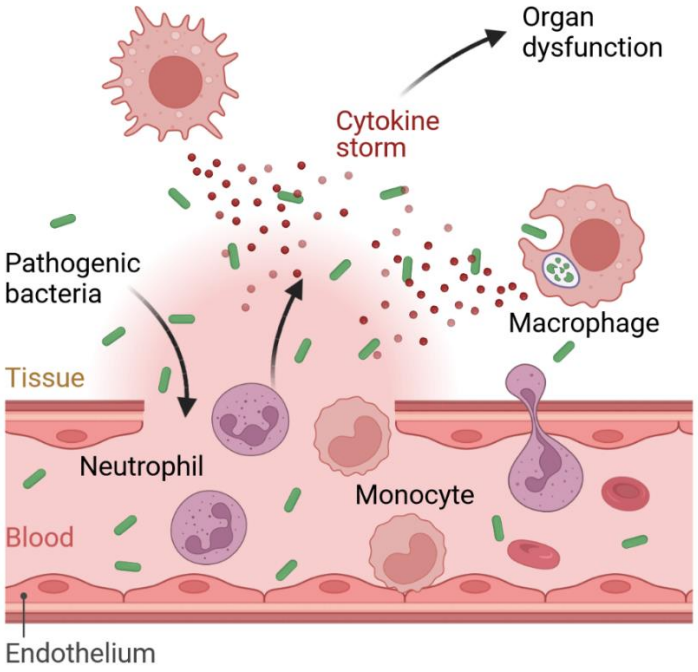

Figure 1 Inflammatory immune response in sepsis.

During sepsis, the bacterial infection causes an over-activated immune response and excessive cytokine production by macrophages, resulting in a cytokine storm that causes tissue damage and allows for bacterial migration into blood vessels and the whole body. From this, systemic immune dysregulation and organ dysfunction can result. Figure inspired by (*25*) and adapted from “Systemic bacterial infection” by BioRender.com (2023).

1.1.2 Immune responses in melanoma

In the United States, cancer is the second leading cause of death, and it is expected to even surpass heart disease in a few years (*26*). Skin cancer is by far the most common of all cancers. In 2020, worldwide, there were around 19.3 million cancer cases and almost 10 million cancer deaths (*27*). Of these, 1.5 million were skin cancers, with 0.3 million melanomas, the most aggressive and deadly skin cancer, causing 0.06 million deaths, and especially metastatic melanoma carries a poor prognosis of only 27% 5-year survival (*26, 27*). Melanomas are malignant tumors that originate from transformed melanocytes in the basal layer of the epidermis and are located, for example, in the skin, uvea, or mucosal epithelia. Melanomas have a high mutational burden, and different factors can promote melanoma development, including mainly exposure to ultraviolet (UV) rays from sunlight but also genetic factors *(28, 29)*. Frequently, alterations in mitogen-activated protein kinase (MAPK) and phosphoinositide 3-kinase (PI3K)/phosphatase and tensin

homolog (PTEN) signaling pathways, such as BRAF (B rapidly accelerated fibrosarcoma) mutations, are found in melanomas (*30*). Inflammation is considered a hallmark of cancer, and melanoma is considered to be an immune-inflamed, so-called “hot tumor” (*31*). “Hot tumors” are characterized by dysfunctional immune responses, making them targetable with immunotherapeutic strategies (*32*). Following initial surgical removal of the primary tumor, nowadays immunotherapies are the standard care for people with metastatic melanoma. In large part, this is thanks to the pioneering work of T. Honjo and J. Allison, who identified the immunosuppressive immune checkpoints programmed death molecule-1 (PD-1) and cytotoxic T-lymphocyte antigen-4 (CTLA-4), leading to Food and Drug Administration (FDA)-approved immune checkpoint inhibitors (ICI) for metastatic melanoma in 2014 and their Nobel Prize award in 2018. However, despite the identification of further next-generation ICI and their unquestionable clinical success, only half of the patients benefit from immunotherapies, underlining the urgent need for more effective melanoma treatments *(33)*. Unfortunately, this gap can also not be filled by targeted therapies using BRAF and mitogen-activated protein kinase kinase (MEK) inhibitors, application of cytokines such as interleukin (IL)-2, oncolytic virus therapies such as Talimogen laherparepvec (T-vec), radiation therapy, or chemotherapies (*34-38*). Lately, increasing research focuses on tumor vaccines, in particular messenger ribonucleic acid (mRNA)-based vaccines, inducing humoral and cellular immune responses *(39)*.

The crucial role of our immune system in tumor development became obvious in 1863 with R. Virchow’s observation that leukocytes heavily infiltrate tumors and was later captured in the model of cancer immune editing, wherein the immune system can both constrain and promote tumor development (*40-42*). In this model, there are three different phases, starting with the elimination phase, in which transformed cells are removed by the immune system. Tumor subclones that survived the elimination phase progress into the equilibrium phase, in which net growth is limited (*43*). However, the genetic instability of tumor cells in combination with the constant pressure of the adaptive immune system can select subclones that can evade immune recognition and enter the escape phase of unrestrained growth (*44*). Similar to sepsis, in melanoma and multiple other cancers, highly infiltrating myeloid cells contribute to both pro- and anti-inflammatory signaling, making them effective weapons against malignant cells but also key drivers of the tumor-

promoting inflammation in the tumor microenvironment (TME). Consequently, myeloid cells are often suspected to limit the clinical success of immunotherapies by limiting effective anti-tumor T cell immune responses (*45*). This is because in response to different factors in the TME such as low glucose, high lactate, or hypoxia, myeloid cells, which initially form anti-tumor immune responses, are often differentiated into tumor-promoting myeloid-derived suppressor cells (MDSC) or re-polarized to M2-like tumor-associated macrophages (TAMs) and tumor-associated neutrophils (TANs) (*46*) (Figure 2). Besides, MDSC can rapidly differentiate into TAMs (*47*), and TAMs, TANs, and MDSC frequently accumulate in tumors (*48*). While excessive pro-inflammatory signaling through over-activated myeloid cell activity is unquestionably driving sepsis, in melanoma this is more complex, and inflammatory myeloid cell signaling is often described as a “double-edged sword”. On the one hand, a precise myeloid cell immune response causing acute inflammation is beneficial in directly killing tumor cells and driving anti-tumor-specific T cell responses (*49*), but on the other hand, myeloid cells can create an inflammatory environment and a persisting immune response, and chronic inflammation can change the myeloid cell’s character so that they detrimentally contribute to the generation of an immunosuppressive, tumor-promoting TME and help extravasation, survival, and subsequent growth of tumor cells (*50*). Already in the 1890s, “the father of cancer immunotherapy”, W. B. Coley, successfully used acute inflammation induced by certain microbial preparations to treat cancers, and still, one such preparation is currently used in the treatment of bladder cancer (*51*), underlining the anti-tumor effects of acute inflammation. In line with Coley’s famous work, cancer patients developing sepsis grow smaller tumors (*52, 53*). Conversely, multiple times, chronic inflammation and constant pro-inflammatory signaling have been described to cause and drive tumor development by building up an immunosuppressive and pro-tumorigenic tumor microenvironment (TME). In line with this, clinical data show sepsis survivors are more likely to develop tumors *(52, 54)*. Consequently, as the main mediators of inflammation and drivers of an immunosuppressive environment, myeloid cells are promising targets for therapeutic cancer strategies. Blocking of macrophage infiltration into the TME with small molecule inhibitors and antibodies targeting either the chemokine (C-C motif) ligand 2 (CCL2)/C-C chemokine receptor type 2 (CCR2) or macrophage colony-stimulating factor (M-CSF)/M-CSF receptor (M-CSFR) signaling axis, killing TAMs with cytotoxic agents such as

Trabectedin, preventing M2-like polarization of macrophages in the tumor through, for example, microRNAs (miRNAs), blocking of signal transducer and activator of transcription 6 (STAT6)-driven M2-like macrophage polarization and re-polarizing M2-like (anti-inflammatory) to M1-like (pro-inflammatory) macrophages are just some examples of considered immunotherapies that target macrophages (*55-62*). Needless to say, a more detailed understanding of inflammatory myeloid cell signaling is indispensable for the improvement of existing and the development of novel immunotherapies.

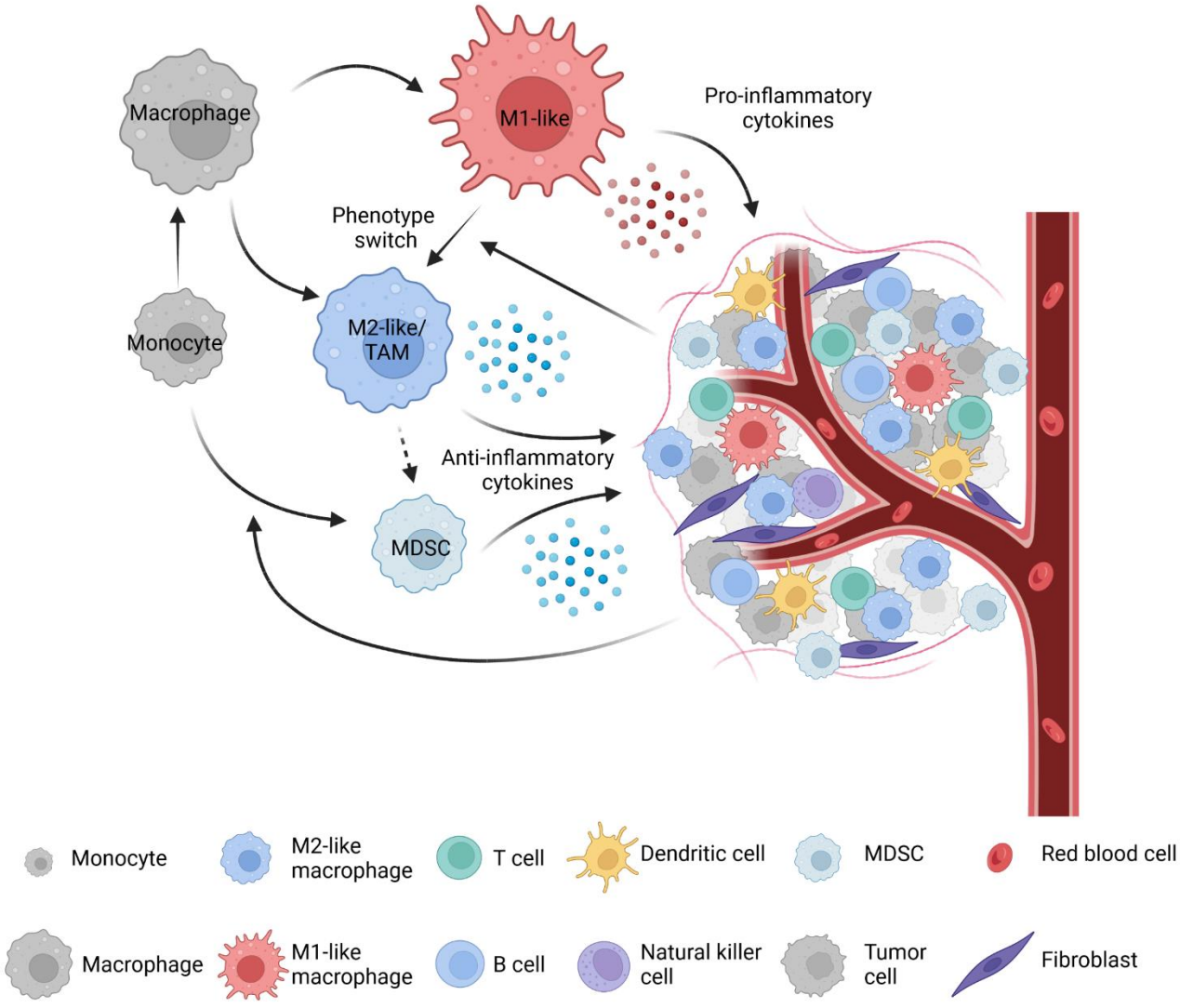

Figure 2 Myeloid cells in tumorigenesis.

Macrophages are recruited to the tumor microenvironment, and as M1-like macrophages, they can stimulate effective anti-tumor immune responses via T cell activation through pro-inflammatory cytokines and remove dying tumor cells through efferocytosis. The tumor microenvironment induces the switch from M1-like to M2-like macrophages and the generation of myeloid-derived suppressor cells (MDSC) and tumor-

associated macrophages (TAMs). These immunosuppressive cells produce anti-inflammatory cytokines, limiting anti-tumor T cell responses and promoting tumor growth. Figure inspired by (*63*) and adapted from “Tumor microenvironment” by BioRender.com (2023).

1.1.3 Myeloid cells

Myeloid cells are immune cells differentiated from common myeloid progenitors (CMP), which are derived from hematopoietic stem cells in the bone marrow (BM) and comprise granulocytes (eosinophils, basophils, and neutrophils) and monocytes, which can further develop into dendritic cells and macrophages. Myeloid cells and especially highly diverse macrophages are involved in several inflammatory diseases, such as bacterial, viral, and parasitic infections; cardiovascular diseases such as atherosclerosis, obesity, and insulin resistance; cancer; asthma; and septic complications (*64*). Macrophages are considered key drivers of sepsis and tumor progression, making them promising targets for immunotherapies. In 1883, I. Metchnikoff, who later shared the 1908 Nobel Prize with P. Ehrlich, was the first to describe macrophages (Greek: *big eater*) and the process of phagocytosis (Greek: *cell eating*) when he studied defensive mechanisms in yeast-infected *Daphnia* and rose-thorn-stuck starfish larvae (*65*). Macrophages are resident in almost all tissues and can be derived from the embryonic tissues (fetal liver and yolk sac) or via a monocytic stage from the adult tissue (BM) (*66*). Depending on their tissue-specific localization in the body, they can have further names such as Langerhans cells in the epidermis, Kupffer cells in the liver, or microglia in the brain (*67-69*).

Once a pathogen has entered the body, tissue-resident myeloid cells and monocytes from the BM, which differentiate into macrophages, are recruited to the site of infection, where they function as sensor cells and get activated through their PRR-mediated recognition of PAMPs. They engulf and kill pathogens via phagocytosis (*5*) and secrete a variety of cytokines and chemokines to induce inflammation and recruit other immune cells. As antigen-presenting cells, after moving to lymph nodes, macrophages and dendritic cells are also involved in the activation of adaptive T cell immune responses. Due to their high plasticity, macrophages can change their activation state from a pro-inflammatory state (referred to as classical or M1-like macrophages) to a more immunosuppressive state (referred to as non-classical or M2-like macrophages), which in the year 2000 was captured in the M1/M2 macrophage paradigm by C.D. Mills (*70*).

However, macrophage nomenclature was still heavily debated, and multiple further models, such as the sub-grouping of M2 macrophages into M2a, M2b, and M2c macrophages based on the specific stimuli applied and the resulting transcriptional alterations from A. Mantovani in 2004, were suggested (*71*). In the basic M1/M2 paradigm, typical M1 macrophages are, for example, induced by LPS, IFN-γ, and granulocyte-macrophage colony-stimulating factor (GM-CSF), and, via nuclear factor k-light-chain-enhancer of activated B cells (NF-κB), STAT1, and interferon regulatory factor 5 (IRF5) signaling, pro-inflammatory cytokines are produced to mediate tumor resistance, killing of intracellular pathogens, tissue damage, and Th1 (pro-inflammatory CD4+ T cell) responses *(70)* (Figure 3). These macrophages are characterized by markers such as IL-1β, IL-6, tumor necrosis factor α (TNFα), IL-12, IL-23, MHCII, CD86, reactive oxygen species (ROS), inducible nitric oxide synthase (iNOS), and CD38 (*72, 73*). Atypical M2 macrophage polarization is, for example, induced by IL-4, IL-10, IL-13, and M-CSF, and, via STAT3, STAT6, and IRF4 signaling, this results in the expression of anti-inflammatory cytokines, mediating parasite control, tissue remodeling, angiogenesis, immune regulation, tumor promotion, and Th2 (anti-inflammatory CD4+ T cell) responses (*73*) (Figure 3). Markers of M2 macrophages are, for example, IL-10, transforming growth factor beta (TGFβ), vascular endothelial growth factor (VEGF), CD163, CD206, arginase-1 (Arg-1), and early growth response protein 2 (Egr2) (*72, 73*). M1 and M2 macrophages demonstrate distinct metabolic patterns, with M1 macrophages showing increased glycolytic activity and M2 macrophages being more dependent on oxidative phosphorylation (*74, 75*).

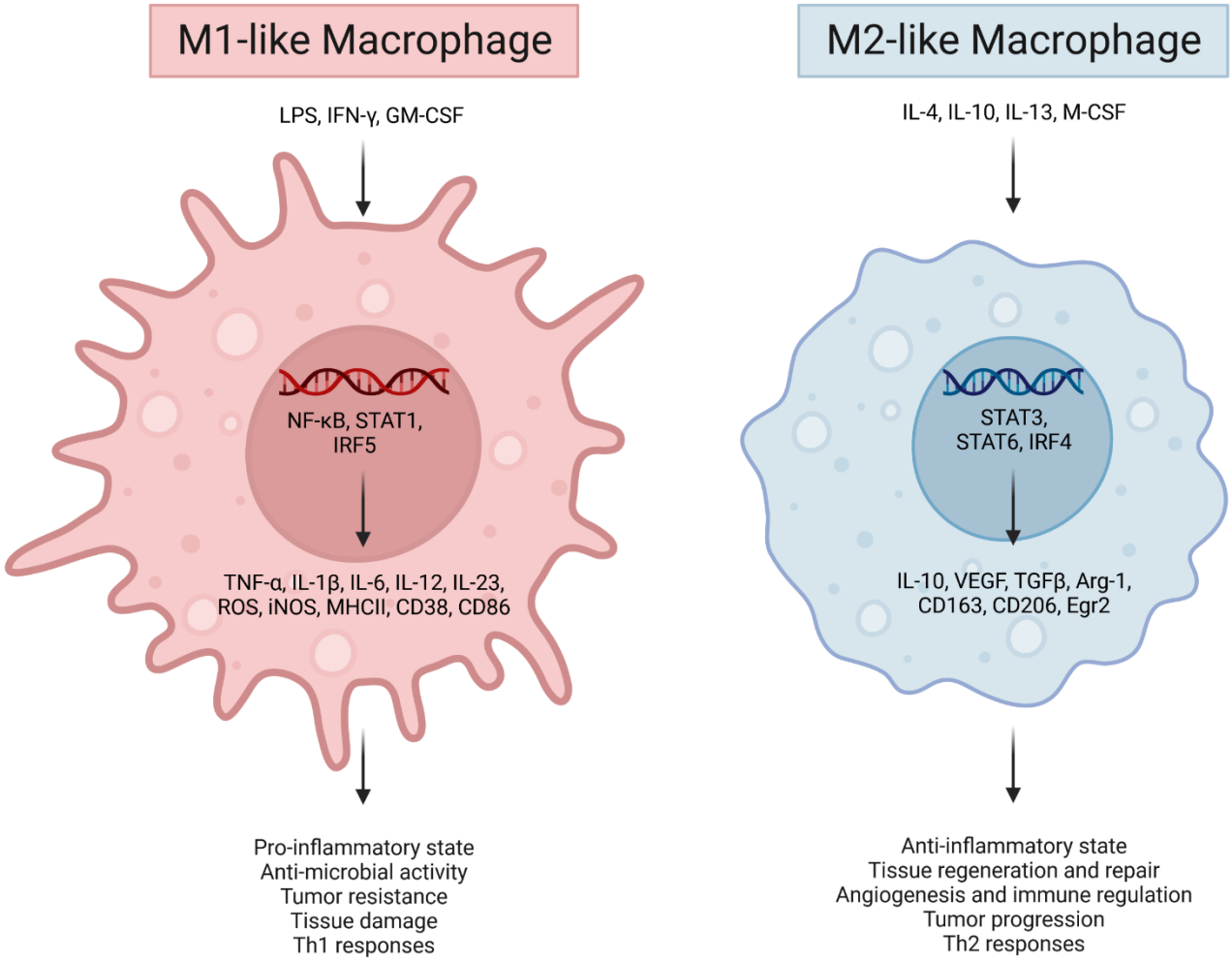

Figure 3 Stimuli, transcription factors, and markers of M1-like and M2-like macrophages.
The M1/M2 macrophage paradigm separates M1-like macrophages, which are induced by LPS, IFN-γ or GM-CSF and express the markers TNFα, IL-1β, IL-6, IL-12, IL-23, ROS, iNOS, MHCII, CD38, and CD86 via NF-κB, STAT1, and IRF5 activity to mediate a pro-inflammatory state, anti-microbial activity, tumor resistance, tissue damage, and Th1 responses, from M2-like macrophages, which are induced by IL-4, IL-10, IL-13, or M-CSF and express the markers IL-10, VEGF, TGFβ, Arg-1, CD163, CD206, and Egr2 via STAT3, STAT6 and IRF4 activity to mediate an anti-inflammatory state, tissue regeneration and repair, angiogenesis and immune regulation, tumor progression, and Th2 responses. Figure inspired by (*72, 73*) and adapted from "Macrophage polarization: M1 and M2 subtypes" by BioRender.com (2023).

Nowadays, the M1/M2 macrophage paradigm is seen as an oversimplified approach to classifying macrophages as it does not adequately describe the broad spectrum of different macrophages, which in reality are highly dynamic and co-expressing many M1-like and M2-like macrophage markers context-dependently (*73*). While in a precisely functioning immune response, the shift towards anti-inflammatory M2-like macrophages

is crucial for the resolution of inflammation when the pathogenic invaders are removed, an unbalanced M1-like/M2-like macrophage ratio and macrophage over-activation are detrimental disease drivers (*46*). Therefore, understanding the processes of macrophage activation and targeting the major molecular pathways in inflammatory macrophages at the right time is crucial for re-directing adequate macrophage responses in inflammation-driven diseases.

1.1.4 Inflammatory TLR4 signaling in macrophages

As one of the major pathways in host defense, TLR signaling in activated macrophages initiates inflammation during sepsis, cancer, and other diseases. TLRs are a class of transmembrane PRRs that recognize PAMPs and DAMPs and trigger signaling cascades to activate the innate immune response via stimulation of downstream signaling molecules (*76*). TLRs are expressed in a wide range of cell types, encompassing both immune and non-immune cells such as monocytes, macrophages, dendritic cells, neutrophils, B cells, T cells, fibroblasts, endothelial cells, epithelial cells, and tumor cells (*77, 78*). Identified by R. M. Medzhitov in 1997, TLR4 was the first TLR identified in human monocytes and named after its homology with the Drosophila protein Toll, which mediates innate immunity in the fly (*79, 80*). Nowadays, ten functional TLRs (TLR1-10) in humans and twelve TLRs in mice (TLR1-9, TLR11-13) are known. TLR3, 7, 8, and 9 can be found in the membranes of endolysosomal compartments and have the capacity to recognize nucleic acids; the others are expressed on the cell membranes to recognize surface components of pathogens (*81, 82*). In M1-like activated macrophages, TLR4 signaling is among the well-studied pathways mediating inflammatory macrophage responses. During gram-negative bacterial sepsis, TLR4 signaling is activated by LPS (referred to as bacterial endotoxin), the main molecular component of the cell wall of gram-negative bacteria. In tumors, TLR4 signaling can be induced by multiple TLR4 ligands such as S100 calcium-binding protein A8/A9 (S100A8/9), heat-shock protein 90α (HSP90α), high-mobility group protein B1 (HMGB1), and bacterial LPS, which is frequently found in tumors (*83-89*). As it applies to inflammation in general, TLR4 activation can boost anti-tumor immune responses and fight bacterial infection but also give rise to tumor progression and cause detrimental cytokine storms in the context of sepsis (*78*).

To initiate LPS-induced signaling, LPS binding protein (LBP) binds LPS from bacterial membranes and transfers it to CD14, which can be soluble or membrane-bound via a glycosylphosphatidylinositol anchor (*90*). CD14 either mediates LPS-induced endocytosis of TLR4 or delivers LPS to the surface TLR4-myeloid differentiation factor 2 (MD-2) complex, allowing for LPS-induced TLR4-MD-2 dimerization (*91, 92*). Subsequently, intracellular myeloid differentiation primary response 88 (MyD88)-dependent and TIR-domain-containing adaptor-inducing interferon-β (TRIF)-dependent pathways get activated (Figure 4). Noteworthy, except for TLR3, all TLRs mediate signal transduction through MyD88 recruitment (*93*). In the MyD88-dependent pathway, the adaptor protein intracellular Toll/interleukin-1 receptor (TIR) domain containing adaptor protein (TIRAP; referred to as MAL) is recruited to the dimer of TIR domains of the dimerized TLR4. It forms a homodimer and possesses a phosphatidylinositol 4,5-bisphosphate (PIP_2)- and a phosphatidylinositol 3,4,5-triphosphate (PIP_3) binding domain that are necessary for its membrane anchoring to the plasma membrane and the endosomal membrane, respectively *(94)*. This forms the interface for binding of another adaptor protein, MyD88, which itself, via its death domains, binds the death domains of the serine/threonine kinases, interleukin-1 receptor-associated kinases (IRAK) 1/2 and 4, forming the so-called myddosome. The myddosome formation promotes IRAK4 auto-phosphorylation. IRAK1 has the ability to bind to the MyD88-IRAK4 complex and undergo phosphorylation by IRAK4. Besides MyD88, an additional adaptor protein known as Toll-interacting protein (Tollip) also associates with TLR4 and IRAK-1/2, inhibiting IRAK-1/2 auto-phosphorylation but not promoting IRAK-1/2 degradation (*95*). To date, Tollip is thought to inhibit TLR-mediated immune responses to control inflammatory cytokine production. However, it is also noteworthy that complete *Tollip* deficiency in mice significantly impaired cytokine production (*96*), underlining its regulatory potential. TNF receptor-associated factor 6 (TRAF6) binds to phosphorylated IRAK1, and IRAK1 phosphorylates TRAF6. TRAF6 is an E3 ubiquitin ligase, which promotes poly-ubiquitination of itself at lysine 63, and the polyubiquitin chains of TRAF6 are recognized by mitogen-activated protein kinase kinase kinase 7 (TAK1)-binding proteins 1 and 2 (TAB1 and 2; together referred to as TABs) and nuclear factor of kappa light polypeptide gene enhancer in B-cells inhibitor (IκB) kinase (IKK) γ subunit (referred to as NF-κB essential modulator, NEMO) of the multi-subunit IKK-complex (consisting of IKKα, IKKβ, and IKKγ). Activated TAK1 phosphorylates and

activates downstream IKK, which causes the catalytic subunits IKKα and IKKβ to phosphorylate IκBα. This promotes ubiquitin-dependent proteasomal degradation of IκB and the release of the transcription factor NF-κB (consisting of different dimers of the subunits p50, p65 (RelA), RelB, and c-Rel) into the nucleus, where it can induce pro-inflammatory gene expression *(97, 98)*. Noteworthy, through delayed feedback loops, MyD88-dependent signaling can also result in the expression of anti-inflammatory mediators such as IL-10 and PD-ligand 1 (PD-L1) to terminate the inflammation (*99-101*). Endocytosis of TLR4 into endosomes allows for TRIF-mediated production of IRF3-dependent pro-inflammatory genes and termination of signaling (*102*).

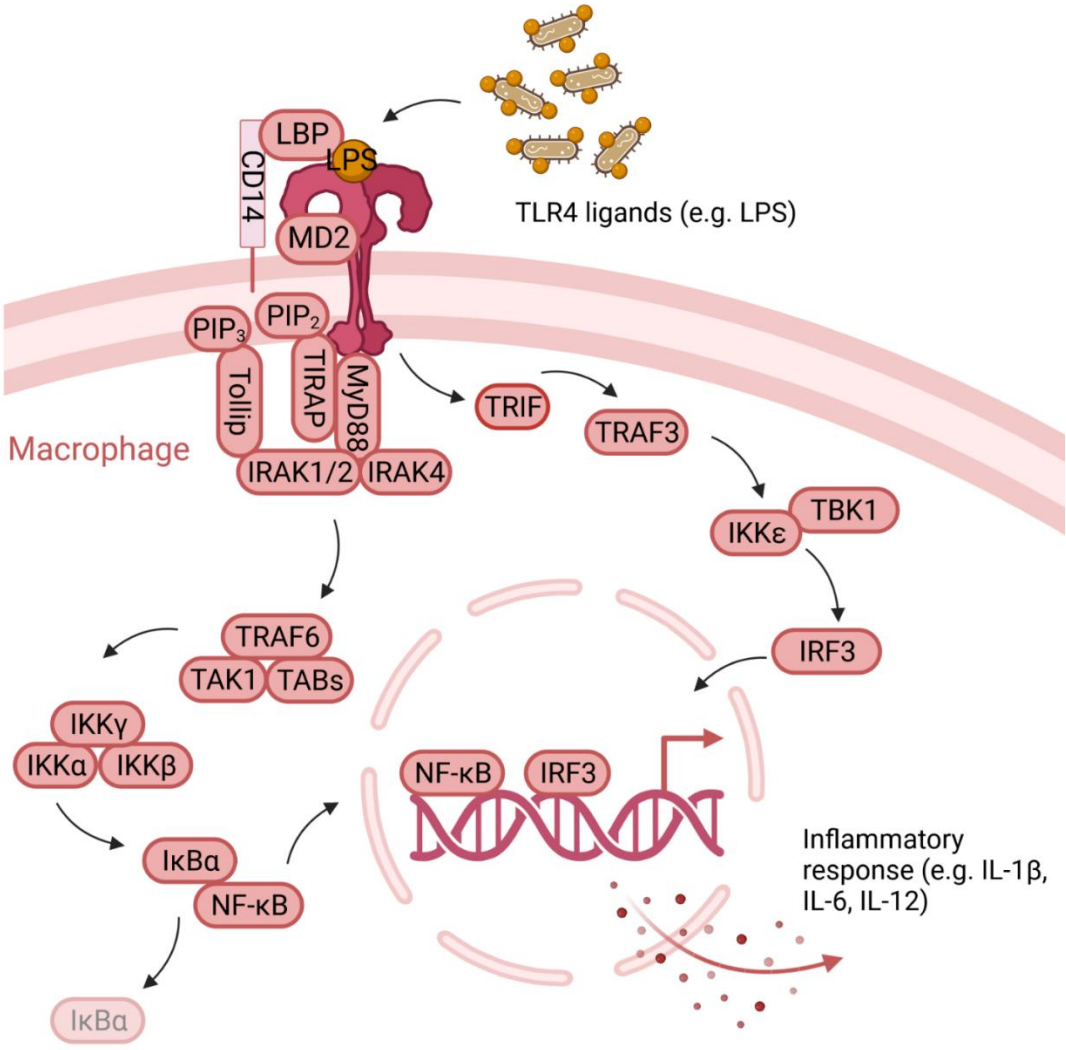

Figure 4 TLR4 signaling pathway in macrophages.

LBP/CD14/MD-2-mediated binding of the TLR4 ligand LPS causes TLR4 dimerization and intracellular recruitment of the adaptor proteins TIRAP and MyD88 or TRIF to trigger a downstream cascade, which

starts pro-inflammatory gene expression via the MyD88-dependent NF-κB or TRIF-dependent IRF3 arm, respectively. TANK-binding kinase 1, TBK1

Like many other signaling processes, TLR4 signaling predominately takes place in special 10-200 nm small membrane micro-domains, so-called lipid rafts, which function as platforms for signal transduction processes associated with cell adhesion, migration, cell survival, proliferation, apoptosis, and immune signaling (*103, 104*). The idea of lipid rafts originates from the “Fluid mosaic model” of S. J. Singer and G. Nicolson in 1972 and the later observation that lipids were not uniformly distributed in the cell membrane (*105-108*). Lipid rafts (referred to as caveolae) are rich in sterols, caveolin, G protein-coupled receptors (GPCRs), and sphingolipids, and upon LPS stimulation, TLR4, CD14, and their associated proteins get recruited, allowing for signaling initiation (*109-111*) (Figure 5).

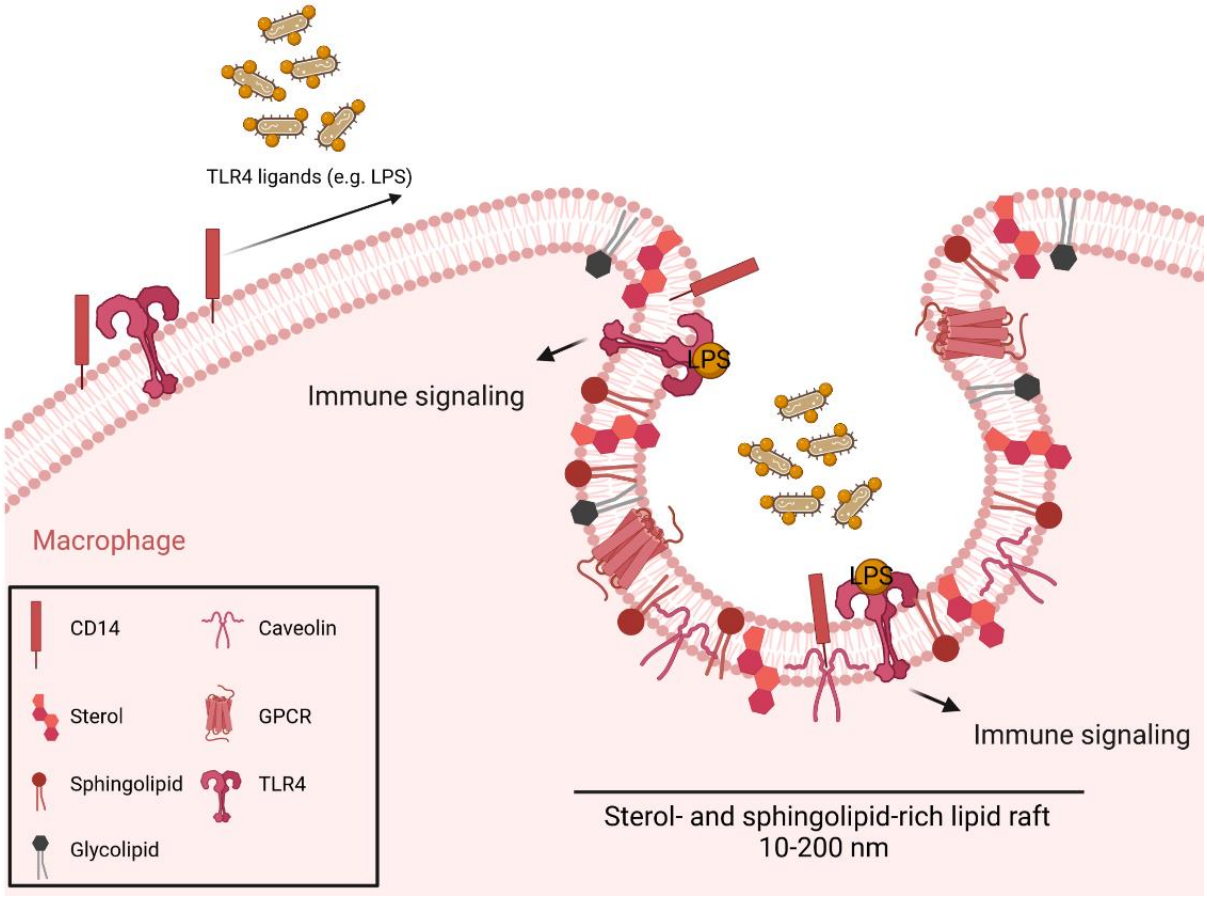

Figure 5 TLR4 signaling predominately takes place in lipid rafts.

Lipid rafts are 10-200 nm-wide membrane micro-domains that are rich in sterols, sphingolipids, caveolin, and GPCRs. Upon LPS challenge, TLR4, CD14, and associated proteins get recruited to lipid rafts and initiate inflammatory signaling pathways.

Even though many components of the TLR4-signaling pathway have been well characterized, some questions about the participation of lipid raft components in signaling regulation, whether the membrane recruitment of adaptor proteins is dependent solely on protein-protein interactions, how the signaling is confined, and the role of the signaling in the pathology of different diseases remain open (*112*). Therefore, the identification of TLR4-regulating factors is crucial to completely understanding how inflammatory signaling is driven.

Originally, metabolites were known to fuel bioenergetics and biosynthetic pathways, but in the past few years, it became clear that they often also regulate immune cell function, signal transduction, and lineage commitment, suggesting metabolite profiles as potential targets for modulation of immune cell functions. Apart from fulfilling energy storage functions and segregating internal constituents from the external environment in membranes, lipids turned out to have crucial roles as messengers in signal transduction and molecular recognition processes (*113*). Membrane lipids can be divided into glycerophospholipids, sterols, and sphingolipids, of which, in the past decades, especially bioactive sphingolipids have emerged as a novel class of interest for their critical roles in major biological processes and signaling pathways (*114, 115*).

1.2 Sphingolipids

Sphingolipids represent a complex class of polar lipids with both signaling and structural functions (*116*). They appear in all plants, animals, fungi, and some prokaryotes and viruses, where, due to their amphiphilic nature, they can mostly be found in membranes (*117*). In macrophages, they make up about 20% of all membrane lipids (*118, 119*). However, sphingolipids can also be found in biological fluids and transported by proteins (*120*). Named by J. L. W. Thudichum in the 1870s for their enigmatic properties (*1*), sphingolipids have been increasingly studied in the past decades to understand their impact on multiple biological processes in health and disease. Yet, until today, many enigmas about bioactive sphingolipids remain unsolved.

1.2.1 Sphingolipid structure and metabolism

Structurally, sphingolipids share the aliphatic amino-alcohol sphingosine, which is condensed to a fatty acid via an amide bond, forming ceramide (Cer), which represents the core of most sphingolipids (*117*). Further, a variety of different moieties can be attached, forming complex sphingolipids with both polar and nonpolar regions. In detail, the *de novo* pathway of sphingolipid metabolism begins with the pyridoxal-5'-phosphate (PLP)-dependent, irreversible, and rate-limiting condensation of L-serine and palmitoyl-coenzyme A (CoA) to 3-ketosphinganine (3-KDS), as catalyzed by the enzyme serine palmitoyltransferase (SPT) (Figure 6). SPT is embedded in the endoplasmic reticulum (ER) membrane and consists of a dimer of the two major subunits, SPT long chain base subunit 1 (Sptlc1) and the catalytically active subunit Sptlc2, and the small subunits ssSPTa and ssSPTb, which regulate substrate specificity (*121, 122*). In 2006, a third SPT subunit, Sptlc3, which has 68% amino acid sequence identity to Sptlc2, was identified (*123*). Following reduction to sphinganine (Sa; referred to as dihydrosphingosine), different ceramide synthases generate distinct dihydroceramides through N-acylation, which are then desaturated through the introduction of a *trans*-Δ4 double bond in the sphingoid backbone to generate ceramides, which can be modified to various sphingolipid species. Ceramides can be transformed in the ER and Golgi apparatus through ceramide kinase to ceramide-1-phosphate (C1P), through sphingomyelin synthase to sphingomyelin, through galactosylceramide synthase to galactosylceramide, or through glucosylceramide synthase to glucosylceramide (GlcCer), and then to cerebrosides and gangliosides. Additionally, ceramides can be deacylated to form sphingosine and subsequently phosphorylated to sphingosine-1-phosphate (S1P). S1P can be degraded via S1P lyase to form phosphoethanolamine and hexadecenal, which are precursors for glycerophospholipids (*124, 125*) (Figure 6). Noteworthy, sphingolipids can also be generated in salvage pathways through the degradation of more complex sphingolipids by, for example, ceramidases, exoglycosidases, and sphingomyelinases in endosomal and lysosomal compartments (*117*). The high complexity and rapid compartment-specific interconversion of sphingolipids suggest that such a refined metabolic system has evolved to adapt to the cell's requirements and to control the levels of bioactive sphingolipids, which in turn mediate cellular functions (*117*).

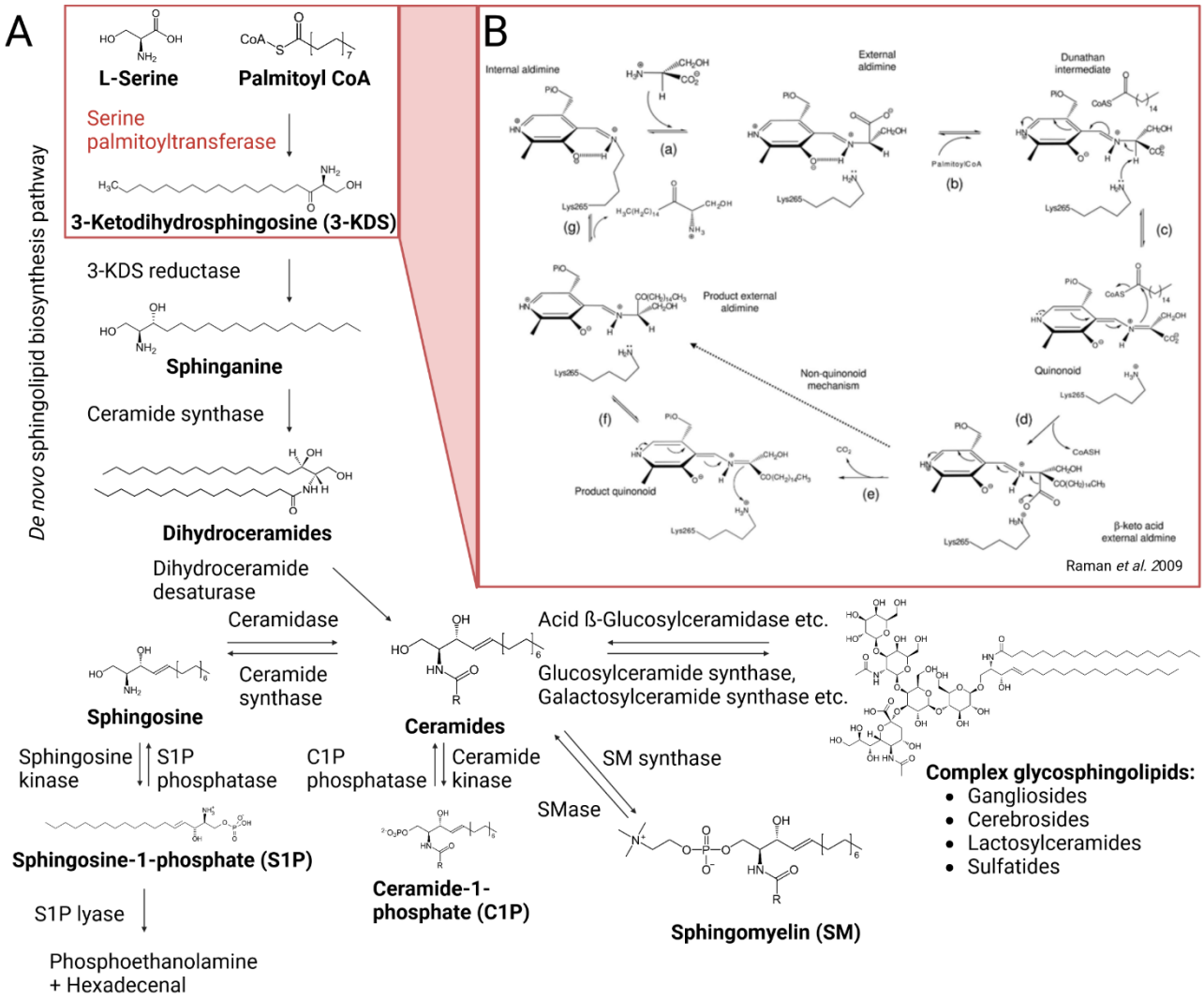

Figure 6 Overview of sphingolipid metabolism with main focus on serine palmitoyltransferase.

(A) *De novo* sphingolipid biosynthesis begins with the condensation of L-serine and palmitoyl-CoA, catalyzed by the enzyme serine palmitoyltransferase (SPT). Via 3-KDS, sphinganine and dihydroceramides form ceramides, which can be converted to sphingomyelin, complex glycosphingolipids, sphingosine, or ceramide-1-phosphate. Sphingosine can be converted to sphingosine-1-phosphate and degraded to phosphoethanolamine and hexadecenal.

(B) The detailed mechanism of the reaction catalyzed by SPT was taken from (*126*).

1.2.2 Biological functions of sphingolipids

Apart from their structural functions as membrane components, it is especially their ability to regulate cellular signaling that makes sphingolipids interesting targets in diverse malignancies. The first to show a bioactive effect of sphingolipids was Y. A. Hannun, who described the role of sphingosine in inhibiting protein kinase C to regulate protein

synthesis relevant to multiple physiologic processes in 1986 (*127*). Sphingolipids are involved in cell growth, adhesion, migration, and death. They can act as intracellular second messengers to transduce extracellular signals, alter the cell's responses by changing the membrane composition, or induce cellular outcomes through binding to cell surface receptors (*117*). Defects in sphingolipid metabolism are linked to neurodegenerative diseases such as lysosomal storage disorders, hereditary sensory and autonomous neuropathy (HSAN), some forms of Parkinson's disease (PD), and amyotrophic lateral sclerosis (ALS) (*128, 129*). For example, in HSAN-1, disruption of sphingolipid metabolism through *SPTLC2* mutations causes a shift in substrate specificity of SPT, leading to the accumulation of neurotoxic atypical deoxy-sphingoid bases and impaired CD8+ T cell responses (*130, 131*). Moreover, several studies suggest the crucial roles of sphingolipids in inflammation-driven diseases, as altered levels of different sphingolipid species severely impact immune cell functions and thereby inflammation (*132-134*). Recently, it was reported that certain sphingolipids are enriched in B16 melanoma, murine sarcoma, Lewis lung carcinoma, human head and neck squamous cell carcinoma (HNSCC), rat nephroma-RA, and breast cancer (*133*). Furthermore, it was reported that severe acute respiratory syndrome coronavirus type 2 (SARS-CoV-2) infection induced elevation of sphingolipid levels in both cells and sera of infected mice (*135*) and also in sepsis, sphingolipid metabolites were increased (*136*).

Due to their high complexity and ability to interconvert, sphingolipids are thought to be rapidly metabolized following a certain stimulus and thereby regulate cell fate. The most prominent example of this is captured in the so-called "sphingolipid rheostat" from 1996, which suggested that ceramide, by promoting apoptosis, and S1P, by promoting cell proliferation and survival and thereby tumor progression, induce opposing signaling pathways (*137*). Mechanistically, in many cells, S1P was reported to be induced upon activation of sphingosine kinases in response to cytokines or growth factors and secreted to then act in an autocrine or paracrine manner through specific G protein-coupled S1P receptors (S1PRs), which is also known as inside-out signaling by S1P (*138*). S1PR activation can activate the pro-survival extracellular signal-regulated kinase (Erk) and protein kinase B (Akt) signaling pathways, and S1PR3 can activate the mechanistic target of rapamycin (mTOR) pathway cascade that inhibits ceramide-mediated autophagy (*139*). The E3 ubiquitin ligase TRAF2 is another intracellular target activated through the binding

of S1P, allowing for downstream pro-growth NF-κB signaling and thus driving inflammatory immune responses (*140*). Further, S1P can increase histone acetylation by binding to and inhibiting histone deacetylases 1 and 2 and can thereby epigenetically regulate the expression of specific target genes (*141*). Ceramide, on the other hand, is induced following apoptotic stimuli such as TNFα or nitric oxide (NO) and allows for the formation of large protein-permeable channels in the outer mitochondrial membrane, allowing for the release of pro-apoptotic proteins from the mitochondria (*142-145*). Noteworthy, ceramides with different fatty acid chain lengths can be either pro- or anti-apoptotic (*146*). As a result, targeting several ceramide- and S1P-associated enzymes, such as oncogenic sphingosine kinase 1 (SphK1), became a promising approach for manipulating the ceramide/S1P axis to control cell proliferation and death in cancer (*147-149*). There are numerous more examples of bioactive sphingolipids that regulate cellular processes, such as glucosylceramides, which cause tissue inflammation in the lysosomal storage disease Gaucher's disease (*150*), or sphingomyelin, which regulates cell adhesion through lowering C-X-C motif chemokine 12 (CXCL12)-induced cell migration (*114, 151*). Unsurprisingly, in the course of deciphering the role of sphingolipids in inflammation, TLR4-mediated inflammatory signaling has also been extensively studied in the past few years (*152*).

1.2.3 Sphingolipids in TLR4 signaling

Apart from causing metabolic adaptations such as enhancing aerobic glycolysis (*153, 154*) and tricarboxylic acid (TCA) cycle activity (*155-157*), TLR activation also induces changes in lipid metabolism, especially in the sphingolipid composition of cellular membranes (*118, 158-161*). In 2010, it was found that LPS rapidly increases sphinganine levels, which is followed by increased downstream metabolites such as ceramides (Cer), glycosphingolipids, and sphingomyelins (*118, 161*). One year later, Sptlc2 expression and activity were reported to be induced by LPS via NF-κB (*162*). Remarkably, the sphingolipid production kinetics in macrophages propose that, in addition to TLR4 signaling inducing sphingolipids, certain sphingolipid species have the ability to specifically modulate either the early pro-inflammatory stages or the later resolution phases of TLR4 activation (*152*). While gangliosides prevent TLR4 localization to lipid rafts and MyD88 binding, thereby inhibiting TLR4 signaling (*163, 164*), other sphingolipids such as sphingomyelin and the

key enzyme Sptlc2 promote TLR4/NF-kB signaling in macrophages by so far unknown mechanisms (*161, 165*). In line with this, the assembly and activation of the TLR4 receptor subsequent to LPS binding to CD14 necessitate the production of ceramides (*166*). Contrary to this, in 2015 it was reported that *Sptlc2* ablation did not impact macrophage polarization (*167*), but in the same year, another report stated that sphingolipids, and especially different ceramides, regulate the TLR4-mediated innate immune response in M1-like macrophages (*116*). In more detail, certain ceramide species enhance (e.g., N-C18:0 (OH)-Cer) or diminish (e.g., N-C8:0 (2H)-Cer) LPS-induced IL-6 release in RAW 264.7 cells upon LPS treatment (*116*). Supporting this, the SPT inhibitor myriocin (*168*) inhibits pro-inflammatory gene expression in LPS-activated RAW 264.7 macrophages (*169*). Mechanistically, regulation of lipid raft formation and TLR4 complex assembly and internalization in activated macrophages is thought to be the mode of action by which sphingolipids regulate TLR4 signaling (*152*). However, more detailed mechanistic insights into how sphingolipids positively regulate TLR4 signaling, which could potentially allow for sphingolipid-targeting pharmacological options to interfere with inflammatory TLR4 signaling in macrophages, have been absent until today.

2. Aims of the work

Macrophages are attributed to being involved in both limiting and driving inflammation, which is crucial for the formation but also the clearance of different diseases. Sphingolipid metabolism increasingly emerges as a regulator of inflammatory processes. From literature research and previous *in vitro* gain- and loss-of-function models using chemical inhibitors of sphingolipid metabolism, I suspected sphingolipid *de novo* biosynthesis via Sptlc2 to be important for M1-like macrophage polarization (Hering, M.; 2020; *To study the role of sphingolipids in macrophage polarization*; Master's thesis (*170*); Supplementary Figure 32).

The primary aim of this project was to decipher how Sptlc2-dependent sphingolipid generation differs between un-activated (M0-like) and differently activated (M1- and M2-like) macrophage subtypes and how this regulates macrophage function (Figure 7). The follow-up aim was to mechanistically understand the mode of action by which sphingolipids regulate cellular processes in macrophages. The third aim was to transfer the findings from aims 1 and 2 into suitable *in vivo* disease mouse models. In other words, the objectives of this work can be summarized in the following questions:

1. How does the sphingolipidome differ between macrophage subtypes, and are these differences metabolically, phenotypically, or functionally relevant?

2. Which macrophage pathways are regulated by sphingolipids, and what are the underlying mechanisms?

3. In which disease scenarios are these relevant?

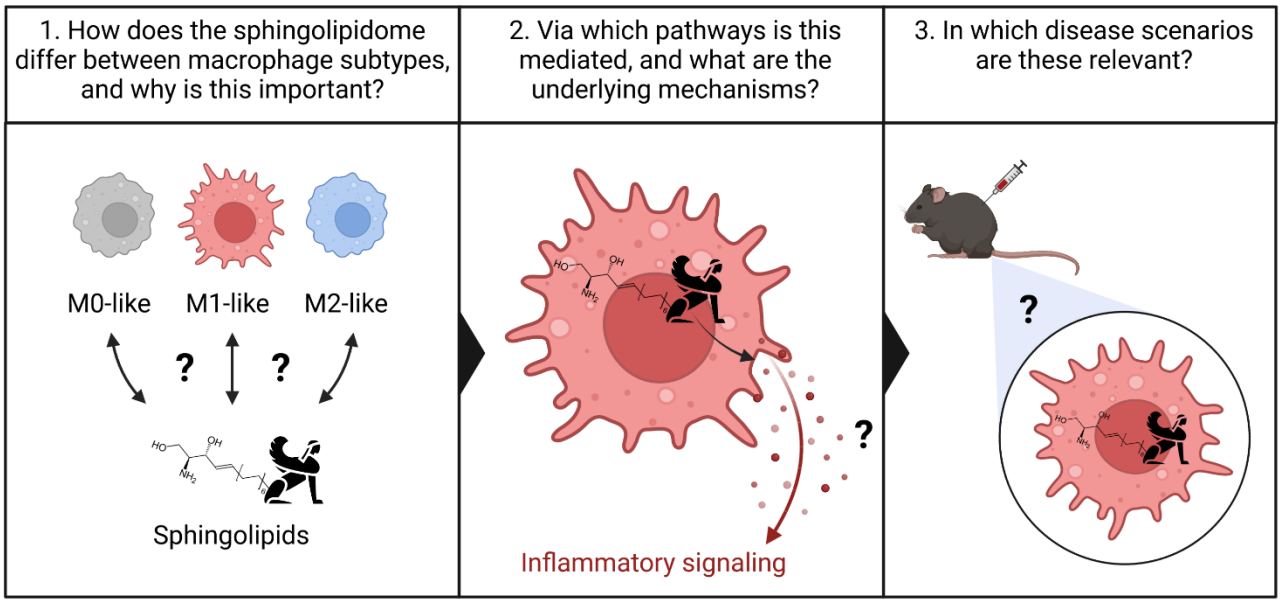

Figure 7 Aims of the project.

First, sphingolipid profiles of un-activated (M0), M1-, and M2-activated macrophage subtypes were analyzed. Second, the role of sphingolipid metabolism on macrophage signaling pathways was studied. Third, the findings were transferred to *in vivo* mouse models.

The long-term aim of this work is to contribute to deciphering the signaling role of sphingolipid metabolism in immune cell functions and to provide potential targets for pharmacological modulation of sphingolipid metabolism.

3. Materials

3.1 Biological materials

3.1.1 Mouse strains

Table 1 Mouse strains

Short name	Complete name	Source/Reference	Identifier
CD11c-cre	B6.Cg-Tg(Itax-cre)1-1Reiz/J	The Jackson Laboratory (Bar Harbor, USA), (*171*)	MGI:J:125869
Lysozyme 2 (*Lyz2)*-cre	B6.129P2-*Lyz2*$^{tm1(cre)Ifo}$/J	The Jackson Laboratory (Bar Harbor, USA), (*172*)	MGI:J:67924
P14	Tg(TcrLCMV)327Sdz	Prof. Dr. Hanspeter Pircher, Max Planck Institut für Immunbiologie und Epigenetik, Freiburg, Germany, (*173*)	MGI:2665105
Sptlc2^{Flox}	*Sptlc2*$^{Flox/Flox}$	Prof. Xian-cheng Jiang (State University of New York (SUNY) Downstate Medical Center, New York, USA), (*174*)	

3.1.2 Mammalian cell lines and bacteria

Table 2 Mammalian cell lines and bacteria

Cells or bacteria	Source/Reference	Identifier
B16-F10 cells	Prof. Dr. Hanspeter Pircher, Max Planck Institut für Immunbiologie und Epigenetik, Freiburg, Germany	
Human embryonic kidney (HEK) 293T cells	Prof. Dr. Susan Kaech, Salk Institute for Biological Sciences, La Jolla, USA	
Ret cells (established from skin melanomas of *ret* transgenic mice)	Prof. Dr. Viktor Umansky, Skin Cancer Unit, DKFZ, Heidelberg, Germany and Department of Dermatology, Venereology, and Allergology, UMM, Mannheim, Germany, (*175*)	
Subcloning efficiency™ DH5α competent cells	Thermo Fisher Scientific (Waltham, USA)	18265017

3.1.3 Chemicals, reagents, and solutions

Isoflurane for mouse anesthesia was acquired from the German Cancer Research Center's narcotics pharmacy.

Table 3 Chemicals, reagents, and solutions

Chemical, reagent, or solution	Source	Identifier
10× H buffer	Takara (Kusatsu, Japan)	SD0007
$^{13}C_3{}^{15}N_1$ L-serine	Sigma-Aldrich (St. Louis, USA)	608130
2-deoxy-D-glucose (2-DG)	Cayman Chemical (Ann Arbor, USA)	14325
3-ketosphinganine (d18:0)	Cayman Chemical (Ann Arbor, USA)	Cay24380
4′,6-diamidino-2-phenylindole (DAPI), dihydrochloride	Sigma-Aldrich (St. Louis, USA)	268298
Acrylamide/Bis solution, 29:1 (30% w/v)	Serva (Heidelberg, Germany)	10687
Agar	Merck Millipore (Darmstadt, Germany)	05039
Agarose	Sigma-Aldrich (St. Louis, USA)	A9539
Amersham™ enhanced chemiluminescence (ECL) select™ western blotting detection reagent	Cytiva (Marlborough, USA)	RPN2235
AminoLink™ plus coupling resin	Thermo Fisher Scientific (Waltham, USA)	20505
Ammonium persulfate (APS)	Bio-Rad Laboratories (Hercules, USA)	1610700

Ampicillin (Amp)	Sigma-Aldrich (St. Louis, USA)	A5354
Antimycin A (AA) from *Streptomyces sp.*	Sigma-Aldrich (St. Louis, USA)	A8674
Biotin	Sigma-Aldrich (St. Louis, USA)	B4501
Bis(sulfosuccinimidyl) suberat (BS3)	Thermo Fisher Scientific (Waltham, USA)	21580
Bovine serum albumin (BSA)	Sigma-Aldrich (St. Louis, USA)	A9647
Carbonyl cyanide 4-(trifluoromethoxy) phenylhydrazone (FCCP)	Cayman Chemical (Ann Arbor, USA)	15218-50
Clarity western ECL substrate	Bio-Rad Laboratories (Hercules, USA)	1705061
Coomassie Brilliant Blue De-staining solution	G-Biosciences (Saint Louis, USA)	786-499
Coomassie Brilliant Blue R-250 solution	G-Biosciences (Saint Louis, USA)	786-498
CutSmart™ buffer	New England Biolabs (Ipswich, USA)	B7204
D-(+)-glucose solution	Sigma-Aldrich (St. Louis, USA)	G8644
Dimethyl sulfoxide (DMSO)	Sigma-Aldrich (St. Louis, USA)	D8418
Ethanol (EtOH)	Sigma-Aldrich (St. Louis, USA)	32205
Fetal bovine serum (FBS)	Sigma-Aldrich (St. Louis, USA)	F0804

Fixation buffer (4% paraformaldehyde)	BioLegend (San Diego, USA)	420801
Fluoromount™ aqueous mounting medium	Sigma-Aldrich (St. Louis, USA)	F4680
GeneRuler 1 kb Plus DNA ladder	Thermo Fisher Scientific (Waltham, USA)	SM1332
Geneticin disulphate (G418) solution	Carl Roth (Karlsruhe, Germany)	0239.3
Gibco™ 2-mercaptoethanol	Thermo Fisher Scientific (Waltham, USA)	31350010
Gibco™ Ammonium-chloride-potassium (ACK) lysing buffer	Thermo Fisher Scientific (Waltham, USA)	A1049201
Gibco™ Dulbecco's phosphate-buffered saline (DPBS) (calcium, magnesium), PBS	Thermo Fisher Scientific (Waltham, USA)	14040
Gibco™ Dulbecco's modified Eagle Medium (DMEM; high glucose)	Thermo Fisher Scientific (Waltham, USA)	41965
Gibco™ Hanks' balanced salt solution (HBSS)	Thermo Fisher Scientific (Waltham, USA)	14175095
Gibco™ Iscove's modified Dulbecco's medium (IMDM)	Thermo Fisher Scientific (Waltham, USA)	21980032
Gibco™ MEM non-essential amino acids (NEAA) solution (100×)	Thermo Fisher Scientific (Waltham, USA)	11140050
Gibco™ Opti-MEM™ I reduced serum medium	Thermo Fisher Scientific (Waltham, USA)	31985062

Gibco™ Penicillin-streptomycin (Pen-Strep) (10 000 U/mL)	Thermo Fisher Scientific (Waltham, USA)	14140122
Gibco™ Roswell Park Memorial Institute (RPMI) 1640 medium	Thermo Fisher Scientific (Waltham, USA)	21875034
Gibco™ trypsin-ethylenediaminetetraacetic acid (EDTA) (0.25%)	Thermo Fisher Scientific (Waltham, USA)	25200056
Glycine	Gerbu Biotechnik (Heidelberg, Germany)	1023.1000
Hydrochloric acid (HCl)	Chemlab (Zedelgem, Belgium)	CL00.0319
Invitrogen™ CellTrace™ blue stain	Thermo Fisher Scientific (Waltham, USA)	C34574
Invitrogen™ CellTrace™ violet cell proliferation kit, for flow cytometry	Thermo Fisher Scientific (Waltham, USA)	C34557
Invitrogen™ Dynabeads™ M-280 streptavidin	Thermo Fisher Scientific (Waltham, USA)	11206D
Invitrogen™ Dynabeads™ protein A for immunoprecipitation	Thermo Fisher Scientific (Waltham, USA)	10002D
Invitrogen™ eBioscience™ Forkhead box P3 (Foxp3)/transcription factor staining buffer set	Thermo Fisher Scientific (Waltham, USA)	00-5523-00
Invitrogen™ eBioscience™ permeabilization buffer (10×)	Thermo Fisher Scientific (Waltham, USA)	00-8333-56

Invitrogen™ SYBR™ Safe DNA gel stain	Thermo Fisher Scientific (Waltham, USA)	S33102
Isopropanol	Sigma-Aldrich (St. Louis, USA)	33539
Laemmli sample buffer (2×) (2× loading dye, 2× LD)	Bio-Rad Laboratories (Hercules, USA)	1610737
Laemmli sample buffer (4×)	Bio-Rad Laboratories (Hercules, USA)	1610747
Laemmli sodium dodecyl sulfate (SDS) sample buffer, reducing (6×)	Thermo Fisher Scientific (Waltham, USA)	J61337
L-glutamine solution	Sigma-Aldrich (St. Louis, USA)	G7513
LIVE/DEAD™ fixable red dead cell stain kit, for 488 nm excitation	Thermo Fisher Scientific (Waltham, USA)	L34972
Magnesium chloride ($MgCl_2$)	Sigma-Aldrich (St. Louis, USA)	M8266
Methanol	Merck Millipore (Darmstadt, Germany)	106009
Milk powder	Carl Roth (Karlsruhe, Germany)	T145.3
Murine stem cell virus (MSCV)-internal ribosome entry site (IRES)-green fluorescent protein (GFP) vector (MigR1-GFP)	Addgene (Watertown, USA)	20672
NaCl solution (0.9%)	B. Braun (Melsungen, Germany)	3570410
NM_010851 (MyD88-containing plasmid)	OriGene (Rockville, USA)	MR227105

Nuclease-free water	Qiagen (Venlo, Netherlands)	129117
Oligomycin	Sigma-Aldrich (St. Louis, USA)	495455
PageRuler™ prestained protein ladder	Thermo Fisher Scientific (Waltham, USA)	26616
PageRuler™ unstained protein ladder	Thermo Fisher Scientific (Waltham, USA)	26614
Palmitic acid	Sigma-Aldrich (St. Louis, USA)	P0500
pCL-Eco (eco-helper plasmid)	Addgene (Watertown, USA)	12371
Radioimmunoprecipitation assay buffer (RIPA) lysis buffer system	Santa Cruz Biotechnology (Dallas, USA)	sc-24948
Rotenone (Rot)	Cayman Chemical (Ann Arbor, USA)	13995-5
Sodium azide (NaN_3)	Sigma-Aldrich (St. Louis, USA)	S2002
Sodium chloride (NaCl)	Sigma-Aldrich (St. Louis, USA)	S9888
Sodium cyanoborohydride solution	Sigma-Aldrich (St. Louis, USA)	296945
Sodium hydroxide (NaOH)	Carl Roth (Karlsruhe, Germany)	T135.1
Sodium phosphate	Sigma-Aldrich (St. Louis, USA)	342483
Sodium pyruvate	Sigma-Aldrich (St. Louis, USA)	P5280
Sphinganine (d18:0)	Cayman Chemical (Ann Arbor, USA)	Cay10007945

Sphinganine-biotin	Echelon Biosciences (Logan, USA)	S-110B
Sphingomyelin	Enzo Life Sciences (Farmingdale, USA)	BML-SL135
Sulfuric acid (H_2SO_4)	Sigma-Aldrich (St. Louis, USA)	339741
Tetramethylethylenediamine (TEMED)	Bio-Rad Laboratories (Hercules, USA)	161-0801
Triton X-100	Bio-Rad Laboratories (Hercules, USA)	161-0407
TriTrack DNA LD (6×)	Thermo Fisher Scientific (Waltham, USA)	R1161
Trizma® base (Tris)	Sigma-Aldrich (St. Louis, USA)	T1503
Trypan blue solution	Sigma-Aldrich (St. Louis, USA)	T8154
Tryptone/peptone ex casein	Carl Roth (Karlsruhe, Germany)	8952.2
Tween® 20, molecular biology grade	Promega (Madison, USA)	H5152
XF base medium	Agilent Technologies (Santa Clara, USA)	102353-100
XF calibrant	Agilent Technologies (Santa Clara, USA)	100840-000
X-tremeGENE™ HP DNA transfection reagent	Roche (Basel, Switzerland)	6366244001
Yeast extract, ultrapure	Gerbu Biotechnik (Heidelberg, Germany)	1133

3.2 Buffers

For buffer preparation, double-distilled water (ddH_2O) was used.

Table 4 Home-made buffers

Buffer	Composition
Complete DMEM	10% (v/v) FBS 1% (v/v) Pen-Strep DMEM
Complete IMDM	10% (v/v) FBS 1% (v/v) Pen-Strep IMDM
Complete RPMI	10% (v/v) FBS 1% (v/v) Pen-Strep RPMI 1640
ELISA blocking buffer	1% (w/v) BSA PBS pH 7.2-7.4
ELISA stop solution	2 N H_2SO_4
ELISA substrate solution	1:1 Mixture of color reagent A (H_20_2) and color reagent B (tetramethylbenzidine)
ELISA wash buffer	0.05% Tween® 20 PBS pH 7.2-7.4
FACS buffer	2% (v/v) FBS PBS
Freezing medium	10% (v/v) DMSO FBS
LB agar (for plates)	1.5% (w/v) Agar LB medium
LB medium	1% (w/v) Tryptone/peptone 0.5% (w/v) Yeast extract 0.17 M NaCl

	ddH_2O
MACS buffer	0.5% (v/v) FBS
	PBS
Microscopy buffer	5% (w/v) BSA
	PBS
PBS-Tween® 20 (PBS-T)	0.01% (v/v) Triton X-100
	PBS
SDS running buffer	25 mM Tris
	0.19 M Glycine
	1% (w/v) SDS
	ddH_2O
SDS polyacrylamide gel electrophoresis (SDS-PAGE) resolving gel (8%)	8% Acrylamide/bis solution
	375 mM Tris-HCl, pH 8.8
	0.1% (w/v) SDS
	0.1% (w/v) APS
	0.04% (w/v) TEMED
	ddH_2O
SDS-PAGE stacking gel (5%)	5% Acrylamide/bis solution
	125 mM Tris-HCl, pH 6.8
	0.1% (w/v) SDS
	0.1% (w/v) APS
	0.04% (w/v) TEMED
	ddH_2O
Tris-acetate-EDTA-buffer (TAE) buffer	40 mM Tris-acetate
	1 mM EDTA
	ddH_2O
	pH 7.4
Western blot blocking buffer	5% (w/v) Milk powder
	PBS-T
Western blot transfer buffer	25 mM Tris
	190 mM Glycine

	20% (v/v) Methanol ddH_2O
1.0 M Tris-HCl buffer (for gels)	1.0 M Tris ddH_2O pH 6.8
1.0 M Tris-HCl buffer (for genotyping)	1.5 M Tris ddH_2O pH 7.8
1.5 M Tris-HCl buffer (for gels)	1.5 M Tris ddH_2O pH 8.8

3.3 Kits

Table 5 Kits

Kit	Source	Identifier
CD8a+ T cell isolation kit	Miltenyi Biotec (Bergisch Gladbach, Germany)	130-104-075
Invitrogen™ SilverQuest™ staining kit	Thermo Fisher Scientific (Waltham, USA)	LC6070
Mouse IFN-gamma DuoSet™ ELISA	R&D Systems (Minneapolis, USA)	DY485
Mouse IL-1 beta/IL-1F2 DuoSet™ ELISA	R&D Systems (Minneapolis, USA)	DY401
Mouse IL-10 DuoSet™ ELISA	R&D Systems (Minneapolis, USA)	DY417
Mouse IL-12 p70 DuoSet™ ELISA	R&D Systems (Minneapolis, USA)	DY419
Mouse IL-12/IL-23 p40 non allele-specific DuoSet™ ELISA	R&D Systems (Minneapolis, USA)	DY2398

Mouse IL-18 DuoSet™ ELISA	R&D Systems (Minneapolis, USA)	DY7625
Mouse IL-6 DuoSet™ ELISA	R&D Systems (Minneapolis, USA)	M406
Mouse TNF-alpha DuoSet™ ELISA	R&D Systems (Minneapolis, USA)	DY410
MxP® Quant 500 XL kit	Biocrates life sciences ag (Innsbruck, Austria)	21469.2
Pierce™ bicinchoninic acid (BCA) protein assay kit	Thermo Fisher Scientific (Waltham, USA)	23227
Pierce™ chromogenic endotoxin quant kit (Limulus amebocyte lysate (LAL) assay)	Thermo Fisher Scientific (Waltham, USA)	A39552
Proteome profiler mouse cytokine array kit, Panel A	R&D Systems (Minneapolis, USA)	ARY006
QIAprep PCR purification kit	Qiagen (Venlo, Netherlands)	28104
QIAprep spin Miniprep kit	Qiagen (Venlo, Netherlands)	27104
QIAquick gel extraction kit	Qiagen (Venlo, Netherlands)	28706

3.4 Antibodies

3.4.1 Fluorochrome-coupled antibodies

Table 6 Fluorochrome-coupled antibodies

Antibody	Clone	Dilution (Use)	Source	Identifier
Alexa Fluor® 488 anti-GFP	FM264G	1:200 (Fluorescence-activated cell sorting, FACS); 1:50 (Confocal fluorescence microscopy, CFM)	BioLegend (San Diego, USA)	338008
Alexa Fluor® 488 donkey anti-rabbit immunoglobulin G (IgG)	Poly4064	1:200 (FACS)	BioLegend (San Diego, USA)	406416
Alexa Fluor® 647 donkey anti-rabbit IgG	Poly4064	1:200 (FACS)	BioLegend (San Diego, USA)	406414
APC anti-mouse CD284 (TLR4)	MTS510	1:50 (CFM)	Miltenyi Biotec (Bergisch Gladbach, Germany)	130-102-509
APC anti-mouse EGF-like module-containing mucin-like hormone receptor-like 1 (F4/80)	RE126	1:200 (FACS)	Miltenyi Biotec (Bergisch Gladbach, Germany)	130-116-547
APC anti-mouse IL-6	REA1034	1:200 (FACS)	Miltenyi Biotec (Bergisch Gladbach, Germany)	130-117-434

APC anti-mouse/human CD11b	M1/70	1:200 (FACS)	BioLegend (San Diego, USA)	101212
APC goat anti-rat IgG	Poly4054	1:100 (CFM)	BioLegend (San Diego, USA)	405407
APC/Cyanine7 anti-mouse CD38	90	1:200 (FACS)	BioLegend (San Diego, USA)	102728
APC/Cyanine7 anti-mouse/human CD11b	M1/70	1:200 (FACS)	BioLegend (San Diego, USA)	101226
APC/Fire™ 750 anti-human/mouse granzyme B recombinant antibody	QA16A02	1:200 (FACS)	BioLegend (San Diego, USA)	372210
Brilliant Violet 421™ anti-mouse IgM	RMM-1	1:200 (FACS)	BioLegend (San Diego, USA)	406517
Brilliant Violet 711™ anti-mouse CD45	30-F11	1:200 (FACS)	BioLegend (San Diego, USA)	103147
Brilliant Violet 711™ anti-mouse/human CD44	IM7	1:200 (FACS)	BioLegend (San Diego, USA)	103057
Brilliant Violet 785™ anti-mouse CD45	30-F11	1:200 (FACS)	BioLegend (San Diego, USA)	103149
FITC anti-mouse CD4	GK1.5	1:200 (FACS)	BioLegend (San Diego, USA)	100406

FITC anti-mouse CD8a	5H10-1	1:200 (FACS)	BioLegend (San Diego, USA)	100804
FITC anti-mouse Lymphocyte antigen 6 complex, locus C1 (Ly6C)	HK1.4	1:200 (FACS)	BioLegend (San Diego, USA)	128006
PE anti-mouse CD86	GL-1	1:200 (FACS)	BioLegend (San Diego, USA)	105008
PE anti-mouse Egr2	REA869	1:100 (FACS)	Miltenyi Biotec (Bergisch Gladbach, Germany)	130-114-256
PE anti-mouse I-A/I-E (MHCII)	M5/114.15.2	1:200 (FACS)	BioLegend (San Diego, USA)	107608
PE anti-mouse IL-12 (p40/p70)	REA136	1:200 (FACS)	Miltenyi Biotec (Bergisch Gladbach, Germany)	130-102-163
PE anti-mouse T cell immunoreceptor with immunoglobulin and ITIM domain (TIGIT) (Vstm3)	1G9	1:200 (FACS)	BioLegend (San Diego, USA)	142104
PE anti-mouse TNFα	MP6-XT22	1:200 (FACS)	BioLegend (San Diego, USA)	506306

PE donkey anti-rabbit IgG	Poly4064	1:200 (FACS); 1:100 (CFM)	BioLegend (San Diego, USA)	406421
PE/Cyanine7 anti-mouse CD279 (PD-1)	29F.1A12	1:200 (FACS)	BioLegend (San Diego, USA)	135216
PE/Cyanine7 anti-mouse CD69	H1.2F3	1:200 (FACS)	BioLegend (San Diego, USA)	104512
PE/Cyanine7 anti-mouse F4/80	BM8	1:200 (FACS)	BioLegend (San Diego, USA)	123114
PerCP/Cyanine5.5 anti-mouse CD8a	53-6.7	1:200 (FACS)	BioLegend (San Diego, USA)	100734
PerCP/Cyanine5.5 anti-mouse H-2D^{b} (MHCI)	KH95	1:200 (FACS)	BioLegend (San Diego, USA)	111518
PerCP/Cyanine5.5 anti-mouse I-A/I-E (MHCII)	M5/114.15.2	1:200 (FACS)	BioLegend (San Diego, USA)	107626
PerCP/Cyanine5.5 anti-mouse Ki-67	16A8	1:200 (FACS)	BioLegend (San Diego, USA)	652424
PerCP-Vio700 anti-mouse CD38	REA616	1:200 (FACS)	Miltenyi Biotec (Bergisch Gladbach, Germany)	130-128-224
PerCP-Vio700 anti-mouse F4/80	REA126	1:200 (FACS)	Miltenyi Biotec (Bergisch	130-118-327

			Gladbach, Germany)	
Pe-Vio770 anti-mouse CD3	REA641	1:200 (FACS)	Miltenyi Biotec (Bergisch Gladbach, Germany)	130-116-530
Pe-Vio770 anti-mouse CD45 receptor (CD45R) (B220)	REA755	1:200 (FACS)	Miltenyi Biotec (Bergisch Gladbach, Germany)	130-110-711
Pe-Vio770 anti-mouse NK1.1	PK136	1:200 (FACS)	Miltenyi Biotec (Bergisch Gladbach, Germany)	130-116-533
VioBlue anti-mouse Lymphocyte antigen 6 complex locus G6D (Ly6G)	REA526	1:200 (FACS)	Miltenyi Biotec (Bergisch Gladbach, Germany)	130-119-902

3.4.2 Horseradish peroxidase-/Biotin-coupled antibodies

Table 7 Horseradish peroxidase-/Biotin-coupled antibodies

Antibody	Clone	Dilution (Use)	Source	Identifier
Horseradish peroxidase (HRP) donkey anti-rabbit IgG	Poly4064	1:2000 (Western blot, WB)	BioLegend (San Diego, USA)	406401
HRP goat anti-mouse IgG	Poly4053	1:2000 (WB)	BioLegend (San Diego, USA)	405306

3.4.3 Unconjugated antibodies

Table 8 Unconjugated antibodies

Antibody	Clone	Dilution (Use)	Source	Identifier
Anti-LPS	C6	1:1000 (WB)	Thermo Fisher Scientific (Waltham, USA)	MA5-41631
Anti-mouse Akt	polyclonal	1:1000 (WB)	Cell Signaling Technology (Danvers, USA)	9272
Anti-mouse Arginase-1 (Arg-1)	D4E3M™	1:1000 (WB); 1:200 (FACS)	Cell Signaling Technology (Danvers, USA)	93668
Anti-mouse B-cell lymphoma 2 (Bcl-2)	D17C4	1:1000 (WB)	Cell Signaling Technology (Danvers, USA)	3498
Anti-mouse ceramide	MID 15B4	1:200 (FACS)	Enzo Life Sciences (Farmingdale, USA)	ALX-804-196-T050
Anti-mouse heat-shock protein 90 kDa beta member 1 (Grp94)	D6X2Q	1:1000 (WB)	Cell Signaling Technology (Danvers, USA)	20292
Anti-mouse IκBα	44D4	1:1000 (WB)	Cell Signaling Technology (Danvers, USA)	4812
Anti-mouse Jun activation domain-binding protein (c-Jun)	60A8	1:1000 (WB)	Cell Signaling Technology (Danvers, USA)	9165

Anti-mouse MEK1/2	polyclonal	1:1000 (WB)	Cell Signaling Technology (Danvers, USA)	9122
Anti-mouse MyD88	D80F5	1:1000 (WB); 1:50 (CFM)	Cell Signaling Technology (Danvers, USA)	4283
Anti-mouse p44 MAP kinase (Erk1)	polyclonal	1:1000 (WB)	Cell Signaling Technology (Danvers, USA)	4372
Anti-mouse phospho-NF-κB p65 (Ser536)	93H1	1:1000 (WB)	Cell Signaling Technology (Danvers, USA)	3033
Anti-mouse phospho-Stat1 (Tyr701)	58D6	1:1000 (WB)	Cell Signaling Technology (Danvers, USA)	9167
Anti-mouse Sptlc2	polyclonal	1:1000 (WB); 1:200 (FACS)	OriGene (Rockville, USA)	TA319780
Anti-mouse TIRAP	D6M9Z	1:1000 (WB)	Cell Signaling Technology (Danvers, USA)	13077
Ultra-LEAF™ purified anti-mouse CD16/32 antibody	93	1:500 (FACS)	BioLegend (San Diego, USA)	101330
Ultra-LEAF™ purified anti-mouse CD28 antibody	37.51	0.2-0.5 µg/mL (cell culture)	BioLegend (San Diego, USA)	102116
Ultra-LEAF™ purified anti-mouse CD3 antibody	17A2	0.2-1 µg/mL (cell culture)	BioLegend (San Diego, USA)	100253

3.5 Endotoxins, peptides, enzymes, and cytokines

Table 9 Endotoxins, peptides, enzymes, and cytokines

Peptide, enzyme, or cytokine	Source	Identifier
AsiSI (SgfI)	New England Biolabs (Ipswich, USA)	R0630
BglIII	Takara (Kusatsu, Japan)	1021A
DpnI	New England Biolabs (Ipswich, USA)	R0176S
LPS from *E. coli* 0111:B4 for i.p. injections	Sigma-Aldrich (St. Louis, USA)	L2630
LPS from *E. coli* 055:B5 for immunoblotting positive control	Sigma-Aldrich (St. Louis, USA)	L2637
LPS from *E. coli* 0111:B4 for bone marrow-derived macrophage (BMDM) activation	Sigma-Aldrich (St. Louis, USA)	LPS25
Lymphocytic choriomeningitis mammarenavirus (LCMV) gp33-41	MedChemExpress (Monmouth Junction, USA)	HY-P1569
MluI	New England Biolabs (Ipswich, USA)	R3198
Mouse M-CSF	Miltenyi Biotec (Bergisch Gladbach, Germany)	130-101-700

Phusion® High-fidelity DNA polymerase system	New England Biolabs (Ipswich, USA)	M0530, M0531
Recombinant mouse IL-13 (carrier-free)	BioLegend (San Diego, USA)	575904
Recombinant mouse IL-4 (carrier-free)	BioLegend (San Diego, USA)	574304
Recombinant murine IFN-γ	PeproTech (Hamburg, Germany)	315-05
T4 ligase system (enzyme, 10× buffer)	New England Biolabs (Ipswich, USA)	M0201, B0202
Taq 5× master mix	New England Biolabs (Ipswich, USA)	M0285L
XhoI	Takara (Kusatsu, Japan)	1094A

3.6 Consumables

3.6.1 Disposable consumables

Table 10 Disposable consumables

Consumable	Source	Identifier
Braintree scientific Goldenrot™ animal lancet (5 mm)	Thermo Fisher Scientific (Waltham, USA)	NC9416572
Cell culture flask 75 cm² (T75 flask)	Techno Plastic Products TPP (Trasadingen, Switzerland)	90076
Corning® small cell scraper	Corning (Glendale, USA)	3010

Corning™ Costar™ 50 mL reagent reservoir	Thermo Fisher Scientific (Waltham, USA)	10320551
Corning™ serological pipet (5 mL)	Thermo Fisher Scientific (Waltham, USA)	10420201
Corning™ serological pipet (10 mL)	Thermo Fisher Scientific (Waltham, USA)	10084450
Corning™ serological pipet (25 mL)	Thermo Fisher Scientific (Waltham, USA)	10606151
Cryovial (2 mL)	Biozym Scientific (Hessisch Oldendorf, Germany)	710522
Epredia™ Menzel™ microscope coverslips	Thermo Fisher Scientific (Waltham, USA)	11708701
Epredia™ SuperFrost Plus™ adhesion slides	Thermo Fisher Scientific (Waltham, USA)	10149870
Falcon™ 15 mL conical centrifuge tube	Thermo Fisher Scientific (Waltham, USA)	352096
Falcon™ 50 mL conical centrifuge tube	Thermo Fisher Scientific (Waltham, USA)	352070
Falcon™ cell strainer (70 µM; Nylon)	Thermo Fisher Scientific (Waltham, USA)	352350
Falcon™ round-bottom polystyrene test tube	Thermo Fisher Scientific (Waltham, USA)	352054
Feather® disposable scalpel	Feather (Osaka, Japan)	02.001.30.023
Greiner bio-one polystyrene Petri dishes	Thermo Fisher Scientific (Waltham, USA)	10364451
Hydrion® Insta-Check® 0-13 pH test paper	Sigma-Aldrich (St. Louis, USA)	Z264768
Immobilon®-P^{SQ} polyvinylidene difluoride	Merck Millipore (Darmstadt, Germany)	ISEQ00010

(PVDF) transfer membrane (0.2 µm pore size)		
LS columns	Miltenyi Biotec (Bergisch Gladbach, Germany)	130-042-401
Medline™ Pasteur pipet	Thermo Fisher Scientific (Waltham, USA)	12887605
Micro sample tube citrate 3.2%, venous blood collection	SARSTEDT (Nümbrecht, Germany)	41.1506
NORM-JECT®-F luer solo syringe	B.Braun (Melsungen, Germany)	NJ-9166017
Nylon mesh SEFAR NITEX	Sefar (Edling, Germany)	3A03-0150-115-00
Pierce™ blotting paper	Thermo Fisher Scientific (Waltham, USA)	LC2010
Safe lock tube 0.5 mL	Eppendorf (Hamburg, Germany)	30121503
Safe lock tube 1.5 mL	Eppendorf (Hamburg, Germany)	30120086
Safe lock tube 2 mL	Eppendorf (Hamburg, Germany)	30120094
Safe lock tube 5 mL	Eppendorf (Hamburg, Germany)	30119487
Seahorse XF cell culture microplate	Agilent Technologies (Santa Clara, USA)	101085-004
Seahorse XFe96 FluxPak	Agilent Technologies (Santa Clara, USA)	102416-100
Sterican® insulin cannula (27G)	B.Braun (Melsungen, Germany)	4665406
SuperFrost® Plus glass microscopic slides	Thermo Fisher Scientific (Waltham, USA)	630-0950

TipOne 10 µL graduated tip	StarLab (Hamburg, Germany)	S1111-3700
TipOne 1000 µL graduated tip	StarLab (Hamburg, Germany)	S1111-6701
TipOne 200 µL yellow tip	StarLab (Hamburg, Germany)	S1111-0706
Tissue culture test plate 12-well	Techno Plastic Products TPP (Trasadingen, Switzerland)	92012
Tissue culture test plate 6-well	Techno Plastic Products TPP (Trasadingen, Switzerland)	92006
Tissue culture test plate 96-well flat bottom	Techno Plastic Products TPP (Trasadingen, Switzerland)	92696
Tissue culture test plate 96-well U-bottom	Techno Plastic Products TPP (Trasadingen, Switzerland)	92697

3.6.2 Reusable consumables

Table 11 Reusable consumables

Consumable	Source	Identifier
BRAND™ multichannel pipet (200 µL)	Thermo Fisher Scientific (Waltham, USA)	10796164
Counting chamber BLAUBRAND® Neubauer pattern, w/o clips double ruling	Brand (Wertheim, Germany)	718605
Digital calipers	Tesa Technology (Renens, Switzerland)	725202

Dounce homogenizer	Carl Roth (Karlsruhe, Germany)	CXE2.1
Ear puncher	Hauptner-Herberholz (Solingen, Germany)	73855000
Eppendorf™ multi-channel pipet (10 µL)	Thermo Fisher Scientific (Waltham, USA)	15773469
Gilson™ PIPETMAN™ (10 µL)	Thermo Fisher Scientific (Waltham, USA)	10236072
Gilson™ PIPETMAN™ (1000 µL)	Thermo Fisher Scientific (Waltham, USA)	10044463
Gilson™ PIPETMAN™ (200 µL)	Thermo Fisher Scientific (Waltham, USA)	10327282
Invitrogen™ DynaMag™ spin magnet	Thermo Fisher Scientific (Waltham, USA)	12320D
Isis GT421 shaver	Aesculap (Tuttlingen, Germany)	90119
Mr. Frosty™ freezing container	Thermo Fisher Scientific (Waltham, USA)	5100-0001
PIPETBOY Acu 2 (Pink Sunrise)	Integra Biosciences (Wallisellen, Switzerland)	155024
QuadroMACS™ separator	Miltenyi Biotec (Bergisch Gladbach, Germany)	130-091-051

Scissors	Dimeda (Tuttlingen, Germany)	08.121.11
Tweezer Dumoxel	Dumont (Montignez, Switzerland)	0101-7-PO-1

3.7 Machines and instruments

Table 12 Machines and instruments

Machine or instrument	Source
Block heater SBH130D	Cole-Parmer (Staffordshire, United Kingdom)
Cell incubator Hera cell 150	Heraeus (Hanau, Germany)
Centrifuge 5415R	Eppendorf (Hamburg, Germany)
Centrifuge 5810R	Eppendorf (Hamburg, Germany)
Centrifuge 5920R	Eppendorf (Hamburg, Germany)
Chemiluminescence imager Fusion FX6	Vilber Lourmat (Eberhardzell, Germany)
Electrophoresis power supply E864	Consort (Turnhout, Belgium)
FACSCanto™ II flow cytometer	Becton Dickinson (BD) (Franklin Lakes, USA)
Flak-line ice machine	Wessamat (Kaiserslautern, Germany)
HERAsafe hood	Heraeus (Hanau, Germany)
Horizon® 11.14 Gibco BRL gel electrophoresis apparatus	Thermo Fisher Scientific (Waltham, USA)
Incucyte® S3	Sartorius (Göttingen, Germany)
Infinite M1000 Pro microplate reader	Tecan (Männedorf, Switzerland)
Infors HT Multitron Standard (CO2-free incubator)	Infors (Bottmingen, Switzerland)

Innova® U725 upright freezer	Eppendorf (Hamburg, Germany)
Isoflurane vapor 19.3	Drägerwerk (Lübeck, Germany)
LSRFortessa™ flow cytometer	Becton Dickinson (Franklin Lakes, USA)
LSRII flow cytometer	Becton Dickinson (Franklin Lakes, USA)
Mastercycler	Eppendorf (Hamburg, Germany)
MediLine freezer	Liebherr (Bulle, Switzerland)
MediLine fridge	Liebherr (Bulle, Switzerland)
Megafuge3.0RS	Heraeus (Hanau, Germany)
Microwave R-941STW	Sharp (Osaka, Japan)
Mini trans-blot electrophoretic transfer cell	BioRad Laboratories (Hercules, USA)
Molecular imager GelDoc XR+	BioRad Laboratories (Hercules, USA)
NanoDrop™ One	Thermo Fisher Scientific (Waltham, USA)
pH 50 Benchmeter VioLab	XS Instruments (Carpi, Italy)
PowerPac™ basic power supply	BioRad Laboratories (Hercules, USA)
Rotator RS-RR 5	Phoenix Instrument (Naperville, USA)
Sartorius analytic	Sartorius (Göttingen, Germany)
Sartorius universal	Sartorius (Göttingen, Germany)
Seahorse XFe96 analyzer	Agilent Technologies (Santa Clara, USA)
Shaker	Edmund Bühler (Bodelshausen, Germany)
Sorvall® evolution RC centrifuge	Thermo Fisher Scientific (Waltham, USA)
Stirrer D-6010	NeoLab (Heidelberg, Germany)
T100™ thermal cycler	BioRad Laboratories (Hercules, USA)
Thermomixer compact	Eppendorf (Hamburg, Germany)
Vortex genie 2	Scientific Industries (Bohemia, USA)
VWR digital heat block	VWR (Radnor, USA)

Water bath WNE7	Memmert (Schwabach, Germany)
Zeiss Auriga scanning electron microscope	Zeiss Microscopy (Jena, Germany)
Zeiss cell observer	Zeiss Microscopy (Jena, Germany)
Zeiss LSM710 ConfoCor3	Zeiss Microscopy (Jena, Germany)

3.8 Software

Table 13 Software

Software	Source/Reference
Basic Local Alignment Search Tool (BLAST)	National Institutes of Health (NIH) (Bethesda, USA)
BioRender	BioRender (Toronto, Canada)
EndNote 20.4	Thomson Reuters (Toronto, Canada)
FACS Diva™	Becton Dickinson (Franklin Lakes, USA)
FlowJo V10.1	Becton Dickinson (Franklin Lakes, USA)
Fusion evolution-capt edge	Vilber Lourmat (Eberhardzell, Germany)
GraphPad Prism 7.05	GraphPad Software (San Diego, USA)
ImageJ/FIJI	NIH (Bethesda, USA)
Incucyte® 2028B	Sartorius (Göttingen, Germany)
Microsoft Office Professional Plus 2013	Microsoft (Redmond, USA)
Wave 2.6.0	Agilent Technologies (Santa Clara, USA)
ZEN software (Blue and Black versions)	Zeiss Microscopy (Jena, Germany)

4. Methods

4.1 Mouse work

All animal experiments were approved by the German regional council at the Regierungspräsidium Karlsruhe, Germany, and were performed in accordance with internal DKFZ regulations. In rare cases, mice with fighting wounds were excluded from the experimental analysis. The sample collection and processing were not performed in a blinded manner.

4.1.1 Maintenance and housing

Mice were bred and maintained in the German Cancer Research Center's specific-pathogen-free animal facility. Live mice were handled under sterile conditions. Male and female 7-12 week-old mice were used for experiments. In each experiment, sex-matched and age-matched mice were used.

4.1.2 Breeding pattern

The *Sptlc2*$^{Flox/Flox}$ mice were kindly provided by Professor Xian-cheng Jiang (SUNY Downstate Medical Center, New York, USA) via Professor Vishwa Dixit (Yale University, New Haven, USA) and Professor Susan Kaech (Salk Institute for Biological Studies, La Jolla, USA) (*174*). In these mice, exon 1 of *Sptlc2* is flanked by two LoxP sites and is excised after crossing with a Cre-expression mouse strain. *Lyz2*-cre mice (*172*) and *CD11c*-cre mice were from the Jackson Laboratory (*171*). For the generation of myeloid cell- or dendritic cell-specific *Sptlc2* knockout (KO) mice, *Sptlc2*$^{Flox/Flox}$ mice were bred with *Lyz2*-cre or *CD11c*-cre mice, respectively. Offspring from this breeding, which had one allele of *Sptlc2* floxed and which had a *Lyz2*- or *CD11c*-cre, were again bred with *Sptlc2*$^{Flox/Flox}$ mice to generate *Sptlc2*$^{Flox/Flox}$ *Lyz2*- or *CD11c*-cre mice.

4.1.3 Mouse genotyping

The genotypes of mice were determined as either wildtype (WT; *Sptlc2*-sufficient) or *Lyz2*-cre (*Sptlc2*-deficient; heterozygous cre expression) after weaning (4 weeks after birth) and again upon experimental use (re-genotyping). Ear biopsies (see Section 4.2.7) were boiled in 100 µL NaOH (50 mM) in 1.5 mL Eppendorf tubes at 95°C for 30 minutes. After

a short incubation on ice, 10 µL Tris-HCl (1 M; pH 7.8) was added for neutralization. Reaction A and B polymerase chain reactions (PCR) with *Taq* 5× master mix and primers from Jackson Laboratory (see "separated PCR" for B6.129P2-*Lyz2*$^{tm1(cre)Ifo}$/J mice from Jackson Laboratory) were run (Table 14-15). Samples were analyzed by agarose gel electrophoresis (see Section 4.4.1).

Table 14 Genotyping primers (Jackson Laboratory)

Primer	Sequence 5' → 3'	Label primer type	Reaction
oIMR3066	CCC AGA AAT GCC AGA TTA CG	Mutant	A
oIMR3067	CTT GGG CTG CCA GAA TTT CTC	Common	A, B
oIMR3068	TTA CAG TCG GCC AGG CTG AC	Wildtype	B

Table 15 Genotyping PCR program

Time	Temperature	Number of cycles
5 minutes	94°C	1
30 seconds	94°C	34
30 seconds	58°C	
45 seconds	68°C	
10 minutes	68°C	1

4.1.4 Tumor implantation

One day before the tumor cell injection, mice were shaved at the site of tumor implantation. On the day of tumor implantation, B16-F10 and Ret melanoma cells (~70% confluency) were resuspended in plain DMEM supplemented with 1% non-essential amino acids (MEM NEAA) at a final density of 0.5, 2, or 5 million cells/mL. Mice were anesthetized using isoflurane (2% v/v in oxygen), and 100 µL of B16-F10 or Ret cell suspension (0.05, 0.2, or 0.5 million cells/mouse) were injected subcutaneously. The injection was made into the right flank at a flow rate of 10 µL/second with a 27G cannula.

4.1.5 Tumor size measurement

Using digital calipers, tumor size was measured every 2-3 days starting on day 7 after tumor implantation. Two perpendicular diameters were measured, and the size was calculated using the following formula:

$$size = \frac{\text{length} \times \text{width}^2}{2}$$

When more than one tumor was palpable, the total tumor size was calculated as the sum of the individual tumor sizes. Mice were sacrificed when tumors were ulcerative and/or necrotic or when the longest diameter (or the sum of the longest diameters) exceeded 15 mm.

4.1.6 Intraperitoneal injections

Per mouse, 150 µg LPS from *E. coli* 0111:B4 (L2630, Sigma-Aldrich) in 150 µL PBS was intraperitoneally injected.

4.2 Mouse organ harvesting and preparation

Mice were sacrificed by cervical dislocation, sprayed with 70% ethanol, and their organs harvested under sterile conditions.

4.2.1 Blood

Using a lancet, mouse blood was collected from the submandibular vein into blood collection tubes containing 20 µL of 3.2% sodium citrate. The tubes were flipped ten times and kept on ice until further processing. Blood samples (70 µL-100 µL) were centrifuged (13200 rpm, 10 minutes, 4°C). The supernatant (plasma) was collected in new 1.5 mL Eppendorf tubes without disturbing the red blood cells in the bottom of the tubes, and plasma was stored at -20°C.

4.2.2 Intraperitoneal flushing

Mouse abdominal skin was carefully cut open with scissors without damaging the peritoneum. With a 27G cannula, 1 mL cold PBS (2% FBS) was intraperitoneally injected, the mouse abdomen was gently massaged, and, after opening the peritoneum, the intraperitoneal flush was collected with a Pasteur pipet into a 1.5 mL Eppendorf tube. The

intraperitoneal cells were centrifuged (2000 rpm, 10 minutes, 4°C), resuspended in PBS (1% FBS), and counted (see Section 4.3.3).

4.2.3 Bones

With sterile scissors and tweezers, the femur and tibia were isolated from the mouse legs and cut open. The BM was rinsed from the bones with IMDM (10% FBS, 1% Pen-Strep) with a 27G cannula and pressed through a 70 µm cell strainer using the plunger of a syringe. Strainers were washed with 5-10 mL IMDM (10% FBS, 1% Pen-Strep), and the cells were centrifuged (2000 rpm, 2 minutes). The supernatant was discarded, red blood cells were lysed with ACK lysing buffer for 1 minute, and the reaction was stopped by the addition of four times the volume of IMDM (10% FBS, 1% Pen-Strep). After centrifugation (2000 rpm, 2 minutes), pellets were resuspended in IMDM (10% FBS, 1% Pen-Strep), transferred through nylon mesh, and BM cells were counted (see Section 4.3.3).

4.2.4 Tumors

Using digital calipers, mouse tumor size was determined, and tumors were collected in 50 mL falcon tubes containing 5 mL of RPMI (1% FBS) on ice. The tumor weight was determined, and solid tumors were then pressed through 70 µm cell strainers using the plunger of a syringe. Strainers were washed with 5-10 mL RPMI (1% FBS) and cells were centrifuged (2000 rpm, 2 minutes). Pellets were resuspended in 1 mL ACK lysing buffer and incubated for 1 minute at room temperature, followed by the addition of 4 mL RPMI (1% FBS) and centrifugation (2000 rpm, 2 minutes). Finally, the pellet was resuspended in 1 mL RPMI (10% FBS, 1% Pen-Strep), passed through nylon mesh, and cells were counted (see Section 4.3.3).

4.2.5 Spleens

Mouse spleens were harvested in 1.5 mL Eppendorf tubes containing cold RPMI (1% FBS). Spleens were then pressed through a 70 µm cell strainer using the plunger of a syringe. Strainers were washed with 5-10 mL RPMI (1% FBS), and cells were centrifuged (2000 rpm, 2 minutes). Pellets were resuspended in 1 mL ACK lysis buffer and incubated for 1 minute at room temperature, followed by the addition of 4 mL RPMI (1% FBS) and centrifugation (2000 rpm, 2 minutes). Finally, the pellet was resuspended in 1 mL RPMI

(10% FBS, 1% Pen-Strep), passed through nylon mesh, and cells were counted (see Section 4.3.3).

4.2.6 Skin

Mouse 1 cm^2-2cm^2 skin pieces were cut out from the (no tumor-bearing) left flank and harvested in 1.5 mL Eppendorf tubes containing cold RPMI (1% FBS). Using a Dounce homogenizer, skin pieces were pressed through a 70 µm cell strainer. Strainers were washed with 5-10 mL RPMI (1% FBS), and cells were centrifuged (2000 rpm, 2 minutes). Pellets were lysed with the RIPA lysis buffer system (see Section 4.6.1).

4.2.7 Ear biopsies

Mouse 1 mm^2-2 mm^2 ear pieces were cut out with scissors or an ear puncher and harvested in 1.5 mL Eppendorf tubes.

4.3 Cell biology

Cells were handled under sterile conditions using a laminar flow hood and grown in an incubator at 37°C, 5% CO_2.

4.3.1 Bone marrow-derived macrophage generation

If not indicated differently, 3 million BM cells in 2 mL IMDM (10% FBS, 1% Pen-Strep) supplemented with 10 ng/mL M-CSF per well of a 6-well plate were seeded and cultured for six days. On day 3, the medium was changed, and if indicated, DMSO or sphingolipids (sphinganine, 3-ketosphinganine, sphinganine-fluorescein, or sphingomyelin) were supplemented. On day 6, differentiated BMDM were polarized for 20-24 hours (or as indicated) with PBS towards M0-like or, if indicated, with only 100 ng/mL LPS (LPS25, Sigma-Aldrich), otherwise in combination with 50 ng/mL IFN-γ to M1-like or with 10 ng/mL IL-4/10 ng/mL IL-13 to M2-like macrophage phenotypes. For subsequent analyses, BMDM were washed in cold PBS and detached from culture plates using cell scrapers.

4.3.2 Cell culture of immortalized cell lines

B16-F10 cells were maintained in DMEM (10% FBS, 1% Pen-Strep) supplemented with 200 µg/mL G418. Ret cells were maintained in RPMI (10% FBS, 1% Pen-Strep). HEK293T cells were maintained in DMEM (10% FBS, 1% Pen-Strep). Cells were cultured in T75 flasks and split when they reached 70-80% confluency. For splitting, the medium was removed and cells were washed with 10 mL PBS. Then, cells were incubated with 5 mL of 0.25% trypsin-EDTA for 5 minutes at 37°C, 5% CO_2, washed with 10 mL DMEM (10% FBS, 1% Pen-Strep), transferred to 50 mL falcon tubes, and centrifuged (2000 rpm, 2 minutes). Pellets were resuspended in 1 mL DMEM (10% FBS, 1% Pen-Strep) and cultured at 1:4-1:100 of their initial density. One day before tumor implantation, B16-F10 or Ret cells were split to achieve 70% confluency on injection day (see Section 4.1.4). For long-term storage of cells, 5 million cells were resuspended in 1 mL freezing medium in cryovials and frozen in a Mr. Frosty™ freezing container half-filled with isopropanol at -80°C. Frozen cells were rapidly thawed in a 37°C water bath, washed with 20 mL DMEM (10% FBS, 1% Pen-Strep), and seeded in T75 flasks. One day later, the medium was changed to remove floating dead cells, and cells were split.

4.3.3 Cell counting

Single-cell suspensions were diluted 1:100 in Trypan Blue, and 10 µL were loaded on a counting chamber. Colorless cells in all four squares were counted and averaged, and the final cell count (million cells/mL) was calculated using the formula:

$$Cell\ number = 100\ (\text{dilution factor}) \times 10^4 \times averaged\ count\ per\ square$$

4.3.4 pH measurement

The pH values of the BMDM culture medium were determined with a pH meter. Between measurements, the electrode was carefully rinsed with ddH_20, and to avoid temperature-induced pH changes, the pH was determined immediately after the plates were removed from the incubator. Additionally, pH was determined by the deposition of one drop of cell culture supernatant onto pH indicator paper.

4.3.5 Confluency analysis

In a 12-well plate, 2.5×10^5 BM cells in 1 mL IMDM (10% FBS, 1% Pen-Strep) supplemented with 10 ng/mL M-CSF per well were differentiated to BMDM (see Section 4.3.1). After a medium change on day 3 of BMDM cultivation, cells were placed in an Incucyte® S3 instrument, and for the next six days, images of BMDM confluency were recorded every 4 hours. On day 6 of BMDM cultivation (3 days after confluency measurement was started), BMDM were polarized to M0-like or M1-like macrophage states (see Section 4.3.1) and directly placed back into the Incucyte® S3 instrument. Confluency analysis was performed in the Incucyte® 2028B software.

4.3.6 Retrovirus production (Transfection)

The plasmids MSCV-IRES-EGFP retroviral construct (MigR1-GFP), MigR1-GFP-MyD88, MigR1-GFP-MyD88^{L252P}, and MigR1-GFP-MyrisMyD88 (see Sections 4.4.4-4.4.6) were used for overexpression in HEK293T cells and are thus referred to as “overexpression plasmids” in the following sections. Per well of a 6-well plate, 0.5 million HEK293T cells were seeded in 2 mL DMEM (10% FBS, 1% Pen-Strep). On the following day, in a 2 mL Eppendorf tube, 100 µL Opti-MEM™, 4 µL X-tremeGENE™ HP DNA transfection reagent, 1 µg overexpression plasmid, and 0.5 µg eco-helper plasmid (*176*) per reaction were gently mixed and incubated at room temperature for 20 minutes. Single drops of the mixture were added to the HEK293T cells, and the cells were cultured at 37°C, 5% CO_2. One day after transfection, 0.8 mL cell culture supernatant was discarded. On the following day, the supernatant (containing viral particles) was collected, centrifuged (13200 rpm, 1 minute) to remove floating cells, and frozen at -80°C or used immediately for BMDM spin infection.

4.3.7 Spin infection (Retroviral transduction)

On day 3 of BMDM generation (see Section 4.3.1), the BMDM culture medium was removed and 1 mL IMDM (10% FBS, 1% Pen-Strep) supplemented with 20 ng/mL M-CSF mixed with 1 mL viral particle-containing HEK293T supernatant was added per well. BMDM were transduced by spinning at 1500 g for 60 minutes at 32°C, followed by incubation at 37°C, 5% CO_2 for 4 hours. Then, the medium was removed, and cells were

cultured in fresh 2 mL IMDM (10% FBS, 1% Pen-Strep) supplemented with 10 ng/mL M-CSF for 3 more days and finally polarized (see Section 4.3.1).

4.3.8 CD8a+ T cell selection

CD8+ T cells from P14 mice were negatively selected using the CD8a+ T cell isolation kit according to the manufacturer's instructions. Isolated splenocytes were resuspended in cold PBS (2% FBS; 40 µL per 10 million cells), mixed with a biotin-antibody cocktail (10 µL per 10 million cells), and incubated at 4°C for 10 minutes. Cells were then washed with 3 mL cold PBS (2% FBS) and centrifuged (2000 rpm, 2 minutes). Pellets were resuspended in cold PBS (2% FBS; 80 µL per 10 million cells), premixed with anti-biotin microbeads (20 µL microbeads per 10 million cells), and incubated for 10 minutes at 4°C. Then, cells were passed through LS columns, which were prewashed with 3 mL PBS (2% FBS) and installed in a magnetic-activated cell sorting (MACS) separator. Columns were washed twice with cold 3 mL PBS (2% FBS), and the flow-through (containing CD8+ T cells) was collected in 15 mL falcon tubes. After centrifugation (2000 rpm, 2 minutes), the pellets were resuspended in 1 mL RPMI (10% FBS, 1% Pen-Strep, 1% MEM NEAA, 0.1% 2-mercaptoethanol) and counted. At least one hour before CD8a+ T cell isolation, wells of a 96-well U-bottom plate were coated with 0.5 µg/µL anti-CD3 in PBS at 37°C, 5% CO_2. Wells of the anti-CD3-coated plate were washed with 200 µL cold PBS, and per well, 0.2 million CD8+ T cells were seeded in 200 µL RPMI (10% FBS, 1% Pen-Strep, 1% MEM NEAA, 0.1% 2-mercaptoethanol), supplemented with 0.2 µg/mL anti-CD28 for overnight activation.

4.3.9 CellTrace violet labeling

Anti-CD3/CD28-activated CD8+ T cells were pooled and washed with cold PBS. Cells were resuspended in RPMI (10% FBS, 1% Pen-Strep, 1% MEM NEAA, 0.1% 2-mercaptoethanol) containing 5 µM CellTrace violet (CTV) at a density of 5 million cells/mL and incubated for 20 minutes at 37°C, 5% CO_2. Then, cells were washed twice with cold PBS, resuspended in 1 mL RPMI (10% FBS, 1% Pen-Strep, 1% MEM NEAA, 0.1% 2-mercaptoethanol), and used for BMDM co-culture.

4.3.10 BMDM - CD8+ T cell co-culture

One day before setup of the BMDM-CD8+ T cell co-culture, six days-old BMDM (see Section 4.3.1) were detached with cell scrapers, washed in cold PBS, and re-seeded at a density of 0.01 or 0.05 million cells in 200 µL IMDM (10% FBS, 1% Pen-Strep) supplemented with 100 ng/mL LPS (LPS25, Sigma-Aldrich) and with or without 10 ng/µL gp33-41 per well of a 96-well flat bottom plate for overnight activation and antigen pulsing. On the day of the co-culture setup, the LPS-activated gp33-41-pulsed BMDM were washed in 200 µL IMDM (10% FBS, 1% Pen-Strep), followed by the addition of the CTV-labeled and anti-CD3/28 activated CD8+ T cells in the ratio 1:5 (BMDM: CD8+ T cell). The co-culture was shortly spun to settle the CD8+ T cells onto the BMDM and cultured for 2-3 days in the incubator.

4.3.11 Scanning electron microscopy

(In collaboration with Dr. K. Richter, Electron Microscopy Group (W230), German Cancer Research Center (DKFZ), Heidelberg, Germany)

In each well, 0.1-0.25 million BMDM were grown on glass coverslips in 12-well plates; if indicated, BMDM were supplemented with sphinganine or DMSO and LPS-activated (see Section 4.3.1). Cells were submitted to the Electron Microscopy Group (W230), German Cancer Research Center (DKFZ), Heidelberg, Germany. Cells were fixed with 2% buffered glutaraldehyde (100 mM cacodylate at pH 7.2, supplemented with 1 mM $MgCl_2$ and 1 mM $CaCl_2$), post-fixed with 1% OsO_4, and dehydrated in a graded ethanol series. After critical point drying (Balzers 030), samples were sputter coated with Au/Pd 80:20 (Balzers 050) for immediate scanning electron microscopy (SEM) observation. Scanning electron micrographs were taken with a Zeiss Auriga SEM at a 5 kV acceleration voltage and an approximately 2 mm work distance with an in-lens detector for secondary electrons.

4.4 DNA methods

4.4.1 Agarose gel electrophoresis

Agarose gels were prepared by boiling 1 g agarose (for cloning) or 3 g (for genotyping) in 100 mL-150 mL 1× TAE buffer for ~2 minutes or until a clear solution was obtained. After cooling the solution down for ~5 minutes and adding 5 µL SYBR™ safe DNA gel stain,

the solution was poured into a gel cast with 30-well or 40-well combs. After ~20 minutes, when the gels solidified, combs were removed and samples (up to 20 µL premixed with 6× TriTrack DNA LD) were loaded along with 10 µL DNA plus ladder. Gels were run at 130 V for 20-30 minutes and imaged using the Molecular Imager GelDoc XR+.

4.4.2 Agar plate preparation

LB agar was boiled on a stirrer until complete dissolution and then autoclaved at 121°C for 15 minutes. After cooling down, ampicillin (50 µg/mL) was added, and the solution was poured into plates. After hardening, plates were stored upside down in plastic bags at 4°C.

4.4.3 Bacterial transformation

Bacterial plasmid amplification was performed through the transformation of DH5α competent *E. coli* cells. First, LB-ampicillin plates (see Section 4.4.2, as the herein-used plasmids contained ampicillin resistance gene cassettes) were placed at room temperature, and bacteria (50 µL/tube) were thawed on ice for 15 minutes. Per 50 µL bacteria, 5 µL-20 µL plasmid (see Sections 4.4.4-4.4.6) was added and incubated for 20-30 minutes on ice. Then, the mixtures were heat-shocked at 42°C for 30-60 seconds (depending on the plasmid size) and immediately stored on ice for 1 minute. Per reaction, 250 µL plain LB medium was added for incubation at 220 rpm and 37°C for 1 hour. On 50 µg/mL ampicillin-containing agar plates, 200 µL of the mixture was plated out and equally spread using sterile glass beads. The plates were dried for 5-10 minutes on the bench and then placed in plastic bags upside-down into a 37°C incubator for overnight growth. On the following day, colonies were picked with pipet tips and used for inoculation in 5 mL liquid LB medium containing 50 µg/mL ampicillin. After ~16 hours, DNA was isolated from the bacteria using the QIAprep Spin Miniprep Kit following the manufacturer's protocol.

4.4.4 Cloning

A murine MyD88 (NM_010851)-tagged open reading frame (ORF) plasmid was purchased from OriGene. The MyD88-containing plasmid as well as the MSCV-IRES-GFP retroviral vector, MigR1-GFP (modified to include restriction sites for SgfI, AscI, RsrII, and MluI in its multiple cloning site), were digested for 4 hours at 37°C using the restriction enzymes SgfI and MluI in CutSmart buffer (Table 16).

Table 16 Restriction digestion reaction mix (SgfI/MluI)

Reagent	Volume or mass
Plasmid DNA	20 µL (2 µg)
SgfI	1 µL
MluI	1 µL
10× CutSmart buffer	4 µL
Nuclease-free water	top up to 40 µL

The digested plasmids were used for agarose gel electrophoresis (see Section 4.4.1), and the MyD88 sequence (~900 bp) and linearized MigR1-GFP (~7 kbp) were cut out from the gel and purified using the QIAquick gel extraction kit according to the manufacturer's instructions. DNA concentrations were measured with a NanoDrop spectrophotometer (NanoDrop™ One). The purified MyD88 insert and MigR1-GFP vector were ligated overnight at 4°C using the T4 ligation system (Table 17).

Table 17 MigR1-GFP/MyD88 ligation reaction mix

Reagent	Volume or mass
MigR1-GFP	1 µL (62 ng)
MyD88 ORF	4.3 µL (24.3 ng)
10× T4 ligase buffer	1 µL
T4 ligase	1 µL
Nuclease-free water	top up to 10 µL

Next, the ligation product was amplified through the transformation of DH5α competent cells, and DNA was purified from individual colonies (see Section 4.4.3). To identify MyD88-positive clones, a control digest of 2 µL purified DNA with the restriction enzymes SgfI and MluI was performed (adapted volumes from Table 16), followed by agarose gel electrophoresis. Positive clones showing a band at ~900 bp, representing the mouse MyD88 ORF, were sent for Sanger sequencing to Eurofins (Luxembourg, Luxembourg), and sequencing results were used in NIH's Basic Local Alignment Tool (BLAST) to ensure the correct MyD88 sequence was inserted.

4.4.5 Site-directed mutagenesis (MyD88^{L252P})

To generate a constitutively active variant of MyD88, a point mutation was introduced into the TIR domain of MyD88. By replacing the thymidine nucleotide at position 755 with a cytosine nucleotide, the codon CTG (encoding leucine, L) was changed to CCG (encoding proline, P). By doing so, the amino acid leucine at position 252 was substituted with proline, resulting in an L252P mutant, referred to as MyD88^{L252P}. The MigR1-GFP-MyD88^{L252P} plasmid was derived from the MigR1-GFP plasmid through a PCR using the customized MyD88^{L252P} forward (fw) primer (5' GGTGTCCAACAGAAGCGACCGATTCCTATTAAATACAAG 3') and the MyD88^{L252P} reverse (rv) primer (5' CTTGTATTTAATAGGAATCGGTCGCTTCTGTTGGACACC 3') from Eurofins (Luxembourg, Luxembourg) (Table 18-19).

Table 18 Site-directed mutagenesis PCR

Reagent	Volume or mass
2× Phusion master mix	12.5 µL
10 µM MyD88^{L252P} fw primer	1.25 µL
10 µM MyD88^{L252P} rv primer	1.25 µL
MigR1-GFP-MyD88	1.25 µL (50 ng)
DMSO	1.25 µL
Nuclease-free water	top up to 25 µL

Table 19 Site-directed mutagenesis PCR program

Time	Temperature	Number of cycles
30 seconds	98°C	1
30 seconds	98°C	18
45 seconds	Gradient 55°C -70°C	
10 minutes	72°C	
10 minutes	72°C	1

The PCR product was agarose gel purified, and for removal of parental DNA, an overnight DpnI digest at 37°C was set up (Table 20).

Table 20 DpnI digestion reaction mix

Reagent	Volume or mass
PCR product	60 µL
DpnI	1.5 µL

The product of this reaction was amplified through the transformation of DH5α competent cells, and DNA was purified from individual colonies (see Section 4.4.3). A control digest of 2 µL purified DNA using SgfI and MluI restriction enzymes was performed as described above (adapted volumes from Table 16), followed by agarose gel electrophoresis. Positive clones showing a band at ~900 bp representing the MyD88^{L252P} and 7 kbp representing the backbone were sent for Sanger sequencing to Eurofins (Luxembourg, Luxembourg). Sequencing results were run in BLAST to ensure that MyD88 was L252P-mutated.

4.4.6 Introduction of myristoylation signal sequence (MyrisMyD88)

To generate a membrane-anchored variant of MyD88, a myristoylation (Myris) signal sequence was introduced in front of the MyD88 sequence (*177, 178*). The MigR1-GFP-MyrisMyD88 plasmid was derived from the MigR1-GFP plasmid through PCR using the customized MyrisMyD88 fw primer (5' GAAGATCTATGGGCAGCAGCAAGAGCAAGCCCAAGGA CCCCAGCCAGAGG ATGTCTGCGGGAGACCC 3') and the MyrisMyD88 rv primer (5' CCGCTCGAGTCAGGGCAGGGACAAAGCCTTGG 3') from Eurofins (Luxembourg, Luxembourg) (Table 21-22). The MyrisMyD88 forward primer contained a protective base (5' GA 3'), a BglII restriction site (5' AGATCT 3'), a myristoylation signal sequence (5' ATGGGCAGCAGCAAGAGCAAGCCCAAGGACCCCAGCCAGAGG 3') and the first 15 nucleotides of the MyD88 sequence (5' ATGTCTGCGGGAGACCC 3'). The MyrisMyD88 reverse primer contained a protective base (5' CCG 3'), an XhoI restriction site (5' CTCGAG 3'), and the reverse complement sequence of the last MyD88 nucleotides (5' TCAGGGCAGGGACAAAGCCTTGG 3'). Before use in PCR, primers were premixed and kept at 95°C for 5 minutes.

Table 21 MyrisMyD88 PCR

Reagent	Volume or mass
2× Phusion master mix	12.5 µL
10 µM MyrisMyD88 fw primer	1.25 µL
10 µM MyrisMyD88 rv primer	1.25 µL
MigR1-GFP-MyD88	4 µL (10 ng)
DMSO	1.25 µL
Nuclease-free water	top up to 25 µL

Table 22 MyrisMyD88 PCR program

Time	Temperature	Number of cycles
30 seconds	98°C	1
10 seconds	98°C	25
45 seconds	Gradient 55°C -70°C	
2 minutes	72°C	
10 minutes	72°C	1

The PCR product was agarose gel purified and digested with the restriction enzymes BglII and XhoI for overnight at 37°C (Table 23). Simultaneously, 2 µg MigR1-GFP were digested with BglII and XhoI (Table 23).

Table 23 Restriction digestion reaction mix (BglII/XhoI)

Reagent	Volume or mass
PCR product or MigR1-GFP	30 µL or 2 µg (1.54 µL)
BglII	1.5 µL
XhoI	1.5 µL
10× H buffer	5 µL
Nuclease-free water	top up to 50 µL

The digested plasmid and PCR product were used for agarose gel electrophoresis (see Section 4.4.1), and the PCR product (~1000 bp) and linearized MigR1-GFP (~7 kbp) were cut out from the gel and purified using the QIAquick gel extraction kit. DNA concentrations were measured using the NanoDrop™ One. The purified PCR product and MigR1-GFP vector were ligated overnight at 16°C using the T4 ligation system (Table 24).

Table 24 MigR1-GFP/MyrisMyD88 ligation reaction mix

Reagent	Volume or mass
MigR1-GFP	2 µL (50 ng)
PCR product	0.8 µL (23.4 ng)
10× T4 ligase buffer	1 µL
T4 ligase	1 µL
Nuclease-free water	top up to 10 µL

Next, the ligation product was amplified through the transformation of DH5α competent cells, and DNA was purified from individual colonies (see Section 4.4.3). A control digest of 2 µL purified DNA using BglII and XhoI restriction enzymes was performed for 2 hours (adapted volumes from Table 23), followed by agarose gel electrophoresis. Positive clones showing a band at ~1000 bp, representing MyrisMyD88, and at 7 kbp, representing the backbone, were sent for Sanger sequencing to Eurofins (Luxembourg, Luxembourg), and sequencing results were run in BLAST to ensure that the MyrisMyD88 sequence was inserted.

4.5 RNA methods

For analysis of pre-published RNA sequencing data, R versions 3.6.2 and 4.0.4 were used (*179*).

4.5.1 Analysis of raw RNA sequencing data

Raw RNA sequencing counts were downloaded from Gene Expression Omnibus (GEO) using the accession code GSE140610. Normalization and differential gene expression analysis were performed using the edgeR package version 3.28.1 (*180*). To filter out lowly expressed genes, a counts-per-million (cpm) threshold was set to 1 before normalization.

4.5.2 Analysis of normalized RNA sequencing data

Normalized RNA sequencing counts were downloaded from GEO using the accession code GSE139913.

4.6 Protein methods

4.6.1 Cell lysis

Cold PBS-washed and scraped BMDM were lysed in 1.5 mL Eppendorf tubes for 1 hour on a rotator at 4°C followed by 15 minutes of incubation at -80°C in the RIPA lysis buffer system (1 µL per 0.3 million seeded BM cells) according to the manufacturer's instructions or in 1% Triton X-100 in PBS (supplemented with 200 mM phenylmethylsulfonyl fluoride (PMSF), proteinase inhibitor in DMSO, and 100 mM sodium orthovanadate in water from the RIPA lysis buffer system) when pulldown was performed, or RIPA lysis buffer diluted in PBS (to reduce the SDS concentration) when immunoprecipitation was performed before immunoblotting. Samples were centrifuged (13200 rpm, 3 minutes, 4°C) and without disturbing the cell pellet, the supernatant was collected in 1.5 mL Eppendorf tubes.

4.6.2 Protein concentration measurement

The protein concentration of BMDM lysate (see Section 4.3.1) was measured using the Pierce™ BCA protein assay kit according to the manufacturer's instructions. Each sample was 1:5 diluted with ddH_2O and used for the analysis. Sample absorbance was determined at 562 nm in a microplate reader, and equal amounts of protein were used for pulldown/immunoprecipitation assays (see Sections 4.6.3-4.6.5) or SDS-PAGE (see Section 4.6.7).

4.6.3 Sphinganine-biotin pulldown assay

For the identification of sphinganine-interacting proteins, sphinganine-biotin pulldown was performed. Per reaction, 1 mg of total BMDM protein lysate (see Section 4.6.1) in 400-700 µL 1% Triton X-100 in PBS (supplemented with 200 mM PMSF, proteinase inhibitor in DMSO, and 100 mM sodium orthovanadate in water from the RIPA lysis buffer system) was incubated with 10 µg sphinganine-biotin or control biotin in ethanol for 14 hours on a rotator at 4°C. Subsequently, PBS-T-washed Dynabeads™ M-280 streptavidin was added

to the mixture for 9 hours on a rotator at 4°C. The samples were placed on a magnet, and the supernatant was removed. Magnetic beads were washed three times with PBS-T, and immobilized proteins were eluted from the beads by boiling them in 6× SDS sample buffer for 10 minutes at 95°C. Then, samples were vortexed and placed back into the magnet. The supernatant was transferred to new tubes and either directly used for SDS-PAGE or stored at -20°C.

4.6.4 Sphinganine-agarose pulldown assay

An alternative approach for the identification of sphinganine-interacting proteins was their pulldown through sphinganine coupled to agarose beads. For coupling the agarose to the beads, per reaction, 200 µL AminoLink™ Plus coupling resin was transferred to a spin column placed in a 15 mL falcon tube. The resin was washed with 2 mL of cold 30%, then 70%, and then 100% ethanol to generate a hydrophobic binding condition. To the resin, 2 mL PBS containing sphinganine (50-200 µg) or control DMSO was added and incubated on a rotator at 4°C for 4 hours or overnight. Next, the resin was washed three times with 2 mL PBS and per reaction, 50 mM sodium cyanoborohydride solution in 2 mL PBS was added for 6 hours or overnight on a rotator at 4°C. The resin was washed three times with 4 mL quenching buffer (1 M Tris-HCl, pH 7.4), and a 50 mM sodium cyanoborohydride solution in 2 mL quenching buffer was added. After 30 minutes of incubation on a rotator at 4°C, the column was placed in a new 2 mL Eppendorf tube, and the mixture was collected. The resin was washed three times with 2 mL PBS, and 0.5-1 mg BMDM lysate (see Section 4.6.1) was added to the sphinganine-coupled resin for overnight incubation at 4°C on a rotator. On the following day, the resin was washed three times with PBS-T, and after the addition of 50 µL PBS-T, the column was cut open and placed upside-down into a new 2 mL Eppendorf tube, which was installed in a 50 mL falcon tube for centrifugation (2000 rpm, 2 minutes). The slurry in the 2 mL Eppendorf tube was spun again (2000 rpm, 2 minutes), and the supernatant was discarded. For elution, 100 µL 6× Laemmli buffer was added, and reactions were boiled for 10 minutes at 95°C and directly used for SDS-PAGE or stored at -20°C.

4.6.5 Immunoprecipitation assay

For the identification of Sptlc2-interacting proteins, 1.5 mg Dynabeads™ protein A and 10 µL α-Sptlc2-antibody or IgG isotype control were incubated overnight on a rotator at 4°C. On the next day, 5 mM BS3 in conjugation buffer (20 mM sodium phosphate, 0.15 M sodium chloride (pH 7-9)), and 1 M Tris-HCl (pH 7.5; quenching buffer) were used for crosslinking the antibody to the beads according to the manufacturer's instructions. Per reaction, 1 mg BMDM lysate in SDS-free RIPA lysis buffer (see Section 4.6.1) was added and incubated on a rotator overnight at 4°C. On the following day, the beads were washed three times in 200 µL PBS-T in a magnet and then eluted at 70°C, 1100 rpm for 10 minutes using 30 µL elution buffer (50 mM glycine pH 2.8) pre-mixed with 2× LD containing 2-mercaptoethanol. Samples were vortexed and placed back into the magnet. The supernatant was transferred to new tubes and directly used for SDS-PAGE or stored at -20°C.

4.6.6 Sodium dodecyl sulfate polyacrylamide gel electrophoresis sample preparation

BMDM lysate (for LPS western blots: 3 µL RIPA lysis buffer system per mg tissue; otherwise: 10-30 µg total protein) was mixed with the appropriate volume of 2× or 4× Laemmli buffer containing 2-mercaptoethanol and boiled for 10 minutes at 95°C. Samples were shortly cooled to room temperature and used for SDS-PAGE.

4.6.7 Sodium dodecyl sulfate polyacrylamide gel electrophoresis

Before use, the glass plates and the comb were washed with ddH_2O. For the preparation of SDS-polyacrylamide gels, the resolving gel mixture (8-12% acrylamide) was poured between glass slides with a 1.5 mm spacer, followed by smoothening of the resolving gel surface through the addition of 1 mL isopropanol. After ~15 minutes, when the gel was polymerized, isopropanol was removed and the stacking gel mixture was poured. The 10- or 15-well comb was inserted, and stacking gel was polymerized for another ~15 minutes. Gels were stored in ddH_2O-soaked paper towels at 4°C and used within one week. Gels were installed in a Mini-PROTEAN tetra cell chamber, which was filled with SDS running buffer, and after removal of the comb, equal amounts of samples were loaded along with

a 10 µL pre-stained protein ladder. Samples were run for 15 minutes at 70 V and ~60-90 minutes at 120 V. After disassembling the SDS-PAGE apparatus, gels were used for Coomassie staining (see Section 4.6.9), silver staining (see Section 4.6.10), or blotting proteins to PVDF membranes (see Section 4.6.8).

4.6.8 Western blotting

For blotting proteins to PVDF membranes (also referred to as immunoblotting), the resolving gel was removed and a PVDF membrane was activated in methanol for 1 minute. A wet-transfer sandwich was assembled in the transfer buffer in the following order from bottom to top: black side of the gel holder cassette, foam pad, western blotting filter paper, gel, PVDF membrane, western blotting filter paper, foam pad, and white side of the gel holder cassette. The wet transfer was performed at 100 V for 2 hours on ice. After disassembling the blotting apparatus, the membrane was blocked in 5% milk for 2 hours while shaking at room temperature and incubated in primary antibody (in 5% BSA in PBS-T) overnight while shaking at 4°C. On the following day, membranes were washed three times for 10 minutes in PBS-T and incubated for at least 2 hours in HRP-conjugated secondary antibodies of the appropriate specificity (in 5% BSA in PBS-T) while shaking at room temperature. After washing the membranes at least another three times in PBS-T for 10 minutes, a 1:1 mixture of the Clarity™ Western ECL substrate was added to the membrane, and protein bands were detected in the chemiluminescence imager Fusion system. Band intensities were quantified in the NIH ImageJ/FIJI program. For re-staining proteins, membranes were stripped by washing in 0.2 M NaOH for 20 minutes. Membranes were then washed three times for 10 minutes with PBS-T and again blocked and stained.

4.6.9 Coomassie staining

For Coomassie staining, gels were washed three times in dd$H_2$0 for 10 minutes, stained with Coomassie Brilliant Blue R-250 solution for 1 hour on a shaker (or until all bands of the un-stained protein ladder became visible), and de-stained in Coomassie Brilliant Blue De-Staining solution and ddH_2O. Visible gel bands in the region of interest were cut from the gel with a scalpel and sent in 0.5 mL tubes filled with 0.2% NaN_3 in ddH_2O to the Proteomics Core Facility (PCF), European Molecular Biology Laboratory (EMBL),

Heidelberg, Germany, for liquid chromatography-tandem mass spectrometry (LC-MS/MS) analysis.

4.6.10 Silver staining

For silver staining of proteins, gels were stained according to the manufacturer's instructions. Images of the stained gels were recorded by the Fusion system.

4.6.11 Identification of sphinganine-binding partners by liquid chromatography-tandem mass spectrometry

(In collaboration with Proteomics Core Facility (PCF), European Molecular Biology Laboratory (EMBL), Heidelberg, Germany)

Briefly, the procedure employed was akin to the one described earlier (*181*). Samples were subjected to in-gel digestion with trypsin (*182*). Peptides were extracted from the gel by sonication for 15 minutes, followed by centrifugation and supernatant collection. A solution of 50% water and 50% acetonitrile with 1% formic acid was added for a second extraction. The samples were again sonicated for 15 minutes and centrifuged, and the supernatant was pooled with the first extract. The supernatants were dried down, reconstituted in 10 µL 4% acetonitrile and 1% formic acid in water, and analyzed with LC-MS/MS. An UltiMate 3000 RSLC nano-LC system (Dionex, Sunnyvale, USA) equipped with a trapping cartridge (µ-Precolumn C18 PepMap 100, 5 µm, 300 µm i.d. x 5 mm, 100 Å) and an analytical column (nanoEase™ M/Z HSS T3 column 75 µm x 250 mm C18, 1.8 µm, 100 Å, Waters, Milford, USA) was coupled directly to an Orbitrap Fusion™ Lumos™ Tribrid™ Mass Spectrometer (Thermo Fisher Scientific, Waltham, USA) with the Nanospray Flex™ ion source in positive ion mode. Trapping was performed with a constant flow rate of 30 µL/minute of 0.05% trifluoroacetic acid in water for 4 minutes. Subsequently, peptides were eluted via the analytical column at a constant flowrate of 0.3 µL/minute with running solvent A (0.1% formic acid in water, 3% DMSO) and an increasing percentage of solvent B (0.1% formic acid in acetonitrile, 3% DMSO) from 2% to 8% in 1 minute; 8% to 23% for 39 minutes; 23% to 38% in another 5 minutes; an increase in B to 85% in 4 minutes; and re-equilibration back to 2% B for 6 minutes. The peptides were introduced into the Orbitrap Fusion Lumos via a Pico-Tip Emitter (360 µm OD × 20 µm ID; 10 µm tip, CoAnn technologies, Richland, USA) and an applied spray voltage of 2.4 kV.

The capillary temperature was set at 275°C. Full mass scans were acquired from 350 to 1500 m/z in profile mode in the Orbitrap with a resolution of 120000. The maximum fill time was set to 250 milliseconds. The instrument was operated in data-dependent acquisition mode, and MS/MS scans were acquired in the ion trap in rapid mode, with a fill time as high as 35 milliseconds and an AGC target set to standard. A normalized collision energy of 30 was applied, and the activation type was HCD. MS/MS data were acquired in centroid mode. The raw data were processed with MaxQuant (v1.6.3.4) (*183*) and searched against the UniProt *Mus musculus* database (17114 entries, July 2022). Carbamidomethyl (C) was set as a fixed modification, and acetyl (N-terminal) and oxidation (M) were set as variable modifications. The mass error tolerance for the full-scan MS spectra was set to 20 ppm for MS/MS spectra at 0.5 Da. No more than two missed cleavages were allowed. For protein identification, a minimum of one unique peptide with a peptide length of at least 7 amino acids and a false discovery rate below 0.01 were required at the peptide and protein levels. The calculation of intensity-based absolute quantification (iBAQ) values was enabled (*184*). The raw output files of MaxQuant (proteinGroups.txt file) were processed with the R programming language (ISBN 3-900051-07-0). As a quality filter, only proteins quantified with at least two unique peptides were allowed. A total of 1136 proteins were identified for sphinganine-biotin samples, and 565 proteins were identified for biotin samples. Raw iBAQ values were used in the analysis. Missing values were imputed with the knn method with the Msnbase package (*185*). Differential abundance was evaluated by the computation of the respective ratio of iBAQ signals.

4.6.12 Enzyme-linked immunosorbent assay

Plasma (7-15 µL) of PBS/LPS-injected mice or supernatant (100 µL) of PBS- or LPS/IFN-γ-stimulated BMDM was analyzed by enzyme-linked immunosorbent assay (ELISA) according to the manufacturer's instructions. Optical densities at 450 nm were determined in a microplate reader, and for wavelength correction, readings at 540 nm were subtracted.

4.6.13 Cytokine array

Each membrane was probed with plasma from a different PBS- or LPS-injected (L2630, Sigma-Aldrich) mouse, and the cytokine array was performed according to the manufacturer's instructions. Images of the membranes were recorded with the ECL method in the Fusion system, and dot pixel densities were quantified in ImageJ/FIJI.

4.6.14 Flow cytometry

In all flow cytometric (also referred to as fluorescence-activated cell sorting, FACS) experiments, single-stain controls (containing sample mix stained with only one antibody) were used for the setting of voltages and compensation, and fluorescence-minus-one (FMO) controls (containing sample mix stained with all antibodies except one) were used for the setting of gates. Additionally, an all-stain control (a sample mix stained with all antibodies) and a no-stain control (a sample mix with no antibodies) were included. Staining panels were prepared not more than 3 days before the staining. Cells were transferred into 96-well U-bottom plates and incubated for at least 15 minutes on ice with Ultra-LEAF™ purified anti-mouse CD16/32 antibody (2.5 µg/mL) in FACS buffer to prevent non-specific antibody binding to Fc receptors. Cells were washed with 150 µL FACS buffer and centrifuged (2000 rpm, 2 minutes), followed by disposal of the supernatant. For surface antigen staining, cells were incubated in 50 µL fluorophore-conjugated surface antibody mix in FACS buffer for at least 30 minutes on ice in the dark. Upon surface antigen staining only, cells were washed with 150 µL FACS buffer, centrifuged (2000 rpm, 2 minutes), and incubated in 100 µL fixation buffer containing 4% paraformaldehyde for at least 30 minutes on ice in the dark. Upon intracellular cytokine staining, cells were washed, fixed equally, and then washed twice in 200 µL 1× permeabilization buffer and centrifuged (2000 rpm, 2 minutes). Then, cells were incubated in 50 µL intracellular antibody mix in 1× permeabilization buffer in ddH_2O for at least 30 minutes on ice in the dark. For staining of all other intracellular or nuclear antigens, cells were washed with 150 µL FACS buffer, centrifuged (2000 rpm, 2 minutes), and incubated in 200 µL Foxp3 fixation buffer (Foxp3 fixation/permeabilization concentrate with Foxp3 fixation/permeabilization diluent mixed 1:3) for at least 30 minutes on ice in the dark. Then, cells were incubated in 50 µL intracellular antibody mix in 1× permeabilization buffer for at least 30 minutes on ice in the dark, washed twice in 200 µL 1× permeabilization buffer,

and centrifuged (2000 rpm, 2 minutes). When cells were stained with primary intracellular antibodies without fluorophores, after primary intracellular antibody staining, cells were washed twice in 200 µL 1× permeabilization buffer and stained in 50 µL secondary antibody mix in 1× permeabilization buffer (in which antibodies that were specific to the host of the primary antibody were coupled to fluorophores) for another 30 minutes on ice in the dark. After surface and/or intracellular staining, samples were washed with 150 µL FACS buffer, centrifuged (2000 rpm, 2 minutes), and resuspended in 100 µL FACS buffer. Samples were stored at 4°C and measured within 3 days after staining and fixation on BD LSR II, BD FACSCanto™, or BD LSRFortessa™ flow cytometers and analyzed in FlowJo software.

4.6.15 Confocal fluorescence microscopy

For confocal fluorescence microscopy (CFM), per well, 0.5 million BMDM were grown and polarized on glass coverslips in 12-well plates (see Section 4.3.1). Medium was carefully removed from the wells, and cells were washed in 500 mL microscopy buffer for 5 minutes on a shaker at room temperature. Microscopy buffer was removed, and cells were incubated for at least 15 minutes on ice with 500 µL Ultra-LEAF™ purified anti-mouse CD16/32 antibody (2.5 µg/mL) in microscopy buffer to prevent non-specific antibody binding to Fc receptors. Fc-blocking buffer was discarded, and for TLR4 surface antigen staining, cells were incubated in 250 µL fluorophore-conjugated α-TLR4 antibody in microscopy buffer while shaking for at least 1 hour on ice in the dark. The following incubation and washing steps were all performed on ice while shaking in the dark. The staining solution was removed, and cells were washed twice in 500 mL microscopy washing buffer for 5 minutes. After removal of the washing buffer, cells were incubated in 500 µL fixation buffer containing 4% paraformaldehyde for at least 30 minutes. The fixation buffer was removed, and cells were incubated twice in 500 µL 1× permeabilization buffer for 5 minutes. Cells were incubated in 250 µL intracellular antibody mix (fluorophore-conjugated α-GFP and primary α-MyD88 antibody) in microscopy buffer. On the following day, the staining solution was removed, and cells were incubated twice in 500 µL 1× permeabilization buffer for 5 minutes. The solution was removed, and for secondary intracellular antibody staining, cells were incubated in 250 µL secondary antibody (coupled to a fluorophore and specific to the host of the primary antibody) in 1×

permeabilization buffer for at least 2 hours. The staining solution was removed, and cells were incubated twice in 500 µL 1× permeabilization buffer for 5 minutes. The solution was removed, and for nuclei staining, cells were incubated in 500 µL DAPI in 1× permeabilization buffer for 5 minutes. The staining solution was removed, and cells were incubated twice in 500 µL 1× permeabilization buffer for 5 minutes. Coverslips were removed from the wells using tweezers and mounted upside down onto 1 drop of mounting medium on adhesion slides. Mounted slides were stored at 4°C and imaged within one day under a confocal laser scanning microscope 710 (LSM710) in ZEN Black software and analyzed in ZEN Blue software and ImageJ/FIJI.

4.6.16 Limulus amebocyte lysate assay

To measure LPS concentrations in lysate from mouse spleen, tumor, and skin samples, a limulus amebocyte lysate (LAL) assay was performed according to the manufacturer's instructions. Optical densities at 405 nm were determined in a microplate reader.

4.7 Cellular metabolism methods

4.7.1 Seahorse extracellular flux analysis

On the day before the assay, each well of the Seahorse sensor cartridge from the Seahorse XFe96 FluxPak was hydrated using 200 µL ddH_2O in the utility plate overnight at 37°C. BMDM were grown (see Section 4.3.1), and on day 6, BMDM were washed in cold PBS, detached with 0.25% trypsin-EDTA, counted, and 0.07-0.1 million BMDM in 200 µL polarization medium per well were re-seeded into Seahorse XF cell culture microplates for overnight polarization (see Section 4.3.1). On the day of the assay, ddH_2O was removed from the utility plate, and 200 µL Seahorse XF calibrant per well was added for incubation in a non-CO_2 incubator at 37°C for at least 30 minutes. The medium was removed from the BMDM, and cells were washed twice in cold PBS. To perform mitochondrial stress testing, per well, 180 µL Seahorse FX base medium supplemented with 2 mM glutamine, 10 mM D-(+)-glucose, and 1 mM sodium pyruvate were added for 30-60 minutes in a non-CO_2 incubator at 37°C. Meanwhile, drugs were prepared in the same medium, loaded into the cartridge, and injected during the assay (Table 25).

Table 25 Drug injection protocol for mitochondrial stress test

Drug	Target	Final concentration	Port	Volume
Oligomycin	Complex V (adenosine triphosphate (ATP) synthase)	20 µM	A	20 µL
FCCP	Inner mitochondrial membrane	1 µM	B	22 µL
Rotenone + Antimycin A	Complex I and III	2 µM each	C	25 µL

To perform glycolysis stress testing, per well, 180 µL Seahorse FX base medium supplemented with 2 mM glutamine was added for 30-60 minutes in a non-CO_2 incubator at 37°C. Meanwhile, drugs were prepared in the same medium, loaded into the cartridge, and injected during the assay (Table 26).

Table 26 Drug injection protocol for glycolysis stress test

Drug	Target	Final concentration	Port	Volume
Glucose	Glycolysis	20 mM	A	20 µL
Oligomycin	Complex V (ATP synthase)	10 µM	B	22 µL
2-DG	Glycolysis	50 mM	C	25 µL

Edge wells only contained Seahorse FX base medium (supplementation depending on the assay as described above) without cells and served as background controls. The cartridge and the Seahorse XF Cell Culture microplate were placed in the Seahorse XFe96 analyzer and in the Wave software, the following program was started (Table 27).

Table 27 Seahorse program

Step	Time	Cycles
Calibration and equilibration	Standard	-
Baseline	Mix (3 minutes) and measure (3 minutes)	3
Port A injection		3
Port B injection		3
Port C injection		3
Final measurement		3

4.7.2 Sphingolipid-metabolomics by liquid chromatography coupled-tandem mass spectrometry

(In collaboration with Dr. R. Sandhoff, Lipid Pathobiochemistry Group (A411), German Cancer Research Center (DKFZ), Heidelberg, Germany)

LPS-polarized BMDM were washed in cold PBS, scraped from the culture dishes (see Section 4.3.1), re-suspended in HBSS (1% FBS), and counted. Per reaction, 2 million BMDM in 1 mL HBSS (1% FBS) were pulse-chased with tracer-labeled 500 µM $^{13}C_3{}^{15}N_1$ L-serine and 10 µM BSA-conjugated palmitic acid in NaOH for 2 hours at 37°C, 5% CO_2. Every 30 minutes, the cells were gently mixed, and subsequently, the cells were washed twice in cold PBS, and the pellets were immediately snap-frozen on dry ice and stored at -80°C. The cell pellets were submitted to the Lipid Pathobiochemistry Group (A411), German Cancer Research Center (DKFZ), Heidelberg, Germany, and subjected to lipid extraction and analysis by LC-MS/MS as described previously (*186*). In addition to the internal standards described, D7-sphingosine (d18:1), D7-sphinganine (d18:0), and sphingosine (d20:1)-1-phosphate (all from Avanti Polar Lipids) were used to quantify the respective sphingoid bases. The gradient to analyze free sphingoid bases started with a more polar composition of 65% solvent A. Additionally, monitored sphingosine-1-phosphates and sphinganine-1-phosphates were recorded with the transition of protonated molecular species to the fragments remaining after loss of H_3PO_4 + H_20 (at 8 eV) and loss of H_3PO_4 (at 12 eV), respectively.

4.7.3 Targeted metabolic profiling

(In collaboration with Dr. G. Poschet, Metabolomics Core Technology Platform, Centre for Organismal Studies (COS) Heidelberg, Heidelberg, Germany)

Briefly, the procedure employed was akin to the one described earlier (*187, 188*). BMDM were M0-like, M1-like, or M2-like polarized for 24 hours (see Section 4.3.1). The polarization medium of BMDM was collected, centrifuged (2000 rpm, 2 minutes) to remove floating cells, and stored at -80°C. BMDM were washed in 2 mL ice-cold 0.9% NaCl solution, and after removal of the washing solution, 0.7 mL 0.9% NaCl solution was added per well. BMDM from 2 wells were gently scraped and transferred into pre-cooled 1.5 mL Eppendorf tubes. BMDM were counted for later normalization, and after centrifugation (2000 rpm, 2 minutes), the supernatant was removed completely, and pellets were snap-frozen and stored at -80°C. Cell pellets and 100 µL supernatant were submitted to the Metabolomics Core Technology Platform, Centre for Organismal Studies (COS) Heidelberg, Heidelberg, Germany. Cell extracts for downstream metabolomics analyses were prepared as described by Andresen *et al.* (2022) using the “75% EtOH/MTBE” protocol (*188*). In total, 1019 metabolites covering 14 small molecules and 25 different lipid classes were analyzed using the MxP® Quant 500 XL kit (Biocrates) following the manufacturer’s protocol. In brief, 10 µl of cell culture supernatants or cell extracts were pipetted on a 96-well plate containing internal standards and dried under a nitrogen stream using a positive pressure manifold (Waters). Subsequently, 50 µl of a 5% phenyl isothiocyanate solution was added to each well to derivatize amino acids and biogenic amines. After 1 hour of incubation at room temperature, the plate was dried again. To extract the metabolites, 300 µl 5 mM ammonium acetate in methanol was pipetted to each filter and incubated for 30 minutes. The extract was eluted into a new 96-well plate under positive pressure. For further LC-MS/MS analyses, 150 µl of the extract was diluted with an equal volume of water. For FIA-MS/MS analyses, 10 µl extract was diluted with 490 µl of FIA solvent (provided by Biocrates). For the preparation of the FIA XL plate, 10 µl of cell culture supernatants or cell extracts were pipetted onto a second 96 well-plate containing internal standards and dried under a nitrogen stream as described above. Subsequently, 300 µl extraction solvent (19 mg ammonium acetate in 50 mL methanol) was added to each well, and after 30 minutes of incubation, it was eluted into a new 96-well plate using positive pressure. For FIA XL-MS/MS analyses, 50 µl extract was diluted

with 450 µl of FIA solvent. After dilution, LC-MS/MS and FIA (XL)-MS/MS measurements were performed. Chromatographic separation was performed with a UPLC I-class PLUS (Waters) system coupled to a SCIEX QTRAP 6500+ mass spectrometry system in electrospray ionization (ESI) mode. Data was generated using the Analyst (Sciex) software suite and transferred to the WebIDQ software (Biocrates), which was used for further data processing and analysis. All metabolites were identified with isotopically labeled internal standards and multiple reaction monitoring (MRM) with optimized MS conditions as provided by Biocrates. For quantification, either a seven-point calibration curve or a one-point calibration was used, depending on the metabolite class.

4.8 Statistics

GraphPad Prism was used to perform statistical analysis. When comparing two groups, first it was determined whether the data points were normally distributed. The statistical analysis of normally distributed data was performed with the two-tailed Student's *t* test. Statistical analysis of data points that were not normally distributed was performed with the Mann-Whitney U test (also known as the Wilcoxon rank sum test). Simultaneous comparisons of more than two groups were performed with a one-way analysis of variance (ANOVA). In all cases, $P<0.05$ was considered statistically significant. Sample sizes are indicated in the figure legends. Data are presented as mean ± SD, or as specified in the figure legends.

5. Results

5.1 LPS induces sphingolipid synthesis in macrophages

To study different macrophage activation states, with slight modifications, I established the previously described *in vitro* model of BMDM in our laboratory (*189*) (Figure 8A). BM cells from the femur and tibia were isolated and cultured for six days in the presence of M-CSF to generate BMDM, which were polarized for one day to either M0-like, M1-like, or M2-like macrophage phenotypes through supplementation with PBS, LPS/IFN-γ, or IL-4/IL-13, respectively.

To identify metabolites regulating signal transduction in different macrophage subtypes, in collaboration with Dr. G. Poschet (Metabolomics Core Technology Platform, Centre for Organismal Studies (COS) Heidelberg, Heidelberg, Germany), I performed a large targeted metabolomics screening via the Biocrates MxP® Quant 500 XL kit to determine up to 1019 metabolites in BMDM treated with PBS (M0-like macrophages), LPS/IFN-γ (M1-like macrophages), and IL-4/IL-13 (M2-like macrophages) for 24 hours (Figure 8B). LPS/IFN-γ treatment increased the concentrations of the amino acid citrulline, whereas IL-4/IL-13 treatment increased the levels of the amino acid kynurenine, thus echoing previous results indicating that in M1-like macrophages, arginine is metabolized to nitric oxide and citrulline, whereas in M2-like macrophages, kynurenine is generated from tryptophan degradation (*190*), respectively (Figure 8B). M2-like macrophages, which are known to depend on fatty acid oxidation but not LPS/IFN-γ-treated macrophages, which are dependent on glycolysis, showed significantly increased levels of the fatty acid eicosenoic acid (20:1) compared to PBS-treated macrophages (Figure 8B). Although no clear differences in the levels of acylcarnitines or bile acids were observed between untreated and LPS/IFN-γ-treated macrophages, metabolites belonging to various lipid subclasses were elevated in LPS/IFN-γ-treated and IL-4/IL-13-treated macrophages, including phospholipids (e.g., phosphatidylethanolamines, phosphatidylcholines), glycerophospholipids (e.g., phosphatidylglycerols, phosphatidylinositols), and triacylglycerols (Figure 8B). Treatment with LPS/IFN-γ and, to a lesser extent, IL-4/IL-13 resulted in significantly greater levels of sphingolipids (ceramides, glycosylceramides, dihydroceramides, sphingomyelins, and sphingoid bases) than observed in untreated macrophages (Figure 8B). Sphinganine d16:0 was significantly enriched in LPS/IFN-γ-

treated macrophages compared with untreated macrophages but was not significantly enriched in IL-4/IL-13-treated macrophages (Figure 8B). Collectively, these results suggested that M1-like and M2-like macrophage stimuli enriched sphingolipid metabolites in macrophages.

To better understand through which sphingolipid pathway (*de novo* or recycling pathway) certain sphingolipids were enriched following LPS stimulation in M1-like macrophages, I mined previously published mouse RNA sequencing datasets to check for the expression of sphingolipid metabolism-associated enzymes (*191*) and found that LPS stimulation increased the mRNA levels of *Sptlc2*, but not mRNA levels of *Sptlc1* and the recycling pathway-associated enzymes, ceramidase (*Asah1-2*), sphingomyelinase (*Smpd1-4*), sphingosine-1-phosphate phosphatase (*Sgpp1*), glucosylceramidase (*Gba, Gba2*) and galactosylceramidase (*Galc*) in BMDM, suggesting that the *de novo* biosynthesis pathway rather than a recycling pathway is actively induced by LPS (Figure 8C).

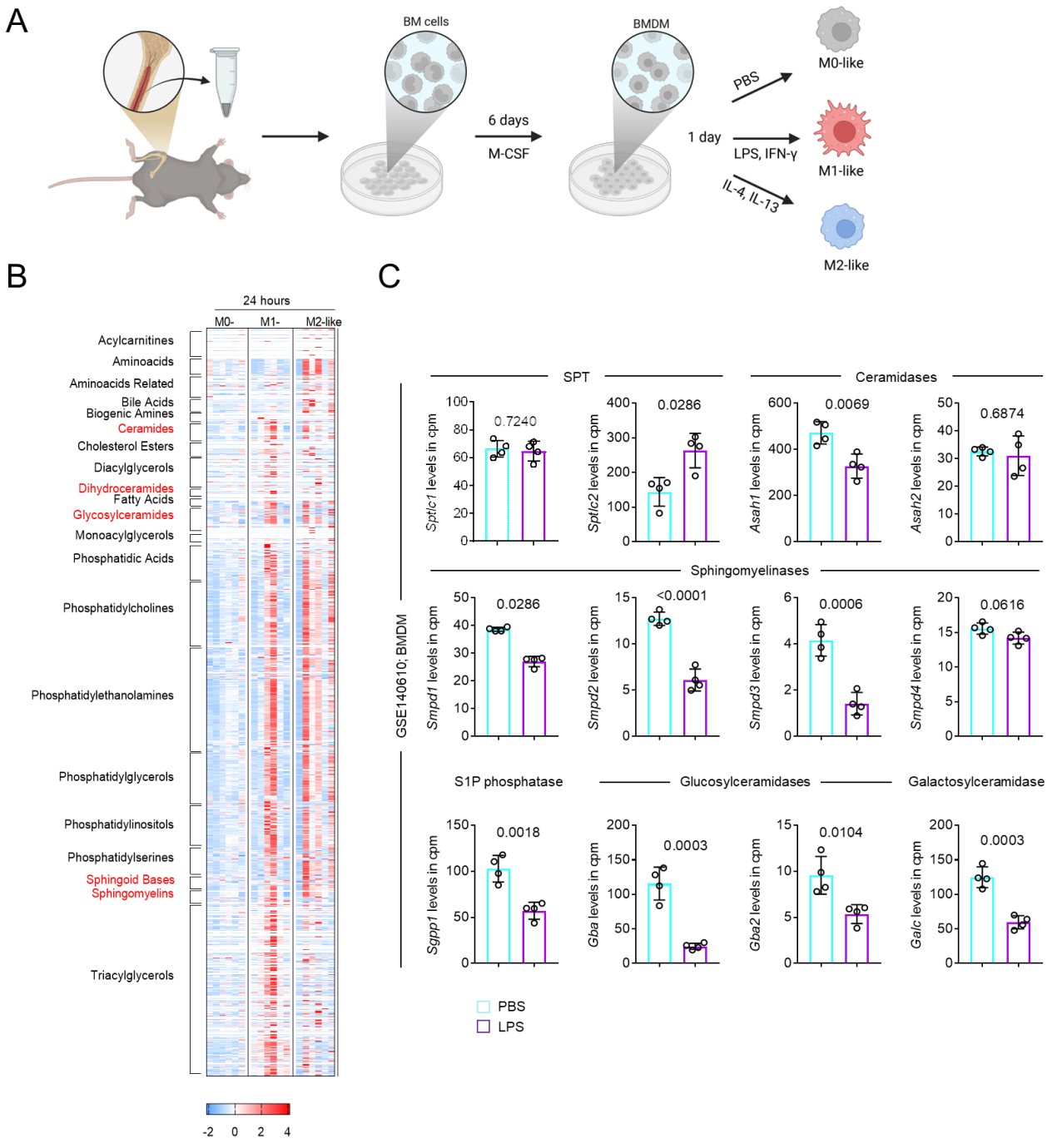

Figure 8 Sphingolipid metabolites are enhanced in M1-like BMDM.

(A) Illustration of the experimental design of the bone marrow-derived macrophage (BMDM) model. Bone marrow (BM) cells of C57BL/6 mice were isolated from femur and tibia samples and differentiated over six days in the presence of M-CSF to BMDM. BMDM were polarized as indicated toward M0-like, M1-like, or M2-like macrophage phenotypes by PBS, LPS (100 ng/mL)/IFN-γ (50 ng/mL), or IL-4 (10 ng/mL)/IL-13 (10 ng/mL) stimulation, respectively. Figure adapted from “Murine monocyte and macrophage culture” by BioRender.com (2023).

(B) Heat map showing concentration *z*-scores of targeted metabolomics analysis via the Biocrates MxP® Quant 500 XL kit. BMDM were generated as shown in A, and 1019 metabolites were quantified. In collaboration with Dr. G. Poschet, Metabolomics Core Technology Platform, Centre for Organismal Studies (COS) Heidelberg, Heidelberg, Germany.
(C) Bar graphs showing RNA sequencing analysis of *Sptlc1*, *Sptlc2*, *Asah1*, *Asah2*, *Smpd1*, *Smpd2*, *Smpd3*, *Smpd4*, *Sgpp1*, *Gba*, *Gba2*, *Galc* in mouse BMDM after PBS or LPS treatment (N=4). The original RNA sequencing dataset was previously published (*191*). Cpm, counts per million. Data are presented as mean (B) or mean ± SD (C). Statistical comparisons were performed with two-tailed Student's *t* tests (C; data points were normally distributed). Figures 8B-C are included in (*192*).

To investigate whether M1-like macrophage stimuli also induced Sptlc2 on the protein level, I identified different macrophage subtypes based on their exclusive M1-like (CD38) or M2-like (Egr2) macrophage marker expression (*72*) in flow cytometry and checked their Sptlc2 levels (Figure 9A). Echoing the RNA sequencing and the metabolomics results, the Sptlc2 protein and ceramide levels, respectively, were higher in M1-like than in M0-like macrophages (Figure 9B). In contrast to the metabolomics results, in which M2-like macrophages, similarly to M1-like macrophages, seemed to induce levels of most sphingolipids (not sphinganine d16:0), flow cytometry results suggested that Sptlc2-dependent generation of some sphingolipids, such as, for example, distinct ceramides, is stronger induced in M1-like than M2-like macrophages.

To narrow down whether LPS alone was sufficient for this phenotype, I stimulated BMDM with only LPS but no IFN-γ, and checked Sptlc2 protein levels by immunoblotting (Figure 9C). In line with the literature, LPS alone induced Sptlc2 levels, a process that was shown before to be NF-κB-mediated (Figure 9C-D) (*162, 193-196*). Collectively, these results suggested that LPS induced sphingolipid anabolism via the Sptlc2 axis in M1-like macrophages.

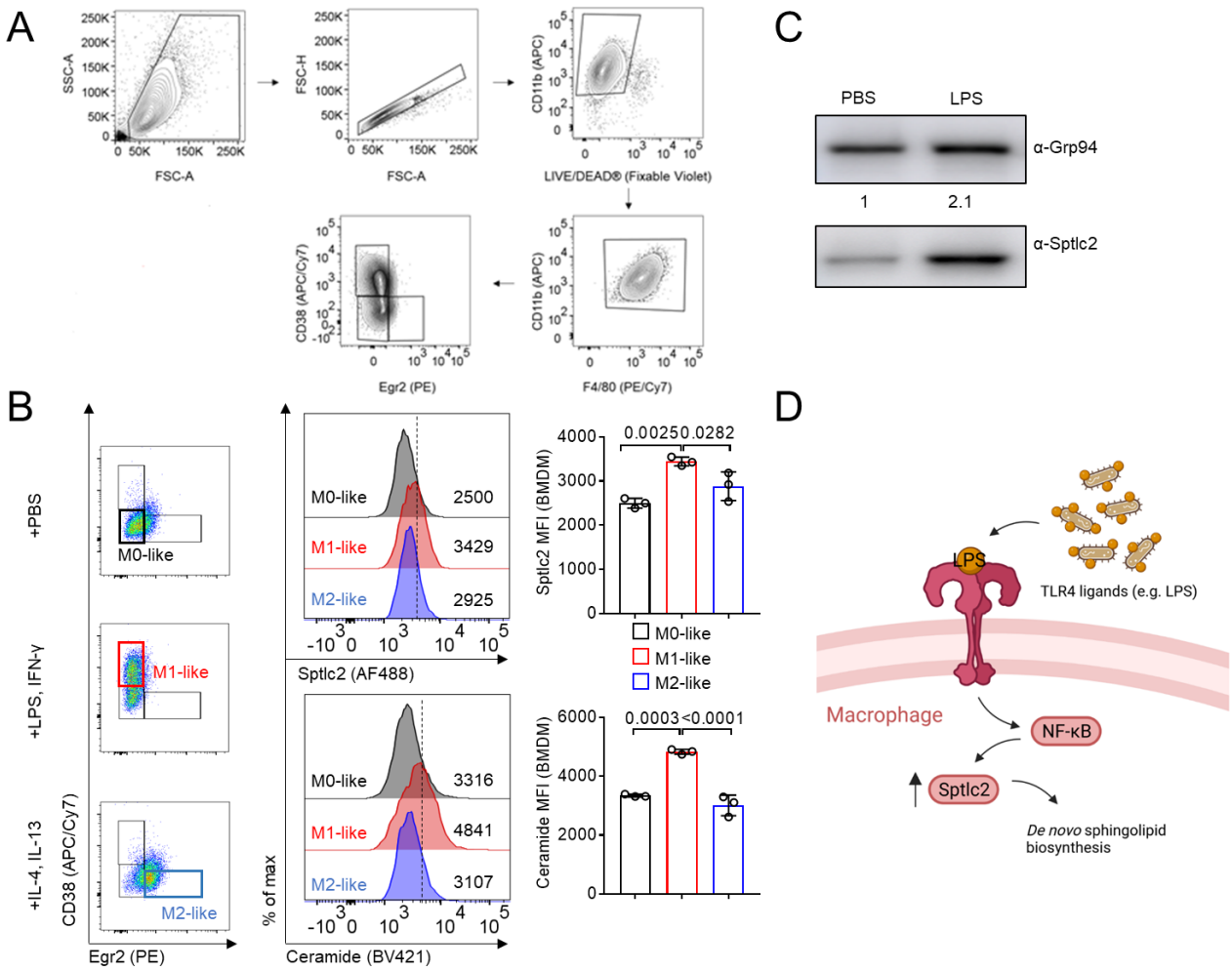

Figure 9 LPS increases Sptlc2 levels in M1-like macrophages.

(A) Representative flow cytometry contour plots showing the gating strategy used in B to identify M0-like (live CD11b+F4/80+CD38-Egr2- cells), M1-like (live CD11b+F4/80+CD38+Egr2- cells) and M2-like (live CD11b+F4/80+CD38-Egr2+ cells) BMDM. The example shows M1-like BMDM.

(B) Representative flow cytometry plots displaying the expression of the M1-like macrophage marker CD38 and the M2-like macrophage marker Egr2 in BMDM (live CD45+CD11b+F4/80+ cells) under M0-like, M1-like, or M2-like macrophage stimuli. Flow cytometry histograms and bar graphs showing the Sptlc2 and ceramide mean fluorescence intensity (MFI) of M0-like, M1-like, and M2-like BMDM (N=3).

(C) Immunoblot analysis of Sptlc2 protein expression in BMDM lysate from WT mice after 20 hours of treatment with PBS or LPS (100 ng/mL). Grp94 served as a loading control. Quantification was performed in FIJI, and numbers refer to relative band intensities.

(D) Schematic summarizing LPS-induced enrichment of Sptlc2-dependent sphingolipid *de novo* biosynthesis is NF-κB-mediated (*162*). Data are presented as mean ± SD (B). Statistical comparisons were performed with ANOVA tests (B; for simultaneous comparisons of more than two groups). Figures 9A-C are included in (*192*).

5.2 LPS induces Sptlc2 in macrophages

During my master's thesis, I studied the effect of chemical inhibitors of sphingolipid metabolism on macrophage polarization (Hering, M.; 2020; To study the role of sphingolipids in macrophage polarization; Master's thesis (*170*); Supplementary Figure 32). Inhibition of Sptlc2 by myriocin showed a trend towards increased M2-like (Arginase-1, Egr2) and decreased M1-like (CD38) macrophage markers on BMDM (Supplementary Figure 32A, C). In contrast, fumonisin B_1, an inhibitor of ceramide synthase, was used to increase sphinganine levels and thereby mimic high Sptlc2 activity, which was found to show a trend towards reduced M2-like and increased M1-like macrophage markers (Supplementary Figure 32B). Collectively, from these data, I concluded that LPS-induced sphingolipid enrichment was not only an inconsequential correlation but was also actively affecting macrophage signaling, and thus Sptlc2 activity might be relevant for macrophage polarization.

To build on these observations by studying Sptlc2-dependent sphingolipids, first, mice with a myeloid cell-specific ablation of *Sptlc2* (referred to as *Lyz2*-cre or *Sptlc2*-deficient mice) were generated in our laboratory (*172, 174*). While germline deficiency of *Sptlc2* is embryonically lethal (*174*), tissue-specific deletion of *Sptlc2* using the Cre-lox system allowed for the study of this enzyme in myeloid cells specifically. For this, *Sptlc2*$^{Flox/Flox}$ mice were bred with *Lyz2*-cre mice (*172, 174*). Offspring from this breeding, which had one allele of *Sptlc2* floxed and which had a *Lyz2*-cre, were again bred with *Sptlc2*$^{Flox/Flox}$ mice to generate *Sptlc2*$^{Flox/Flox}$ *Lyz2*-cre mice (heterozygous for *Lyz2*-cre; Figure 10A). Mice, which expressed no cre recombinase (see Sections 4.1.2-4.1.3), served as control animals (referred to as WT in the following work). Mouse genotypes were determined with genotyping primers and the protocol from Jackson Laboratory for B6.129P2-*Lyz2*$^{tm1(cre)Ifo}$/J (see Section 4.1.3; Figure 10B). Further, I then performed western blotting to confirm the deletion of *Sptlc2* at the protein level (Figure 10C). As previous results (Figure 9C-D) suggested that LPS induced Sptlc2 expression, I included an LPS-treated group and found that LPS did not induce Sptlc2 expression in the *Lyz2*-cre BMDM (Figure 10C).

To transfer these findings into an *in vivo* model, I intraperitoneally injected mice with LPS and measured Sptlc2 levels by flow cytometry (Figure 10D-E). In line with the *in vitro* results, intraperitoneal injection of LPS increased Sptlc2 protein levels in intraperitoneal and splenic macrophages (Figure 10D-E). Collectively, these results suggested that LPS

enhances the expression of Sptlc2 to induce sphingolipid synthesis in macrophages *in vitro* and *in vivo,* and that a suitable mouse model to study Sptlc2-derived sphingolipids in LPS-induced macrophage signal transduction and polarization was set up.

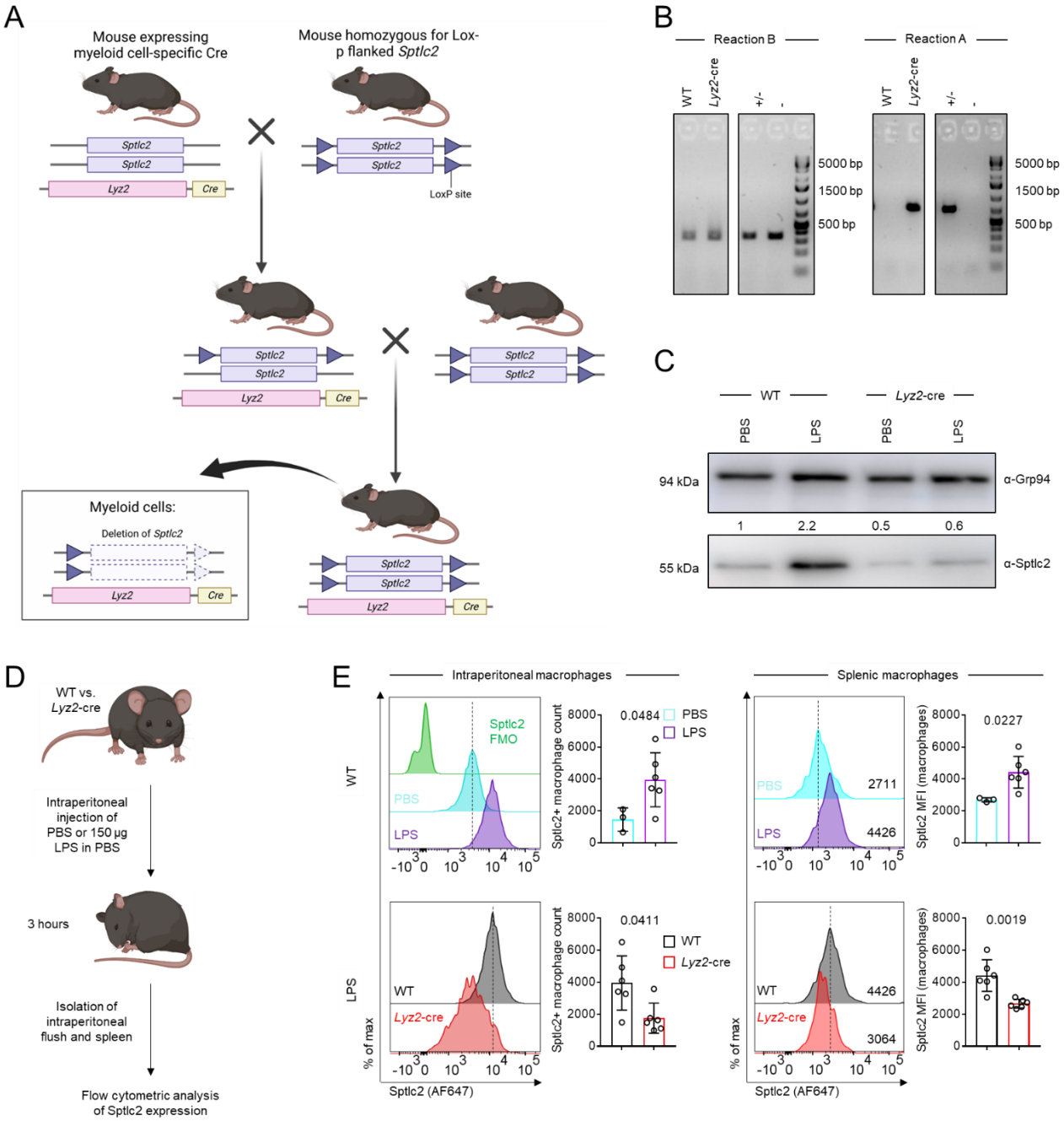

Figure 10 LPS increases Sptlc2 expression in M1-like WT but not in *Sptlc2*-deficient macrophages.

(A) Breeding scheme for the generation of myeloid cell-specific *Sptlc2*-deficient mice. Figure adapted from "Generation of Cre-LoxP-mediated conditional knockout mice" by BioRender.com (2023).

(B) Representative genotype analysis of the WT or *Lyz2*-cre mouse used in C. Genotyping primers were used according to the protocol for "separated PCR" for B6.129P2-*Lyz2*$^{tm1(cre)Ifo}$/J from Jackson Laboratory

(see Section 4.1.3 and manufacturer's instructions for additional primer details for reactions A and B). Heterozygous ~700 bp and ~350 bp; wildtype ~350 bp; +/-, positive control (heterozygous); -, negative control (wildtype).
(C) Immunoblot analysis of Sptlc2 protein expression in BMDM lysate from WT or *Lyz2*-cre mice after 20 hours of PBS or LPS (100 ng/mL) stimulation. Grp94 was used as a loading control. Quantification was done in FIJI, and numbers refer to relative band intensities.
(D) Illustration of the experimental design in E. PBS or LPS (150 µg) was intraperitoneally injected into WT or *Lyz2*-cre mice, and after 3 hours, mice were sacrificed and samples for flow cytometric Sptlc2 protein analysis were isolated.
(E) Flow cytometry histograms and bar graphs documenting the expression of Sptlc2 in intraperitoneal and splenic macrophages (live CD45+CD11b+CD3-B220-NK1.1-Ly6G-F4/80+ cells) from WT mice 3 hours after PBS (N=3) or 150 µg LPS (N=6) injection (top) and from WT or *Lyz2*-cre mice 3 hours after 150 µg LPS (N=6) injection (bottom). Data are presented as mean ± SD (E). Statistical comparisons were performed with two-tailed Student's *t* tests (E: graph top left, graphs on the right; data points were normally distributed) and two-tailed Mann-Whitney U tests (E: graph bottom left; data points were not normally distributed). Figures 10B-E are included in (*192*).

5.3 *Sptlc2* deficiency decreases macrophage cell growth and metabolic fitness

During the cultivation of the BMDM, I observed that the medium of *Sptlc2*-sufficient macrophages, particularly M1-like macrophages, appeared more yellow than that of *Sptlc2*-deficient macrophages (Figure 11A). Follow-up pH measurements confirmed that the medium of *Sptlc2*-sufficient macrophages was more acidic than that of *Sptlc2*-deficient macrophages and that the M1-like macrophage medium was the most acidic (Figure 11A). I hypothesized that pH changes in the culture medium can be caused by differences in cell numbers, metabolic activities, or both. To test the first, I used an Incucyte® S3 for analysis of cell confluency and found that *Sptlc2*-sufficient macrophages showed higher confluency than *Sptlc2*-deficient macrophages upon LPS, but not PBS stimulation (Figure 11B). First, I suspected that not a difference in cell numbers between WT or *Lyz2*-cre BMDM causes the confluency difference, but rather that the existing WT cells grew upon LPS challenge, whilst *Lyz2*-cre BMDM did not. To have a closer look into this, I decided to use scanning electron microscopy (SEM) analysis in collaboration with Dr. K. Richter (Electron Microscopy Group (W230), German Cancer Research Center (DKFZ), Heidelberg, Germany), which revealed that *Sptlc2*-sufficient and *Sptlc2*-deficient macrophages had distinct morphologies upon LPS-induced activation: The LPS-

polarized, *Sptlc2*-sufficient macrophages showed a bumpy cell body in the center, from which filopodia and lamellipodia extended, whereas the *Sptlc2*-deficient macrophages showed a flat cell body and very few filopodia (Figure 11C-D). Supplementing the Sptlc2 downstream metabolite sphinganine restored the morphology of *Sptlc2*-deficient macrophages (Figure 11C-D). Collectively, these results suggested that Sptlc2 was required for LPS-induced cell growth and morphological changes in macrophages.

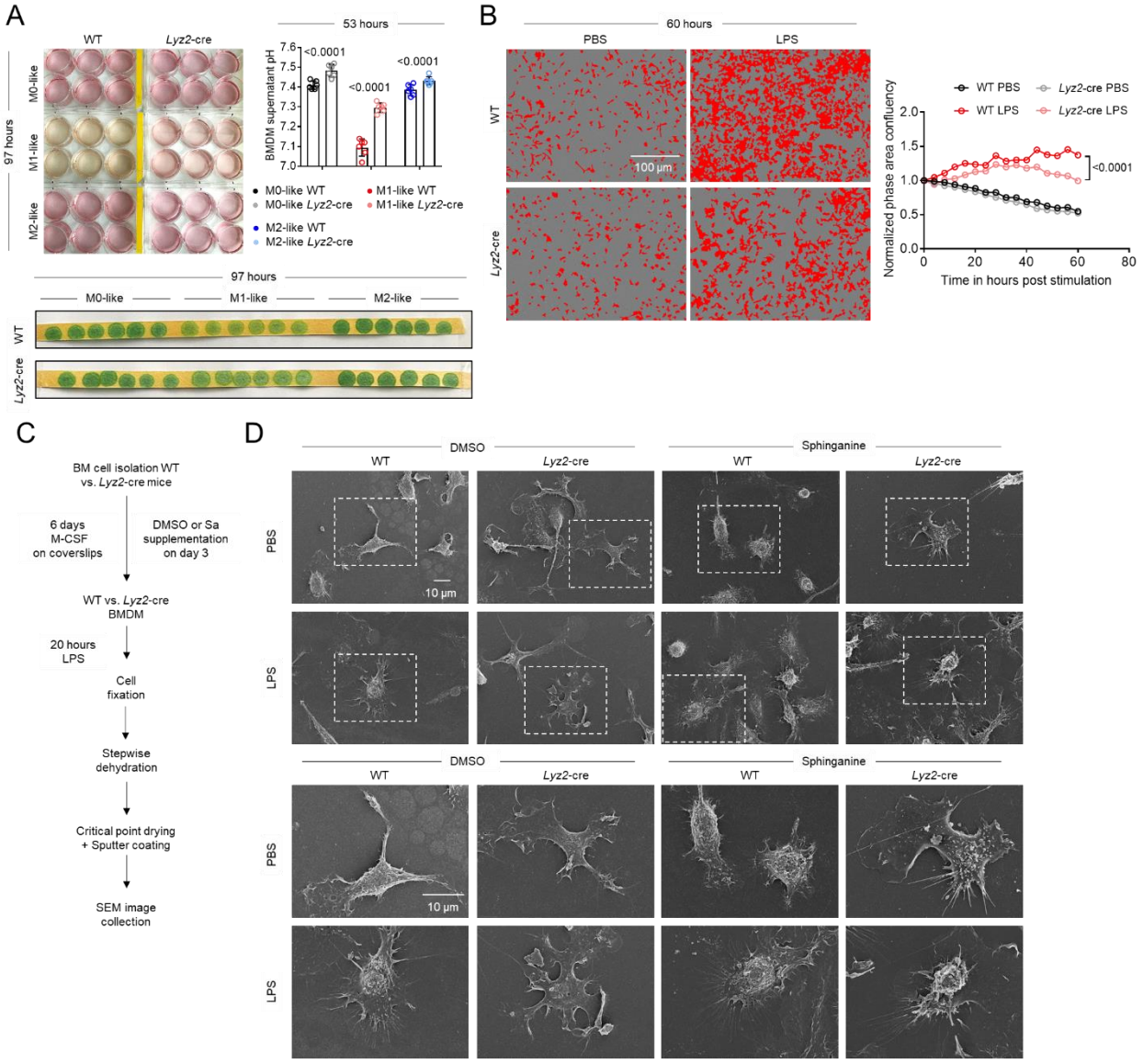

Figure 11 Deficiency of *Sptlc2* decreases M1-like macrophage confluency and morphology, which can be restored by sphinganine.

(A) Picture of M0-like, M1-like, and M2-like WT or *Lyz2*-cre BMDM in 6-well plates showing medium color change (97 hours after stimulation) and a bar graph showing pH measurement of cell culture medium (53

hours after stimulation) (N=6). Images of pH indicator paper, which was used to test supernatants of WT or *Lyz2*-cre BMDM 97 hours after M0-like, M1-like, and M2-like macrophage stimuli (N=6).
(B) Representative Incucyte® S3 images with an overlaid confluency mask in red (60 hours after PBS or LPS; left) and a line graph (normalized confluency; right) illustrating the confluency of PBS or LPS-treated WT or *Lyz2*-cre BMDM over time (N=16).
(C) Illustration of the experimental design for the scanning electron microscopy (SEM) analysis in D. Sa, sphinganine
(D) Representative scanning electron microscopy images of WT or *Lyz2*-cre BMDM after DMSO treatment or supplementation with sphinganine for 3 days and PBS or LPS polarization for 24 hours (N=30). Dashed white boxes in the upper panel mark the enlarged cells shown below. In collaboration with Dr. K. Richter, Electron Microscopy Group (W230), German Cancer Research Center (DKFZ), Heidelberg, Germany. Data are presented as mean ± SD (A) or mean only (B). Statistical comparisons were performed with ANOVA tests (A; for simultaneous comparisons of more than two groups) or two-tailed Student's *t* tests (B; data points were normally distributed). Figures 11 A-B, D are included in (*192*).

To test whether *Sptlc2* deficiency, in addition to macrophage morphology, might influence cellular metabolism, I performed Seahorse extracellular flux analysis to assess the mitochondrial respiratory and glycolytic states of M1-like and M2-like BMDM (Figure 12A-B). In agreement with findings from a previous study (*75*), M1-like macrophages, compared with M2-like macrophages, showed higher glycolytic rates at the expense of oxidative phosphorylation (Figure 12C-D). Moreover, *Sptlc2* deficiency decreased the oxygen consumption rate (OCR) of M2-like macrophages and the extracellular acidification rate (ECAR) of M1-like macrophages (Figure 12C-D). The basal OCR, the maximal OCR, and the spare respiratory capacity (SRC; the difference in basal and maximal OCR) of M2-like and the basal ECAR, the glycolytic capacity (maximal ECAR), and the glycolytic reserve (the difference in glycolytic response ECAR and maximal ECAR) of M1-like BMDM were drastically impaired upon deficiency of *Sptlc2* (Figure 12C-D). Collectively, these results suggested that Sptlc2 was required for the metabolic fitness of M1- and M2-like macrophages.

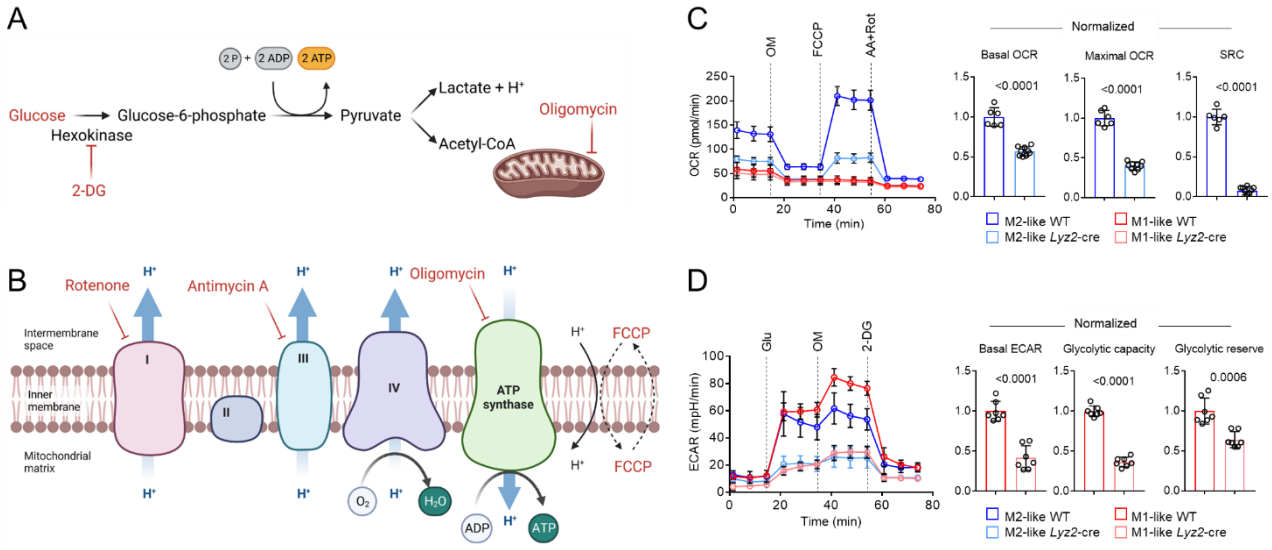

Figure 12 *Sptlc2* deficiency dampens the glycolytic and mitochondrial metabolic activity of M1-like and M2-like BMDM, respectively.

(A) Schematic of the glycolysis stress test showing deployed drugs and their respective targets. ADP, adenosine diphosphate; 2-DG, 2-deoxyglucose

(B) Schematic of mitochondrial stress test showing deployed drugs and their respective targets. Figure adapted from "Electron transport chain" by BioRender.com (2023).

(C) Line graphs showing changes in the oxygen consumption rate (OCR) of M1-like and M2-like WT or *Lyz2*-cre BMDM (N=6) measured with Seahorse extracellular flux analysis. Bar graphs show normalized basal OCR, maximal OCR, and spare respiratory capacity (SRC; the difference in basal and maximal OCR) for M2-like WT or *Lyz2*-cre BMDM. OM, oligomycin; FCCP, carbonyl cyanide-p-trifluoromethoxyphenylhydrazone; AA, antimycin A; Rot, rotenone

(D) Line graphs showing changes in the extracellular acidification rate (ECAR) of M1-like and M2-like WT or *Lyz2*-cre BMDM (N=7) measured with Seahorse extracellular flux analysis. Bar graphs show normalized basal ECAR, glycolytic capacity (maximal ECAR), and glycolytic reserve (the difference in glycolytic response ECAR and maximal ECAR) for M1-like WT or *Lyz2*-cre BMDM. Black dashed lines in line graphs indicate time points of sequential injections of the indicated drugs for assessment of mitochondrial respiratory or glycolytic states. Glu, glucose. Data are presented as mean ± SD (C-D). Statistical comparisons were performed with two-tailed Student's *t* tests (C-D; data points were normally distributed) or two-tailed Mann-Whitney U tests (D; when data points were not normally distributed). Figures 12C-D are included in (*192*).

To examine the sphingolipid profile and synthesis in *Sptlc2*-sufficient or *Sptlc2*-deficient macrophages, I cultured *Sptlc2*-sufficient or *Sptlc2*-deficient macrophages with $^{13}C_3{}^{15}N_1$ L-serine for 2 hours before measuring the incorporation of tracers into sphingolipids in

collaboration with Dr. R. Sandhoff (Lipid Pathobiochemistry Group (A411), German Cancer Research Center (DKFZ), Heidelberg, Germany) (Figure 13A). Almost all measured endogenous and stable isotope-labeled sphingolipids were significantly diminished in *Lyz2*-cre BMDM, thus suggesting that *Sptlc2* deletion strongly altered the sphingolipidome in macrophages (Figure 13B).

To find out which sphingolipid deficiency exactly caused the metabolic and morphological deficits of *Sptlc2*-deficient BMDM, I supplemented different sphingolipids to *Sptlc2*-sufficient and -deficient BMDM for 3 days and measured BMDM size by flow cytometry. It has been previously reported that M1-like macrophages are characterized by their increased cell size (*197*), making BMDM size a measurable characteristic of M1-like macrophage polarization. In agreement with the BMDM confluency results (Figure 11B), *Sptlc2*-deficient macrophages significantly decreased in size (Figure 13C), as demonstrated by the lower percentages of forward scatter-area (FSC-A)^{high}, side scatter-area (SSC-A)^{high} cells among the total *Sptlc2*-deficient macrophages. Supplementation with sphinganine and with 3-KDS, which is rapidly metabolized to sphinganine (*114, 198*), but not with sphingomyelin, significantly increased the percentages of FSC-A^{high}, SSC-A^{high} cells (Figure 13C). Together, these results underlined that Sptlc2 was crucial for levels of various sphingolipids. Furthermore, they suggested that sphinganine restored *Sptlc2* deficiency-dampened macrophage growth.

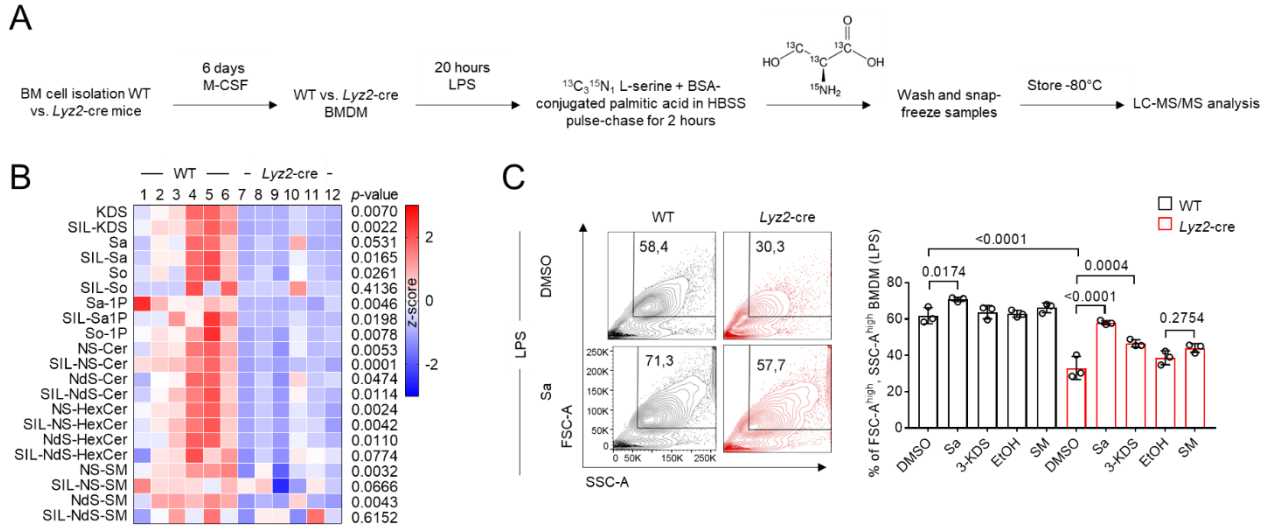

Figure 13 *Sptlc2* deficiency-induced reduction of sphingolipid levels dampens BMDM growth and can be restored by sphinganine supplementation.

(A) Illustration of the experimental design for the metabolomics analysis in B.

(B) Heat map showing concentration *z*-scores of the indicated endogenous and stable isotope labeled (SIL) sphingolipids in LPS-polarized WT or *Lyz2*-cre BMDM quantified by LC-MS/MS (N=6). In collaboration with Dr. R. Sandhoff, Lipid Pathobiochemistry Group (A411), German Cancer Research Center (DKFZ), Heidelberg, Germany. So, sphingosine; Sa-1P, sphinganine-1-phosphate; So-1P, sphingosine-1-phosphate; HexCer, hexosylceramide; NS, non-hydroxy-fatty acid sphingosine; NdS, non-hydroxy-fatty acid dihydro-sphingosine

(C) Flow cytometry contour plots and a bar graph showing the percentage of FSC-A^{high}, SSC-A^{high} WT or *Lyz2*-cre LPS-activated BMDM after DMSO, sphinganine (Sa), ethanol (EtOH), or sphingomyelin (SM) supplementation for 3 days (N=3). Data are presented as mean only (B) or mean ± SD (C). Statistical comparisons were performed with two-tailed Student's *t* tests (B: KDS, SIL-KDS, So, So-1P, NS-Cer, SIL-NS-Cer, NdS-Cer, SIL-NdS-Cer, NS-HexCer, NdS-HexCer, SIL-NdS-HexCer, SNS-SM, SSIL-NS-SM and SSILNdS-SM and G; data points were normally distributed), two-tailed Mann-Whitney U tests (in B: Sa, SIL-Sa, SIL-So, Sa-1P, SIL-Sa-1P, SIL-So-1P, SIL-NS-HexCer, and SNdS-SM; data points were not normally distributed), or ANOVA tests (C; for simultaneous comparisons of more than two groups). Figures 13A-C are included in (*192*).

5.4 Sptlc2 is required for LPS-induced recruitment of MyD88 to TLR4

As I found that *Sptlc2* deletion diminished LPS-induced macrophage morphology and M1-like and M2-like macrophage metabolic activity, one could argue that, upon *Sptlc2* deletion, sphingolipids are lacking solely as building blocks, limiting cell growth and leading to no anaerobic conditions and no lactate generation. However, as metabolic adaptations are often linked to altered cell signaling and previous experiments with chemical modulators of sphingolipid metabolism-associated enzymes suggested an effect on macrophage polarization (Supplementary Figure 32), I also analyzed the BMDM polarization states of the *Lyz2*-cre mice (Figure 14A). In more detail, I analyzed the expression of CD38 and Egr2, which are known to be exclusive M1-like and M2-like macrophage markers, respectively, and regulated by LPS (*72, 199*). I detected significantly lower levels of CD38 and higher levels of Egr2 in *Sptlc2*-deficient macrophages than in *Sptlc2*-sufficient macrophages (Figure 14A), thus suggesting that *Sptlc2* deficiency partially reversed LPS-induced M1-like macrophage signaling.

Next, I examined the protein levels of components in the LPS-TLR4-NF-κB signaling pathway, as this is the major pathway known to mediate LPS-induced CD38 expression in M1-like macrophages (*200*). Due to the known oscillatory activation of NF-κB signaling, different LPS stimulation times were used (*201*). After 10 minutes of LPS stimulation, IκBα

levels decreased only in *Sptlc2*-sufficient BMDM, indicating less active NF-κB signaling in *Sptlc2*-deficient BMDM (Figure 14B). In line with these findings, after 24 hours, I found that phosphorylation of NF-κB p65 (Ser536), which has been associated with NF-κB signaling inhibition in macrophages (*202-205*), was markedly enhanced by *Sptlc2* deficiency (Figure 14B). Noteworthy, human NF-κB p65 (Ser536) is the homolog of murine NF-κB p65 (Ser534), but as the herein-used mouse-reactive antibody targets Ser536, in the following, NF-κB p65 (Ser536) is used to describe this modification in mice as well (*205*). In line with previous reports, LPS induced MyD88 expression (*206*). In contrast to TIRAP, whose expression was not influenced by *Sptlc2* deficiency, MyD88 protein levels were lower in *Sptlc2*-deficient macrophages than those in *Sptlc2*-sufficient macrophages (Figure 14B). As LPS-induced, MyD88-dependent TLR4 signaling is known to not only induce NF-κB-, but also Stat1- (*207*) and activator protein 1 (AP-1)-dependent (*208*) target gene expression, I also analyzed the activity of these pathways through measurement of phospho-Stat1 and c-Jun levels, respectively (Figure 14C-D). Immunoblotting revealed that phospho-Stat1 (Tyr701) and c-Jun levels were slightly less induced by LPS in *Sptlc2*-deficient BMDM, but the strongest phenotype was seen for phospho-NF-κB-p65 (Figure 14C-D).

In line with the immunoblot, flow cytometry analysis confirmed that Sptlc2 was required for the LPS-induced upregulation of MyD88 protein levels (Figure 14E). Collectively, these results suggested that Sptlc2 was important for LPS-induced M1-like macrophage polarization via the TLR4-MyD88-NF-κB-axis.

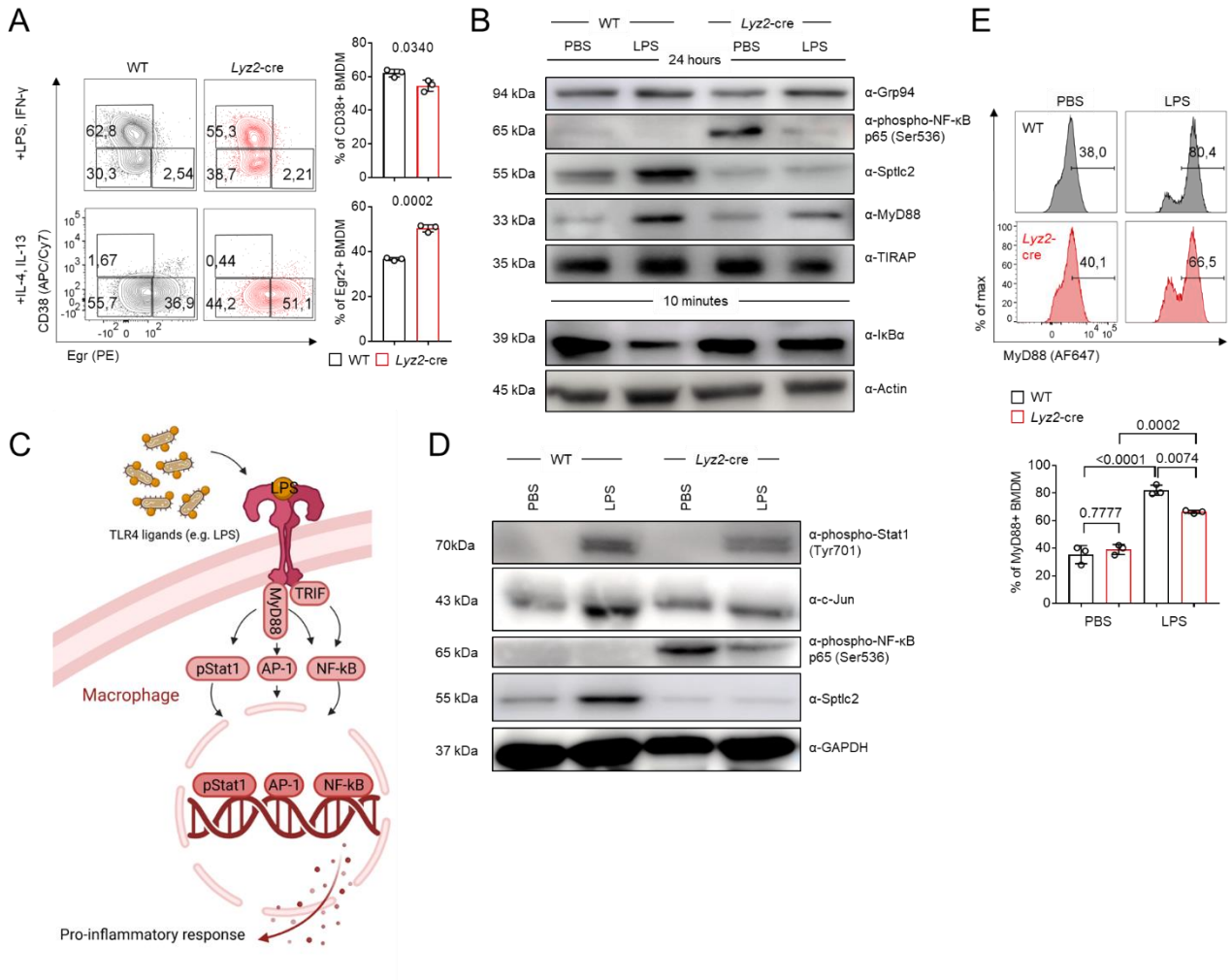

Figure 14 Deficiency of *Sptlc2* dampens the M1-like macrophage phenotype by preventing LPS-induced TLR4-MyD88-NF-κB signaling.

(A) Flow cytometry histograms and bar graphs showing percentages of CD38+ or Egr2+ BMDM among all live BMDM from WT and *Lyz2*-cre mice after M1-like or M2-like stimulation, respectively (N=3).

(B) Immunoblot analysis of IκBα (10 minutes PBS/LPS stimulation; bottom) or phospho-NF-κB p65 (Ser536), Sptlc2, MyD88, and TIRAP (24 hours PBS/LPS stimulation; top) expression in cell lysate from WT or *Lyz2*-cre BMDM. Actin (10 minutes of PBS/LPS stimulation; bottom) and Grp94 (24 hours of PBS/LPS stimulation; top) were used as loading controls.

(C) Schematic of LPS-induced MyD88-dependent transcription factors phospho-Stat1 (pStat1), AP-1, and NF-κB in macrophages, inducing inflammatory cytokine responses. Figure inspired by (*207, 208*).

(D) Immunoblot analysis of phospho-Stat1 (Tyr701), c-Jun, phospho-NF-κB p65 (Ser536), and Sptlc2 expression in cell lysate from WT or *Lyz2*-cre BMDM after PBS or LPS stimulation for 24 hours. Glyceraldehyde 3-phosphate dehydrogenase (GAPDH) was used as a loading control.

(E) Flow cytometry histograms and bar graphs showing the percentage of MyD88-expressing BMDM after PBS or LPS stimulation for 20 hours. Data are presented as mean ± SD (A, E). Statistical comparisons were

performed with two-tailed Student's *t* tests (A; data points were normally distributed) and ANOVA tests (E; for simultaneous comparisons of more than two groups). Figures 14A-B, E are included in (*192*).

To evaluate whether the slight defect in MyD88 upregulation upon LPS in *Sptlc2*-deficient macrophages was responsible for the strongly inhibited NF-κB signaling (indicated by higher levels of phospho-NF-κB p65 (Ser536) and IκBα) and the defects in M1-like macrophage cell growth, glycolytic activity, and marker expression, I overexpressed MyD88 and analyzed if this could rescue the *Sptlc2* deficiency-induced BMDM growth deficit. For this, I retrovirally transduced macrophages with a MyD88-expressing vector (Figure 15A-B). Additionally, I generated a vector for expression of MyD88 with the point mutation L252P (homolog to the human L265P mutation), as in B cells, this mutation was previously described to result in an over-activated MyD88 mutant, constitutively activating the NF-κB pathway (*209-211*). For the generation of these plasmids, first I shuttled MyD88 into the backbone MigR1-GFP and then I used site-directed mutagenesis to introduce the mutation (Figure 15A). Control digests and Sanger sequencing were used to ensure the correctness of the cloning process (Figure 15B). Once the vectors were generated, I used them together with the eco-helper plasmid (*176*) for transfection of HEK293T cells, and subsequently, viral particles from the HEK293T cell supernatant were used for retroviral transduction of BMDM (Figure 15C).

When measuring the cell size of BMDM by flow cytometry, I found that *Sptlc2*-deficient macrophages overexpressing the MigR1-GFP empty vector had lower percentages of FSC-A^{high}, SSC-A^{high} big cells than *Sptlc2*-sufficient macrophages (Figure 15D), a phenotype similar to that observed in non-transduced macrophages before (Figure 13C). However, I found that neither overexpression of WT nor L252P-mutated MyD88 increased the cell size of *Lyz2*-cre BMDM significantly (Figure 15D). Collectively, these data suggested that mere overexpression of MyD88 could not rescue *Sptlc2* deficiency-associated BMDM growth deficits.

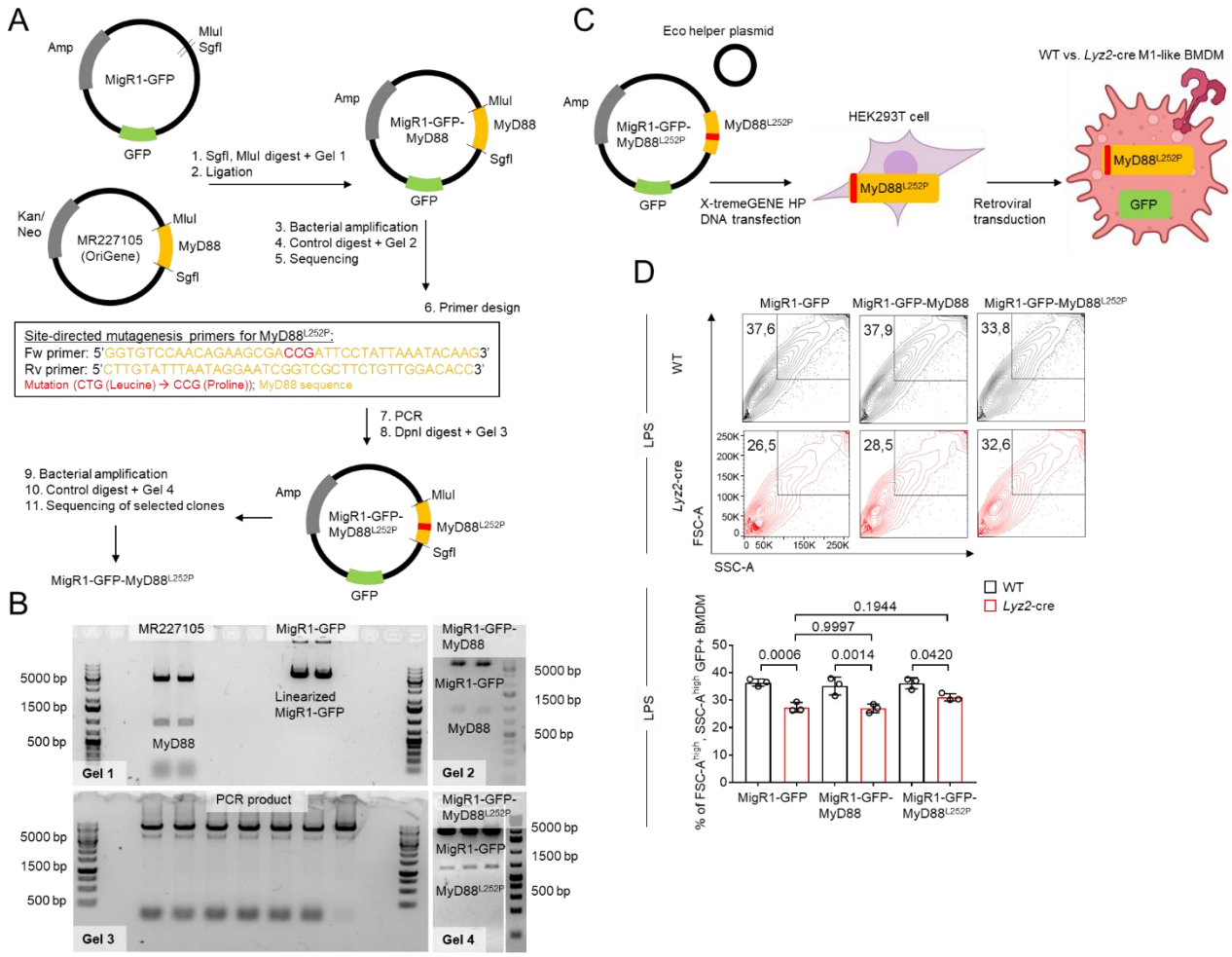

Figure 15 Overexpression of L252P-mutated MyD88 does not rescue the size of *Sptlc2*-deficient BMDM.

(A) Illustration of the MigR1-GFP-MyD88^{L252P} generation. The MyD88 sequence was shuttled from the commercially available plasmid MR227105 into the MigR1-GFP plasmid using the restriction enzymes MluI and SgfI. Using site-directed mutagenesis, the L252P point mutation was introduced to generate the MigR1-GFP-MyD88^{L252P} plasmid. For control, the MigR1-GFP-MyD88 plasmid was generated. Kan, Kanamycin; Neo, Neomycin

(B) Agarose gels for generation of the MigR1-GFP-MyD88^{L252P} plasmid (see A for gel nomenclature).

(C) Illustration of the MigR1-GFP-MyD88^{L252P} overexpression in WT or *Lyz2*-cre BMDM. First, HEK293T cells were transfected with the eco helper plasmid and MigR1-GFP-MyD88^{L252P} with X-tremeGENE HP DNA transfection reagent, and then viral particles from the supernatant were used for spin infection (retroviral transduction) of WT or *Lyz2*-cre BMDM. For control, the MigR1-GFP-MyD88 plasmid was used.

(D) Representative flow cytometry contour plots and bar graphs showing the percentage of FSC-A^{high}, SSC-A^{high} GFP+ LPS-stimulated WT or *Lyz2*-cre BMDM (N=3). Data are presented as mean ± SD (D). Statistical comparisons were performed with ANOVA tests (D; for simultaneous comparisons of more than two groups).

It is important to consider that it is not the mere upregulation of MyD88 levels that mediates LPS-induced TLR4 signaling but rather the MyD88 recruitment and TLR4 binding through TIR-TIR interactions, which allows for further downstream signaling (*212, 213*). To examine whether Sptlc2, in addition to influencing MyD88 expression, influenced TLR4-directed MyD88 recruitment, I performed confocal fluorescence microscopy (Figure 16). In line with previous western blot and flow cytometry results, in the bigger *Sptlc2*-sufficient macrophages, LPS stimulation resulted in higher levels of MyD88 protein and, additionally, enrichment of MyD88 at the cell membrane (Figure 16B). By contrast, LPS treatment scarcely altered MyD88 protein levels or changed recruitment to the cell membrane in *Sptlc2*-deficient macrophages (Figure 16B). Collectively, these results suggested that *Sptlc2* deficiency decreased the LPS-induced cell membrane recruitment of MyD88.

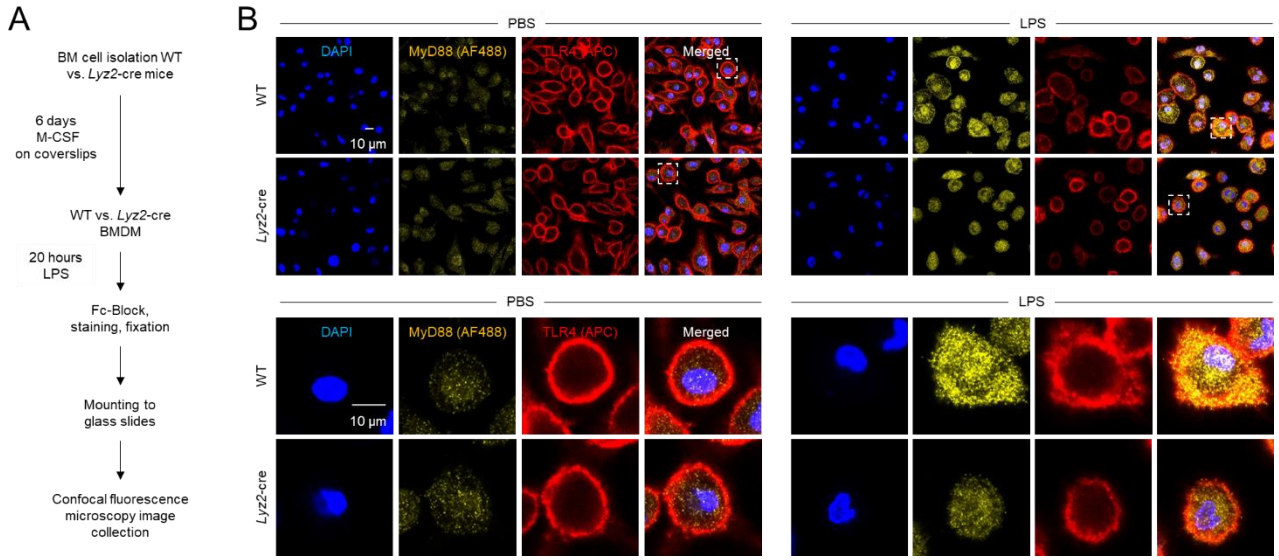

Figure 16 Deficiency of *Sptlc2* prevents LPS-induced co-localization of MyD88 and TLR4 at the cell membrane.

(A) Illustration of the experimental design for the confocal fluorescence microscopic analysis in B.

(B) Confocal fluorescence microscopy images showing cell size differences and cellular localization of MyD88 and TLR4 in WT or *Lyz2*-cre BMDM after 20 hours of PBS or LPS stimulation. Dashed white boxes in the upper panel mark the enlarged cells shown below. Figure 16B is included in (*192*).

From previous rescue experiments through overexpression of MyD88 and MyD88^{L252P} and the confocal fluorescence microscopic images, I hypothesized that instead of rescuing the mere LPS-induced MyD88 upregulation, promoting the LPS-induced TLR4-

MyD88 co-localization might rescue the downstream signaling and M1-like macrophage growth in *Lyz2*-cre BMDM. To test this, I generated and overexpressed a vector expressing MyD88 fused with an N-myristoylation (Myris) membrane-attachment signal sequence in BMDM, referred to as MigR1-GFP-MyrisMyD88 (Figure 17A-C). N-myristoylation, a co-translational lipid modification specific to the alpha-amino group of an N-terminal glycine residue of proteins, enables membrane anchoring of these proteins (*214, 215*). Overexpression of Myris-MyD88 enhanced the membrane localization of MyD88 as well as the cell size of *Sptlc2*-deficient macrophages (Figure 17D).

Furthermore, I performed flow cytometry to monitor the percentages of FSC-A^{high}, SSC-A^{high} cells among the virally transduced macrophages, which I identified through the expression of a GFP reporter (Figure 17E-F). As seen before in non-transduced macrophages (Figure 13C) and MigR1-GFP-transduced BMDM (Figure 15D), again, *Sptlc2*-deficient macrophages overexpressing the MigR1-GFP control vector had lower percentages of FSC-A^{high}, SSC-A^{high} big cells compared to their *Sptlc2*-sufficient counterparts (Figure 17F). Overexpression of Myris-MyD88 increased cell size and CD38 expression of *Sptlc2*-deficient macrophages to comparable levels as seen in *Sptlc2*-sufficient macrophages (Figure 17F-G). Collectively, the rescue of M1-like BMDM growth and marker expression through overexpression of a membrane-anchored MyD88 in *Sptlc2*-deficient BMDM suggested that Sptlc2 promoted the cell membrane recruitment of MyD88 to initiate LPS-induced TLR4 signaling in macrophages.

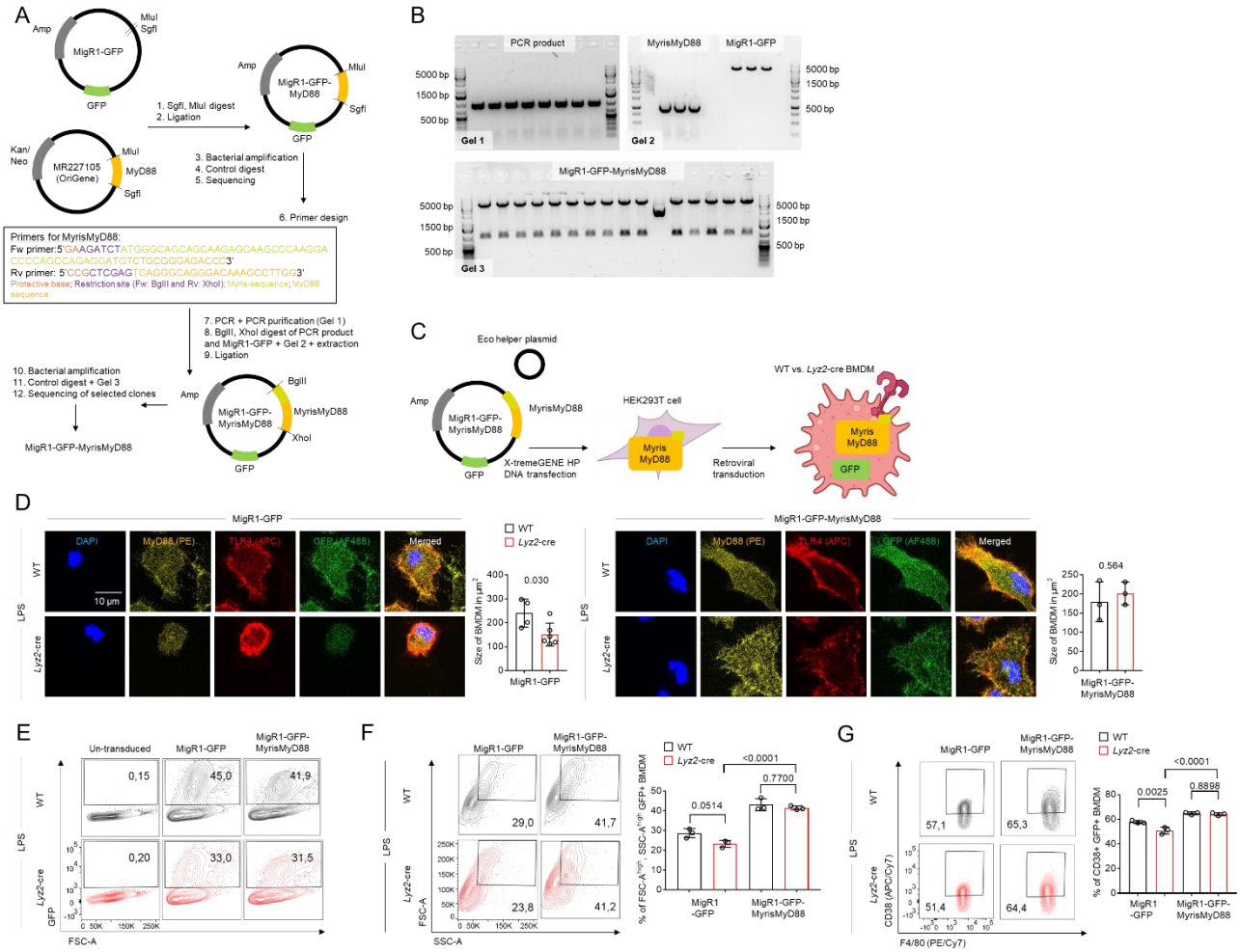

Figure 17 Overexpression of membrane-anchored MyrisMyD88 rescues size and M1-like macrophage marker expression in *Sptlc2*-deficient BMDM.

(A) Illustration of the MigR1-GFP-MyrisMyD88 generation. The MyD88 sequence was shuttled from the commercially available plasmid MR227105 into the MigR1-GFP plasmid using the restriction enzymes MluI and SgfI. Using primers containing a myristoylation (Myris) signal sequence, the MigR1-GFP-MyrisMyD88 plasmid was generated.

(B) Agarose gels for generation of the MigR1-GFP-MyrisMyD88 plasmid (see A for gel nomenclature).

(C) Illustration of the MigR1-GFP-MyrisMyD88 overexpression in WT or *Lyz2*-cre BMDM. First, HEK293T cells were transfected with the eco-helper plasmid and MigR1-GFP-MyrisMyD88 with X-tremeGENE HP DNA transfection reagent, and then viral particles from the supernatant were used for spin infection (retroviral transduction) of WT or *Lyz2*-cre BMDM.

(D) Confocal fluorescence microscopy images showing cellular localization of MyD88 and TLR4 and cell size of PBS- or LPS-treated WT or *Lyz2*-cre BMDM overexpressing MigR1-GFP or MigR1-GFP-MyrisMyD88. Cell sizes were quantified in FIJI and visualized in bar graphs (N=3-6).

(E) Representative flow cytometry contour plots showing GFP signal-based transduction efficiency in LPS-activated WT or *Lyz2*-cre BMDM.

(F) Representative flow cytometry contour plots and bar graphs showing the percentage of FSC-A^{high}, SSC-A^{high} GFP+ LPS-stimulated WT or *Lyz2*-cre BMDM (N=3).

(G) Representative flow cytometry contour plots and bar graphs showing the percentage of CD38+GFP+ LPS-stimulated BMDM (N=3). Data are representative of nine images from three pairs of mice in three independent experiments (D) and presented as mean ± SD (D, F-G). Statistical comparisons were performed with two-tailed Student's *t* tests (D; data points were normally distributed) or ANOVA tests (F-G; for simultaneous comparisons of more than two groups). Figures 17C-G are included in (*192*).

5.5 Sphinganine physically interacts with the TLR4 signaling components

To better understand the mechanisms through which Sptlc2 promotes the recruitment of MyD88 to the cell membrane, I tested whether sphinganine, the metabolite restoring the cell size and morphology of *Sptlc2*-deficient macrophages (Figures 11, 13), might enhance LPS-induced MyD88 localization to the membrane. Because sphingolipids have been shown to directly interact with proteins in regulating signal transduction (*216*), I hypothesized that sphinganine might physically interact with proteins in the TLR4 signaling pathway. To test this hypothesis, I incubated macrophage lysate with biotinylated sphinganine and then performed precipitation with streptavidin-conjugated magnetic beads (Figure 18A). After sphinganine-biotin (but also a little less after biotin control pulldown), I found a band at around 45 kDa, which LC-MS/MS analysis, in collaboration with the Proteomics Core Facility (PCF), European Molecular Biology Laboratory (EMBL), Heidelberg, Germany, revealed to represent actin (Figure 18B; Supplementary Table 28). However, as this pulldown was not entirely exclusive for sphinganine-biotin and as the TLR4 adaptors Tollip, MyD88, and TIRAP, which I suspected from previous results (Figure 14) to be involved in sphingolipid-regulated TLR4 signaling, have molecular weights between 30 kDa and 40 kDa, I also checked specifically this region of the gel. Collaborative LC-MS/MS analysis with PCF, EMBL, Heidelberg, Germany, revealed that both TLR4 adaptor proteins MyD88 and Tollip were pulled down through biotinylated sphinganine but not control biotin (Figure 18B; Supplementary Table 29). Through western blotting, I further confirmed that sphinganine interacted with actin (again, not exclusively, as biotin alone pulled down some, but less, actin) and with MyD88 and Tollip, and additionally, I showed an exclusive interaction of sphinganine with TIRAP (Figure 18C-D). Remarkably, Tollip staining showed two bands, one at 50 kDa and one at 30 kDa, and it has to be noted that only the upper band of Tollip was detected after

sphinganine pulldown (Figure 18D). The interactions between sphinganine and the adaptor proteins were specific, as demonstrated by the lack of binding between sphinganine and several other proteins involved in LPS-induced TLR4 signal transduction, such as MEK1/2, Erk1, and Akt (Figure 18E). Furthermore, when I cultured macrophages with fluorescently labeled sphinganine (sphinganine-fluorescein), I observed co-localization of TIRAP and sphinganine near the cell membrane, particularly upon LPS treatment (Figure 18F). Collectively, these results suggested that sphinganine directly interacted with the TLR4 adaptor proteins TIRAP, Tollip, and MyD88.

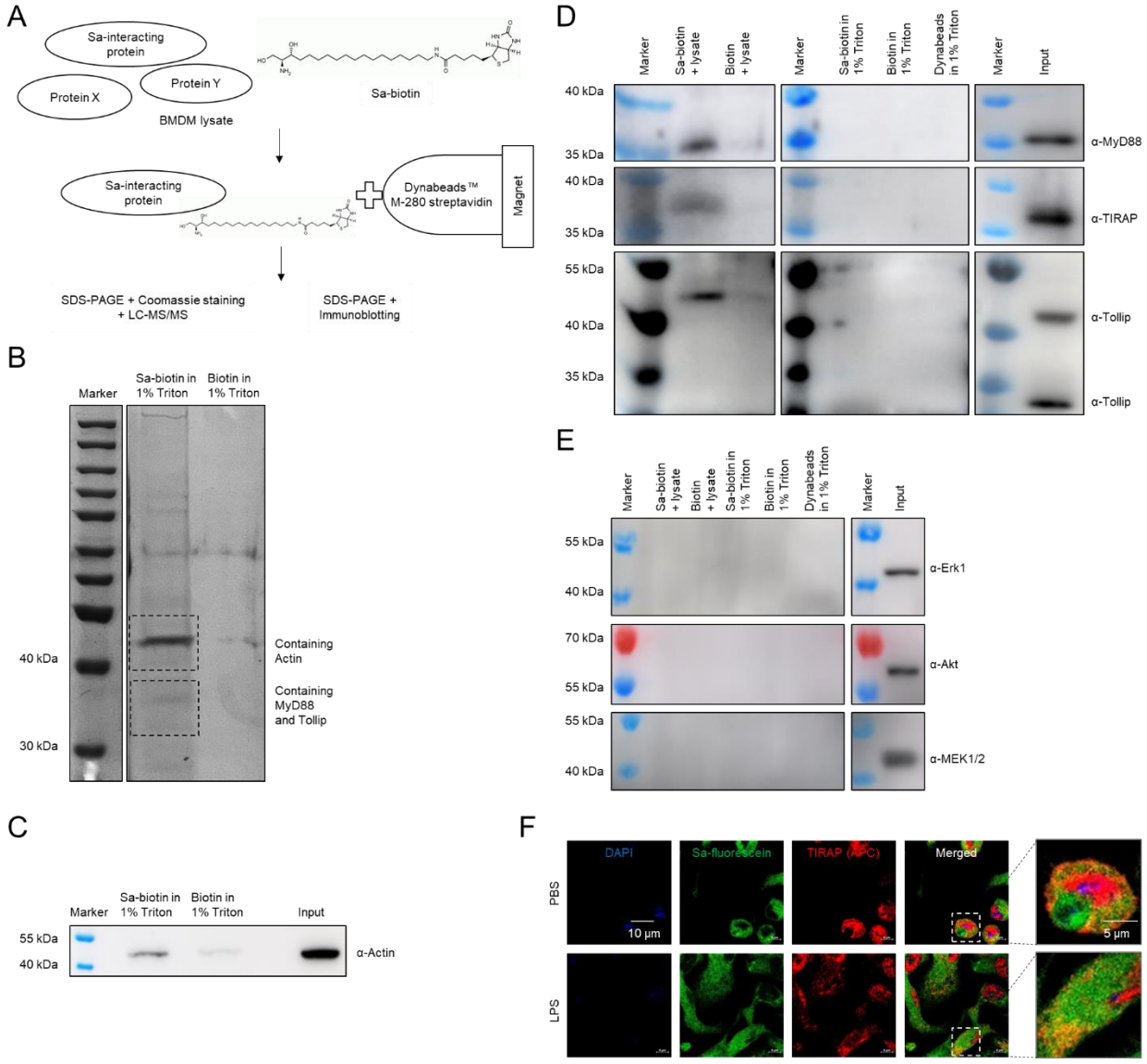

Figure 18 Sphinganine physically interacts with the TLR4 adaptors TIRAP, Tollip, and MyD88.

(A) Illustration of the experimental design in B-E. Sphinganine (Sa)-interacting proteins were pulled down from WT BMDM lysate with sphinganine-biotin coupled to streptavidin-Dynabeads™ with a magnet and

identified through non-biased Coomassie staining and subsequent LC-MS/MS (in B) and validated with a biased immunoblotting approach (in C-E).
(B) Proteins in the indicated Coomassie gel blocks after sphinganine (Sa)-biotin or biotin control pulldown were identified by LC-MS/MS. MyD88, Tollip, and actin are highlighted in the respective boxes. Additional information is provided in Supplementary Tables 28-29. In collaboration with the Proteomics Core Facility (PCF), European Molecular Biology Laboratory (EMBL), Heidelberg, Germany.
(C) Immunoblot analysis of actin after sphinganine (Sa)-biotin and biotin control pulldown. The input sample validates the correct location of the respective proteins on the membrane.
(D) Immunoblot analysis of TIRAP, Tollip, and MyD88 after sphinganine (Sa)-biotin and biotin control pulldown. Sa-biotin, biotin, and Dynabeads™ in lysis buffer (1% Triton X-100 in PBS) served as controls for the pulldown and input samples to validate the correct location of the respective proteins on the membrane.
(E) Immunoblot analysis of Erk, Akt, and MEK1/2 after sphinganine (Sa)-biotin and biotin control pulldown. Sa-biotin, biotin, and Dynabeads™ in lysis buffer (1% Triton X-100 in PBS) served as controls for the pulldown and input samples to validate the correct location of the respective proteins on the membrane.
(F) Confocal fluorescence microscopy images, showing subcellular localization of supplemented sphinganine (Sa)-fluorescein and TIRAP in WT BMDM after PBS or LPS stimulation. Data are representative of 12 images from four mice (F). Figures 18A-B, D-F are included in (*192*).

In sphinganine-biotin, the biotin group was conjugated to the end of the N-acyl chain of sphinganine (Figure 18A). Therefore, the N-acyl chain of sphinganine was occupied, making it less likely to be available for interacting with adaptor proteins. To further narrow down which chemical groups in sphinganine are responsible for the interaction with TLR4 adaptor proteins, I also used agarose beads coupled to the head group of sphinganine via Schiff base formation (Figure 19A). Unlike after pulldown with sphinganine-biotin (Figure 18), in the Coomassie-stained gel, after different doses of sphinganine-agarose and control agarose, no difference in the stained lanes between 30 kDa to 40 kDa was detected, and LC-MS/MS analysis, in collaboration with the Proteomics Core Facility (PCF), European Molecular Biology Laboratory (EMBL), Heidelberg, Germany, did not reveal any adaptor pulldown with the sphinganine-agarose (Figure 19B). To provide further evidence that sphinganine does not interact with Tollip, TIRAP, and MyD88 when its head group is occupied by agarose, I validated in western blotting that no TLR4 adaptor proteins were pulled down by sphinganine-agarose (Figure 19C). Collectively, these

results suggested that sphinganine interacted with the adaptor proteins through its head group and not the N-acyl chain.

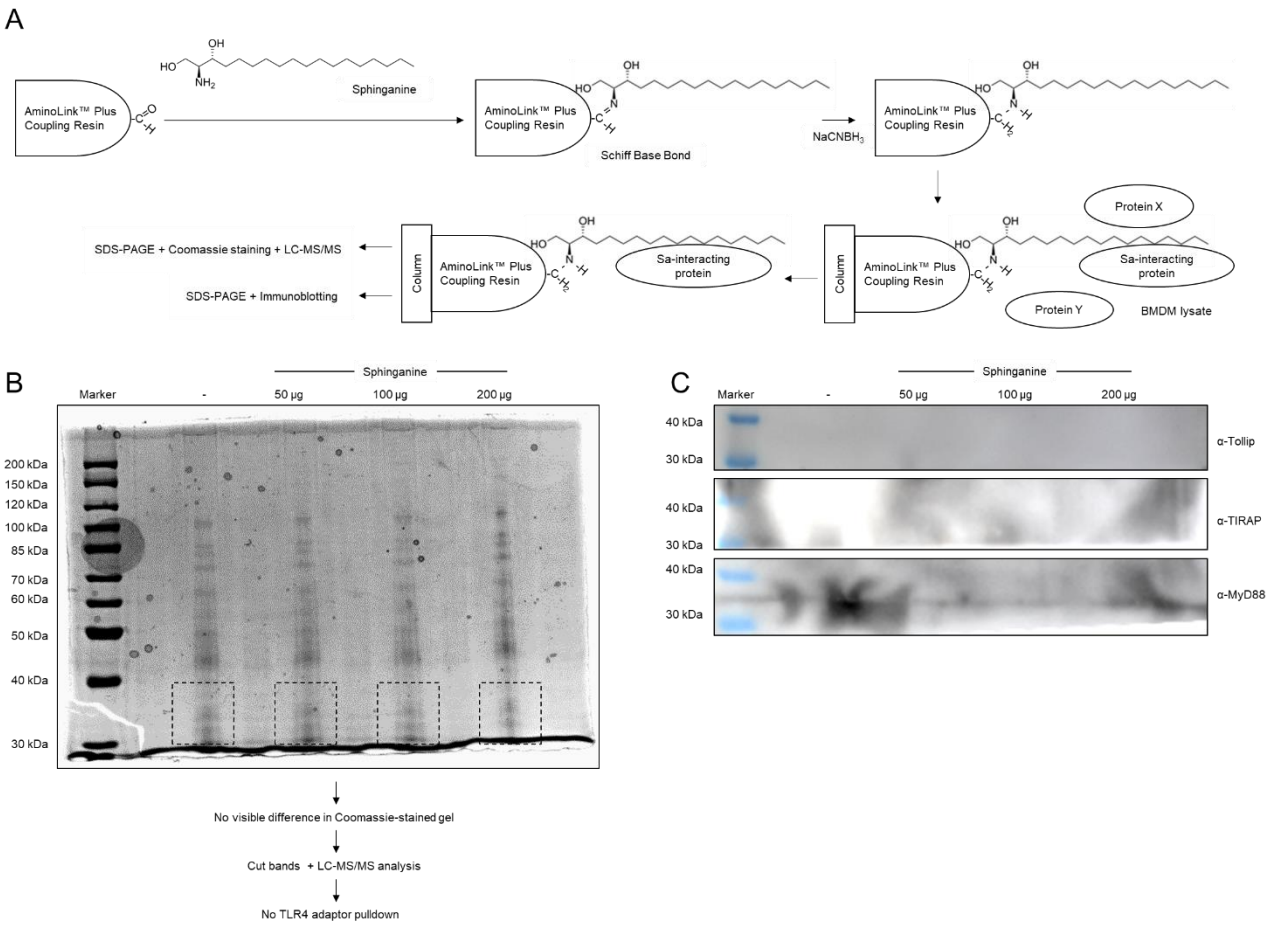

Figure 19 Identification of sphinganine-interacting proteins by sphinganine-agarose pulldown.

(A) Illustration of the experimental design in B-C. Sphinganine-interacting proteins were pulled down from WT BMDM lysate using sphinganine, which was immobilized via Schiff base formation on AminoLink™ Plus Coupling Resin (agarose beads). Controls contained agarose beads but no sphinganine. For the identification of sphinganine-interacting proteins, non-biased Coomassie staining and subsequent LC-MS/MS and a biased immunoblotting approach with specific antibodies for detection were used.

(B) Coomassie blue staining of WT BMDM lysate after sphinganine pulldown. Visible protein bands between 30 kDa to 40 kDa were cut from the gel and analyzed by LC-MS/MS. In collaboration with the Proteomics Core Facility (PCF), European Molecular Biology Laboratory (EMBL), Heidelberg, Germany.

(C) Immunoblot analysis of TIRAP, MyD88, and Tollip after sphinganine-agarose pulldown.

To test whether, in addition to Sptlc2-derived sphinganine, Sptlc2 itself could physically interact with TLR4 adaptors, I also used immunoprecipitation experiments to identify potential Sptlc2-interacting proteins (Figure 20A). For this, I BS3-crosslinked the Sptlc2-

reactive antibody to magnetic beads and incubated it with BMDM lysate. As a control for the pulldown, I stained for Sptlc2 in a western blot (Figure 20B). In parallel, Coomassie staining and subsequent LC-MS/MS analysis of the ~55 kDa gel region in collaboration with the Proteomics Core Facility (PCF, European Molecular Biology Laboratory (EMBL), Heidelberg, Germany) were used. Echoing results from the western blot, in LC-MS/MS analysis, Sptlc2 was among the immune precipitates (Figure 20B). Visually, highly sensitive silver staining did not show immunoprecipitation of any Sptlc2-interacting proteins between 30 kDa and 40 kDa (Figure 20B). However, to completely exclude a direct Sptlc2-TLR4 adaptor interaction, quantitative analysis using LC-MS/MS is required.

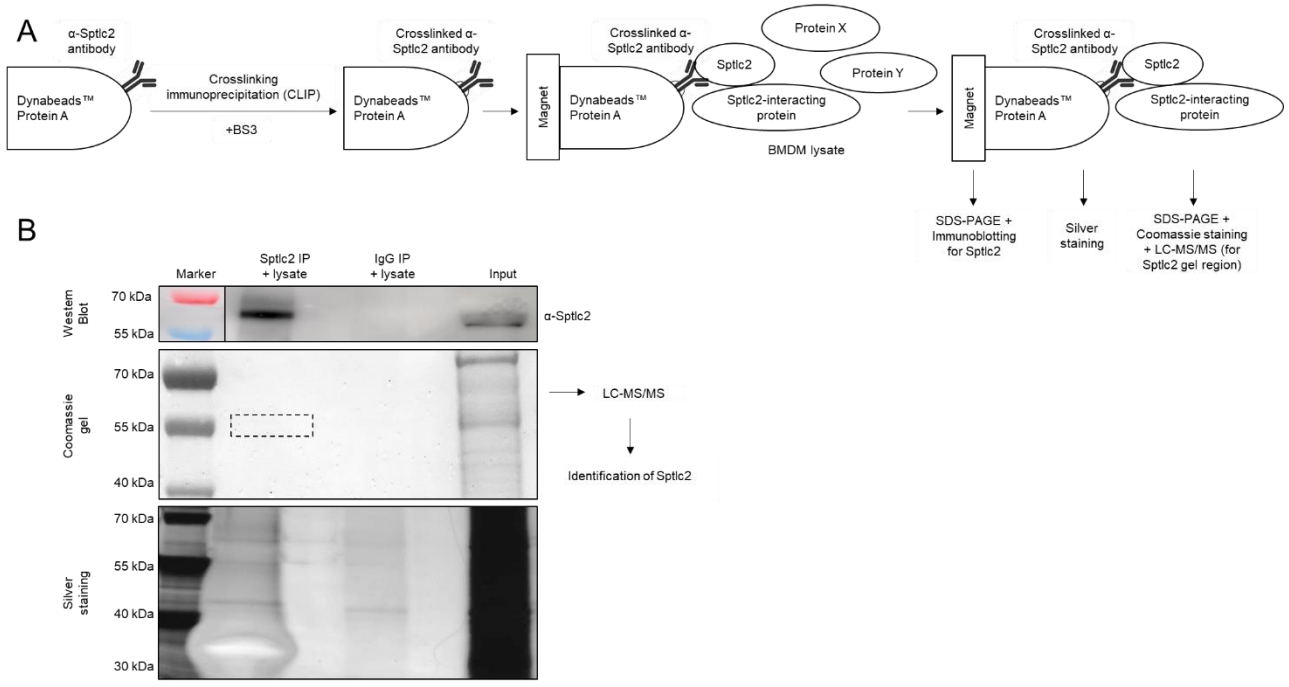

Figure 20 Identification of Sptlc2-interacting proteins in BMDM.

(A) Illustration of the experimental design in B. Sptlc2-interacting proteins were pulled down from WT BMDM lysate using the Sptlc2 antibody, which was immobilized on Protein A Dynabeads™. To prevent later antibody interference, the Sptlc2 antibody was crosslinked to the beads using BS3. For the identification of pulled-down proteins, non-biased silver staining was used, and, in parallel, Sptlc2 was visualized by western blotting and identified by Coomassie staining followed by LC-MS/MS.

(B) Western blot analysis of Sptlc2, Coomassie blue, and silver staining of WT BMDM lysate and isotype control after Sptlc2 pulldown. Protein bands at ~55 kDa were cut from the Coomassie gel and analyzed by LC-MS/MS. In collaboration with the Proteomics Core Facility (PCF), European Molecular Biology Laboratory (EMBL), Heidelberg, Germany. IP, immunoprecipitation

5.6 *Sptlc2* deficiency ameliorates LPS-induced sepsis symptoms

LPS is widely acknowledged as the most potent microbial mediator implicated in the pathogenesis of sepsis (*217*), in which sphingolipids have also been extensively discussed (*132*). Re-analysis of previously published RNA sequencing data indicated that during sepsis, the RNA levels of *Sptlc2* in CD14+ monocytes of patients were increased compared to those in healthy individuals (*218*) (Figure 21A).

To test whether Sptlc2 might be required for LPS-induced inflammatory responses during sepsis, I used an *in vivo* LPS-induced sepsis mouse model. I intraperitoneally injected PBS or LPS into mice with myeloid cell-specific deficiency of *Sptlc2* and wild-type littermates (Figure 21B). Half of the *Sptlc2*-sufficient mice showed a loss of movement and a hunched posture 6 hours after LPS injection, whereas only approximately 20% of the *Sptlc2*-deficient mice showed these LPS-induced phenotypes (Figure 21C-D). Because plasma cytokine levels have been reported to peak within the first hours after LPS exposure (*219*), I sacrificed mice 3-6 hours after the LPS challenge; by that time, no weight loss or differences in splenocyte numbers were observed in WT or *Lyz2*-cre mice (Figure 21E-F).

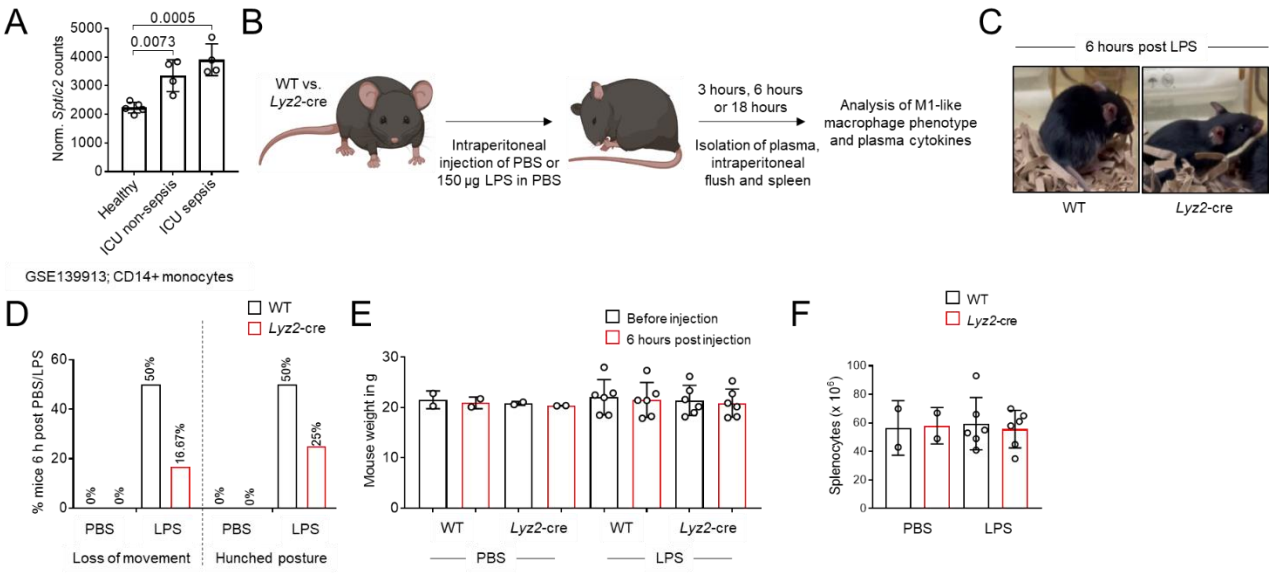

Figure 21 Deficiency of *Sptlc2* weakens LPS-induced sepsis symptoms.

(A) Bar graph showing RNA sequencing analysis of *Sptlc2* in circulating CD14+ monocytes from healthy volunteers without sepsis and intensive care unit (ICU) non-sepsis and sepsis patients. The original RNA sequencing dataset was previously published (*218*).

(B) Illustration of the experimental design of LPS-induced sepsis models in C-F and Figures 22 and 24. LPS was intraperitoneally injected into WT or *Lyz2*-cre mice, and the movement and posture of the mice were

monitored. At the indicated time points, mice were sacrificed, and samples for ELISA, cytokine array, and flow cytometry analysis were isolated.
(C-D) Representative images of WT or *Lyz2*-cre mice taken 6 hours after intraperitoneal LPS injection and bar graphs, illustrating the percentages of WT or *Lyz2*-cre mice that showed loss of movement and hunched posture 6 hours after intraperitoneal PBS or LPS injection (PBS: N=2, LPS: N=6).
(E) Bar graphs showing the weight of mice before and 6 hours after PBS or LPS injection (PBS: N=2; LPS: N= 6).
(F) Bar graphs showing splenocyte counts 6 hours after PBS or LPS injection (PBS: N=2; LPS: N= 6). Data are presented as mean ± SD (A, E-F). Statistical comparisons were performed with ANOVA tests (A; for simultaneous comparisons of more than two groups). Figures 21A-F are included in (*192*).

I performed flow cytometry to analyze the numbers and markers of intraperitoneal and splenic myeloid cells in septic mice. In line with my *in vitro* data (Figure 10C), Sptlc2 expression was induced by LPS challenge in *Sptlc2*-sufficient but not *Sptlc2*-deficient intraperitoneal and splenic macrophages (Figure 10E) and splenic monocytes (Figure 22B). After PBS injection, *Sptlc2*-deficient and *Sptlc2*-sufficient mice showed comparable levels of macrophages (F4/80+ cells of all Ly6G- myeloid cells), but 3 hours and 18 hours after the LPS challenge, I found fewer intraperitoneal macrophages and fewer myeloid cells in *Sptlc2*-deficient mice, respectively, supporting *in vitro* data indicating that not macrophage differentiation but rather activation is highly Sptlc2-dependent (Figure 22C).

Similar to the *in vitro* BMDM data, *Sptlc2* deficiency caused a decrease in the percentage of CD38-expressing macrophages, accompanied by an increase in the percentage of intraperitoneal macrophages expressing the M2-like macrophage marker arginase-1 (Figure 22D). Additionally, the TNFα MFI 6 hours after LPS and the numbers of MHCII-expressing macrophages and monocytes and IL-6-expressing macrophages 18 hours after LPS were higher in *Sptlc2*-sufficient intraperitoneal macrophages (Figure 22D). Moreover, 3 hours after LPS, splenic macrophages deficient for *Sptlc2* showed lower percentages of IL-6 and reduced Ki-67 MFIs in macrophages and neutrophils, and Ki-67 MFI of monocytes and IL-12 MFI of monocytes, macrophages, and neutrophils were higher in the *Sptlc2*-sufficient group 6 hours after LPS (Figure 22E). Collectively, these results suggested that *Sptlc2* deficiency reduced the M1-like macrophage phenotype and cytokine production during LPS-induced sepsis.

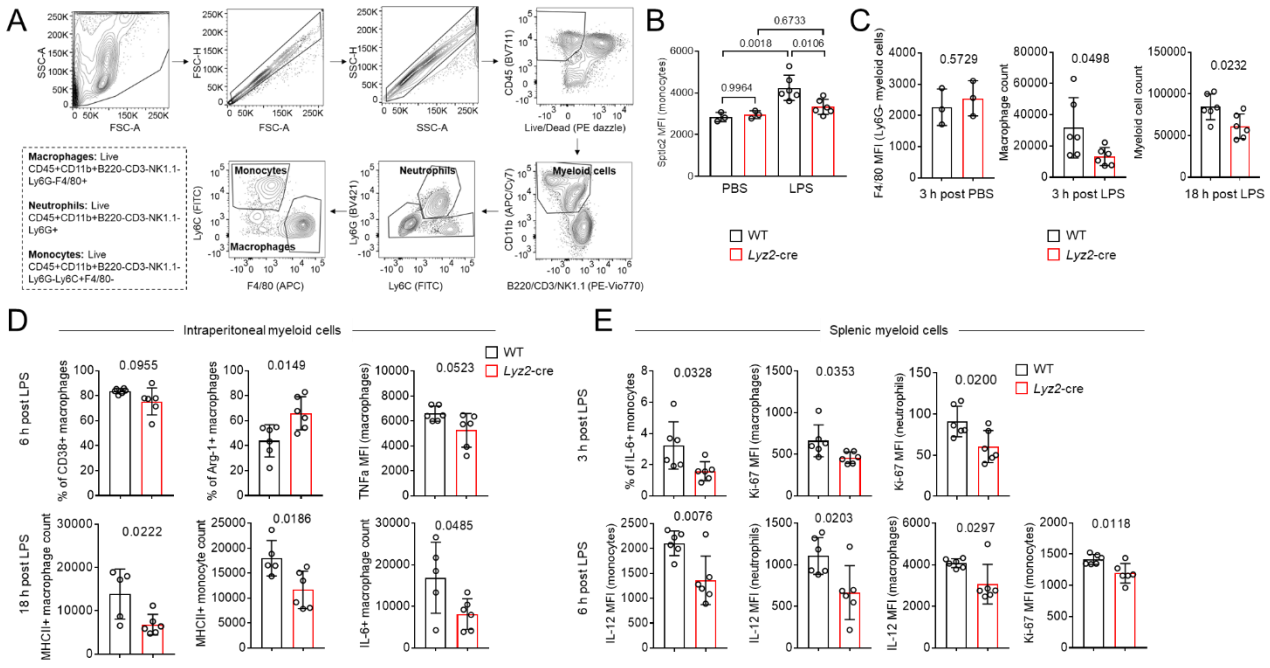

Figure 22 Deficiency of *Sptlc2* dampens the pro-inflammatory M1-like macrophage phenotype.

(A) Contour plots, showing the gating strategy used in B-E to identify monocytes (live CD45+CD11b+NK1.1-CD3-B220-Ly6G-Ly6C+F4/80- cells) and macrophages (live CD45+CD11b+NK1.1-CD3-B220-Ly6G-F4/80+ cells).

(B) Bar graphs documenting the expression of Sptlc2 in splenic monocytes (live CD45+CD11b+CD3-B220-NK1.1-Ly6G-Ly6C+F4/80-) from WT or *Lyz2*-cre mice 3 hours after PBS (N=3) or 150 µg LPS (N=6) injection.

(C) Bar graphs depicting WT or *Lyz2*-cre intraperitoneal flush myeloid cell counts 18 hours after intraperitoneal 150 µg LPS or PBS injection and macrophage counts and F4/80 MFI of Ly6G- myeloid cells 3 hours after intraperitoneal 150 µg LPS or PBS injection measured by flow cytometry (PBS: N=3; LPS: WT: N=5-6, *Lyz2*-cre: N=6).

(D) Percentages of CD38+ or Arginase-1 (Arg-1)+ macrophages and TNFα MFI of macrophages from intraperitoneal flush 6 hours after intraperitoneal 150 µg LPS injection are depicted in bar graphs. Bar graphs show counts of MHCII+ WT or *Lyz2*-cre monocytes and macrophages and IL-6+ macrophages from intraperitoneal flush 18 hours after 150 µg LPS injection (WT: N=5-6, *Lyz2*-cre: N=6).

(E) Bar graphs showing percentages of IL-6+ WT or *Lyz2*-cre splenic monocytes and Ki-67 MFI of splenic macrophages and neutrophils from WT or *Lyz2*-cre mice 3 hours after intraperitoneal 150 µg LPS injection. Bar graphs showing IL-12 MFI of splenic monocytes, neutrophils, and macrophages and of Ki-67 on splenic monocytes from WT or *Lyz2*-cre mice 6 hours after intraperitoneal 150 µg LPS injection (N=6). Data are presented as mean ± SD (B-E). Statistical comparisons were performed with ANOVA tests (B; for simultaneous comparisons of more than two groups) and two-tailed Student's *t* tests (C-E; data points were normally distributed). Figures 22A, C are included in (*192*).

The main effector mechanism of M1-like macrophages, leading to detrimental inflammation and organ dysfunction in the course of sepsis, is the excessive production, secretion, and systemic effect of cytokines (referred to as the “cytokine storm”). Flow cytometric analyses suggested reduced cytokine production in intraperitoneal and splenic *Sptlc2*-deficient macrophages, but it is noteworthy that this measurement did not track the already-secreted cytokines (Figure 22D-E). To analyze bloodstream-circulating M1-like cytokines during sepsis, I used plasma from WT or *Lyz2*-cre septic mice in enzyme-linked immunosorbent assays (ELISAs) (Figure 23). In line with the literature, LPS stimulated distinct cytokine kinetics differently, with most cytokines peaking within the first 6 hours after LPS and decreasing afterward (*219*). More precisely, the investigated cytokines could be grouped into “early-induced” (TNFα and IL-10; peaking within the first 2 hours after LPS), “medium-induced” (IL-1β, IL-6, and IL-18; peaking 2-3 hours after LPS), and “late-induced” (IFN-γ, IL-12, and IL-23; peaking 5-6 hours after LPS) (Figure 23A). From previous flow cytometry results showing reduced IL-12 levels in *Sptlc2*-deficient macrophages (Figure 22E) and its NF-κB-dependent expression, special interest was drawn to IL-12 (*220*). In the literature, pro-inflammatory IL-12 is controversially discussed in sepsis as it is generally considered to cause LPS- but not bacteria-induced sepsis-associated death as it also has a role in mediating sepsis resistance (*221-223*). In ELISAs, I found the concentrations of IL-12/IL-23 p40 levels 3 hours and 16 hours after LPS and bioactive IL-12 p70 3 hours after LPS in the plasma of *Sptlc2*-sufficient mice were higher than in *Sptlc2*-deficient mice (Figure 23B). Using ELISAs, I also checked TNFα, IL-10, IL-1β, IL-18, IL-6, and IFN-γ levels in the plasma of *Sptlc2*-sufficient and -deficient mice, but no significant difference between WT or *Lyz2*-cre mice was observed (data not shown).

Next, I transferred the findings about IL-12 back to a suitable *in vitro* model, in which I measured reduced IL-12/IL-23 p40, IL-12 p70, and IL-6 levels from the supernatant of LPS/IFN-γ-activated BMDM upon *Sptlc2* deficiency (Figure 23C). Matching the MyrisMyD88-mediated rescue of macrophage size and CD38 levels upon *Sptlc2* deficiency (Figure 17F-G), I also found IL-12 p70 and IL-6 levels in *Sptlc2*-deficient BMDM to be rescued through overexpression of MyrisMyD88 (Figure 23D). Collectively, these results suggested that during LPS-induced sepsis, *Sptlc2* deficiency-associated loss of MyD88 membrane recruitment impaired IL-12 production and secretion.

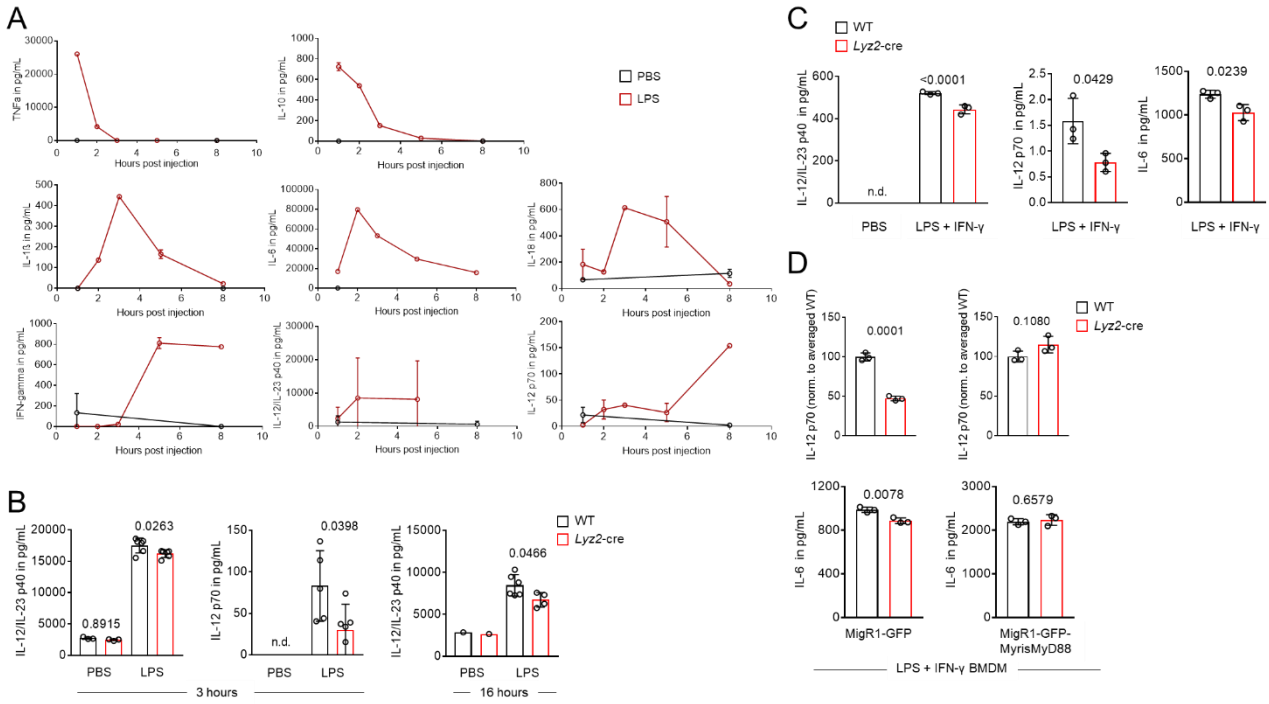

Figure 23 *Sptlc2* deficiency reduces LPS-induced IL-12 levels *in vivo* and *in vitro*.

(A) Line graphs showing plasma cytokine levels of IL-1β, IL-6, IL-18, TNFα, IFN-γ, IL-10, IL-12/IL-23 p40, and IL12 p70 following different kinetics measured by ELISA from the plasma of WT mice every 2 hours for up to 8 hours after intraperitoneal LPS injection (N=1-3).

(B) Bar graphs showing plasma IL-12/IL-23 p40 and IL-12 p70 levels 3 hours after PBS or LPS injection measured by ELISA (PBS: N=1-3; LPS: N=5-6).

(C) Bar graphs showing IL-12/IL-23 p40, IL-12 p70, and IL-6 levels in the culture medium of 4 hours IFN-γ + LPS-activated WT or *Lyz2*-cre BMDM (N=3).

(D) Bar graphs showing normalized IL-12 p70 and IL-6 levels in the culture medium of 4 hours IFN-γ + LPS-activated WT or *Lyz2*-cre BMDM overexpressing MigR1-GFP or MigR1-GFP-MyrisMyD88 (N=3). Data are presented as mean ± SD (A-D). Statistical comparisons were performed with ANOVA tests (B-C; for simultaneous comparisons of more than two groups) and unpaired two-tailed Student's *t* tests (C-D; data points were normally distributed). Figures 23B, D are included in (*192*).

To gain a broader view of the influence of *Sptlc2* deficiency on LPS-induced inflammation *in vivo*, I used a cytokine array to simultaneously monitor 40 cytokines in the plasma (Figure 24A). In line with the IL-12 ELISAs (Figure 23B), after PBS stimulation, no difference in cytokine levels between *Sptlc2*-sufficient and -deficient groups was observed (Figure 24B), but I found that upon LPS challenge, *Sptlc2* deficiency caused a general decrease in inflammation-associated proteins, including I-309 (CCL1), eotaxin (CCL11),

IL-12 p70, and IL-23 (Figure 24C). Collectively, these results suggested that *Sptlc2* deficiency decreased systemic LPS-induced inflammation *in vivo*, ameliorating sepsis symptoms.

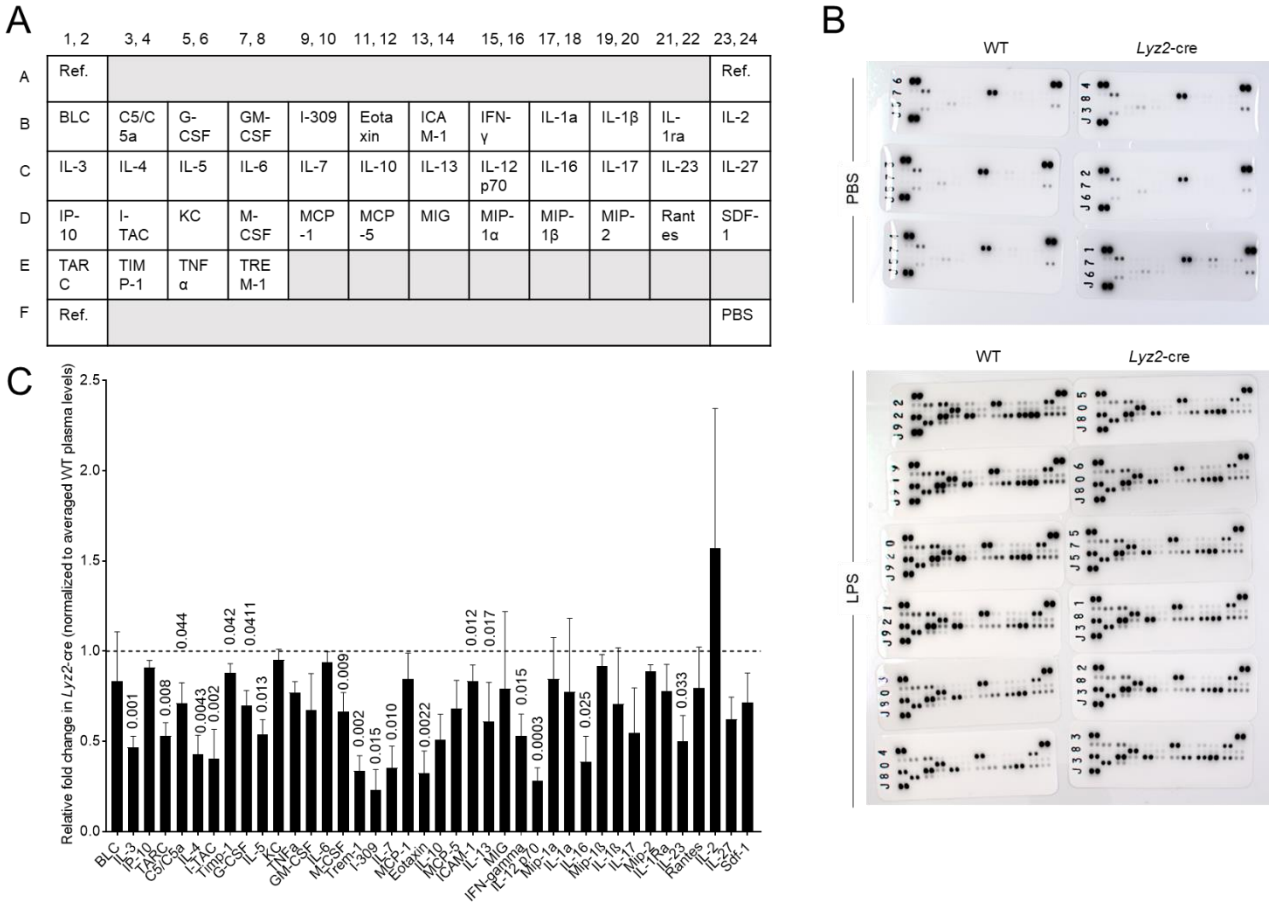

Figure 24 Deficiency of *Sptlc2* weakens LPS-induced cytokine levels *in vivo*.

(A) Overview depicting the layout of the cytokine array used in B-C.

(B) Uncropped cytokine array membranes spotted in duplicates with capture antibodies to specific target proteins probed with plasma from WT or *Lyz2*-cre mice 3 hours after PBS (N=3) or LPS injection (N=6).

(C) Bar graph showing pixel density of cytokine dots of *Lyz2*-cre plasma normalized to WT plasma after LPS challenge. Quantification was done in FIJI. A black dashed line separates up- and down-regulated cytokines in *Lyz2*-cre mice. Data are presented as mean ± SD (C). Statistical comparisons were performed with two-tailed Student's *t* tests (C: all except IL-4, G-CSF, Eotaxin; data points were normally distributed) and Mann-Whitney U tests (C: IL-4, G-CSF, Eotaxin; data points were not normally distributed). BLC, B lymphocyte chemoattractant; IP-10, Interferon-gamma-induced protein 10; TARC, Thymus- and activation-regulated chemokine; C5, complement component 5; I-TAC, Interferon-inducible T-cell alpha chemoattractant; Timp-1, Tissue inhibitor of metalloproteinases; G-CSF, Granulocyte colony-stimulating factor; KC, Keratinocyte chemoattractant; Trem-1, Triggering receptor expressed on myeloid cells 1; MCP-5, Monocyte chemotactic protein 5; ICAM-1, Intracellular adhesion molecule 1; MIG, Monokine induced by

Gamma-Interferon; Mip-1, Macrophage inflammatory protein-1; Rantes, Regulated upon activation, normal T cell expressed and presumably secreted; Sdf-1, Stromal cell-derived factor 1. Figures 24A-C are included in (*192*).

5.7 Myeloid cell-specific *Sptlc2* deficiency can influence tumorigenesis

As in sepsis, in melanoma, inflammatory TLR4 signaling is a key pathway regulating macrophage function (*224*). To test the generalizability of the Sptlc2 requirement for TLR4 signaling in macrophages and transfer the finding that Sptlc2-driven sphinganine biosynthesis serves as a checkpoint involved in pattern recognition by macrophages to another *in vivo* disease context, I also studied the role of sphingolipid metabolism in myeloid cells in the course of melanoma. However, unlike in sepsis, in which over-activated M1-like macrophages and excessive TLR4 signaling result in detrimental inflammation, during tumorigenesis, the role of macrophage TLR4 signaling is more complex as it can drive initially beneficial but long-term detrimental inflammatory processes (*78*).

5.7.1 Myeloid cell-specific *Sptlc2* deficiency can affect B16 melanoma development

The B16 melanoma mouse model is the most commonly used melanoma model for preclinical studies. The B16-F10 cell line was generated as the 10th serial passage sub-clone of the B16 parent tumor line in C57BL/6 mice, and subcutaneous injection of B16-F10 cells into syngeneic C57BL/6 mice causes solid tumor formation (*225*).

5.7.1.1 Myeloid cell-specific *Sptlc2* deficiency weakens anti-tumor myeloid cell activity and increases B16 tumor growth

In the past few years, many TLR4 ligands have been identified in the tumor microenvironment (*78, 226*). To test if the B16 melanoma model is suitable to study the LPS-induced and sphingolipid-mediated regulation of TLR4 signaling in macrophage tumor immune responses, I subcutaneously implanted B16-F10 tumor cells in WT mice, and after solid tumor formation, I checked the LPS levels in tumors, spleens, and the skin of tumor-bearing mice (Figure 25A-B). In line with recently reported findings (*83-89*), LPS was readily detectable in B16 tumors through immunoblotting and limulus amebocyte

lysate assays, and both the 055:B5 and 0111:B4 serotypes of LPS were more enriched in the tumor than the spleen (Figure 25B). The abundance of the 055:B5 serotype of LPS was comparable between tumor and skin tissue, and tumors had higher amounts of the 0111:B4 serotype of LPS than skin (Figure 25B).

Next, I used flow cytometry to check for Sptlc2 levels, and I found that TAMs expressed higher levels of Sptlc2 protein than splenic macrophages from the same mice (Figure 25C). Together with the presence of LPS in the B16 tumor microenvironment, this suggested that, similar to the sepsis model, Sptlc2 might be involved in LPS-induced inflammatory (anti- or pro-tumor) macrophage signaling. To test this hypothesis, I implanted B16-F10 tumor cells in WT or *Lyz2*-cre mice and monitored tumor growth for 19 days (Figure 25A). *Sptlc2* deficiency in myeloid cells increased the tumor growth longitudinally and the tumor weight at the endpoint on day 19 (Figure 25D-E). The numbers of splenocytes and tumor-infiltrating leukocytes did not differ between *Sptlc2*-sufficient and *Sptlc2*-deficient B16 tumor-bearing mice (Figure 25F). Collectively, these results suggested that myeloid cell-specific *Sptlc2* deficiency increased B16 tumor growth, proposing that myeloid cells rely on Sptlc2-driven sphingolipids for mediating anti-tumor immune responses.

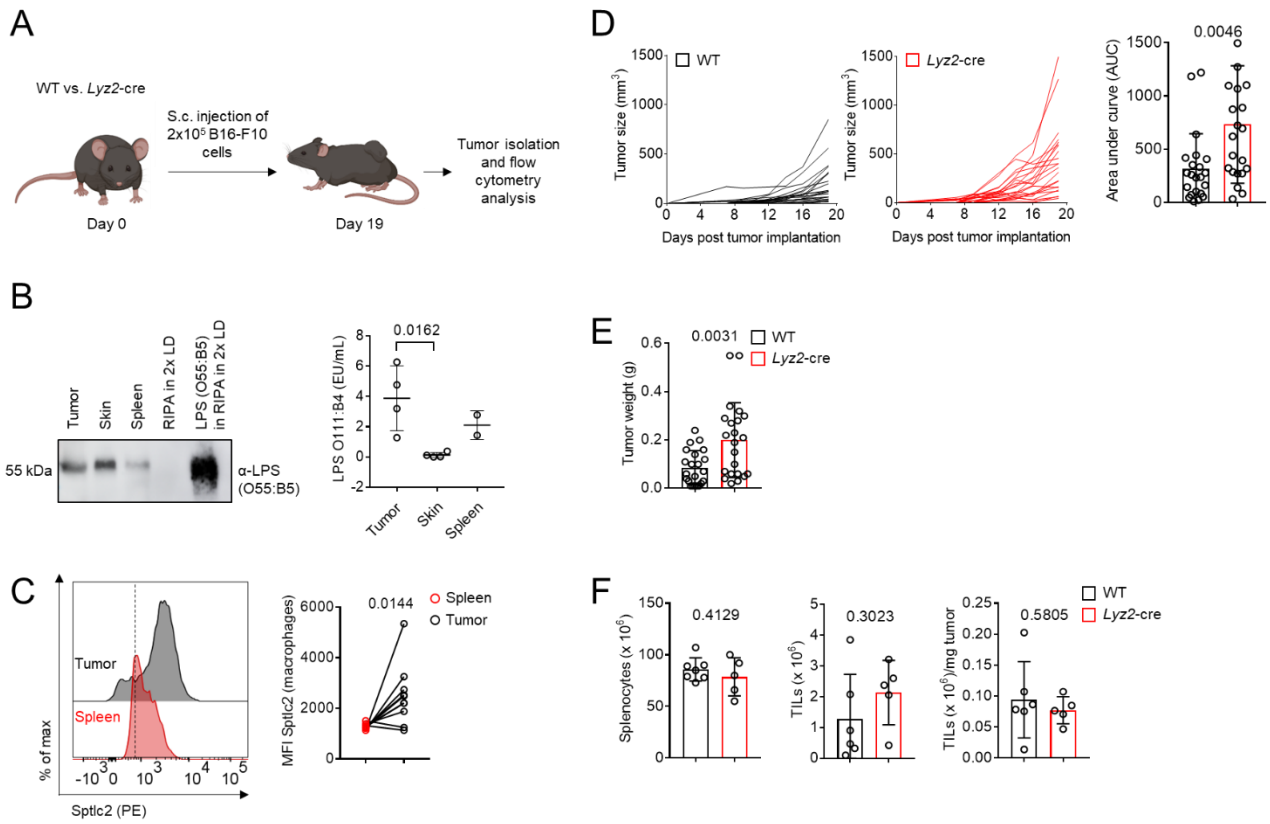

Figure 25 Mouse B16-F10 tumors contain LPS, and *Sptlc2* deficiency increases B16 tumor growth.

(A) Illustration of the experimental design of the B16 tumor model in B-F and Figures 26-27. A total of 2×10^5 B16-F10 cells were injected subcutaneously (s.c.) into C57BL/6 WT or *Lyz2*-cre mice, and on day 19, the mice were sacrificed and tumor and spleen samples were isolated.

(B) Left: Immunoblot analysis of LPS (055:B5) in tumor, skin, and spleen lysates of B16-F10 tumor-bearing WT mouse; 100 ng LPS (055:B5) was used as a loading control. Right: Scatter dot plot showing LPS (0111:B4) concentration in tumor, spleen, and skin of B16-F10 tumor-bearing mice measured by limulus amebocyte lysate assay.

(C) Representative flow cytometry histograms and graph showing Sptlc2 MFI of macrophages from the spleen and tumors of WT mice (N=10).

(D) Left: Line graphs showing B16-F10 melanoma growth in WT or *Lyz2*-cre littermate mice over time after subcutaneous injection of 2×10^5 B16-F10 melanoma cells. Right: Bar graph showing the area under the curve (AUC) of the tumor growth plots (N=22).

(E) Bar graph showing the tumor weight of WT or *Lyz2*-cre mice at the endpoint on day 19 (N=22).

(F) Bar graphs showing counts of splenocytes, tumor-infiltrating leukocytes (TILs; live CD45+ cells in tumors), and TILs/mg tumor of WT or *Lyz2*-cre mice on day 19 from the B16-F10 tumor model. Data are representative of eight independent experiments (C) and pooled from three (D-E) independent experiments and presented as mean ± SD (B, D-F) and symbols with connecting lines, highlighting paired samples (C). Tumor growth curves were evaluated longitudinally, and the AUC was calculated for each tumor growth

curve (D). Statistical comparisons were performed with ANOVA tests (B; for simultaneous comparisons of more than two groups), two-tailed Mann-Whitney U tests (D; data points were not normally distributed), and unpaired two-tailed Student's *t* tests (E-F; data points were normally distributed). Figures 25A-F are included in (*192*).

To study if the increased tumor burden of *Sptlc2*-deficient mice was caused by alteration of the inflammatory LPS-TLR4-NF-κB signaling axis in tumor-associated myeloid cells or different mechanisms, I used flow cytometry to analyze various myeloid cell subsets from the tumor and spleen of B16 tumor-bearing mice (Figure 26A-C). As Ly6C^{high} and Ly6C^{low} macrophages differ in their phenotype, function, and origin (*227*), F4/80+ macrophages were divided into Ly6C^{high} (in tumors further referred to as TAMs1) and Ly6C^{low} (in tumors further referred to as TAMs2) macrophages (Figure 26A). The protein levels of Sptlc2 were relatively lower in *Lyz2*-cre monocytes, TAMs1, and TAMs2 (Figure 26B). *Sptlc2* deficiency significantly decreased the percentage of monocytes but not TAMs2 (Figure 26B). Moreover, I observed a trend toward relatively lower percentages of TAMs1 in *Sptlc2*-deficient mice, although this finding was not statistically significant (Figure 26B). LPS stimulation induces macrophage proliferation and MHCII expression via NF-κB-mediated signaling (*228*). *Sptlc2* deficiency decreased macrophage proliferation, as indicated by reduced Ki-67 expression, and lowered MHCII expression in monocytes and TAMs1 but not TAMs2 (Figure 26B). Remarkably, in TAMs, PD-L1 expression can be stimulated via LPS through NF-κB signaling (*100*). *Sptlc2* deficiency showed a trend towards decreased PD-L1 levels on monocytes and on TAMs1, but not on TAMs2 (Figure 26B). Collectively, these results suggested that *Sptlc2* deficiency might have impaired NF-κB-mediated gene expression in tumor-associated myeloid cells.

As the spleen is the main extramedullary hematopoiesis site in tumor-bearing hosts, generating significant amounts of myeloid cells (*229*), I also analyzed marker expression of myeloid cells from the spleens of B16 tumor-bearing mice by flow cytometry (Figure 26C). Splenic monocytes and Ly6C^{high} and Ly6C^{low} macrophages from *Lyz2*-cre B16 tumor-bearing mice showed reduced Sptlc2 protein levels (Figure 26C). Cell proliferation (measured in terms of Ki-67 expression) of monocytes, but not macrophages, and MHCII expression of monocytes or macrophages were reduced in *Sptlc2*-deficient mice (Figure 26C). Furthermore, matching the data from the sepsis model (Figure 22-24), levels of

inflammatory IL-12 on splenic monocytes and Ly6C^{high} but not Ly6C^{low} macrophages also showed a trend towards reduction upon *Sptlc2* deficiency (Figure 26C). Collectively, these results suggested that, during tumorigenesis, Sptlc2 was required for the expression of NF-κB target genes in monocytes and macrophages from the tumor and spleen. As introduced before, NF-κB-mediated TLR4 signaling in macrophages can have anti-tumor functions but also drive tumor progression. Together with previous results showing increased tumor growth in *Sptlc2*-deficient mice (Figure 25D-E), my data suggested that, at least in the settings of the herein-used model, sphingolipid-regulated NF-κB signaling is crucial for monocyte and macrophage-mediated anti-tumor responses.

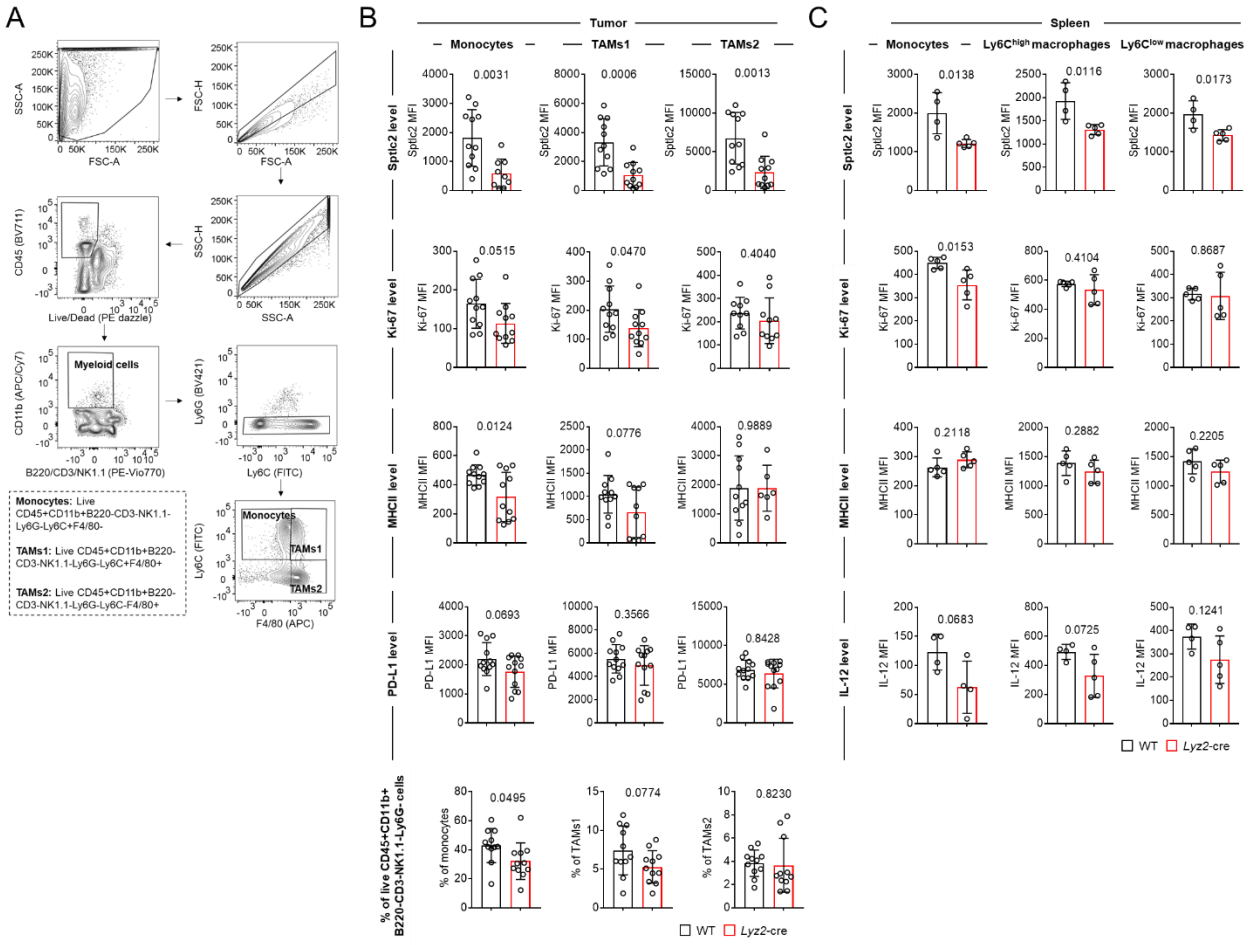

Figure 26 *Sptlc2* deficiency regulates myeloid cell marker expression in B16-F10 tumors.

(A) Flow cytometry contour plots showing the gating strategy used in B-C to identify monocytes (live CD45+CD11b+NK1.1-CD3-B220-Ly6G-Ly6C+F4/80- cells) and macrophages (TAMs1/Ly6C^{high}: live CD45+CD11b+NK1.1-CD3-B220-Ly6G-Ly6C+F4/80+ cells; TAMs2/Ly6C^{low}: live CD45+CD11b+NK1.1-CD3-B220-Ly6G-Ly6C-F4/80+ cells) from the tumor or spleen of tumor-bearing mice. The example shows tumor monocytes and macrophages.

(B) Bar graphs showing Sptlc2, Ki-67, MHCII, and PD-L1 expression of WT or *Lyz2*-cre monocytes, TAMs1, and TAMs2, and their percentage among all live CD45+B220-CD3-NK1.1-CD11b+Ly6G- cells from the tumor (N=11).

(C) Bar graphs showing Sptlc2, Ki-67, MHCII, and IL-12 expression of WT or *Lyz2*-cre monocytes, Ly6C^{high}, and Ly6C^{low} macrophages from the spleen of tumor-bearing mice (N=4-5). Data are presented as mean ± SD (B-C). Statistical comparisons were performed with unpaired two-tailed Student's *t* tests (B-C; data points were normally distributed) and two-tailed Mann-Whitney U tests (B; data points were not normally distributed). Figures 26A-B are included in (*192*).

Unlike in the sepsis model, in which mice were only exposed to the disease for 3-6 hours, in the almost 3-week-lasting melanoma model, adaptive immune responses were also activated. The inverse correlation between higher tumor growth and lower MHCII expression in the *Sptlc2*-deficient mice implied that other immune cells, such as T cells, were also involved in limiting tumor growth in WT mice, but to a lesser degree in *Lyz2*-cre mice. To test this hypothesis, I used flow cytometry to identify T cells from the B16 tumors and found that *Sptlc2*-sufficient mice showed higher percentages of CD3+ T cells among all live leukocytes (Figure 27A). Moreover, the percentage of NK cells among all live leukocytes was reduced in *Sptlc2*-deficient mice (Figure 27A). *Sptlc2* deficiency increased the percentages of CD8a+CD44+ T cells expressing immune checkpoint molecules PD1 and TIGIT (Figure 27B-C).

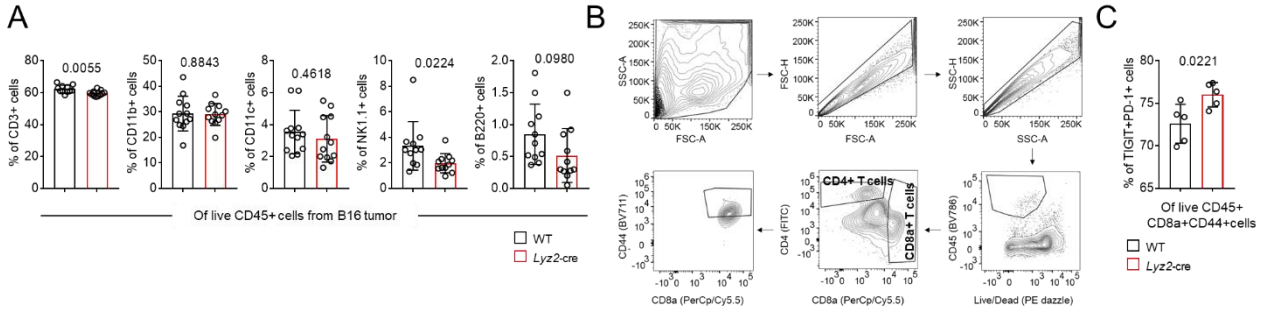

Figure 27 *Sptlc2* deficiency in myeloid cells decreases T and NK cell numbers in B16 tumors and increases the immune checkpoint molecules PD-1 and TIGIT on T cells.

(A) Bar graphs showing B16 tumor-infiltrating leucocyte (TIL; all live CD45+ cells from the tumor) subpopulations in WT or *Lyz2*-cre mice.

(B) Contour plots showing the gating strategy used in C to identify CD8+ T cells (live CD45+CD8+CD44+ cells).

(C) Bar graph showing the percentage of TIGIT+PD-1+ cells among all live CD45+CD8+CD44+ cells from the tumors of WT or *Lyz2*-cre mice (N=5). Data are presented as mean ± SD (A, C). Statistical comparisons

were performed with unpaired two-tailed Student's *t* tests (A, C; data points were normally distributed) and two-tailed Mann-Whitney U tests (A; data points were not normally distributed). Figures 27A-C are included in (*192*).

To test if reduced MHC-expression on *Sptlc2*-deficient macrophages impaired their function to activate anti-tumor CD8+ T cells, I co-cultured *in vitro*-generated LCMV gp33-41-pulsed and LPS-activated WT or *Lyz2*-cre BMDM with CellTrace violet-labeled CD8+ T cells from P14 mice and checked T cell proliferation and activation by flow cytometry (Figure 28A-B). T cells from P14 mice express a transgenic T cell receptor that specifically recognizes the LCMV-derived peptide gp33-41 (*230*). Co-culture with *Sptlc2*-deficient BMDM resulted in decreased expression of the activation marker CD44 and effector protein granzyme B in CD8+ T cells and lower CD8+ T cell proliferation, indicated by a higher CTV signal (Figure 28C-E). Moreover, WT macrophages showed higher MHCII/CD86 and, even more importantly for CD8+ T cells, MHCI/CD86 co-expression than *Lyz2*-cre macrophages (Figure 28F-G). Collectively, these results suggested that Sptlc2 was required for MHC-mediated macrophage activation of antigen-specific T cells.

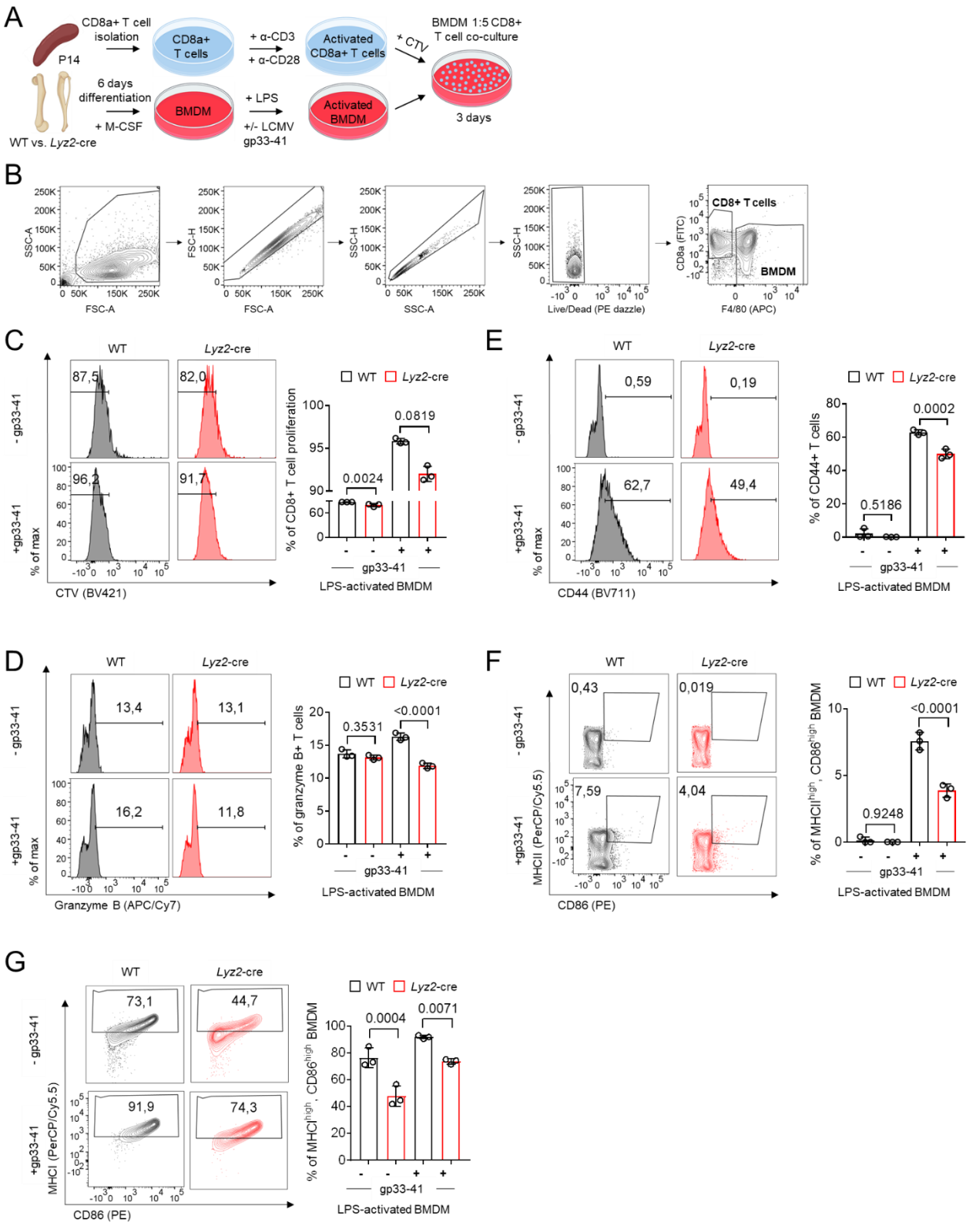

Figure 28 *Sptlc2* deficiency decreases the ability of macrophages to activate CD8+ T cells.

(A) Illustration of the experimental design in C-G. T cells were isolated from the spleens of P14 mice, α-CD3/α-CD28 activated, and CellTrace violet (CTV) labeled. WT or *Lyz2*-cre BMDM were grown as described

above and pulsed with LCMV gp33-41 and LPS-activated. Co-cultures (BMDM 1:5 T cells) were set up for 3 days, and flow cytometry was used to determine CD8+ T cell activation and BMDM MHCI/II and CD86 expression.

(B) Representative flow cytometry contour plots, showing the gating strategy used in C-G to identify BMDM (live F4/80+ cells) and CD8+ T cells (live CD8a+ cells).

(C-E) Representative histograms and bar graphs, showing CD8+ T cell proliferation (C), granzyme B expression (D), and CD44 expression (E) in CD8+ T cells co-cultured with LCMV gp33-41/control-pulsed LPS-activated WT or *Lyz2*-cre macrophages (N=3).

(F-G) Representative contour plots and bar graphs, showing the percentage of (F) $MHCII^{high}$, $CD86^{high}$ WT, or *Lyz2*-cre BMDM and (G) $MHCI^{high}$, $CD86^{high}$ WT, or *Lyz2*-cre BMDM after LCMV gp33-41 pulsing and LPS activation (N=3). Data are presented as mean ± SD (C-G). Statistical comparisons were performed with ANOVA tests (C-G; for simultaneous comparisons of more than two groups). Figures 28E, G are included in (*192*).

5.7.1.2 Dendritic cell-specific *Sptlc2* deficiency does not significantly change B16 tumor growth

A subset of dendritic cells also expressed lysozyme M (*231*). To evaluate the degree to which *Sptlc2* deficiency in dendritic cells shaped the anti-tumor immune response, *Sptlc2*$^{Flox/Flox}$ *CD11c*-cre mice, which had a dendritic cell-specific *Sptlc2* deficiency (referred to as *CD11c*-cre), were generated. In the B16 melanoma model, compared to their wildtype littermates, *CD11c*-cre mice grew tumors of similar size and not significantly different weights (Figure 29A-C), thus suggesting that the enhanced tumor growth observed in *Lyz2*-cre mice was not due to the non-specific deletion of *Sptlc2* in dendritic cells.

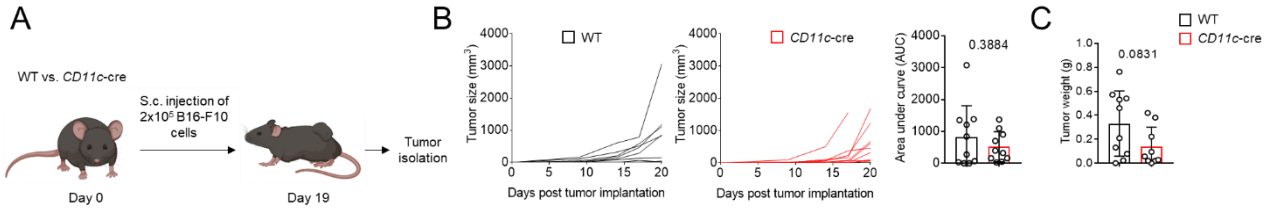

Figure 29 *Sptlc2* deficiency in CD11c-expressing cells does not significantly impact B16 tumor growth.

(A) Illustration of the experimental design in B-C. A total of 2×10^5 B16-F10 cells were injected subcutaneously into C57BL/6 WT and *CD11c*-cre mice. On day 19, the mice were sacrificed, and tumor size and weight were measured.

(B) Line graphs showing B16-F10 melanoma growth in WT and *CD11c*-cre mice over time after subcutaneous injection of 2×10^5 B16-F10 melanoma cells. Bar graph, showing the area under the curve (AUC) of the tumor growth plots (N=10).
(C) Bar graph showing the tumor weight of WT or *CD11c*-cre mice at the endpoint on day 19 (N=10). Data are presented as mean ± SD (B-C). Tumor growth curves were evaluated longitudinally, and the AUC was calculated for each tumor growth curve (B). Statistical comparisons were performed with unpaired two-tailed Student's *t* tests (B-C; data points were normally distributed). Figures 29B-C are included in (*192*).

5.7.2 Myeloid cell-specific *Sptlc2* deficiency does not affect Ret melanoma growth

To transfer the B16 tumor findings to another melanoma mouse model, I used the Ret melanoma mouse model to study the influence of Sptlc2-dependent inflammatory macrophage signaling on tumor development. Ret cells were previously established from skin melanomas in *ret* transgenic mice (*175*). Similar to the B16 model, Ret melanoma cells were subcutaneously injected into WT or *Lyz2*-cre mice, and tumor growth was recorded over time (Figure 30A). I tested different Ret melanoma cell doses (0.05, 0.2, or 0.5 million Ret cells/mouse) and observed that Ret tumors developed faster than B16 tumors, reaching endpoint criteria at around 9 days after tumor cell injection, with no difference in tumor development between *Sptlc2*-sufficient and -deficient mice (Figure 30B).

Using flow cytometry, I found the protein levels of Sptlc2 were lower in *Sptlc2*-deficient monocytes, TAMs1, and TAMs2 (Figure 30D-E). However, unlike in the B16 model, *Sptlc2* deficiency did not alter percentages of monocytes, TAMs1 or TAMs2, their Ki-67 and MHCII expression, or T cell numbers (Figure 30E). Collectively, these results suggested that, in the Ret melanoma model, *Sptlc2* deficiency in myeloid cells did not affect tumor development, potentially due to the more aggressive tumor growth.

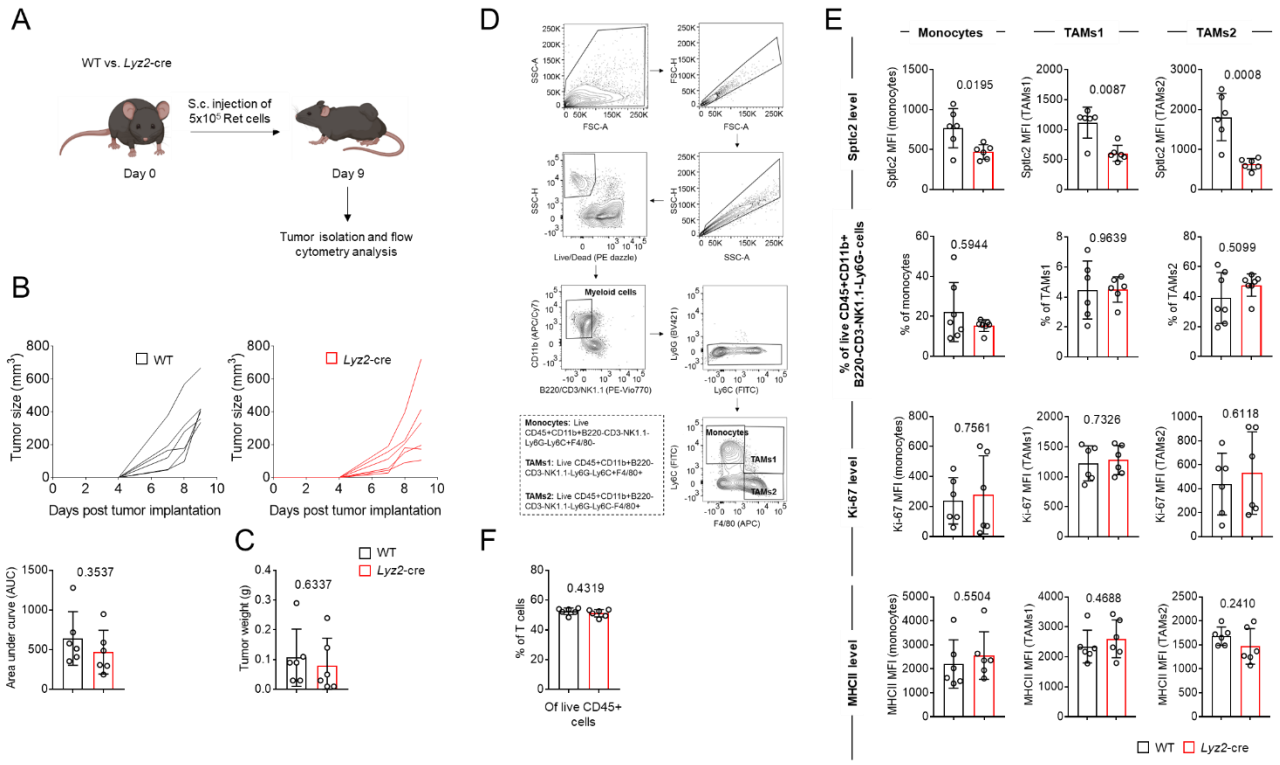

Figure 30 *Sptlc2* deficiency does not affect tumor growth or myeloid cell phenotype in the Ret melanoma model.

(A) Illustration of the experimental design in B-E. A total of 5×10^5 Ret melanoma cells were subcutaneously injected into WT or *Lyz2*-cre mice, and tumor growth and weight on day 9 were monitored. After the mice were sacrificed, tumors were isolated, and flow cytometry analysis was performed to investigate immune cell numbers and markers. Injection of only 0.05 or 0.2×10^5 Ret cells resulted in slightly slower tumor formation but comparable results.

(B) Line graphs showing Ret melanoma growth in WT or *Lyz2*-cre littermate mice over time after subcutaneous injection of 5×10^5 Ret melanoma cells. Bar graph, showing the area under the curve (AUC) of the tumor growth plots (N=6).

(C) Bar graph showing the Ret tumor weight of WT or *Lyz2*-cre mice at the endpoint on day 9 (N=6).

(D) Flow cytometry contour plots, showing the gating strategy used in E to identify monocytes (live CD45+CD11b+NK1.1-CD3-B220-Ly6G-Ly6C+F4/80- cells) and macrophages (TAMs1: live CD45+CD11b+NK1.1-CD3-B220-Ly6G-Ly6C+F4/80+ cells; TAMs2: live CD45+CD11b+NK1.1-CD3-B220-Ly6G-Ly6C-F4/80+ cells).

(E) Bar graphs showing Sptlc2, Ki-67, and MHCII levels of WT or *Lyz2*-cre monocytes, TAMs1, and TAMs2 and their percentage among all live CD45+B220-CD3-NK1.1-CD11b+Ly6G- cells from the tumor (N=6).

(F) Bar graph showing the percentage of CD3+ cells among all live CD45+ WT or *Lyz2*-cre cells (N=6) from the tumor. Data are representative of two independent experiments and presented as mean ± SD (B-C, E-F). Tumor growth curves were evaluated longitudinally, and the AUC was calculated for each tumor growth curve (B). Statistical comparisons were performed with two-tailed Student's *t* tests (B-C, E-F; data points

were normally distributed) and two-tailed Mann-Whitney U tests (E; when data points were not normally distributed).

6. Discussion

I found that sphinganine physically interacts with the TLR4 adaptor proteins, increases MyD88 recruitment to the cell membrane, and promotes LPS-induced macrophage growth, M1-like macrophage marker expression, and inflammatory cytokine production. My work reveals Sptlc2-derived sphinganine as a metabolic checkpoint involved in pattern recognition by macrophages in two different inflammation-associated mouse models. Thereby, this work expands the traditional view of sphingolipids as building blocks that support biosynthesis and reveals a role for sphingolipids in directly engaging innate immune cell signal transduction and macrophage activation. So, it sheds new light on the multifaceted role of sphingolipids as signaling molecules in innate immunity.

6.1 Cellular (sphingolipid) metabolism shapes immune responses

In the past two decades, metabolism-focused research has boomed and increasingly infiltrated many research fields such as cancer biology, genetics, microbiology, structural and systems biology, and immunology (*232*). The fusion of immunology and metabolism created the research field “Immunometabolism”, in which cellular metabolism is seen as a central regulator for the function and activation of immune cells (*233, 234*). In line with literature, this is represented by my data, which showed different metabolic states of M1-like and M2-like macrophages, which facilitate different functional states (*75, 233, 234*). Accumulating evidence has indicated the existence of a metabolic-inflammatory circuit, in which bi-directional communication between metabolism and inflammation intricately links cellular metabolic pathways to inflammation-associated signal transduction (*235*). For example, inhibiting the biosynthesis of cholesterol sensitizes macrophages to di-cyclic nucleotides and enhances antiviral immunity (*236*). Furthermore, inhibition of *de novo* fatty acid synthesis attenuates IL-17-producing helper T (Th17) cell differentiation and limits Th17 cell-mediated inflammation (*237*). Linked to these examples, my work showed that the inflammatory stimulus LPS induced the expression and activity of Sptlc2 and the *de novo* synthesis of sphingolipids. Inhibiting *de novo* synthesis of sphingolipids antagonized TLR4 adaptor protein recruitment to the cell membrane and impaired downstream signal transduction, thereby providing an example of pattern recognition coupling lipid

metabolism and inflammation and inducing a self-enhancing metabolic-inflammatory circuit in macrophages.

6.2 Sptlc2 is increased during inflammation and is important for M1-like macrophages

Just like the field of “Immunometabolism”, sphingolipid research has evolved a lot in the past two decades. As major components of lipid rafts, sphingolipids have been associated with regulating a variety of cellular signaling processes (*238*). For example, the sphingolipid S1P can epigenetically regulate gene expression through modulation of histone acetylation in the nucleus (*141*) or act as a co-factor for the E3-ubiquitin ligase TRAF2, regulating NF-κB activation (*140*). In line with studies describing increased sphingolipid metabolism upon inflammatory conditions in SARS-CoV-2 (*135*), sepsis (*136*), or cancer (*133*), my work identified increased sphingolipid levels of *in vitro* M1-like-activated BMDM and elevated levels of sphingolipid metabolism’s key enzyme, Sptlc2, in LPS-stimulated BMDM *in vitro* as well as in macrophages and monocytes in sepsis and tumor mouse models *in vivo*. It is believed that increased sphingolipid metabolism following LPS is caused by increased glucose uptake (*152*). Via glycolysis, the TCA cycle, and fatty acid synthase, glucose is metabolized to palmitoyl-CoA, which is used for sphingolipid biosynthesis by Sptlc2 (*152, 198*). Simultaneously, via the glycolytic enzyme phosphoglycerate dehydrogenase, serine is generated from glucose (*239*). At the same time, LPS increases Sptlc2 expression via NF-κB activation (*162*), but whether sphingolipids modulate LPS-mediated signaling is not yet fully understood (*152*).

Inspired by the observation that inflammatory conditions induced Sptlc2 levels in macrophages, *Sptlc2*-deficient mice, which allowed me to study Sptlc2-derived sphingolipids specifically in myeloid cells, were generated in our laboratory. LPS-stimulated, *Sptlc2*-deficient BMDM had lower levels of many different sphingolipids, pointing out that salvage and recycling pathways could not compensate for the loss of the Sptlc2-dependent *de novo* pathway. Nevertheless, whether *Sptlc2* deficiency induced such pathways and further compensatory mechanisms, such as increasing the transportation of extracellular sphingolipids, remains unknown.

Whereas in well-oxygenated conditions, typically pyruvate is used in the TCA cycle, in anaerobic conditions it is converted to lactate. However, upon M1-like macrophage

activation, macrophage metabolism shifts to aerobic glycolysis and increased lactate production independently of oxygen concentration, a phenomenon known from tumor cells as the Warburg effect (*240, 241*). I conclude that additionally to the increased metabolic requirements and enhanced glucose uptake resulting from larger cell size and morphologic changes, this metabolic shift was augmented in M1-like WT compared to *Sptlc2*-deficient BMDM and caused increased lactate generation and more acidic pH values.

One could argue that upon *Sptlc2* deletion, sphingolipids were lacking solely as building blocks, limiting metabolic activity, cell growth, and the morphologic development of macrophages. However, as mentioned before, metabolic adaptations are often linked to altered cell signaling, and consequently, I analyzed the BMDM polarization states of *Sptlc2*-sufficient and -deficient macrophages. Notably, the strict M1/M2 categorization of macrophage activation nowadays is seen as an oversimplification, as many markers are co-expressed context-dependently. To exclude this as best as possible, I measured M1-like macrophage growth and focused on the exclusive M1-like and M2-like macrophage markers CD38 and Egr2, respectively (*72*). *Sptlc2* deficiency increased M2-like and decreased M1-like macrophage activation. While my work contradicts reports stating Sptlc2 is dispensable for macrophage polarization (*167*), it is in line with the ones showing Sptlc2 and sphingolipids being crucial for LPS-induced M1-like macrophage signaling via TLR4 (*161, 165*). Apart from cell growth and marker expression, M1-like macrophage activation is characterized by increased cell proliferation and pro-inflammatory cytokine production (*220*), which I also found decreased upon *Sptlc2* deficiency. The observation that *Sptlc2*-deficient macrophages were not equally M1-like and, in turn, even M2-like-polarized, ruled out the idea that sphingolipids were lacking solely as building blocks and rather suggested that Sptlc2-derived sphingolipids decide over the polarization fate of macrophages. This was further supported by the observation that *Sptlc2* deficiency only had minor to no effects on macrophage differentiation. When there was no polarization stimulus, measurements of confluency and MyD88 levels of PBS-treated *Sptlc2*-deficient and *Sptlc2*-sufficient BMDM and macrophage numbers and cytokine levels of PBS-injected *Sptlc2*-deficient and *Sptlc2*-sufficient mice were largely comparable. Nonetheless, it cannot be entirely excluded that Sptlc2-derived sphingolipids affected macrophage differentiation, cell membrane composition, and lipid raft formation,

subsequently contributing to differences in *Sptlc2*-deficient and *Sptlc2*-sufficient macrophage activation beyond what was measured here. To study this in more detail, it could be useful to time-dependently delete *Sptlc2* right after the differentiation and before the polarization. For this, either mice with a tamoxifen-inducible *Sptlc2* deletion through the breeding of *Sptlc2*$^{Flox/Flox}$ mice and commercially available *Lyz2*$^{tm1(cre/ERT2)Grtn}$/J mice (*242*) could be generated, or a commercially available trans-activator of transcription (TAT)-cre recombinase could be used to *in vitro* delete *Sptlc2* from the BMDM of *Sptlc2*$^{Flox/Flox}$ mice (*243*). Supporting the idea that sphingolipids are more than building blocks was the fact that in *Sptlc2*-deficient macrophages, LPS-induced macrophage growth was rescued specifically by the sphingolipid sphinganine but not the sphingolipid sphingomyelin, which was previously described as a membrane building block (*244*). Sphingomyelin was previously linked to activating TLR4 signaling (*245*), but my data suggested that, unlike sphinganine, sphingomyelin supplementation was not enough to rescue M1-like macrophage growth in *Sptlc2*-deficient macrophages. Given this unique role of sphinganine, the question came up: By which mechanism did Sptlc2-derived sphinganine contribute to LPS-induced M1-like macrophage signaling and macrophage growth?

6.3 Sphinganine-dependent MyD88 recruitment to TLR4 drives M1-like NF-κB-signaling in macrophages

To get a clearer understanding of sphingolipid-regulated M1-like macrophage signaling, I focused on LPS-induced signaling and not the combinatorial M1-like macrophage stimuli LPS/IFN-γ. My data and previous work have demonstrated that LPS alone, similar to a combination with IFN-γ, results in M1-like activation of macrophages (*246*). Consequently, how sphingolipids are involved in IFN-γ-induced M1-like macrophage signaling remains unanswered from this work. Downstream of LPS, it is TLR4 signaling that drives macrophages to a preferentially M1-like phenotype (*247*). Notably, downstream of LPS-induced TLR4 activation, TRIF and MyD88 signaling pathways mediate inflammatory responses. The MyD88 arm was shown to be the primary driver for LPS-dependent NF-κB signaling (*248*). MyD88-directed signaling induces NF-κB, AP-1, and also Stat1-mediated gene expression (*207, 208*). Sphingolipids have been reported multiple times to regulate the LPS-TLR4-MyD88-NF-κB axis, but a detailed mechanistic understanding is

still absent (*152*). While NF-κB p65 (Ser536) phosphorylation status was strongly altered by *Sptlc2* deficiency, AP-1 and Stat1 activity only showed a slight trend to decrease. Therefore, to what degree AP-1 and Stat1-mediated target gene expression is regulated through sphingolipids remains elusive. NF-κB activation could additionally be analyzed by measuring further activating or inhibiting phosphorylations of NF-κB subunits (*249*) or phosphorylation levels of IκBα and IKK subunits. Hereby, due to the oscillations of NF-κB signaling, special attention should be paid to the optimal stimulation time (*201, 250, 251*). I found that Sptlc2-mediated sphingolipid synthesis promoted TLR4 signal transduction by enhancing the expression of MyD88 and, more importantly, the recruitment of the TLR4 adaptor protein MyD88 to the cell membrane. Using pulldown assays and molecular biology tools, I found that this was mediated through direct interactions of Sptlc2-derived sphinganine with MyD88, TIRAP, and Tollip. Given that MyD88 acts downstream of Tollip and TIRAP, I focused on rescuing the MyD88 membrane recruitment by attaching the myristoylation sequence to MyD88. I showed that MyrisMyD88 overexpression rescued CD38 expression, cell size, IL-6, and IL12 p70 levels in *Sptlc2*-deficient macrophages. Notably, the transfection process might have influenced macrophage functions such as cytokine secretion and proliferation (*252*). I cannot exclude additional mechanisms through which Sptlc2 strengthened TLR4 signaling, such as enlarging the pool of sphingolipids and enhancing the formation of lipid rafts. The latter, which was not further studied in this work, would be supported by the observation that actin interacted more with sphinganine than with biotin (not exclusively though). It would be possible that a sphingolipid-actin interaction re-arranges the cytoskeleton to allow for the formation of special membrane compartments and different cell morphologies, contributing to immune signaling induction. Further work in this direction and about the specificity of the sphinganine-pulldown of actin is required, but it is mentionable that sphingolipids and sphingolipid metabolism-associated enzymes were linked to actin modulation and the cytoskeleton before (*253, 254*).

Moreover, some questions about the complete mechanism remain. As Tollip negatively regulates TLR4 signaling (*95*), it would be interesting to see if it is the interaction with sphinganine that causes Tollip removal, allowing for subsequent TIRAP and MyD88 recruitment and downstream signaling. In the input, Tollip staining showed two bands, one at ~30 kDa and one at ~45 kDa. After sphinganine-biotin pulldown, only the band at ~45

kDa was visible, suggesting that sphinganine only interacts with the ~45 kDa version of Tollip. Given that this band at ~45 kDa was visible in several cell lines before (*255, 256*), it is unlikely that this signal was unspecific. To ensure that the signal at ~45 kDa represents a modified version of Tollip, LC-MS/MS analysis could be useful. As Tollip was shown to have a domain that binds ubiquitin, preventing its binding to phosphoinositides and thereby membrane lipid binding (*257*), a potential hypothesis would be that sphinganine mediates ubiquitination of Tollip and alters its function, breaks its inhibitory co-localization with TLR4, or initiates its degradation. In theory, ubiquitination of Tollip would increase its size by ~10 kDa, which indeed would result in a signal at ~40-45 kDa, which would match my observations. Supporting this hypothesis is that in the LC-MS/MS analysis, I also found that sphinganine-biotin interacted with ubiquitination process-associated proteins such as ubiquitin-conjugating enzyme E2 Z (UBE2Z), Ring finger protein 2 (Rnf2), ubiquitin carboxyl-terminal hydrolase isozyme L5 (Uchl5), ubiquitin protein ligase E3 component n-recognin 5 (Ubr5) and ubiquitin thioesterase (Otub1), but not control biotin (Supplementary Table 29). Besides, a role for Tollip in mediating protein SUMOylation was described before (*258*). For testing whether sphinganine recruits SUMOylation- or ubiquitination-associated proteins to remove Tollip from TLR4 to allow for TIRAP-directed MyD88 recruitment, further work is required.

Another open question would be about which chemical group in sphinganine is responsible for the interaction with TLR4 adaptor proteins. The herein-described sphinganine interactions with MyD88, TIRAP, and Tollip were identified using biotinylated sphinganine, in which the biotin was conjugated to the end of the N-acyl chain of sphinganine. Therefore, the N-acyl chain of sphinganine was occupied and was unlikely to be available for interacting with proteins. This hypothesis was supported by the absence of sphinganine-interacting proteins pulled down with agarose beads coupled to the head group of sphinganine via Schiff base formation. Further biochemical analyses are required to more comprehensively test the possibility that the polar head group, rather than the N-acyl chain of sphinganine, mediates the interaction with adaptor proteins. The question about the exact sphinganine contact site is accompanied by the question about the type of interaction. Whether it is an unspecific hydrophobic association or an electrostatic interaction between the adaptor proteins and the sphinganine head group, whether the adaptor proteins share specific binding pockets for sphinganine head groups, or whether

they harbor covalently bound lipid anchors, remains to be studied (*259*). Besides, as previously mentioned, quantitative analysis using LC-MS/MS is required to completely exclude a direct Sptlc2-TLR4 adaptor interaction. However, such an interaction is also unlikely from a spatial point of view, with Sptlc2 sitting at the ER and adaptor proteins being localized close to the membrane.

Altogether, these results support the latest assumption that sphingolipids are crucial for TLR4 signaling by forming lipid rafts allowing for TLR4 complex assembly and internalization (*116, 161, 165, 166*), and extend it further by suggesting a direct role for sphinganine in initiating TLR4 signaling. While it was previously reported that the gangliosides monosialotetrahexosylganglioside (GM1) and GD1a negatively regulate TLR4 signaling by preventing MyD88 binding (*163*), I propose an opposite mechanism for sphinganine to positively regulate TLR4 signaling by enhancing MyD88 binding, allowing for downstream signaling. Whether the negative regulation by gangliosides follows the exact opposite mechanism remains to be studied. Adaptive interconversion in highly dynamic sphingolipid metabolism, like sphinganine being metabolized to gangliosides at a higher or lower rate, is a conceivable way for macrophages to regulate TLR4 signaling. This work proposes that, similar to the well-accepted “sphingolipid rheostat” that ceramides mediate apoptosis while S1P mediates cell survival (*260*), another sphingolipid-based antagonism is that gangliosides inhibit TLR4 signaling while sphinganine acts as an activator.

6.4 Sphingolipid-driven inflammatory signaling shapes macrophage immune responses in different disease models

Whether Sptlc2-dependent regulation of inflammatory TLR4 signaling is beneficial or detrimental to health comes along with the not-easily-answerable question of whether inflammation is beneficial or not. While there is agreement that controlled inflammation brings beneficial properties to immune activation, uncontrolled or long-term inflammation is detrimental and suppressive to immune responses, and it is not so clear where exactly the first ends and the second begins. Unequivocally, the same accounts for the role of inflammation-associated TLR4 signaling and M1-like polarization on macrophage function. While initially immune-activating, long-term TLR4 signaling and the production of pro-inflammatory cytokines by M1-like macrophages create an immunosuppressive

environment. Despite definite differences in the type of inflammation in the herein-used tumor and sepsis models (chronic vs. acute), the increased levels of Sptlc2 in macrophages in both models make both models interesting for the study of sphingolipids in inflammatory signaling pathways. Based on these findings, it cannot be concluded that Sptlc2-driven inflammatory macrophage signaling is always beneficial in anti-tumor immune responses or always detrimental in sepsis, but rather that it is a possible target for manipulation to regulate tumor- or sepsis-associated inflammation.

6.4.1 Sptlc2-dependent inflammatory TLR4 signaling drives sepsis

During sepsis, a strong over-activation of innate immune cells, mainly M1-like macrophages, results in excessive production of pro-inflammatory cytokines, making inflammatory signaling, in this scenario, detrimental to health. Previously, sepsis patients showed increased TLR4 expression, and TLR4 pathway modulation was described as a strategy to target sepsis (*261, 262*). In the course of that, different natural compounds with TLR4 pathway antagonistic properties were tested in animal models of sepsis *in vivo* (*97*). Supporting the initial hypothesis that sphingolipid-driven TLR4 signaling in M1-like macrophages aggravates sepsis, RNA sequencing revealed increased Sptlc2 levels in sepsis patients compared to healthy individuals (*218*). To further study the role of sphingolipids in mediating inflammatory macrophage responses during sepsis, *in vivo* mouse models were required. There are three main types of sepsis mouse models to choose from: 1) LPS administration, 2) administration of pathogenic bacteria, or 3) cecum ligation and puncture (CLP) (*263, 264*). Of these, especially the LPS-induced sepsis model is characterized by high pro-inflammatory cytokine levels shortly after LPS injections. LPS injections represent a relatively sterile model for studying the pathophysiology of sepsis within a short timeframe, allowing for the study of only LPS-induced pathways. Consequently, to study whether sphinganine-driven MyD88 recruitment to TLR4 might impact sepsis, I injected *Sptlc2*-sufficient and -deficient mice with LPS. Supporting the *in vitro* mechanism, I found that macrophages from *Sptlc2*-deficient mice showed a less M1-like macrophage phenotype and reduced plasma cytokine levels, resulting in less severe sepsis symptoms. Notably, MHCII expression has been reported to decrease after the onset of sepsis (*265*). The decreased cytokine production in *Sptlc2*-deficient mice might also, in part, be a secondary result of the

decreased macrophage numbers. However, after LPS, macrophage numbers are in turn also dependent on TLR4-mediated cytokines, making these two effects mutually dependent. Moreover, I cannot exclude that further innate immune cells contributed to the LPS-induced cytokine storm. Matching my flow cytometric quantification of macrophages between *Sptlc2*-sufficient and -deficient mice, in previous mouse models, numbers of M1-like macrophages correlated with sepsis severity (*266*). Whether the described phenotypes can also be seen in CLP models or after pathogenic bacterial administration remains to be studied.

Even though LPS is most commonly described for its role in sepsis pathology, accumulating evidence suggests that LPS-induced signaling and immune dysregulation are also relevant in many other chronic diseases (*267*). Along with the generally rising interest in research in the tumor microbiome, increasing literature describes the role of LPS and bacterial products in tumorigenesis (*83-89*). Given that macrophages are key regulators shaping the tumor microenvironment, I found it interesting to also study whether sphingolipids are needed for inflammatory macrophage signaling in the tumor.

6.4.2 Sptlc2-dependent inflammatory signaling regulates tumorigenesis

Noteworthy, the tumor model is by far more complex and not as “clean” as the LPS-induced sepsis model, making the interpretation of whether inflammation in this context is beneficial or detrimental more difficult. Additionally, due to the longer-lasting experimental design, adaptive immune responses also played a role. Beyond LPS, in tumors, additional TLR4 ligands, such as palmitic acid (*268, 269*), HMGB1 (*270*), S100A8/A9 (*271, 272*), and HSP90α (*226*), are enriched, activating downstream signaling. I detected two serotypes of LPS in tumors, but I cannot exclude the possibility that further serotypes and additional ligands of TLR4 might require Sptlc2-mediated sphingolipid synthesis to activate the signal transduction downstream of TLR4. Questions about the origin of the detected LPS and whether bacterial infiltration into tumors is an opportunistic consequence of a misdirected immune response (*273*) or even an antagonistic protective mode, which the immune system allows to initiate immune responses (*274*), were not further followed in this work but are of tremendous importance to fully unravel inflammatory signaling in tumors.

Diverse functions in cancer have been previously described for sphingolipids (*134*). For example, ceramides and S1P are important regulators of apoptosis, cell survival, adhesion, migration, and invasion (*275*); ceramides regulate senescence (*276*) and autophagy (*277*). Therefore, it has to be noted that the data do not exclude that other pathways in macrophages that are not related to TLR4 signaling or not even at all to inflammation are affected by the genetic deletion of *Sptlc2* in the herein-used model. Especially given that Sptlc2-dependent *de novo* biosynthesis is needed for the generation of all sphingolipids, it has to be further unraveled how deficiency of different sphingolipids alters myeloid cell functions in tumors. Even though the spread of tumor sizes was relatively high, myeloid cell-specific *Sptlc2* deficiency increased B16 tumor growth. In the Ret melanoma model, no difference in tumor growth between *Sptlc2*-deficient and *Sptlc2*-sufficient mice was seen. Whether this is due to different LPS levels inducing less M1-like anti-tumor macrophage immune responses or due to the more aggressive tumor growth in the Ret model, hiding Sptlc2-dependent immune responses, requires further investigation.

Moreover, it should be noted that the B16 model represents a relatively un-immunogenic tumor, a so-called “cold tumor”, making alternative models such as the YUMMER1.7 (Yale University Mouse Melanoma Exposed to Radiation 1.7) melanoma mouse model more attractive for studying anti-tumor immune responses (*278*). Additionally, the YUMMER1.7 model carries clinically relevant melanoma driver mutations (such as $Braf^{V600E}$ (valine (V) is substituted by glutamic acid (E) at amino acid 600), $Pten^{-/-}$ and cyclin-dependent kinase inhibitor 2A ($Cdkn2a)^{-/-}$), forms a functional anti-tumor immune response in mice, and is responsive to immune checkpoint inhibitors, making it a more useful model to study melanoma with regards to clinical translation (*278*).

By analyzing NF-κB target genes, especially the ones known to be relevant for macrophage function during cancer, I tried to understand how much of the macrophage response in tumors is modulated by sphingolipid metabolism through this particular transcription factor, but I cannot say with absolute certainty whether these genes were only induced by LPS, only via TLR4, and, in more detail, only via the MyD88-dependent signaling arm. Levels of NF-κB-dependent MHCII, Ki-67 (*228*), and PD-L1 (*100*) were reduced in macrophages of *Sptlc2*-deficient mice. How much the expression of each of these markers affects macrophage tumor control and to what degree Sptlc2-induced

inflammatory signaling is beneficial or detrimental to health cannot be entirely concluded from these data. It would be conceivable that Sptlc2-driven pro-inflammatory M1-like signaling at a later stage contributed to the creation of an immunosuppressive environment. However, in my model, the B16 tumor growth data suggested that Sptlc2 was required for tumor control by myeloid cells. Supporting the assumption that smaller tumors in the *Sptlc2*-sufficient group were limited in growth through sphingolipid-driven anti-tumor signaling are the co-culture experiments showing increased antigen-presentation capacity and an M1-like macrophage phenotype, accompanied by increased T cell proliferation and activation upon *Sptlc2* presence in BMDM. However, in these experiments, potentially resulting from pre-activation with α-CD3 and α-CD28, even in the absence of gp33-41, T cell proliferation and granzyme B levels were relatively high in T cells cultured with non-gp33-41-pulsed BMDM regardless of *Sptlc2* sufficiency, which makes deeper investigation needed. To see if this can be reproduced in *in vivo* settings, co-cultures of myeloid cells, isolated from mouse tumors through FACSorting, and CD8+ T cells could be useful. It remains unclear how tumor-promoting MDSC and M2-like TAMs, which were also affected by the *Sptlc2* deletion, contributed to immune responses during tumorigenesis in the long term. Apart from the effects of myeloid cell-specific *Sptlc2* deficiency on macrophage and T cell function, to get an even broader view, it would also be intriguing to study the fate of various other intra-tumor immune cell types, such as NK cells, which I also discovered to be reduced in the myeloid cell-specific absence of *Sptlc2* and which have also been linked to being in close communication and interaction with myeloid cells in tumors (*279*). Notably, in tumor macrophages, also downstream of other TIR domain-containing receptors such as TLR2 and IL-1R, TIRAP and MyD88 get recruited, activating downstream signaling (*280-282*), but whether sphinganine is involved similarly as in TLR4 signaling remains to be studied.

6.5 Sphingolipid modulation bears potential for clinical translation

My work reveals the Sptlc2-sphinganine pathway to be a new target to manipulate TLR4 signaling in different inflammation-associated diseases. For a while, TLR4 signaling has been a promising target for immunotherapies. Even LPS was considered via different administration routes in clinical trials (*283, 284*). Intratumor LPS injections activate anti-tumor immune cells and decrease tumor growth (*285*), but the strong pro-inflammatory

properties of LPS result in severe adverse effects (*286*). Consequently, only the less toxic LPS derivative monophosphoryl lipid A (MPLA) was FDA-approved, which is, however, a weaker TLR4 agonist than LPS (*287, 288*). This demonstrates the still unmet need for clinically applicable TLR4 signaling modulators, which could not only be useful in sepsis or tumor diseases but also for further inflammatory (TLR4-driven) diseases such as obesity, where in adipose-tissue macrophages (ATM) TLR4-NF-κB signaling creates a chronic low-grade inflammatory environment leading to different follow-up malignancies (*64*), or asthma, where pro-inflammatory M1-like macrophage signaling exacerbates lung injury and accelerates airway remodeling (*64, 289*). In rats, gangliosides, a group of sphingolipids, decreased intestinal inflammation upon LPS (*290*), suggesting that sphingolipid-based therapies open new treatment options for TLR4-mediated inflammation.

Potentially, inhibiting Sptlc2-dependent sphinganine production or stimulating sphinganine conversion to more complex sphingolipids and simultaneously supplementing gangliosides to reduce inflammatory signaling during sepsis while activating initial TLR4 signaling in cancer immunotherapies via sphinganine inducers and ganglioside inhibitors, may be ways to precisely deal with inflammation in the future. A potential difficulty in modulating Sptlc2 levels to pharmacologically regulate inflammatory signaling (*140*) arises from targeting Sptlc2 specifically in macrophages. However, this is urgently needed as Sptlc2 and Sptlc2-derived sphinganine were also observed to play a pivotal role in the functions of other immune cells such as CD8+ T cells (*186*) or regulatory T cells (*291*) (Ma *et al.*, 2023; Manuscript submitted for publication). Besides, broad administration of the Sptlc2 inhibitor myriocin was shown to suppress mouse melanoma growth (*292*) and within tumor cells, LPS-TLR4-MyD88-NF-κB signaling was observed to increase B16-F10 viability (*293*). Therefore, in the future, maybe specific cellular macrophage backpacks, as previously described (*294*), could be loaded with Sptlc2-targeting drugs to ensure target cell specificity. In short, the results of my work are in line with the literature suggesting that modulation of sphingolipid metabolism can ameliorate LPS-induced inflammation, and my findings provide concrete molecular targets for this.

7. Conclusion

Overall, my findings reveal that LPS induces the expression of Sptlc2 and promotes sphingolipid *de novo* synthesis in macrophages (Figure 31). Sphinganine, in turn, bolsters TLR4 signal transduction by physically interacting with TLR4 adaptor proteins and recruiting MyD88 to the cell membrane (Figure 31). My findings suggest that macrophages rewire sphingolipid metabolism in response to LPS stimulation and uncover a molecular link between lipid metabolism and pattern recognition in both physiological and pathological settings.

In addition to the already discussed plans, further experiments might focus on a deeper understanding of *in vivo* sphinganine-driven TLR4 signaling in tumor and septic macrophages. Similar to the *in vitro* part, it has to be confirmed if it is in particular Sptlc2-derived sphinganine that is recruiting adaptor proteins to TLR4 to allow for downstream inflammatory signaling. For this, in *in vivo* rescue experiments, sphinganine and control sphingolipids could be co-administered to *Sptlc2*-deficient mice in sepsis and tumor models, and the M1-like activation status of *Sptlc2*-deficient macrophages could be assessed.

Furthermore, as an initial step for the translation into the human system, human peripheral blood mononuclear cells (PBMC)-derived monocytes can be differentiated into macrophages and polarized to different activation states, and the SPT inhibitor myriocin could be used to assess whether human M1-like macrophage polarization is also driven by Sptlc2-derived sphingolipids. Simultaneously, M1-like TLR4-MyD88-NF-κB-driven cytokine expression and macrophage phenotype could be studied in sepsis or cancer patient biopsies. Differences between mouse and human macrophages, such as the loss of genes such as *Arg1* in human *in vitro* polarized macrophages (*295*) and the translational disconnect between LPS in mouse models and human sepsis involving NF-κB activation (*296*), resulting from the differing responses of humans to LPS (*297-299*), might become further challenges.

A lot more work on modulating sphingolipid metabolism to improve macrophage immune responses is needed, but by identifying sphinganine as a checkpoint involved in macrophage pattern recognition, this work deciphers one more riddle of the enigmatic sphingolipids and adds another foundation to the existing literature to build on to get closer

to unleashing the tremendous potential of pharmacologic sphingolipid modulation to deal with inflammation.

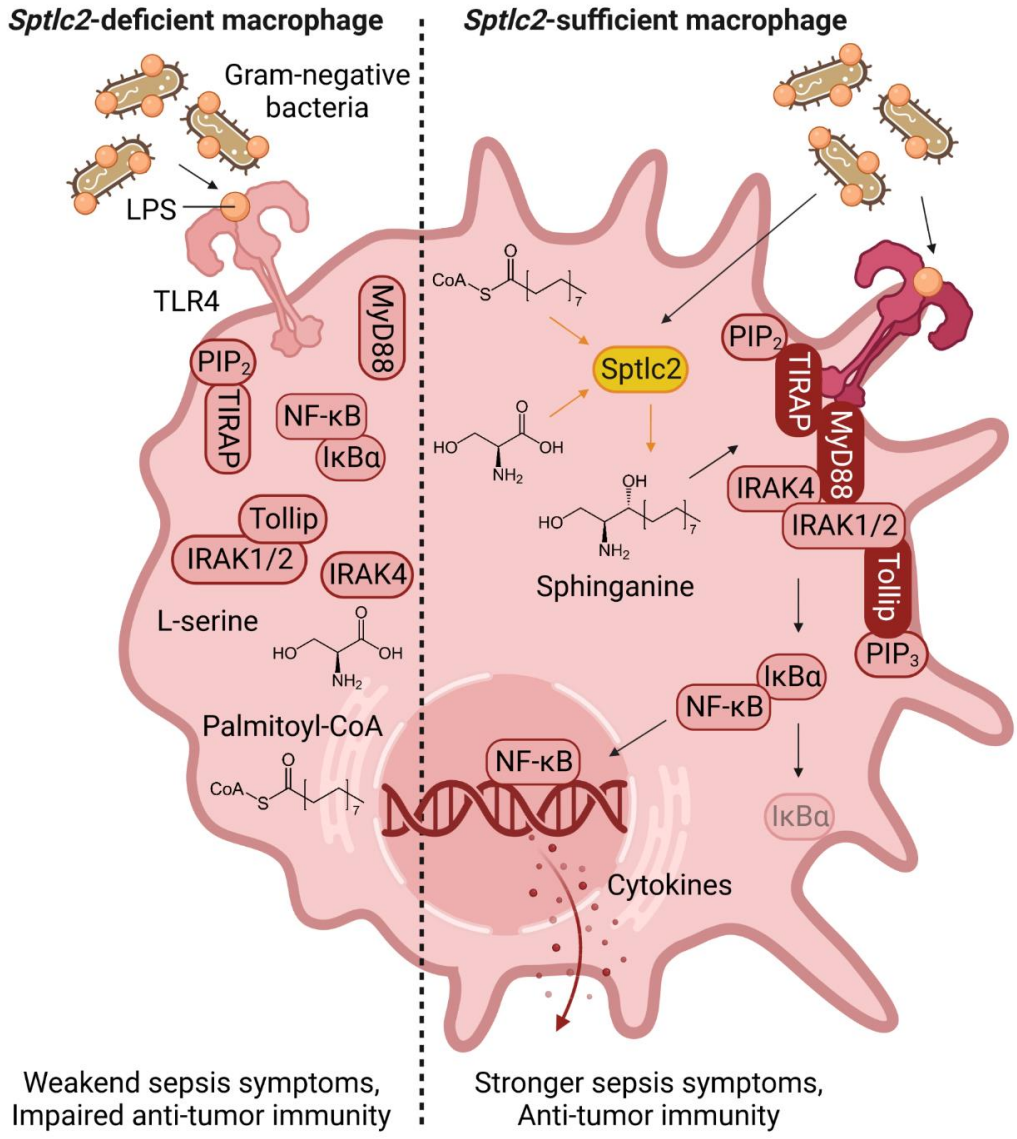

Figure 31 Sptlc2-derived sphinganine allows for the recruitment of the TLR4 adaptor protein MyD88 to TLR4, allowing for NF-κB mediated inflammatory M1-like macrophage signature.

Schematic of the herein-described mechanism of sphingolipid-regulated inflammatory macrophage signaling. On the left, upon LPS recognition, the *Sptlc2*-deficient macrophage is not able to recruit the TLR4 adaptor protein MyD88 to TLR4, resulting in defective NF-κB signaling. On the right, in the WT macrophage, LPS induces Sptlc2-dependent sphinganine production, allowing for sphinganine-driven MyD88 recruitment to TLR4 and downstream NF-κB-mediated inflammatory signaling, which in sepsis and tumor diseases has different outcomes. Figure inspired by (*98*) and included in (*192*).

8. List of publications

- **Hering, M.***, Madi, A., Sandhoff, R., Ma, S., Wu, J., Mieg, A., Richter, K., Mohr, K., ten Bosch, N., Stichling, D., Poschet, G., Umansky, V., Cui, G.*, 2023, *Sphinganine membrane-anchors TLR4 adaptors in macrophages to promote inflammation, Manuscript submitted for publication*

- Weisshaar, N., Madi, A., Mieg, A., Ma, S., Ming, Y., **Hering, M.**, Zettl, F., Mohr, K., ten Bosch, N., Stichling, D., Buettner, M., Poschet, G., Klinke, G., Schulz, M., Kunze-Rohrbach, N., Kerber, C., Klein, I.-M., Wu, J.*, Wang, X.*, Cui, G.*, 2023, *The Malate Shuttle Detoxifies Ammonia and Enhances Antiviral CD8+ T Cell Responses, Manuscript submitted for publication*

- Ma, S.*, Sandhoff, R., Luo, X., Shang, F., Li, Z., Wu, J., Schwarz, F., Ming, Y., Madi, A., Weisshaar, N., Mieg, A., Mohr, K., ten Bosch, N., Li, Z., **Hering, M.**, Poschet, G., Buettner, M., Rodewald, H.-R., Wang, X.*, Gao, P.*, Cui, G.*, 2023, *Serine enrichment in tumors promotes regulatory T cell-mediated immunosuppression through sphinganine*, *Manuscript submitted for publication*

- Madi, A.*, Weisshaar, N., Buettner, M., Poschet, G., Ma, S., Wu , J., Mieg, A., **Hering, M.**, Ming, Y., Mohr, K., Ten Bosch, N., Cui, G.*, 2022, *CD8 agonism functionally activates memory T cells and enhances antitumor immunity,* International Journal of Cancer, 1-12

- Madi, A.*, Wu, J., Ma, S., Weisshaar, N., Mieg, A., **Hering, M.**, Ming, Y., Zettl, F., Mohr, K., Ten Bosch, N., Schlimbach, T., Hertel, F., Cui, G.*, 2022, *Regulatory T cell-derived interleukin-15 promotes the diversity of immunological memory,* European Journal of Immunology, 1-7

- Weisshaar, N., Wu, J., Ming, Y., Madi, A., Hotz-Wagenblatt, A., Ma, S., Mieg, A., **Hering, M.**, Zettl, F., Mohr, K., Schlimbach, T., Ten Bosch, N., Hertel, F., Müller, L., Byren, H., Wang, M., Borgers, H., Munz. M., Schmitt, L., van der Hoeven, F., Kloz, U., Carretero, R., Schleußner, N., Jackstadt, R.-F., Hofmann, I., Cui, G.*, 2022, *Rgs16 promotes antitumor CD8+ T cell exhaustion,* Science Immunology, 7 (71), 1-17

- Wu, J., Madi, A., Mieg, A., Hotz-Wagenblatt, A., Weisshaar, N., Ma, S., Mohr, K., Schlimbach, T., **Hering, M.**, Borgers, H., Cui, G.*, 2020, *T Cell Factor 1 Suppresses CD103+ lung tissue-resident memory T cell development,* Cell Reports, 31 (1), 1-15

- Wu, J., Weisshaar, N., Hotz-Wagenblatt, A., Madi, A., Ma, S., Mieg, A., **Hering, M.**, Mohr, K., Schlimbach, T., Borgers, H., Cui, G.*, 2020, *Skeletal muscle antagonizes CD8+ T cell exhaustion,* Science Advances, 6 (24), 1-11

*Corresponding Author

9. List of abbreviations

°C (unit)	Centigrade
µg (unit)	Microgram
µL (unit)	Microliter
µM (unit)	Micromolar
µm (unit)	Mikrometer
2-DG	2-Deoxy-D-glucose
3-KDS	3-ketosphinganine
A	Adenosine
AA	Antimycin A
ACK	Ammonium-chloride-potassium
ADP	Adenosine diphosphate
AF	Alexa Fluor
Akt	Protein kinase B
ALS	Amyotrophic lateral sclerosis
Amp	Ampicillin
ANOVA	Analysis of variance
AP-1	Activator protein 1
APC	Allophycocyanin
APS	Ammonium persulfate
Arg-1	Arginase-1
Asah1, 2	N-acylsphingosine amidohydrolase 1, 2
ATM	Adipose-tissue macrophages
ATP	Adenosine triphosphate
AUC	Area under the curve
BCA	Bicinchoninic acid
Bcl-2	B-cell lymphoma 2
BLAST	Basic Local Alignment Search Tool
BLC	B Lymphocyte Chemoattractant
BM	Bone marrow
BMDM	Bone marrow-derived macrophages
bp (unit)	Base pair
BRAF	B rapidly accelerated fibrosarcoma
BS3	Bis(sulfosuccinimidyl)suberat
BSA	Bovine serum albumin
BV	Brilliant violet
C	Cytosine
C5	Complement component 5
CCL1, 2, 11	CC-chemokine ligand 1, 2, 11
CCR2	C-C chemokine receptor type 2
CD11c, 14, 16/32, 163, 206, 279, 28, 3, 38, 69, 8, 4, 86 etc.	Cluster of differentiation 11c, 14, 16/32, 163, 206, 279, 28, 3, 38, 69, 8, 4, 86 etc.
CD45R	Cluster of differentiation 45 receptor
Cdkn2a	Cyclin-dependent kinase inhibitor 2A
Cer	Ceramide
CFM	Confocal fluorescence microscopy
c-Jun	Jun activation domain binding protein
CLP	Cecal ligation and puncture
CMP	Common myeloid progenitor
CO_2	Carbon dioxide
CoA	Coenzyme A
COS	Centre for Organismal Studies
Cpm (unit)	Counts per million

CTLA-4	Cytotoxic T-lymphocyte-associated protein 4
CTV	CellTrace Violet
CXCL12	C-X-C motif chemokine 12
Cy7	Cyanine 7
Da (unit)	Dalton
DAMPs	Damage-associated molecular pattern
DAPI	4′,6-diamidino-2-phenylindole
ddH_20	Double distilled water
DKFZ	Deutsches Krebsforschungszentrum
DMEM	Dulbecco's modified Eagle Medium
DMSO	Dimethyl sulfoxide
DNA	Deoxyribonucleic acid
DPBS	Phosphate-buffered saline
Dr.	Doctor
E	Glutamic acid
E. coli	*Escherichia coli*
ECAR	Extracellular acidification rate
ECL	Enhanced chemiluminescence
EDTA	Ethylenediaminetetraacetic acid
Egr2	Early growth response protein 2
ELISA	Enzyme-linked immunosorbent assay
EMBL	European Molecular Biology Laboratory
ER	Endoplasmic reticulum
Erk	Extracellular signal-regulated kinase
EtOH	Ethanol
EU (unit)	Endotoxin units
F4/80	EGF-like module-containing mucin-like hormone receptor-like 1
FACS	Fluorescence-activated cell sorting
FBS	Fetal bovine serum
FCCP	Carbonyl cyanide 4-(trifluoromethoxy) phenylhydrazone
FDA	Food and Drug Administration
FITC	Fluorescein isothiocyanate
FMO	Fluorescence-minus-one
FoxP3	Forkhead box P3
FSC	Forward scatter
fw	Forward
G	Guanine
g (unit)	Gram
G418	Geneticin
Galc	Galactosylceramidase
GAPDH	Glyceraldehyde 3-phosphate dehydrogenase
Gba	Beta-glucocerebrosidase
G-CSF	Granulocyte colony-stimulating factor
GEO	Gene Expression Omnibus
GFP	Green fluorescent protein
Glu	Glucose
GM1	Monosialotetrahexosylganglioside
GM-CSF	Granulocyte-macrophage colony-stimulating factor
GPCR	G protein-coupled receptor
Grp94	Heat-shock protein 90kDa beta member 1
h (unit)	Hour
H+	Hydrogen ion (proton)
H_2SO_4	Sulfuric acid
H_3PO_4	Phosphoric acid
HBSS	Hanks' balanced salt solution
HCl	Hydrochloric acid
HEK	Human embryonic kidney

HexCer	Hexosylceramides
HMGB1	High-mobility-group-protein B1
HNSCC	Head and neck squamous cell carcinoma
HRP	Horseradish peroxidase
HSAN-1	Hereditary sensory and autonomic neuropathy type 1
HSP90α	Heat-shock protein 90α
I-309	CC-chemokine ligand 1, CCL1
iBAQ	Intensity based absolute quantification
ICAM-1	Intercellular Adhesion Molecule 1
ICI	Immune checkpoint inhibition
ICU	Intensive care unit
IFN-γ	Interferon-gamma
IgG	Immunoglobulin G
IKK	IkappaB kinase
IL-1/2/6/10/12/18/23R etc.	Interleukin-1/2/6/10/12/18/23 receptor etc.
IL-2/6/10/12/18/23 etc.	Interleukin-2/6/10/12/18/23 etc.
IMDM	Iscove's modified Dulbecco's medium
iNOS	Inducible nitric oxide synthase
IP	Immunoprecipitation
IP-10	Interferon gamma-induced protein 10
IRAK1	Interleukin-1 receptor-associated kinase 1
IRES	Internal ribosome entry site
IRF3, 4, 5	Interferon regulatory factor 3, 4, 5
I-TAC	Interferon-inducible T-cell alpha chemoattractant
IκBα	Nuclear factor of kappa light polypeptide gene enhancer in B-cells inhibitor, alpha
Kan	Kanamycin
Kb (unit)	Kilobase
KC	Keratinocyte chemoattractant
kDa (unit)	Kilodalton
KO	Knockout
LAL	Limulus amebocyte lysate
LB	Lysogeny broth
LBP	Lipopolysaccharide (LPS)-binding protein
LC-MS/MS	Liquid chromatography-tandem mass spectrometry
LCMV gp	Lymphocytic choriomeningitis mammarenavirus glycoprotein
LD	Loading dye
Leu (L)	Leucine
LPS	Lipopolysaccharide
LSM	Laser scanning microscope
LTA	Lipoteichoic acid
Ly6C	Lymphocyte antigen 6 complex, locus C1
Ly6G	Lymphocyte antigen 6 complex locus G6D
Lyz2	Lysozyme 2
M (unit)	Molar
MACS	Magnetic-activated cell sorting
MAP	Mitogen-activated protein
MAPK	Mitogen-activated protein kinase
max	Maximum
MCP-5	Monocyte chemotactic protein 5
M-CSF	Macrophage colony-stimulating factor
MD-2	Myeloid differentiation factor 2
MDSC	Myeloid-derived suppressor cells
MEK	Mitogen-activated protein kinase kinase
MFI	Mean fluorescence intensity
mg (unit)	Milligram
$MgCl_2$	Magnesium chloride

MHC	Major histocompatibility complex
MIG	Monokine induced by gamma-interferon
MigR1-GFP	MSCV-IRES-EGFP retroviral construct
Min	Minute
MIP-1	Macrophage inflammatory protein-1
miRNA	MicroRNA
mL (unit)	Milliliter
mM (unit)	Millimolar
mm^3 (unit)	Cubic millimeter
MPLA	Monophosphoryl lipid A
mRNA	Messenger RNA
MSCV	Murine stem cell virus
mTOR	Mechanistic target of rapamycin
MyD88	Myeloid differentiation primary response gene 88
Myris	Myristoylation
NaCl	Sodium chloride
NaN_3	Sodium azide
NaOH	Sodium hydroxide
NdS	Non-hydroxy-fatty acid dihydro-sphingosine
NEAA	Non-essential amino acids
Neo	Neomycin
NF-κB	Nuclear factor k-light-chain-enhancer of activated B cells
ng (unit)	Nanograms
NIH	National Institutes of Health
NK	Natural killer
NO	Nitric oxide
NS	Non-hydroxy-fatty acid sphingosine
OCR	Oxygen consumption rate
OM	Oligomycin
ORF	Open reading frame
Otub1	Ubiquitin thioesterase
P	Phosphate
p44	Mitogen-activated protein kinase 3
PAMPs	Pathogen-associated molecular patterns
PBMC	Peripheral blood mononuclear cells
PBS-T	Phosphate-buffered saline with Tween® 20
PCA	Principal component analysis
PCF	Proteomics Core Facility
pCL-Eco	Eco-helper plasmid
PCR	Polymerase chain reaction
PD-1	Programmed cell death protein 1
PD-L1	Programmed cell death 1 ligand 1
PE	Phycoerythrin
Pen-Strep	Penicillin-streptomycin
PerCP/Cy5.5	Peridinin chlorophyll protein-Cyanine5.5
pH	Potentia hydrogenii
PI3K	Phosphoinositide 3-kinase
PIP_2	Phosphatidylinositol-4,5-bisphosphate
PIP_3	Phosphatidylinositol (3,4,5)-trisphosphate
PMSF	Phenylmethylsulfonyl fluorid
Pro (P)	Proline
Prof.	Professor
PRR	Pattern recognition receptor
PTEN	Phosphatase and tensin homolog
PTSD	Post-traumatic stress disorder
PVDF	Polyvinylidene difluoride

Rantes	Regulated upon Activation, Normal T Cell Expressed and Presumably Secreted
RIPA	Radioimmunoprecipitation assay buffer
RNA	Ribonucleic acid
Rnf2	Ring finger protein 2
ROS	Reactive oxygen species
Rot	Rotenone
Rpm (unit)	Rounds per minute
RPMI	Roswell Park Memorial Institute
rv	Reverse
s.c.	Subcutaneously
S100A8/A9	S100 calcium binding protein A8/A9
S1P	Sphingosine-1-phosphate
S1PR	Sphingosine-1-phosphate receptor
Sa	Sphinganine
Sa-1P	Sphinganine-1-phosphate
Sa-biotin	Sphinganine-biotin
SARS-CoV-2	Severe acute respiratory syndrome coronavirus type 2
SD	Standard deviation
SDF-1	Stromal cell-derived factor 1
SDS	Sodium dodecyl sulfate
SDS-PAGE	Sodium dodecyl sulfate-polyacrylamid gel electrophoresis
SEM	Scanning electron microcopy
Ser536	Serine 536
Sgpp1	Sphingosine-1-phosphate phosphatase 1
SIL	Stable isotope labeled
SM	Sphingomyelin
Smpd1, 2, 3, 4	Sphingomyelin phosphodiesterase 1, 2, 3, 4
So	Sphingosine
So-1P	Sphingosine-1-phosphate
SphK1	Sphingosine kinase 1
Spltc1, 2	Serine palmitoyltransferase long chain base subunit 1, 2
SPT	Serine palmitoyltransferase
SRC	Spare respiratory capacity
SSC	Side scatter
STAT1, 3, 6	Signal transducer and activator of transcription 1, 3, 6
SUMO	Small ubiquitin-related modifier
SUNY	State University of New York
T	Thymidine
TABs	TAK1-binding proteins
TAE	TRIS-Acetat-EDTA-buffer
TAK1	Mitogen-activated protein kinase kinase kinase 7
TAMs	Tumor-associated macrophages
TANs	Tumor-associated neutrophils
Taq	Thermus aquaticus
TARC	Thymus- and activation-regulated chemokine
TAT-cre	Trans-activator of transcription-cre
TBK1	TANK-binding kinase 1
TCA	Tricarboxylic acid cycle
TEMED	Tetramethylethylenediamine
TGFβ	Transforming growth factor beta
Th1, 2	T helper cell type 1, 2
Th17	T helper 17 cells
TIGIT	T cell immunoreceptor with immunoglobulin and ITIM domain
TILs	Tumor-infiltrating leucocytes
TIMP-1	Tissue inhibitor of metalloproteinases
TIR	Toll-interleukin-1 receptor

TIRAP	Toll/interleukin-1 receptor domain containing adaptor protein
TLR2, 3, 4, etc.	Toll-like receptor 2, 3, 4, etc.
TME	Tumor microenvironment
TNFα	Tumor necrosis factor α
Tollip	Toll interacting protein
TRAF2, 3, 6 etc.	TNF receptor-associated factor 2, 3, 6 etc.
Treg cell	Regulatory T cell
TREM-1	Triggering receptor expressed on myeloid cells 1
TRIF	TIR-domain-containing adaptor-inducing interferon-β
Tris	Tris(hydroxymethyl)aminomethane
T-vecs	Talimogen laherparepvec
Tyr701	Tyrosine 701
UBE2Z	Ubiquitin conjugating enzyme E2 Z
Ubr5	Ubiquitin protein ligase E3 component n-recognin 5
Uchl5	Ubiquitin carboxyl-terminal hydrolase isozyme L5
UMM	University Medical Center Mannheim
USA	United States of America
UV	Ultraviolet
V	Valine
V (unit)	Volt
v (unit)	Volume
VEGF	Vascular endothelial growth factor
w (unit)	Weight
WB	Western blot
WT	Wildtype
XF	Extracellular flux
YUMMER1.7	Yale university mouse melanoma exposed to radiation
ZEN	ZEISS efficient navigation
α-	Anti-

10. Supplementary

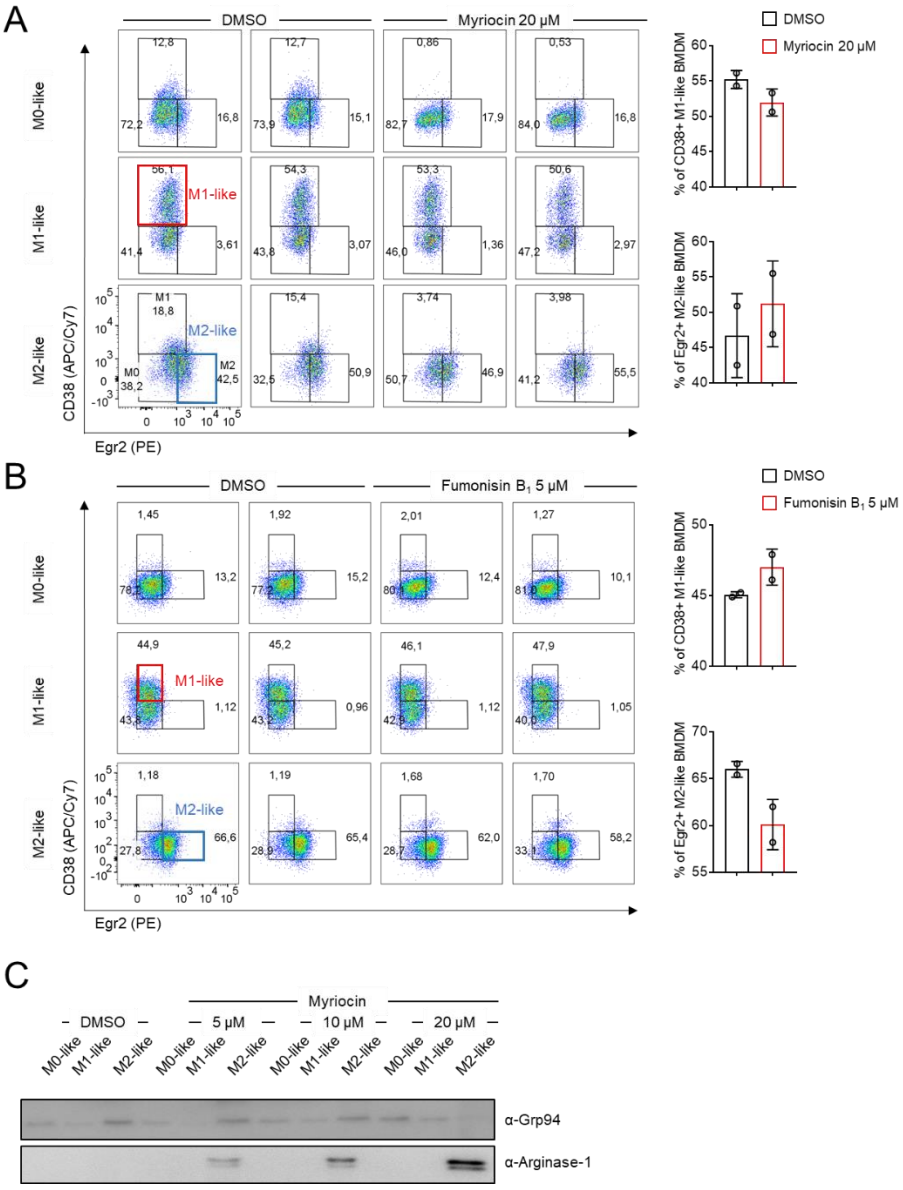

Figure 32 ***In vitro*** **loss-of-function and gain-of-function models mimicking Sptlc2 inhibition and activation change the M1-like/M2-like BMDM ratio.**

Data are re-analyzed from Hering, M.; 2020; To study the role of sphingolipids in macrophage polarization; Master's thesis (170).

(A-B) Flow cytometry dot plots and bar graphs show percentages of CD38+ M1-like and Egr2+ M2-like BMDM after DMSO, myriocin (Sptlc2 inhibitor; in A), or fumonisin B_1 (ceramide synthase inhibitor; in B) treatment (N=2).

(C) Immunoblots show M2-like macrophage marker Arginase-1 expression in M0-like, M1-like, and M2-like WT BMDM after DMSO and 5 µM, 10 µM, and 20 µM myriocin treatment. Grp94 was used as a loading control.

Table 28 Related to Figure 18B. List of proteins pulled down more or only by sphinganine-biotin (40 kDa to 45 kDa)

Shown are proteins pulled down more or only by sphinganine-biotin (sa-b.) compared to control biotin (ctrl b.). Sequence spectral matches (Ssm) correspond to counts of the number of peptides identified as belonging to the protein and sequence coverage in percent of the sequence coverage of the protein. In collaboration with the Proteomics Core Facility (PCF), European Molecular Biology Laboratory (EMBL), Heidelberg, Germany.

Gene name	**Description**	**Ssm**		**Sequence coverage in %**	
Selected proteins pulled down more by sphinganine-biotin		sa-b.	ctrl b.	sa-b.	ctrl b.
Actb	B2RRX1_MOUSE Actin, beta	1163	488	80.6	71.3
Actb	ACTB_MOUSE Actin, cytoplasmic 1	1163	488	80.6	71.3
Actg1	ACTG_MOUSE Actin, cytoplasmic 2	1070	478	80.3	71
Actg1	Q4KL81_MOUSE Actin, cytoplasmic 2	1070	478	80.3	71
Actc1	ACTC_MOUSE Actin, alpha cardiac muscle 1	785	368	41.8	39.4
Acta1	ACTS_MOUSE Actin, alpha skeletal muscle	785	368	41.8	39.4
Actc1	Q497E4_MOUSE Actin, alpha cardiac muscle 1	785	368	41.8	39.4
Only after sphinganine-biotin pulldown					
Actbl2	ACTBL_MOUSE Beta-actin-like protein 2		313		31.8
Gm17087	V9GXQ2_MOUSE Protein Gm17087		99		14.6
Abhd12	ABD12_MOUSE Monoacylglycerol lipase ABHD12		21		20.1
Ap3m1	AP3M1_MOUSE AP-3 complex subunit mu-1		11		21
Rpl3	RL3_MOUSE 60S ribosomal protein L3		7		15.8
Ncl	NUCL_MOUSE Nucleolin		5		6.8
Ctsb	CATB_MOUSE Cathepsin B		5		10.3
Sucla2	SUCB1_MOUSE Succinyl-CoA ligase [ADP-forming] subunit beta, mitochondrial		5		10.8
Erlin2	ERLN2_MOUSE Erlin-2		4		9.1
Trim14	TRI14_MOUSE Tripartite motif-containing protein 14		3		7.3
Ist1	IST1_MOUSE IST1 homolog		3		6.6
Pa2g4	D3YVH7_MOUSE Proliferation-associated protein 2G4 (Fragment)		3		6.2
Gnai2	GNAI2_MOUSE Guanine nucleotide-binding protein G(i) subunit alpha-2		2		7.3
Igtp	Q9DCE9_MOUSE Protein Igtp		2		5.9

Table 29 Related to Figure 18B. List of proteins pulled down by sphinganine-biotin (25 kDa to 42 kDa)

Shown are proteins pulled down by sphinganine-biotin but not by control biotin. Sequence spectral matches (Ssm) correspond to counts of the number of peptides identified as belonging to the protein and sequence coverage in percent of the sequence coverage of the protein. In collaboration with the Proteomics Core Facility (PCF), European Molecular Biology Laboratory (EMBL), Heidelberg, Germany.

Gene name	Description	Ssm	Sequence coverage in %
Tube 1 (gel area from ~40 kDa to ~42 kDa)			
Ncl	NUCL_MOUSE Nucleolin	17	22
Krt83	E9Q1Y9_MOUSE Keratin, type II cuticular Hb3	16	23.1
Krt85	KRT85_MOUSE Keratin, type II cuticular Hb5	15	20.1
Csnk2a1	CSK21_MOUSE Casein kinase II subunit alpha	14	30.9
Tmod3	TMOD3_MOUSE Tropomodulin-3	11	29.7
Pdcl	PHLP_MOUSE Phosducin-like protein	9	26.5
Bub3	BUB3_MOUSE Mitotic checkpoint protein BUB3	9	22.6
Pcyt1a	PCY1A_MOUSE Choline-phosphate cytidylyltransferase A	7	21.7
Eif3c	EIF3C_MOUSE Eukaryotic translation initiation factor 3 subunit C	7	9
Drg2	DRG2_MOUSE Developmentally-regulated GTP-binding protein 2	7	14.2
Krt36	KRT36_MOUSE Keratin, type I cuticular Ha6	6	15.4
Ube2z	UBE2Z_MOUSE Ubiquitin-conjugating enzyme E2 Z	6	19
Lrrc58	LRC58_MOUSE Leucine-rich repeat-containing protein 58	6	19.9
FAM120A	F120A_MOUSE Constitutive coactivator of PPAR-gamma-like protein 1	6	6.8
Eif3m	EIF3M_MOUSE Eukaryotic translation initiation factor 3 subunit M	6	13.6
Svs1	Q6WIZ7_MOUSE Amine oxidase	5	7.4
Tmem43	TMM43_MOUSE Transmembrane protein 43	5	13
Ahnak	E9Q616_MOUSE Protein Ahnak	4	1
Anp32a	AN32A_MOUSE Acidic leucine-rich nuclear phosphoprotein 32 family member A	4	14.9
Dcaf7	DCAF7_MOUSE DDB1- and CUL4-associated factor 7	4	13.1

Eif2ak2	E2AK2_MOUSE Interferon-induced, double-stranded RNA-activated protein kinase	4	7.2
Bst2	BST2_MOUSE Bone marrow stromal antigen 2	4	17.3
Mrps22	RT22_MOUSE 28S ribosomal protein S22, mitochondrial	4	13.1
Galk1	GALK1_MOUSE Galactokinase	4	9.4
Oas1a	OAS1A_MOUSE 2'-5'-oligoadenylate synthase 1A	3	13.9
Tha1	Q6XPS7_MOUSE L-threonine aldolase	3	11.7
Rbm14	RBM14_MOUSE RNA-binding protein 14	3	4.6
Snx2	SNX2_MOUSE Sorting nexin-2	3	7.7
Dnajb12	DJB12_MOUSE DnaJ homolog subfamily B member 12	3	9.3
Gyg1	GLYG_MOUSE Glycogenin-1	3	12.6
Gm17087	V9GXQ2_MOUSE Protein Gm17087	3	14.6
Hbb-b1	HBB1_MOUSE Hemoglobin subunit beta-1	2	15.5
Gtf2f1	T2FA_MOUSE General transcription factor IIF subunit 1	2	3.7
Ptpn7	PTN7_MOUSE Tyrosine-protein phosphatase non-receptor type 7	2	6.7
Rae1	RAE1L_MOUSE mRNA export factor	2	6.5
Eif3b	EIF3B_MOUSE Eukaryotic translation initiation factor 3 subunit B	2	4.5
Paf1	PAF1_MOUSE RNA polymerase II-associated factor 1 homolog	2	5.2
Dr1	NC2B_MOUSE Protein Dr1	1	7.9
Krt6a	K2C6A_MOUSE Keratin, type II cytoskeletal 6A	24	22.2
Krt31	K1H1_MOUSE Keratin, type I cuticular Ha1	14	16.3
Nucks1	A0A087WRY3_MOUSE Nuclear ubiquitous casein and cyclin-dependent kinase substrate 1	12	30.8
Krt35	KRT35_MOUSE Keratin, type I cuticular Ha5	11	14.7
Fcho2	F6RG68_MOUSE F-BAR domain only protein 2	8	8.3
Tial1	TIAR_MOUSE Nucleolysin TIAR	8	16
Tcof1	H3BL37_MOUSE Treacle protein	7	9.1
Osbpl8	A0A0R4J150_MOUSE Oxysterol-binding protein	5	8.3
Bin2	BIN2_MOUSE Bridging integrator 2	5	10.6
Srsf5	SRSF5_MOUSE Serine/arginine-rich splicing factor 5	5	18.1
Stk24	Q3U335_MOUSE Mammalian sterile twenty 3 kinase	5	12.7

Srsf1	H7BX95_MOUSE Serine/arginine-rich-splicing factor 1	4	15.4
Hsp90b1	ENPL_MOUSE Endoplasmin	4	6.1
Dnaja3	DNJA3_MOUSE DnaJ homolog subfamily A member 3, mitochondrial	4	8.5
Hist2h2aa1	B2RWH3_MOUSE Histone H2A	3	26.7
Hist1h2al	F8WIX8_MOUSE Histone H2A	3	27.8
Hist2h2ac	Q149V4_MOUSE Histone H2A	3	26.9
Hist1h2aa	Q8CGP4_MOUSE Histone H2A	3	26.9
Myl1	E9PWG4_MOUSE Myosin light chain 1/3, skeletal muscle isoform	3	22.8
Nmi	NMI_MOUSE N-myc-interactor	3	13.3
Hnrnph1	HNRH1_MOUSE Heterogeneous nuclear ribonucleoprotein H	3	7.3
Cops3	CSN3_MOUSE COP9 signalosome complex subunit 3	3	10.6
Rfc3	Q3TKD1_MOUSE MCG17786, isoform CRA_a	3	11.2
Rnf2	A0A087WQQ3_MOUSE E3 ubiquitin-protein ligase RING2 (Fragment)	2	23
Eno2	A0A0N4SUI6_MOUSE Gamma-enolase (Fragment)	2	52.5
Tube 3 (gel area from ~38 kDa to ~40 kDa)			
Hnrnpdl	HNRDL_MOUSE Heterogeneous nuclear ribonucleoprotein D-like	20	43.7
Caprin1	CAPR1_MOUSE Caprin-1	11	17.5
Ppp1ca	PP1A_MOUSE Serine/threonine-protein phosphatase PP1-alpha catalytic subunit	10	23.9
Ppp1cb	PP1B_MOUSE Serine/threonine-protein phosphatase PP1-beta catalytic subunit	10	27.7
Atp6v0d2	VA0D2_MOUSE V-type proton ATPase subunit d 2	10	20.8
Med4	MED4_MOUSE Mediator of RNA polymerase II transcription subunit 4	10	31.4
Pdia3	PDIA3_MOUSE Protein disulfide-isomerase A3	9	15.8
Akr1b8	ALD2_MOUSE Aldose reductase-related protein 2	9	24.9
Twf1	TWF1_MOUSE Twinfilin-1	9	27.6
Ppp1cc	PP1G_MOUSE Isoform Gamma-2 of Serine/threonine-protein phosphatase PP1-gamma catalytic subunit	8	23.4
Dek	DEK_MOUSE Protein DEK	8	16.3
Abhd12	ABD12_MOUSE Monoacylglycerol lipase ABHD12	8	13.3

Mrps9	RT09_MOUSE 28S ribosomal protein S9, mitochondrial	8	20.5
Wdr5	WDR5_MOUSE WD repeat-containing protein 5	7	27.8
Ncf4	NCF4_MOUSE Neutrophil cytosol factor 4	7	25.9
Cab39	CAB39_MOUSE Calcium-binding protein 39	7	18.7
Pih1d1	PIHD1_MOUSE PIH1 domain-containing protein 1	7	27.1
Iqgap1	IQGA1_MOUSE Ras GTPase-activating-like protein IQGAP1	7	4
Mrpl39	RM39_MOUSE 39S ribosomal protein L39, mitochondrial	7	22
Mcl1	MCL1_MOUSE Induced myeloid leukemia cell differentiation protein Mcl-1 homolog	6	22.9
Eif5b	IF2P_MOUSE Eukaryotic translation initiation factor 5B	6	6.4
Lcp1	PLSL_MOUSE Plastin-2	6	10.4
Ifit1	IFIT1_MOUSE Interferon-induced protein with tetratricopeptide repeats 1	6	15.5
Rwdd1	RWDD1_MOUSE RWD domain-containing protein 1	6	17.2
Lztfl1	LZTL1_MOUSE Leucine zipper transcription factor-like protein 1	6	22
GSN	GELS_BOVIN Gelsolin	5	8.7
Emd	EMD_MOUSE Emerin	5	18.5
Eif3d	EIF3D_MOUSE Eukaryotic translation initiation factor 3 subunit D	5	7.5
Msn	MOES_MOUSE Moesin	5	8.7
Pdia6	Q3TML0_MOUSE Protein disulfide-isomerase A6	5	12.6
Snrnp40	SNR40_MOUSE U5 small nuclear ribonucleoprotein 40 kDa protein	5	16.7
Armcx3	ARMX3_MOUSE Armadillo repeat-containing X-linked protein 3	5	19.5
Mmaa	MMAA_MOUSE Methylmalonic aciduria type A homolog, mitochondrial	5	10.6
Eif3l	EIF3L_MOUSE Eukaryotic translation initiation factor 3 subunit L	5	11.2
Eif3f	EIF3F_MOUSE Eukaryotic translation initiation factor 3 subunit F	5	18.5
Mecr	MECR_MOUSE Trans-2-enoyl-CoA reductase, mitochondrial	5	18.2

Ap3b1	AP3B1_MOUSE AP-3 complex subunit beta-1	5	5.8
Ly9	LY9_MOUSE T-lymphocyte surface antigen Ly-9	4	9.2
Fam76b	FA76B_MOUSE Protein FAM76B	4	11.2
Pcid2	PCID2_MOUSE PCI domain-containing protein 2	4	7.5
Wasf2	WASF2_MOUSE Wiskott-Aldrich syndrome protein family member 2	4	9.2
Rassf2	RASF2_MOUSE Ras association domain-containing protein 2	4	15.3
Hibch	HIBCH_MOUSE 3-hydroxyisobutyryl-CoA hydrolase, mitochondrial	4	10.9
Aimp2	AIMP2_MOUSE Aminoacyl tRNA synthase complex-interacting multifunctional protein 2	4	11.5
Bccip	BCCIP_MOUSE BRCA2 and CDKN1A-interacting protein	4	12.9
Prkar1a	KAP0_MOUSE cAMP-dependent protein kinase type I-alpha regulatory subunit	4	15.2
Itpkb	B2RXC2_MOUSE Inositol 1,4,5-trisphosphate 3-kinase B	3	4
Glyr1	D3YYT1_MOUSE Putative oxidoreductase GLYR1	3	7.4
Ddost	OST48_MOUSE Dolichyl-diphosphooligosaccharide--protein glycosyltransferase 48 kDa subunit	3	7.7
Cfdp1	CFDP1_MOUSE Craniofacial development protein 1	3	12.2
Mpo	PERM_MOUSE Myeloperoxidase	3	4.9
Hhex	HHEX_MOUSE Hematopoietically-expressed homeobox protein Hhex	3	16.2
Cryz	QOR_MOUSE Quinone oxidoreductase	3	12
Msh6	MSH6_MOUSE DNA mismatch repair protein Msh6	3	2.8
Mafb	MAFB_MOUSE Transcription factor MafB	3	9.9
Kcnab1	KCAB1_MOUSE Voltage-gated potassium channel subunit beta-1	3	10
Pml	PML_MOUSE Protein PML	3	4
Ifit2	Q6GTM0_MOUSE Ifit2 protein	3	8.3
Pdcd11	RRP5_MOUSE Protein RRP5 homolog	3	1.5
Mcat	FABD_MOUSE Malonyl-CoA-acyl carrier protein transacylase, mitochondrial	3	9.7
Sec63	SEC63_MOUSE Translocation protein SEC63 homolog	3	5.5

Oasl1	OASL1_MOUSE 2'-5'-oligoadenylate synthase-like protein 1	3	8.8
B3galt6	B3GT6_MOUSE Beta-1,3-galactosyltransferase 6	3	10.7
Sfxn1	SFXN1_MOUSE Sideroflexin-1	3	10.5
Rtcb	RTCB_MOUSE tRNA-splicing ligase RtcB homolog	3	7.5
Dhrs7	DHRS7_MOUSE Dehydrogenase/reductase SDR family member 7	3	9.7
Srfbp1	SRFB1_MOUSE Serum response factor-binding protein 1	3	9.3
Cs	CISY_MOUSE Citrate synthase, mitochondrial	3	7.3
Rrp7a	RRP7A_MOUSE Ribosomal RNA-processing protein 7 homolog A	3	19.2
Cab39l	CB39L_MOUSE Calcium-binding protein 39-like	3	9.5
Ldhb	LDHB_MOUSE L-lactate dehydrogenase B chain	2	5.4
Ncbp3	NCBP3_MOUSE Nuclear cap-binding protein subunit 3	2	4.2
Klf13	KLF13_MOUSE Krueppel-like factor 13	2	12.4
Fam192a	F192A_MOUSE Protein FAM192A	1	5.9
Kcnab2	E0CXZ9_MOUSE Voltage-gated potassium channel subunit beta-2	15	30.8
Adprh	ADPRH_MOUSE [Protein ADP-ribosylarginine] hydrolase	12	23.1
Eif3e	EIF3E_MOUSE Eukaryotic translation initiation factor 3 subunit E	11	20
Vps26a	VP26A_MOUSE Vacuolar protein sorting-associated protein 26A	10	29.6
Gm9755	D3YVN7_MOUSE Elongation factor Tu	9	21.2
Tufm	EFTU_MOUSE Elongation factor Tu, mitochondrial	9	21.2
Csnk2a2	CSK22_MOUSE Casein kinase II subunit alpha'	9	29.3
Ppm1g	A0A0J9YVG0_MOUSE Protein phosphatase 1G	8	18.6
Gsn	GELS_MOUSE Gelsolin	8	12.7
Puf60	PUF60_MOUSE Isoform 2 of Poly(U)-binding-splicing factor PUF60	8	11.7
Tubb6	Q3UMM1_MOUSE Tubulin beta-6 chain	8	12.9
Ilf3	Q45VK5_MOUSE Interleukin enhancer-binding factor 3	8	10.2
2210016L21Rik	A0A0R4J099_MOUSE Protein 2210016L21Rik	7	33.5
Raly	A2AU62_MOUSE RNA-binding protein Raly (Fragment)	7	42.1

Hnrnpk	B2M1R6_MOUSE Heterogeneous nuclear ribonucleoprotein K	7	13.8
Hnrnph3	D3YWT1_MOUSE MCG11326, isoform CRA_b	7	23.8
Htra2	D3YX27_MOUSE Serine protease HTRA2, mitochondrial	7	21.8
Rps3	RS3_MOUSE 40S ribosomal protein S3	7	22.1
Nagk	Q3U2G9_MOUSE N-acetyl-D-glucosamine kinase	7	20.9
Srrt	SRRT_MOUSE Serrate RNA effector molecule homolog	7	6.5
Pik3ap1	BCAP_MOUSE Phosphoinositide 3-kinase adaptor protein 1	7	10
Pdia4	A0A0R4J0Z1_MOUSE Protein disulfide-isomerase A4	6	10.1
Smarca4	A0A0R4J170_MOUSE Transcription activator BRG1	6	3.3
Rpl5	RL5_MOUSE 60S ribosomal protein L5	6	18.1
Ssrp1	SSRP1_MOUSE FACT complex subunit SSRP1	6	8.9
Tmpo	LAP2B_MOUSE Lamina-associated polypeptide 2, isoforms beta/delta/epsilon/gamma	6	21
Ddx5	DDX5_MOUSE Probable ATP-dependent RNA helicase DDX5	6	9.6
Cryl1	A7VMV2_MOUSE Crystallin, lamda 1, isoform CRA_a	5	17.5
Gas7	B1ATI9_MOUSE Growth arrest-specific protein 7	5	11.6
Akr1b7	ALD1_MOUSE Aldose reductase-related protein 1	5	11.4
Ybx1	YBOX1_MOUSE Nuclease-sensitive element-binding protein 1	5	28.8
Tmem173	STING_MOUSE Stimulator of interferon genes protein	5	12.1
Fam45a	Q3TH34_MOUSE Protein FAM45A	5	14.3
Ddx17	Q3U741_MOUSE DEAD (Asp-Glu-Ala-Asp) box polypeptide 17, isoform CRA_a	5	7
Rfc4	Q3UI84_MOUSE Replication factor C subunit 4	5	13.5
Actr3	Q3ULF7_MOUSE Actin-related protein 3	5	10
Hdgfrp2	HDGR2_MOUSE Hepatoma-derived growth factor-related protein 2	5	6.7
Fdps	Q4FJN9_MOUSE Farnesyl pyrophosphate synthase	5	16.1
Eif3g	Q544H0_MOUSE Eukaryotic translation initiation factor 3 subunit G	5	18.1
Brd2	BRD2_MOUSE Bromodomain-containing protein 2	5	7.3

Camk1d	KCC1D_MOUSE Calcium/calmodulin-dependent protein kinase type 1D	5	13.2
Kxd1	E9Q4P0_MOUSE KxDL motif-containing protein 1 (Fragment)	4	19.6
Fam21	A0A0N4SV74_MOUSE WASH complex subunit FAM21 (Fragment)	4	4.7
Acad8	A0A0R4J0P1_MOUSE Acyl-Coenzyme A dehydrogenase family, member 8	4	13
Sirt2	A0A140LHL5_MOUSE NAD-dependent protein deacetylase sirtuin-2	4	15.9
Cdk11b	A2A9P6_MOUSE Cyclin-dependent kinase 11B	4	4.5
Eftud2	A2AH85_MOUSE 116 kDa U5 small nuclear ribonucleoprotein component	4	4.2
Lgmn	A2RTI3_MOUSE Legumain	4	6
Stk25	D3Z359_MOUSE Serine/threonine-protein kinase 25 (Fragment)	4	22.1
Ifit3b	E9PV48_MOUSE Protein Ifit3b	4	8.4
Ifit3	Q5FW82_MOUSE Interferon-induced protein with tetratricopeptide repeats 3	4	8.4
Sash1	F8VQK5_MOUSE SAM and SH3 domain-containing protein 1	4	4.5
Arhgef2	H3BJ40_MOUSE Rho guanine nucleotide exchange factor 2	4	6.3
Cebpb	CEBPB_MOUSE CCAAT/enhancer-binding protein beta	4	17.5
Rps6	RS6_MOUSE 40S ribosomal protein S6	4	16.4
Anp32e	AN32E_MOUSE Acidic leucine-rich nuclear phosphoprotein 32 family member E	4	12.6
Cdk6	Q0VBK8_MOUSE Cyclin-dependent kinase 6	4	14.1
U2af1	Q14C24_MOUSE MCG14259, isoform CRA_a	4	12.5
Eci2	Q3TCD4_MOUSE Enoyl-CoA delta isomerase 2, mitochondrial	4	13.2
Fam175b	F175B_MOUSE BRISC complex subunit Abro1	4	10.6
Hp1bp3	HP1B3_MOUSE Heterochromatin protein 1-binding protein 3	4	8.5
Vps35	Q3TRJ1_MOUSE Vacuolar protein sorting 35, isoform CRA_a	4	6.8

Rfc5	Q5HZI8_MOUSE MCG8761	4	16.2
Btf3	BTF3_MOUSE Transcription factor BTF3	4	19
Pcyt1b	PCY1B_MOUSE Choline-phosphate cytidylyltransferase B	4	13.8
Sfxn3	SFXN3_MOUSE Sideroflexin-3	4	16.5
Ppp1r12a	MYPT1_MOUSE Protein phosphatase 1 regulatory subunit 12A	4	5.6
Uchl5	UCHL5_MOUSE Ubiquitin carboxyl-terminal hydrolase isozyme L5	4	13.6
Ldah	A0A0F6AIX5_MOUSE Lipid droplet-associated hydrolase	3	9.5
Rab11fip5	A0A0N4SW73_MOUSE Rab11 family-interacting protein 5	3	3.2
Smarca2	A0A140LID0_MOUSE Probable global transcription activator SNF2L2 (Fragment)	3	12.3
Hnrnpr	A2AW41_MOUSE Protein Hnrnpr (Fragment)	3	11.4
Crkl	A2RS58_MOUSE Crk-like protein	3	13.5
Flna	B7FAU9_MOUSE Filamin, alpha	3	2
Scamp3	E9Q855_MOUSE Secretory carrier-associated membrane protein 3	3	12.3
Fus	G3UXT7_MOUSE RNA-binding protein FUS (Fragment)	3	29.8
Ppp6r3	G5E8R4_MOUSE SAPS domain family, member 3, isoform CRA_c	3	3.7
Slc25a5	ADT2_MOUSE ADP/ATP translocase 2	3	10.7
Scamp2	Q3TAL2_MOUSE Secretory carrier membrane protein 2	3	10.3
Tor1a	Q3TV62_MOUSE Torsin family 1, member A (Torsin A), isoform CRA_a	3	10.2
Gpd1l	GPD1L_MOUSE Glycerol-3-phosphate dehydrogenase 1-like protein	3	10.5
Eef1g	Q4FZK2_MOUSE Elongation factor 1-gamma	3	8.2
Srrm2	SRRM2_MOUSE Serine/arginine repetitive matrix protein 2	3	1.7
Arhgap25	RHG25_MOUSE Rho GTPase-activating protein 25	3	8.2
Rp2	XRP2_MOUSE Protein XRP2	3	8.9

Ankrd17	A0A0G2JDZ9_MOUSE Ankyrin repeat domain-containing protein 17	2	1.2
Ubr5	E9Q2H1_MOUSE E3 ubiquitin-protein ligase UBR5	2	1.1
Sdcbp	H3BLG5_MOUSE Syntenin-1 (Fragment)	2	12.8
Luc7l3	LC7L3_MOUSE Luc7-like protein 3	2	7.4
Tube 5 (gel area from ~35 to ~38kDa)			
Dhrs1	DHRS1_MOUSE Dehydrogenase/reductase SDR family member 1	14	41.4
Trex1	TREX1_MOUSE Three-prime repair exonuclease 1	12	39.4
37316	MARC2_MOUSE Mitochondrial amidoxime reducing component 2	11	26.5
Polr2c	Q99M46_MOUSE DNA-directed RNA polymerase II subunit RPB3	11	42
Cope	COPE_MOUSE Coatomer subunit epsilon	10	34
Napa	SNAA_MOUSE Alpha-soluble NSF attachment protein	10	32.4
Wash1	WASH1_MOUSE WAS protein family homolog 1	8	10.9
Pdhb	ODPB_MOUSE Pyruvate dehydrogenase E1 component subunit beta, mitochondrial	8	25
Fam49b	FA49B_MOUSE Protein FAM49B	7	16.9
Fbl	FBRL_MOUSE rRNA 2'-O-methyltransferase fibrillarin	6	19.8
Srsf2	SRSF2_MOUSE Serine/arginine-rich splicing factor 2	6	21.6
Fam49a	FA49A_MOUSE Protein FAM49A	5	11.1
Ptgr1	PTGR1_MOUSE Prostaglandin reductase 1	5	16.4
Pstpip2	PPIP2_MOUSE Proline-serine-threonine phosphatase-interacting protein 2	5	16.1
Blvra	BIEA_MOUSE Biliverdin reductase A	5	23
Acbd6	ACBD6_MOUSE Acyl-CoA-binding domain-containing protein 6	5	17
Stub1	CHIP_MOUSE STIP1 homology and U box-containing protein 1	5	18.7
Psmd14	PSDE_MOUSE 26S proteasome non-ATPase regulatory subunit 14	4	11.6
Cops5	CSN5_MOUSE COP9 signalosome complex subunit 5	4	12.8
Hcls1	HCLS1_MOUSE Hematopoietic lineage cell-specific protein	4	9.9
Elavl1	ELAV1_MOUSE ELAV-like protein 1	4	13.1

Aida	AIDA_MOUSE Axin interactor, dorsalization-associated protein	4	15
Arpc2	ARPC2_MOUSE Actin-related protein 2/3 complex subunit 2	4	11.3
Nudt5	NUDT5_MOUSE ADP-sugar pyrophosphatase	4	21.9
Snx20	A0A0R4J0D0_MOUSE Sorting nexin-20	3	12.1
Rcc2	RCC2_MOUSE Protein RCC2	3	7.5
Iba57	CAF17_MOUSE Putative transferase CAF17 homolog, mitochondrial	3	10
Rmnd1	RMND1_MOUSE Required for meiotic nuclear division protein 1 homolog	3	7.5
Sec13	SEC13_MOUSE Protein SEC13 homolog	3	12.1
Igtp	Q9DCE9_MOUSE Protein Igtp	3	11.1
Lpl	LIPL_MOUSE Lipoprotein lipase	2	6.1
Srek1	SREK1_MOUSE Isoform 2 of Splicing regulatory glutamine/lysine-rich protein 1	2	4.1
Ssr1	SSRA_MOUSE Translocon-associated protein subunit alpha	2	8
Gtf2e1	T2EA_MOUSE General transcription factor IIE subunit 1	2	5.9
Pgd	6PGD_MOUSE 6-phosphogluconate dehydrogenase, decarboxylating	2	5.4
Rabl6	RABL6_MOUSE Rab-like protein 6	1	2.3
Rdh13	A0A0R4J1N8_MOUSE Retinol dehydrogenase 13	8	22.7
Zeb2	A0A0J9YV01_MOUSE Zinc finger E-box-binding homeobox 2	7	5
Rprd1b	A0A0R4J195_MOUSE Regulation of nuclear pre-mRNA domain-containing protein 1B	7	25.2
Stau1	A2A5R8_MOUSE Double-stranded RNA-binding protein Staufen homolog 1	6	11.1
Cops6	D3Z0F5_MOUSE COP9 signalosome complex subunit 6	5	18.5
U2af1l4	E9PUZ3_MOUSE Splicing factor U2AF 26 kDa subunit	5	20.7
Vdac2	G3UX26_MOUSE Voltage-dependent anion-selective channel protein 2 (Fragment)	5	24.3
Clint1	Q5SUH6_MOUSE Clathrin interactor 1	5	7.6
Rpl7a-ps3	A0A140T8L1_MOUSE Protein Rpl7a-ps3	4	14.8

Rpl7a	RL7A_MOUSE 60S ribosomal protein L7a	4	15
Tradd	B2RRZ7_MOUSE TNFRSF1A-associated via death domain	4	12.2
Lactb	B2RWI2_MOUSE Lactamase, beta	4	8
Otub1	D3YWF6_MOUSE Ubiquitin thioesterase OTUB1	4	16.1
Akr1b10	D3Z494_MOUSE MCG142264, isoform CRA_a	4	11.1
Rpl6	RL6_MOUSE 60S ribosomal protein L6	4	16.2
Stx3	STX3_MOUSE Syntaxin-3	4	15.5
Ighg1	A0A075B5P4_MOUSE Ig gamma-1 chain C region secreted form (Fragment)	3	12
Stat1	A0A087WSP5_MOUSE Signal transducer and activator of transcription	3	5.6
Ppp6c	A0A0N4SVL9_MOUSE Serine/threonine-protein phosphatase	3	12.7
Syncrip	A0A0R4J259_MOUSE Heterogeneous nuclear ribonucleoprotein Q	3	7.1
Stk26	A2AD84_MOUSE Serine/threonine-protein kinase 26	3	9.4
Ubtf	A2AWT5_MOUSE Nucleolar transcription factor 1	3	3.3
Plekhf2	A8Y5N8_MOUSE Pleckstrin homology domain-containing family F member 2 (Fragment)	3	11.1
Lgals9	B1AQR8_MOUSE Galectin	3	9.9
Cbr1	B2RXY7_MOUSE Carbonyl reductase 1	3	14.4
Thoc6	D3Z131_MOUSE THO complex subunit 6 homolog	3	11.4
Wdr83	D6RGR4_MOUSE WD repeat domain-containing protein 83 (Fragment)	3	14.8
Tor1aip1	E9PWW2_MOUSE Torsin-1A-interacting protein 1	3	8.2
Parvg	E9PYG5_MOUSE Gamma-parvin	3	6.2
Poldip2	F6SQH7_MOUSE Polymerase delta-interacting protein 2 (Fragment)	3	12.6
Ptpn6	PTN6_MOUSE Tyrosine-protein phosphatase non-receptor type 6	3	5.4
Atp6ap2	Q1XID4_MOUSE Renin receptor	3	8.3
Clic1	Q542F1_MOUSE Chloride intracellular channel protein	3	17.4
Rtn4	Q8BH78_MOUSE Reticulon	3	9.8
Mrpl1	RM01_MOUSE 39S ribosomal protein L1, mitochondrial	3	9.2

Actl6a	A0A0A6YWG8_MOUSE Actin-like protein 6A (Fragment)	2	9.8
Rabggtb	A0A0G2JDK3_MOUSE Geranylgeranyl transferase type-2 subunit beta (Fragment)	2	14.7
Osgep	A0A0R4J1Y3_MOUSE Probable tRNA N6-adenosine threonylcarbamoyltransferase	2	8.6
Map7d1	MA7D1_MOUSE MAP7 domain-containing protein 1	2	3.3
Klhdc4	G3UZ63_MOUSE Kelch domain-containing protein 4	2	6
Mxd1	MAD1_MOUSE Max dimerization protein 1	2	12.3
Tube 7 (gel area from ~31 kDa to ~35 kDa)			
Snrpa	SNRPA_MOUSE U1 small nuclear ribonucleoprotein A	13	35.8
Atp5c1	Q8C2Q8_MOUSE ATP synthase subunit gamma	12	37.1
Chmp2a	CHM2A_MOUSE Charged multivesicular body protein 2a	12	31.4
Chmp5	CHMP5_MOUSE Charged multivesicular body protein 5	11	42.3
Rpl8	RL8_MOUSE 60S ribosomal protein L8	10	27.9
Eef1b	EF1B_MOUSE Elongation factor 1-beta	8	27.4
Rack1	RACK1_MOUSE Receptor of activated protein C kinase 1	8	21.7
Lrrc59	LRC59_MOUSE Leucine-rich repeat-containing protein 59	8	29.9
Apool	MIC27_MOUSE MICOS complex subunit Mic27	7	31.2
Dnajc9	DNJC9_MOUSE DnaJ homolog subfamily C member 9	7	22.7
Chchd6	MIC25_MOUSE MICOS complex subunit Mic25	6	21.5
Etfa	ETFA_MOUSE Electron transfer flavoprotein subunit alpha, mitochondrial	6	21
Ifi35	IN35_MOUSE Interferon-induced 35 kDa protein homolog	6	25.8
Smap	SMAP_MOUSE Small acidic protein	6	30.8
Pabpc1	PABP1_MOUSE Polyadenylate-binding protein 1	5	7.5
Bloc1s3	BL1S3_MOUSE Biogenesis of lysosome-related organelles complex 1 subunit 3	5	29.1
C1qbp	Q8R5L1_MOUSE Complement component 1 Q subcomponent-binding protein, mitochondrial	5	18.9
Ccdc124	CC124_MOUSE Coiled-coil domain-containing protein 124	5	21.1

Prkra	PRKRA_MOUSE Interferon-inducible double-stranded RNA-dependent protein kinase activator A	5	15
C3	CO3_BOVIN Complement C3	4	2.7
C1qb	C1QB_MOUSE Complement C1q subcomponent subunit B	4	17.3
Myd88	MYD88_MOUSE Myeloid differentiation primary response protein MyD88	4	14.5
Exosc6	EXOS6_MOUSE Exosome complex component MTR3	4	20.1
Tceb3	ELOA1_MOUSE Transcription elongation factor B polypeptide 3	4	5.2
Mrps2	RT02_MOUSE 28S ribosomal protein S2, mitochondrial	4	15.1
Hibadh	3HIDH_MOUSE 3-hydroxyisobutyrate dehydrogenase, mitochondrial	4	11.3
Slc25a22	GHC1_MOUSE Mitochondrial glutamate carrier 1	4	10.2
Gtf2e2	T2EB_MOUSE General transcription factor IIE subunit 2	4	16
Nek7	NEK7_MOUSE Serine/threonine-protein kinase Nek7	4	18.5
Hnrnpf	HNRPF_MOUSE Heterogeneous nuclear ribonucleoprotein F	4	12.5
Psmb10	PSB10_MOUSE Proteasome subunit beta type-10	3	10.6
Glud1	DHE3_MOUSE Glutamate dehydrogenase 1, mitochondrial	3	5.7
Hist1h1a	H11_MOUSE Histone H1.1	3	11.7
Prpf38a	PR38A_MOUSE Pre-mRNA-splicing factor 38A	3	11.8
Khdrbs1	KHDR1_MOUSE KH domain-containing, RNA-binding, signal transduction-associated protein 1	3	3.8
Pdcl3	PDCL3_MOUSE Phosducin-like protein 3	3	6.6
Nemf	NEMF_MOUSE Nuclear export mediator factor Nemf	3	2.9
Chmp3	CHMP3_MOUSE Charged multivesicular body protein 3	3	12
Hnrnpa0	ROA0_MOUSE Heterogeneous nuclear ribonucleoprotein A0	3	13.4
Dffa	DFFA_MOUSE Isoform ICAD-S of DNA fragmentation factor subunit alpha	2	13.2
Fam177a1	F177A_MOUSE Protein FAM177A1	2	10.6
Cbr3	CBR3_MOUSE Carbonyl reductase [NADPH] 3	2	9.7
Apol9a	Q8VDU3_MOUSE Apol9a protein	2	11.6
Ccdc53	CCD53_MOUSE WASH complex subunit CCDC53	19	40

Luc7l2	LC7L2_MOUSE Putative RNA-binding protein Luc7-like 2	10	18.3
Saraf	A0A0R4J0D1_MOUSE Store-operated calcium entry-associated regulatory factor	8	28
Alyref	THOC4_MOUSE THO complex subunit 4	8	18.4
Alyref2	ALRF2_MOUSE Isoform 2 of Aly/REF export factor 2	8	21.6
Ebna1bp2	A2ACZ1_MOUSE Probable rRNA-processing protein EBP2 (Fragment)	7	27.7
Tomm34	TOM34_MOUSE Mitochondrial import receptor subunit TOM34	7	19.4
Hnrnpl	G5E924_MOUSE Heterogeneous nuclear ribonucleoprotein L (Fragment)	6	6.7
Pitpna	J3QPW1_MOUSE Phosphatidylinositol transfer protein alpha isoform	6	16.1
Psme2	PSME2_MOUSE Proteasome activator complex subunit 2	6	20.4
PSME2b	Q5SVP3_MOUSE MCG22048, isoform CRA_c	6	20.4
Glod4	GLOD4_MOUSE Glyoxalase domain-containing protein 4	6	26.1
Rps2	RS2_MOUSE 40S ribosomal protein S2	5	18
Pycr2	Q3TMZ1_MOUSE Pyrroline-5-carboxylate reductase	5	14
Stx11	Q3U5V8_MOUSE MCG49559	5	19.4
Coro1c	Q499X7_MOUSE Coronin	5	10.9
Decr1	Q4FJK0_MOUSE 2,4-dienoyl-CoA reductase, mitochondrial	5	16.4
Pgam5	PGAM5_MOUSE Serine/threonine-protein phosphatase PGAM5, mitochondrial	5	21.8
Pstpip1	A0A0R4J0P5_MOUSE Proline-serine-threonine phosphatase-interacting protein 1	4	4.3
Wdr61	A0MNP4_MOUSE CDW13/WDR61	4	16.3
Sarnp	B2RXM7_MOUSE MCG113697	4	22.7
Mlec	D3Z1M3_MOUSE Malectin	4	18.8
Mtx1	F7C846_MOUSE Metaxin-1	4	7.8
Atp6v1d	VATD_MOUSE V-type proton ATPase subunit D	4	16.1
Psme3	PSME3_MOUSE Proteasome activator complex subunit 3	4	17.6
Mpst	Q3UW66_MOUSE Sulfurtransferase	4	14.1

Ergic1	Q4FK22_MOUSE 1200007D18Rik protein	4	13.1
Srsf7	SRSF7_MOUSE Serine/arginine-rich splicing factor 7	4	19
Cyc1	CY1_MOUSE Cytochrome c1, heme protein, mitochondrial	4	19.3
Map4	A0A0B4J1F2_MOUSE Microtubule-associated protein	3	4.4
Tra2a	A0A0N4SVC2_MOUSE Transformer-2 protein homolog alpha	3	11.4
Srpk2	A0A0R4J124_MOUSE SRSF protein kinase 2	3	4.5
Epb41	A2A838_MOUSE Protein 4.1 (Fragment)	3	5.8
Magt1	A2ADH1_MOUSE Magnesium transporter protein 1	3	5.1
Wdr82	B2RXQ8_MOUSE MCG19514, isoform CRA_a	3	8.6
Nmral1	D3YU12_MOUSE NmrA-like family domain-containing protein 1	3	12.3
Rbms1	E9PZ21_MOUSE RNA-binding motif, single-stranded-interacting protein 1	3	7.9
Plec	E9Q3W4_MOUSE Plectin	3	0.8
Srsf11	E9Q6E5_MOUSE Protein Srsf11	3	7.6
H2-Ke6	G3UX44_MOUSE Estradiol 17-beta-dehydrogenase 8 (Fragment)	3	17
Hsd17b8	DHB8_MOUSE Estradiol 17-beta-dehydrogenase 8	3	15.4
Stx5a	H3BJ02_MOUSE Syntaxin-5	3	20.4
Stx5	STX5_MOUSE Syntaxin-5	3	14.9
Esd	H3BJL6_MOUSE S-formylglutathione hydrolase	3	18.4
Apoe	APOE_MOUSE Apolipoprotein E	3	11.2
Mapre1	Q3U4H0_MOUSE Microtubule-associated protein RP/EB family member 1	3	18.6
Gdi2	GDIB_MOUSE Rab GDP dissociation inhibitor beta	3	4.9
Use1	E9Q496_MOUSE Vesicle transport protein USE1	2	10.2
Hsd17b7	DHB7_MOUSE 3-keto-steroid reductase	2	8.7
Rrp1	RRP1_MOUSE Ribosomal RNA processing protein 1 homolog A	2	5.3
Ctdsp1	CTDS1_MOUSE Carboxy-terminal domain RNA polymerase II polypeptide A small phosphatase 1	2	10.7
Tube 9 (gel area from ~28 kDa to 31 kDa)			
Snrpa1	RU2A_MOUSE U2 small nuclear ribonucleoprotein A'	14	40.2
Gid8	GID8_MOUSE Glucose-induced degradation protein 8 homolog	10	41.9

Vapa	VAPA_MOUSE Vesicle-associated membrane protein-associated protein A	10	40.8
Lmna	LMNA_MOUSE Prelamin-A/C	9	15.9
Slc25a4	ADT1_MOUSE ADP/ATP translocase 1	9	25.4
Etfb	ETFB_MOUSE Electron transfer flavoprotein subunit beta	9	30.9
Hnrnph2	HNRH2_MOUSE Heterogeneous nuclear ribonucleoprotein H2	8	20.7
Tma16	TMA16_MOUSE Translation machinery-associated protein 16	8	27.5
Hsd17b12	DHB12_MOUSE Very-long-chain 3-oxoacyl-CoA reductase	6	18.8
Rpl10a	Q5XJF6_MOUSE Ribosomal protein	6	28.9
Armc10	ARM10_MOUSE Armadillo repeat-containing protein 10	6	29.3
Bcas2	SPF27_MOUSE Pre-mRNA-splicing factor SPF27	6	28.8
Ndufs3	NDUS3_MOUSE NADH dehydrogenase [ubiquinone] iron-sulfur protein 3, mitochondrial	6	26.1
Anxa7	ANXA7_MOUSE Annexin A7	5	15.1
Snrnp70	RU17_MOUSE U1 small nuclear ribonucleoprotein 70 kDa	5	8
Txndc9	TXND9_MOUSE Thioredoxin domain-containing protein 9	5	23.8
Psmd9	PSMD9_MOUSE 26S proteasome non-ATPase regulatory subunit 9	5	28.3
Eef2	EF2_MOUSE Elongation factor 2	4	5.8
Sbds	SBDS_MOUSE Ribosome maturation protein SBDS	4	21.9
Thrap3	TR150_MOUSE Thyroid hormone receptor-associated protein 3	4	5.7
Mitd1	MITD1_MOUSE MIT domain-containing protein 1	4	18.4
Dhrs4	DHRS4_MOUSE Dehydrogenase/reductase SDR family member 4	4	14.3
Bloc1s4	BL1S4_MOUSE Biogenesis of lysosome-related organelles complex 1 subunit 4	3	11.6
Psma4	PSA4_MOUSE Proteasome subunit alpha type-4	3	12.2
Taf10	TAF10_MOUSE Transcription initiation factor TFIID subunit 10	2	15.5

Emc3	EMC3_MOUSE ER membrane protein complex subunit 3	2	12.6
Rqcd1	RCD1_MOUSE Cell differentiation protein RCD1 homolog	2	10.7
Rhbdd1	RHBL4_MOUSE Rhomboid-related protein 4	1	5.4
Vapb	Q8BH80_MOUSE Vesicle-associated membrane protein, associated protein B and C	13	50
Rsu1	A2AUR7_MOUSE Ras suppressor protein 1	12	34.9
Krt15	B1AQ77_MOUSE Keratin 15, isoform CRA_a	11	10.3
Gtf2f2	Q3UMJ4_MOUSE General transcription factor IIF subunit 2	7	28.8
Clic4	Q543N5_MOUSE Chloride intracellular channel protein	7	26.4
Slc25a3	G5E902_MOUSE MCG10343, isoform CRA_b	6	13.1
Myh14	K3W4R2_MOUSE Myosin-14	6	2.2
Vdac3-ps1	A0A140T8V3_MOUSE Protein Vdac3-ps1	5	26.4
Vdac3	Q3TX38_MOUSE Voltage-dependent anion-selective channel protein 3	5	26.4
Dpm1	A2BDX2_MOUSE Dolichol-phosphate mannosyltransferase subunit 1	5	21.1
Tpd52	D3Z125_MOUSE Tumor protein D52 (Fragment)	5	26.1
Akap8	Q059U9_MOUSE A kinase (PRKA) anchor protein 8	5	4.4
Cdk5	A0A0G2JDL3_MOUSE Cyclin-dependent-like kinase 5	4	13
Snf8	A2A6M1_MOUSE Vacuolar-sorting protein SNF8	4	19.2
Wdr26	E0CYH4_MOUSE WD repeat-containing protein 26	4	7.2
Gclm	GSH0_MOUSE Glutamate--cysteine ligase regulatory subunit	4	18.9
Tuba3a	TBA3_MOUSE Tubulin alpha-3 chain	4	12
Actn4	ACTN4_MOUSE Alpha-actinin-4	4	6.1
Pgls	Q8CBG6_MOUSE 6-phosphogluconolactonase	4	18.5
Ccdc127	E0CYX9_MOUSE Coiled-coil domain-containing protein 127 (Fragment)	3	17.2
Psma3	PSA3_MOUSE Proteasome subunit alpha type-3	3	14.5
Nat2	ARY2_MOUSE Arylamine N-acetyltransferase 2	3	13.1
Ap3s1	Q3U8S0_MOUSE AP-3 complex subunit sigma-1	3	19.6
Cdc5l	Q3UCF2_MOUSE Cell division cycle 5-like protein	3	3.5
Ybx3	YBOX3_MOUSE Y-box-binding protein 3	3	9.1
Aatf	AATF_MOUSE Protein AATF	3	4.9

Rdh11	RDH11_MOUSE Retinol dehydrogenase 11	3	7.9
Epsti1	A0A140T8I6_MOUSE Epithelial stromal interaction 1 (Breast)	2	7
Ehd4	Q3TM70_MOUSE EH domain-containing protein 4	2	5.5
Tollip	Q8C5G6_MOUSE Toll-interacting protein	2	12.7
Tube 11 (gel area from ~25 kDa to ~28 kDa)			
Hmgb2	HMGB2_MOUSE High mobility group protein B2	16	37
Srsf9	SRSF9_MOUSE Serine/arginine-rich splicing factor 9	10	32.7
Prdx4	PRDX4_MOUSE Peroxiredoxin-4	6	18.2
Srsf6	SRSF6_MOUSE Serine/arginine-rich splicing factor 6	5	13.5
Rab5a	RAB5A_MOUSE Ras-related protein Rab-5A	5	22.7
Snrpb2	RU2B_MOUSE U2 small nuclear ribonucleoprotein B''	5	17.3
Stom	STOM_MOUSE Erythrocyte band 7 integral membrane protein	4	9.5
Top2b	TOP2B_MOUSE DNA topoisomerase 2-beta	3	1.5
Pyhin1	IFIX_MOUSE Pyrin and HIN domain-containing protein 1	3	10.5
Chchd3	D3Z0L4_MOUSE MICOS complex subunit (Fragment)	10	36.3
Grb2	B1AT92_MOUSE Growth factor receptor-bound protein 2	8	25
Pdap1	B2RTB0_MOUSE 28 kDa heat- and acid-stable phosphoprotein	6	26.9
Acod1	A0A0R4J027_MOUSE Protein Acod1	5	8
Polr2e	Q3V214_MOUSE DNA-directed RNA polymerases I, II, and III subunit RPABC1	5	15.2
Rpl23a-ps3	A0A140T8M7_MOUSE Protein Rpl23a-ps3	4	18.5
Rpl23a	RL23A_MOUSE 60S ribosomal protein L23a	4	18.5
Psma6	E0CXB1_MOUSE Proteasome subunit alpha type-6	4	15.4
Ctsg	CATG_MOUSE Cathepsin G	4	17.2
Rab5c	RAB5C_MOUSE Ras-related protein Rab-5C	4	19.4
Rab14	Q50HX4_MOUSE RAB14 protein	4	25
Tgm1	A0A0R4J293_MOUSE Protein-glutamine gamma-glutamyltransferase K	3	3.9
Rab5b	B2RPS1_MOUSE RAB5B, member RAS oncogene family	3	19.4
Ranbp1	H7BX22_MOUSE Ran-specific GTPase-activating protein	3	20.1

Rps8	RS8_MOUSE 40S ribosomal protein S8	3	17.2
2700060E02Rik	Q4VA29_MOUSE MCG140066	3	12.2
Rpl29	RL29_MOUSE 60S ribosomal protein L29	2	11.8

11. References

1. J. L. W. Thudichum, *A Treatise on the Chemical Constitution of the Brain*. (Archon Books, 1962).
2. A. H. Merrill, Jr. *et al.*, Sphingolipids--the enigmatic lipid class: biochemistry, physiology, and pathophysiology. *Toxicol Appl Pharmacol* **142**, 208-225 (1997).
3. C. S. Breathnach, Johann Ludwig Wilhelm Thudichum 1829-1901, bane of the Protagonisers. *Hist Psychiatry* **12**, 283-296 (2001).
4. I. H. Mc, Thudichum and the medical chemistry of the 1860s to 1880s. *Proc R Soc Med* **51**, 127-132 (1958).
5. K. W. Murphy, C.; Berg, L., *Janeway's Immunobiology*. (WW Norton & Co, 2022), vol. 10th.
6. D. D. Chaplin, Overview of the immune response. *J Allergy Clin Immunol* **125**, S3-23 (2010).
7. J. R. Dunkelberger, W. C. Song, Complement and its role in innate and adaptive immune responses. *Cell Res* **20**, 34-50 (2010).
8. C. F. Nathan, H. W. Murray, M. E. Wiebe, B. Y. Rubin, Identification of interferon-gamma as the lymphokine that activates human macrophage oxidative metabolism and antimicrobial activity. *J Exp Med* **158**, 670-689 (1983).
9. E. Vivier *et al.*, Innate or adaptive immunity? The example of natural killer cells. *Science* **331**, 44-49 (2011).
10. C. Song *et al.*, Nanomaterials targeting macrophages in sepsis: A promising approach for sepsis management. *Front Immunol* **13**, 1026173 (2022).
11. K. E. Rudd *et al.*, Global, regional, and national sepsis incidence and mortality, 1990-2017: analysis for the Global Burden of Disease Study. *Lancet* **395**, 200-211 (2020).
12. G. L. Lin, J. P. McGinley, S. B. Drysdale, A. J. Pollard, Epidemiology and Immune Pathogenesis of Viral Sepsis. *Front Immunol* **9**, 2147 (2018).
13. D. Jarczak, S. Kluge, A. Nierhaus, Sepsis-Pathophysiology and Therapeutic Concepts. *Front Med (Lausanne)* **8**, 628302 (2021).
14. H. Kumar, T. Kawai, S. Akira, Pathogen recognition by the innate immune system. *Int Rev Immunol* **30**, 16-34 (2011).
15. T. van der Poll, F. L. van de Veerdonk, B. P. Scicluna, M. G. Netea, The immunopathology of sepsis and potential therapeutic targets. *Nat Rev Immunol* **17**, 407-420 (2017).
16. A. Shapouri-Moghaddam *et al.*, Macrophage plasticity, polarization, and function in health and disease. *J Cell Physiol* **233**, 6425-6440 (2018).
17. M. Deng *et al.*, The Endotoxin Delivery Protein HMGB1 Mediates Caspase-11-Dependent Lethality in Sepsis. *Immunity* **49**, 740-753 e747 (2018).
18. B. G. Chousterman, F. K. Swirski, G. F. Weber, Cytokine storm and sepsis disease pathogenesis. *Semin Immunopathol* **39**, 517-528 (2017).
19. D. Rittirsch, M. A. Flierl, P. A. Ward, Harmful molecular mechanisms in sepsis. *Nat Rev Immunol* **8**, 776-787 (2008).
20. D. J. Stearns-Kurosawa, M. F. Osuchowski, C. Valentine, S. Kurosawa, D. G. Remick, The pathogenesis of sepsis. *Annu Rev Pathol* **6**, 19-48 (2011).
21. A. Sindrilaru *et al.*, An unrestrained proinflammatory M1 macrophage population induced by iron impairs wound healing in humans and mice. *J Clin Invest* **121**, 985-997 (2011).
22. C. Nathan, A. Ding, Nonresolving inflammation. *Cell* **140**, 871-882 (2010).
23. M. T. Johnson *et al.*, Impact of previous antibiotic therapy on outcome of Gram-negative severe sepsis. *Crit Care Med* **39**, 1859-1865 (2011).
24. E. C. van der Slikke, A. Y. An, R. E. W. Hancock, H. R. Bouma, Exploring the pathophysiology of post-sepsis syndrome to identify therapeutic opportunities. *EBioMedicine* **61**, 103044 (2020).
25. J. Chen, H. Wei, Immune Intervention in Sepsis. *Front Pharmacol* **12**, 718089 (2021).
26. R. L. Siegel, K. D. Miller, H. E. Fuchs, A. Jemal, Cancer Statistics, 2021. *CA Cancer J Clin* **71**, 7-33 (2021).
27. H. Sung *et al.*, Global Cancer Statistics 2020: GLOBOCAN Estimates of Incidence and Mortality Worldwide for 36 Cancers in 185 Countries. *CA Cancer J Clin* **71**, 209-249 (2021).
28. M. Rastrelli, S. Tropea, C. R. Rossi, M. Alaibac, Melanoma: epidemiology, risk factors, pathogenesis, diagnosis and classification. *In Vivo* **28**, 1005-1011 (2014).

29. X. Sun, N. Zhang, C. Yin, B. Zhu, X. Li, Ultraviolet Radiation and Melanomagenesis: From Mechanism to Immunotherapy. *Front Oncol* **10**, 951 (2020).
30. M. Burotto, V. L. Chiou, J. M. Lee, E. C. Kohn, The MAPK pathway across different malignancies: a new perspective. *Cancer* **120**, 3446-3456 (2014).
31. D. Hanahan, R. A. Weinberg, Hallmarks of cancer: the next generation. *Cell* **144**, 646-674 (2011).
32. A. Mantovani, Cancer: Inflaming metastasis. *Nature* **457**, 36-37 (2009).
33. J. D. Wolchok *et al.*, Long-Term Outcomes With Nivolumab Plus Ipilimumab or Nivolumab Alone Versus Ipilimumab in Patients With Advanced Melanoma. *J Clin Oncol* **40**, 127-137 (2022).
34. J. van Breeschoten *et al.*, First-line BRAF/MEK inhibitors versus anti-PD-1 monotherapy in BRAF(V600)-mutant advanced melanoma patients: a propensity-matched survival analysis. *Br J Cancer* **124**, 1222-1230 (2021).
35. D. Davar *et al.*, High-dose interleukin-2 (HD IL-2) for advanced melanoma: a single center experience from the University of Pittsburgh Cancer Institute. *J Immunother Cancer* **5**, 74 (2017).
36. R. M. Conry, B. Westbrook, S. McKee, T. G. Norwood, Talimogene laherparepvec: First in class oncolytic virotherapy. *Hum Vaccin Immunother* **14**, 839-846 (2018).
37. P. Strojan, Role of radiotherapy in melanoma management. *Radiol Oncol* **44**, 1-12 (2010).
38. J. J. Luke, G. K. Schwartz, Chemotherapy in the management of advanced cutaneous malignant melanoma. *Clin Dermatol* **31**, 290-297 (2013).
39. M. Bidram *et al.*, mRNA-Based Cancer Vaccines: A Therapeutic Strategy for the Treatment of Melanoma Patients. *Vaccines (Basel)* **9**, (2021).
40. R. D. Schreiber, L. J. Old, M. J. Smyth, Cancer immunoediting: integrating immunity's roles in cancer suppression and promotion. *Science* **331**, 1565-1570 (2011).
41. F. Balkwill, A. Mantovani, Inflammation and cancer: back to Virchow? *Lancet* **357**, 539-545 (2001).
42. G. P. Dunn, A. T. Bruce, H. Ikeda, L. J. Old, R. D. Schreiber, Cancer immunoediting: from immunosurveillance to tumor escape. *Nat Immunol* **3**, 991-998 (2002).
43. J. S. O'Donnell, M. W. L. Teng, M. J. Smyth, Cancer immunoediting and resistance to T cell-based immunotherapy. *Nat Rev Clin Oncol* **16**, 151-167 (2019).
44. N. Riaz *et al.*, Tumor and Microenvironment Evolution during Immunotherapy with Nivolumab. *Cell* **171**, 934-949 e916 (2017).
45. A. Hou, K. Hou, Q. Huang, Y. Lei, W. Chen, Targeting Myeloid-Derived Suppressor Cell, a Promising Strategy to Overcome Resistance to Immune Checkpoint Inhibitors. *Front Immunol* **11**, 783 (2020).
46. N. B. Hao *et al.*, Macrophages in tumor microenvironments and the progression of tumors. *Clin Dev Immunol* **2012**, 948098 (2012).
47. V. Kumar, S. Patel, E. Tcyganov, D. I. Gabrilovich, The Nature of Myeloid-Derived Suppressor Cells in the Tumor Microenvironment. *Trends Immunol* **37**, 208-220 (2016).
48. M. C. Schmid, J. A. Varner, Myeloid cells in tumor inflammation. *Vasc Cell* **4**, 14 (2012).
49. G. Heuff *et al.*, Enhanced tumour growth in the rat liver after selective elimination of Kupffer cells. *Cancer Immunol Immunother* **37**, 125-130 (1993).
50. B. Z. Qian, J. W. Pollard, Macrophage diversity enhances tumor progression and metastasis. *Cell* **141**, 39-51 (2010).
51. S. I. Grivennikov, F. R. Greten, M. Karin, Immunity, inflammation, and cancer. *Cell* **140**, 883-899 (2010).
52. A. Mirouse *et al.*, Sepsis and Cancer: An Interplay of Friends and Foes. *Am J Respir Crit Care Med* **202**, 1625-1635 (2020).
53. C. Vigneron *et al.*, Sepsis inhibits tumor growth in mice with cancer through Toll-like receptor 4-associated enhanced Natural Killer cell activity. *Oncoimmunology* **8**, e1641391 (2019).
54. K. A. Cavassani *et al.*, The post sepsis-induced expansion and enhanced function of regulatory T cells create an environment to potentiate tumor growth. *Blood* **115**, 4403-4411 (2010).
55. C. D. Mills, L. L. Lenz, R. A. Harris, A Breakthrough: Macrophage-Directed Cancer Immunotherapy. *Cancer Res* **76**, 513-516 (2016).
56. A. R. Poh, M. Ernst, Targeting Macrophages in Cancer: From Bench to Bedside. *Front Oncol* **8**, 49 (2018).
57. C. W. Wanderley *et al.*, Paclitaxel Reduces Tumor Growth by Reprogramming Tumor-Associated Macrophages to an M1 Profile in a TLR4-Dependent Manner. *Cancer Res* **78**, 5891-5900 (2018).
58. M. Jinushi, Y. Komohara, Tumor-associated macrophages as an emerging target against tumors: Creating a new path from bench to bedside. *Biochim Biophys Acta* **1855**, 123-130 (2015).

59. A. A. Barkal *et al.*, Engagement of MHC class I by the inhibitory receptor LILRB1 suppresses macrophages and is a target of cancer immunotherapy. *Nat Immunol* **19**, 76-84 (2018).
60. C. H. Ries *et al.*, Targeting tumor-associated macrophages with anti-CSF-1R antibody reveals a strategy for cancer therapy. *Cancer Cell* **25**, 846-859 (2014).
61. L. Chen *et al.*, Simultaneous T Cell Activation and Macrophage Polarization to Promote Potent Tumor Suppression by Iron Oxide-Embedded Large-Pore Mesoporous Organosilica Core-Shell Nanospheres. *Adv Healthc Mater* **8**, e1900039 (2019).
62. K. Binnemars-Postma, R. Bansal, G. Storm, J. Prakash, Targeting the Stat6 pathway in tumor-associated macrophages reduces tumor growth and metastatic niche formation in breast cancer. *FASEB J* **32**, 969-978 (2018).
63. I. Vanmeerbeek *et al.*, The Interface of Tumour-Associated Macrophages with Dying Cancer Cells in Immuno-Oncology. *Cells* **11**, (2022).
64. Y. C. Liu, X. B. Zou, Y. F. Chai, Y. M. Yao, Macrophage polarization in inflammatory diseases. *Int J Biol Sci* **10**, 520-529 (2014).
65. J. M. Cavaillon, M. Adib-Conquy, Monocytes/macrophages and sepsis. *Crit Care Med* **33**, S506-509 (2005).
66. L. van de Laar *et al.*, Yolk Sac Macrophages, Fetal Liver, and Adult Monocytes Can Colonize an Empty Niche and Develop into Functional Tissue-Resident Macrophages. *Immunity* **44**, 755-768 (2016).
67. M. Merad, F. Ginhoux, M. Collin, Origin, homeostasis and function of Langerhans cells and other langerin-expressing dendritic cells. *Nat Rev Immunol* **8**, 935-947 (2008).
68. M. Naito, G. Hasegawa, K. Takahashi, Development, differentiation, and maturation of Kupffer cells. *Microsc Res Tech* **39**, 350-364 (1997).
69. V. H. Perry, D. A. Hume, S. Gordon, Immunohistochemical localization of macrophages and microglia in the adult and developing mouse brain. *Neuroscience* **15**, 313-326 (1985).
70. C. D. Mills, K. Kincaid, J. M. Alt, M. J. Heilman, A. M. Hill, M-1/M-2 macrophages and the Th1/Th2 paradigm. *J Immunol* **164**, 6166-6173 (2000).
71. A. Mantovani *et al.*, The chemokine system in diverse forms of macrophage activation and polarization. *Trends Immunol* **25**, 677-686 (2004).
72. K. A. Jablonski *et al.*, Novel Markers to Delineate Murine M1 and M2 Macrophages. *PLoS One* **10**, e0145342 (2015).
73. F. O. Martinez, S. Gordon, The M1 and M2 paradigm of macrophage activation: time for reassessment. *F1000Prime Rep* **6**, 13 (2014).
74. J. Blagih, R. G. Jones, Polarizing macrophages through reprogramming of glucose metabolism. *Cell Metab* **15**, 793-795 (2012).
75. J. Van den Bossche, J. Baardman, M. P. de Winther, Metabolic Characterization of Polarized M1 and M2 Bone Marrow-derived Macrophages Using Real-time Extracellular Flux Analysis. *J Vis Exp*, (2015).
76. R. Medzhitov, C. Janeway, Jr., Innate immunity. *N Engl J Med* **343**, 338-344 (2000).
77. T. Kawasaki, T. Kawai, Toll-like receptor signaling pathways. *Front Immunol* **5**, 461 (2014).
78. J. Li, F. Yang, F. Wei, X. Ren, The role of toll-like receptor 4 in tumor microenvironment. *Oncotarget* **8**, 66656-66667 (2017).
79. R. Medzhitov, Toll-like receptors and innate immunity. *Nat Rev Immunol* **1**, 135-145 (2001).
80. T. Kielian, Overview of toll-like receptors in the CNS. *Curr Top Microbiol Immunol* **336**, 1-14 (2009).
81. M. B. Mielcarska, M. Bossowska-Nowicka, F. N. Toka, Cell Surface Expression of Endosomal Toll-Like Receptors-A Necessity or a Superfluous Duplication? *Front Immunol* **11**, 620972 (2020).
82. C. C. Lee, A. M. Avalos, H. L. Ploegh, Accessory molecules for Toll-like receptors and their function. *Nat Rev Immunol* **12**, 168-179 (2012).
83. L. Narunsky-Haziza *et al.*, Pan-cancer analyses reveal cancer-type-specific fungal ecologies and bacteriome interactions. *Cell* **185**, 3789-3806 e3717 (2022).
84. S. Kaesler *et al.*, Targeting tumor-resident mast cells for effective anti-melanoma immune responses. *JCI Insight* **4**, (2019).
85. R. A. Gaiser *et al.*, Enrichment of oral microbiota in early cystic precursors to invasive pancreatic cancer. *Gut* **68**, 2186-2194 (2019).
86. X. Wu *et al.*, Lipopolysaccharide promotes metastasis via acceleration of glycolysis by the nuclear factor-kappaB/snail/hexokinase3 signaling axis in colorectal cancer. *Cancer Metab* **9**, 23 (2021).

87. S. Kalaora *et al.*, Identification of bacteria-derived HLA-bound peptides in melanoma. *Nature* **592**, 138-143 (2021).
88. L. T. Geller *et al.*, Potential role of intratumor bacteria in mediating tumor resistance to the chemotherapeutic drug gemcitabine. *Science* **357**, 1156-1160 (2017).
89. D. Nejman *et al.*, The human tumor microbiome is composed of tumor type-specific intracellular bacteria. *Science* **368**, 973-980 (2020).
90. D. R. E. Ranoa, S. L. Kelley, R. I. Tapping, Human lipopolysaccharide-binding protein (LBP) and CD14 independently deliver triacylated lipoproteins to Toll-like receptor 1 (TLR1) and TLR2 and enhance formation of the ternary signaling complex. *J Biol Chem* **288**, 9729-9741 (2013).
91. S. J. Kim, H. M. Kim, Dynamic lipopolysaccharide transfer cascade to TLR4/MD2 complex via LBP and CD14. *BMB Rep* **50**, 55-57 (2017).
92. B. S. Park, J. O. Lee, Recognition of lipopolysaccharide pattern by TLR4 complexes. *Exp Mol Med* **45**, e66 (2013).
93. T. Crowley *et al.*, Modulation of TLR3/TLR4 inflammatory signaling by the GABAB receptor agonist baclofen in glia and immune cells: relevance to therapeutic effects in multiple sclerosis. *Front Cell Neurosci* **9**, 284 (2015).
94. M. C. Patra, S. Choi, Insight into Phosphatidylinositol-Dependent Membrane Localization of the Innate Immune Adaptor Protein Toll/Interleukin 1 Receptor Domain-Containing Adaptor Protein. *Front Immunol* **9**, 75 (2018).
95. G. Zhang, S. Ghosh, Negative regulation of toll-like receptor-mediated signaling by Tollip. *J Biol Chem* **277**, 7059-7065 (2002).
96. E. J. A. Kowalski, L. Li, Toll-Interacting Protein in Resolving and Non-Resolving Inflammation. *Front Immunol* **8**, 511 (2017).
97. N. N. Kuzmich *et al.*, TLR4 Signaling Pathway Modulators as Potential Therapeutics in Inflammation and Sepsis. *Vaccines (Basel)* **5**, (2017).
98. D. G. Capelluto, Tollip: a multitasking protein in innate immunity and protein trafficking. *Microbes Infect* **14**, 140-147 (2012).
99. A. Ciesielska, M. Matyjek, K. Kwiatkowska, TLR4 and CD14 trafficking and its influence on LPS-induced pro-inflammatory signaling. *Cell Mol Life Sci* **78**, 1233-1261 (2021).
100. F. Antonangeli *et al.*, Regulation of PD-L1 Expression by NF-kappaB in Cancer. *Front Immunol* **11**, 584626 (2020).
101. O. Ernst *et al.*, Exclusive Temporal Stimulation of IL-10 Expression in LPS-Stimulated Mouse Macrophages by cAMP Inducers and Type I Interferons. *Front Immunol* **10**, 1788 (2019).
102. J. C. Kagan *et al.*, TRAM couples endocytosis of Toll-like receptor 4 to the induction of interferon-beta. *Nat Immunol* **9**, 361-368 (2008).
103. F. Mollinedo, C. Gajate, Lipid rafts as major platforms for signaling regulation in cancer. *Adv Biol Regul* **57**, 130-146 (2015).
104. K. Simons, E. Ikonen, Functional rafts in cell membranes. *Nature* **387**, 569-572 (1997).
105. S. J. Singer, G. L. Nicolson, The fluid mosaic model of the structure of cell membranes. *Science* **175**, 720-731 (1972).
106. M. P. Lisanti, M. Sargiacomo, L. Graeve, A. R. Saltiel, E. Rodriguez-Boulan, Polarized apical distribution of glycosyl-phosphatidylinositol-anchored proteins in a renal epithelial cell line. *Proc Natl Acad Sci U S A* **85**, 9557-9561 (1988).
107. G. van Meer, E. H. Stelzer, R. W. Wijnaendts-van-Resandt, K. Simons, Sorting of sphingolipids in epithelial (Madin-Darby canine kidney) cells. *J Cell Biol* **105**, 1623-1635 (1987).
108. P. Varshney, V. Yadav, N. Saini, Lipid rafts in immune signalling: current progress and future perspective. *Immunology* **149**, 13-24 (2016).
109. M. Triantafilou, K. Miyake, D. T. Golenbock, K. Triantafilou, Mediators of innate immune recognition of bacteria concentrate in lipid rafts and facilitate lipopolysaccharide-induced cell activation. *J Cell Sci* **115**, 2603-2611 (2002).
110. J. Benting, A. Rietveld, I. Ansorge, K. Simons, Acyl and alkyl chain length of GPI-anchors is critical for raft association in vitro. *FEBS Lett* **462**, 47-50 (1999).
111. A. Plociennikowska, A. Hromada-Judycka, K. Borzecka, K. Kwiatkowska, Co-operation of TLR4 and raft proteins in LPS-induced pro-inflammatory signaling. *Cell Mol Life Sci* **72**, 557-581 (2015).
112. L. Swanson *et al.*, TLR4 signaling and macrophage inflammatory responses are dampened by GIV/Girdin. *Proc Natl Acad Sci U S A* **117**, 26895-26906 (2020).

113. G. van Meer, D. R. Voelker, G. W. Feigenson, Membrane lipids: where they are and how they behave. *Nat Rev Mol Cell Biol* **9**, 112-124 (2008).
114. Y. A. Hannun, L. M. Obeid, Sphingolipids and their metabolism in physiology and disease. *Nat Rev Mol Cell Biol* **19**, 175-191 (2018).
115. A. H. Futerman, Y. A. Hannun, The complex life of simple sphingolipids. *EMBO Rep* **5**, 777-782 (2004).
116. M. S. Koberlin *et al.*, A Conserved Circular Network of Coregulated Lipids Modulates Innate Immune Responses. *Cell* **162**, 170-183 (2015).
117. Y. A. Hannun, Luberto, C., Mao, C., Obeid, L. M., Bioactive sphingolipids in cancer biology and therapy. *Springer*, (2015).
118. K. Sims *et al.*, Kdo2-lipid A, a TLR4-specific agonist, induces de novo sphingolipid biosynthesis in RAW264.7 macrophages, which is essential for induction of autophagy. *J Biol Chem* **285**, 38568-38579 (2010).
119. J. C. Holthuis, T. Pomorski, R. J. Raggers, H. Sprong, G. Van Meer, The organizing potential of sphingolipids in intracellular membrane transport. *Physiol Rev* **81**, 1689-1723 (2001).
120. K. Hanada *et al.*, Molecular machinery for non-vesicular trafficking of ceramide. *Nature* **426**, 803-809 (2003).
121. T. Hornemann, Y. Wei, A. von Eckardstein, Is the mammalian serine palmitoyltransferase a high-molecular-mass complex? *Biochem J* **405**, 157-164 (2007).
122. G. Han *et al.*, Identification of small subunits of mammalian serine palmitoyltransferase that confer distinct acyl-CoA substrate specificities. *Proc Natl Acad Sci U S A* **106**, 8186-8191 (2009).
123. T. Hornemann, S. Richard, M. F. Rutti, Y. Wei, A. von Eckardstein, Cloning and initial characterization of a new subunit for mammalian serine-palmitoyltransferase. *J Biol Chem* **281**, 37275-37281 (2006).
124. P. Bandhuvula, J. D. Saba, Sphingosine-1-phosphate lyase in immunity and cancer: silencing the siren. *Trends Mol Med* **13**, 210-217 (2007).
125. M. Ikeda, A. Kihara, Y. Kariya, Y. M. Lee, Y. Igarashi, Sphingolipid-to-glycerophospholipid conversion in SPL-null cells implies the existence of an alternative isozyme. *Biochem Biophys Res Commun* **329**, 474-479 (2005).
126. M. C. C. Raman *et al.*, The external aldimine form of serine palmitoyltransferase: structural, kinetic, and spectroscopic analysis of the wild-type enzyme and HSAN1 mutant mimics. *J Biol Chem* **284**, 17328-17339 (2009).
127. Y. A. Hannun, C. R. Loomis, A. H. Merrill, Jr., R. M. Bell, Sphingosine inhibition of protein kinase C activity and of phorbol dibutyrate binding in vitro and in human platelets. *J Biol Chem* **261**, 12604-12609 (1986).
128. B. M. Barth *et al.*, Gaucher's disease and cancer: a sphingolipid perspective. *Crit Rev Oncog* **18**, 221-234 (2013).
129. X. Pan, D. Dutta, S. Lu, H. J. Bellen, Sphingolipids in neurodegenerative diseases. *Front Neurosci* **17**, 1137893 (2023).
130. A. Rotthier *et al.*, Mutations in the SPTLC2 subunit of serine palmitoyltransferase cause hereditary sensory and autonomic neuropathy type I. *Am J Hum Genet* **87**, 513-522 (2010).
131. A. Penno *et al.*, Hereditary sensory neuropathy type 1 is caused by the accumulation of two neurotoxic sphingolipids. *J Biol Chem* **285**, 11178-11187 (2010).
132. R. A. Claus, M. H. Graeler, Sphingolipidomics in Translational Sepsis Research-Biomedical Considerations and Perspectives. *Front Med (Lausanne)* **7**, 616578 (2020).
133. R. Z. Li *et al.*, The key role of sphingolipid metabolism in cancer: New therapeutic targets, diagnostic and prognostic values, and anti-tumor immunotherapy resistance. *Front Oncol* **12**, 941643 (2022).
134. B. Ogretmen, Sphingolipid metabolism in cancer signalling and therapy. *Nat Rev Cancer* **18**, 33-50 (2018).
135. E. B. Vitner, R. Avraham, B. Politi, S. Melamed, T. Israely, Elevation in sphingolipid upon SARS-CoV-2 infection: possible implications for COVID-19 pathology. *Life Sci Alliance* **5**, (2022).
136. S. H. Lin *et al.*, Exploring plasma metabolomic changes in sepsis: a clinical matching study based on gas chromatography-mass spectrometry. *Ann Transl Med* **8**, 1568 (2020).
137. O. Cuvillier *et al.*, Suppression of ceramide-mediated programmed cell death by sphingosine-1-phosphate. *Nature* **381**, 800-803 (1996).
138. K. Takabe, S. Spiegel, Export of sphingosine-1-phosphate and cancer progression. *J Lipid Res* **55**, 1839-1846 (2014).

139. M. Taniguchi *et al.*, Regulation of autophagy and its associated cell death by "sphingolipid rheostat": reciprocal role of ceramide and sphingosine 1-phosphate in the mammalian target of rapamycin pathway. *J Biol Chem* **287**, 39898-39910 (2012).
140. S. E. Alvarez *et al.*, Sphingosine-1-phosphate is a missing cofactor for the E3 ubiquitin ligase TRAF2. *Nature* **465**, 1084-1088 (2010).
141. N. C. Hait *et al.*, Regulation of histone acetylation in the nucleus by sphingosine-1-phosphate. *Science* **325**, 1254-1257 (2009).
142. Y. Takeda, M. Tashima, A. Takahashi, T. Uchiyama, T. Okazaki, Ceramide generation in nitric oxide-induced apoptosis. Activation of magnesium-dependent neutral sphingomyelinase via caspase-3. *J Biol Chem* **274**, 10654-10660 (1999).
143. L. M. Obeid, C. M. Linardic, L. A. Karolak, Y. A. Hannun, Programmed cell death induced by ceramide. *Science* **259**, 1769-1771 (1993).
144. A. Masamune, Y. Igarashi, S. Hakomori, Regulatory role of ceramide in interleukin (IL)-1 beta-induced E-selectin expression in human umbilical vein endothelial cells. Ceramide enhances IL-1 beta action, but is not sufficient for E-selectin expression. *J Biol Chem* **271**, 9368-9375 (1996).
145. L. J. Siskind, Mitochondrial ceramide and the induction of apoptosis. *J Bioenerg Biomembr* **37**, 143-153 (2005).
146. C. E. Senkal, S. Ponnusamy, J. Bielawski, Y. A. Hannun, B. Ogretmen, Antiapoptotic roles of ceramide-synthase-6-generated C16-ceramide via selective regulation of the ATF6/CHOP arm of ER-stress-response pathways. *FASEB J* **24**, 296-308 (2010).
147. S. A. Morad, M. C. Cabot, Ceramide-orchestrated signalling in cancer cells. *Nat Rev Cancer* **13**, 51-65 (2013).
148. J. P. Truman, M. Garcia-Barros, L. M. Obeid, Y. A. Hannun, Evolving concepts in cancer therapy through targeting sphingolipid metabolism. *Biochim Biophys Acta* **1841**, 1174-1188 (2014).
149. J. Newton, S. Lima, M. Maceyka, S. Spiegel, Revisiting the sphingolipid rheostat: Evolving concepts in cancer therapy. *Exp Cell Res* **333**, 195-200 (2015).
150. H. Mizukami *et al.*, Systemic inflammation in glucocerebrosidase-deficient mice with minimal glucosylceramide storage. *J Clin Invest* **109**, 1215-1221 (2002).
151. S. Asano *et al.*, Regulation of cell migration by sphingomyelin synthases: sphingomyelin in lipid rafts decreases responsiveness to signaling by the CXCL12/CXCR4 pathway. *Mol Cell Biol* **32**, 3242-3252 (2012).
152. A. Olona *et al.*, Sphingolipid metabolism during Toll-like receptor 4 (TLR4)-mediated macrophage activation. *Br J Pharmacol* **178**, 4575-4587 (2021).
153. B. Everts *et al.*, TLR-driven early glycolytic reprogramming via the kinases TBK1-IKKvarepsilon supports the anabolic demands of dendritic cell activation. *Nat Immunol* **15**, 323-332 (2014).
154. G. M. Tannahill *et al.*, Succinate is an inflammatory signal that induces IL-1beta through HIF-1alpha. *Nature* **496**, 238-242 (2013).
155. J. H. Ko *et al.*, BCAT1 affects mitochondrial metabolism independently of leucine transamination in activated human macrophages. *J Cell Sci* **133**, (2020).
156. M. A. Lauterbach *et al.*, Toll-like Receptor Signaling Rewires Macrophage Metabolism and Promotes Histone Acetylation via ATP-Citrate Lyase. *Immunity* **51**, 997-1011 e1017 (2019).
157. G. L. Seim *et al.*, Two-stage metabolic remodelling in macrophages in response to lipopolysaccharide and interferon-gamma stimulation. *Nat Metab* **1**, 731-742 (2019).
158. R. A. Memon *et al.*, Endotoxin and cytokines increase hepatic sphingolipid biosynthesis and produce lipoproteins enriched in ceramides and sphingomyelin. *Arterioscler Thromb Vasc Biol* **18**, 1257-1265 (1998).
159. R. A. Memon *et al.*, Regulation of glycosphingolipid metabolism in liver during the acute phase response. *J Biol Chem* **274**, 19707-19713 (1999).
160. A. Y. Andreyev *et al.*, Subcellular organelle lipidomics in TLR-4-activated macrophages. *J Lipid Res* **51**, 2785-2797 (2010).
161. E. A. Dennis *et al.*, A mouse macrophage lipidome. *J Biol Chem* **285**, 39976-39985 (2010).
162. Z. Q. Chang *et al.*, Endotoxin activates de novo sphingolipid biosynthesis via nuclear factor kappa B-mediated upregulation of Sptlc2. *Prostaglandins Other Lipid Mediat* **94**, 44-52 (2011).
163. S. Nikolaeva *et al.*, GM1 and GD1a gangliosides modulate toxic and inflammatory effects of E. coli lipopolysaccharide by preventing TLR4 translocation into lipid rafts. *Biochim Biophys Acta* **1851**, 239-247 (2015).

164. Y. Wang *et al.*, Ganglioside GD1a suppresses LPS-induced pro-inflammatory cytokines in RAW264.7 macrophages by reducing MAPKs and NF-kappaB signaling pathways through TLR4. *Int Immunopharmacol* **28**, 136-145 (2015).
165. M. Chakraborty *et al.*, Myeloid cell-specific serine palmitoyltransferase subunit 2 haploinsufficiency reduces murine atherosclerosis. *J Clin Invest* **123**, 1784-1797 (2013).
166. J. Cuschieri, E. Bulger, J. Billgrin, I. Garcia, R. V. Maier, Acid sphingomyelinase is required for lipid Raft TLR4 complex formation. *Surg Infect (Larchmt)* **8**, 91-106 (2007).
167. C. D. Camell *et al.*, Macrophage-specific de Novo Synthesis of Ceramide Is Dispensable for Inflammasome-driven Inflammation and Insulin Resistance in Obesity. *J Biol Chem* **290**, 29402-29413 (2015).
168. M. R. Hojjati *et al.*, Effect of myriocin on plasma sphingolipid metabolism and atherosclerosis in apoE-deficient mice. *J Biol Chem* **280**, 10284-10289 (2005).
169. J. Jin *et al.*, Docosahexaenoic acid antagonizes the boosting effect of palmitic acid on LPS inflammatory signaling by inhibiting gene transcription and ceramide synthesis. *PLoS One* **13**, e0193343 (2018).
170. M. Hering, To study the role of sphingolipids in macrophage differentiation. *Master's Thesis Heidelberg University* (2020).
171. M. L. Caton, M. R. Smith-Raska, B. Reizis, Notch-RBP-J signaling controls the homeostasis of CD8- dendritic cells in the spleen. *J Exp Med* **204**, 1653-1664 (2007).
172. B. E. Clausen, C. Burkhardt, W. Reith, R. Renkawitz, I. Förster, Conditional gene targeting in macrophages and granulocytes using LysMcre mice. *Transgenic Res* **8**, 265-277 (1999).
173. H. Pircher, K. Burki, R. Lang, H. Hengartner, R. M. Zinkernagel, Tolerance induction in double specific T-cell receptor transgenic mice varies with antigen. *Nature* **342**, 559-561 (1989).
174. Z. Li *et al.*, Liver-specific deficiency of serine palmitoyltransferase subunit 2 decreases plasma sphingomyelin and increases apolipoprotein E levels. *J Biol Chem* **284**, 27010-27019 (2009).
175. F. Zhao *et al.*, Activation of p38 mitogen-activated protein kinase drives dendritic cells to become tolerogenic in ret transgenic mice spontaneously developing melanoma. *Clin Cancer Res* **15**, 4382-4390 (2009).
176. R. K. Naviaux, E. Costanzi, M. Haas, I. M. Verma, The pCL vector system: rapid production of helper-free, high-titer, recombinant retroviruses. *J Virol* **70**, 5701-5705 (1996).
177. F. R. Cross, E. A. Garber, D. Pellman, H. Hanafusa, A short sequence in the p60src N terminus is required for p60src myristylation and membrane association and for cell transformation. *Mol Cell Biol* **4**, 1834-1842 (1984).
178. A. D. Kohn, F. Takeuchi, R. A. Roth, Akt, a pleckstrin homology domain containing kinase, is activated primarily by phosphorylation. *J Biol Chem* **271**, 21920-21926 (1996).
179. R Core Team, R: A Language and Environment for Statistical Computing. *R Foundation for Statistical Computing*, (2020).
180. Y. Chen *et al.*, edgeR: Empirical Analysis of Digital Gene Expression Data in R. *R package version 3.28.1*, (2020).
181. N. Weisshaar *et al.*, Rgs16 promotes antitumor CD8(+) T cell exhaustion. *Sci Immunol* **7**, eabh1873 (2022).
182. M. M. Savitski *et al.*, Tracking cancer drugs in living cells by thermal profiling of the proteome. *Science* **346**, 1255784 (2014).
183. J. Cox, M. Mann, MaxQuant enables high peptide identification rates, individualized p.p.b.-range mass accuracies and proteome-wide protein quantification. *Nat Biotechnol* **26**, 1367-1372 (2008).
184. B. Schwanhausser *et al.*, Global quantification of mammalian gene expression control. *Nature* **473**, 337-342 (2011).
185. L. Gatto, K. S. Lilley, MSnbase-an R/Bioconductor package for isobaric tagged mass spectrometry data visualization, processing and quantitation. *Bioinformatics* **28**, 288-289 (2012).
186. J. Wu *et al.*, Loss of Neurological Disease HSAN-I-Associated Gene SPTLC2 Impairs CD8(+) T Cell Responses to Infection by Inhibiting T Cell Metabolic Fitness. *Immunity* **50**, 1218-1231 e1215 (2019).
187. D. H. Pfaff, G. Poschet, R. Hell, J. Szendrodi, A. A. Teleman, Walking 200 min per day keeps the bariatric surgeon away. *Heliyon* **9**, e16556 (2023).
188. C. Andresen *et al.*, Comparison of extraction methods for intracellular metabolomics of human tissues. *Front Mol Biosci* **9**, 932261 (2022).

189. G. Toda, T. Yamauchi, T. Kadowaki, K. Ueki, Preparation and culture of bone marrow-derived macrophages from mice for functional analysis. *STAR Protoc* **2**, 100246 (2021).
190. A. Viola, F. Munari, R. Sanchez-Rodriguez, T. Scolaro, A. Castegna, The Metabolic Signature of Macrophage Responses. *Front Immunol* **10**, 1462 (2019).
191. H. C. B. Nguyen, M. Adlanmerini, A. K. Hauck, M. A. Lazar, Dichotomous engagement of HDAC3 activity governs inflammatory responses. *Nature* **584**, 286-290 (2020).
192. M. Hering, Madi, M., Sandhoff, R., Ma, S., Wu, J., Mieg, A., Richter, K., Mohr, K., ten Bosch, N., Stichling, D., Poschet, G., Umansky, V., Cui, G. , Sphinganine membrane-anchors TLR4 adaptors in macrophages to promote inflammation *Manuscript submitted for publication* (2023).
193. O. Sharif, V. N. Bolshakov, S. Raines, P. Newham, N. D. Perkins, Transcriptional profiling of the LPS induced NF-kappaB response in macrophages. *BMC Immunol* **8**, 1 (2007).
194. B. Chaurasia, C. L. Talbot, S. A. Summers, Adipocyte Ceramides-The Nexus of Inflammation and Metabolic Disease. *Front Immunol* **11**, 576347 (2020).
195. M. Maceyka, S. Spiegel, Sphingolipid metabolites in inflammatory disease. *Nature* **510**, 58-67 (2014).
196. M. Gaggini, R. Ndreu, E. Michelucci, S. Rocchiccioli, C. Vassalle, Ceramides as Mediators of Oxidative Stress and Inflammation in Cardiometabolic Disease. *Int J Mol Sci* **23**, (2022).
197. J. Hwang *et al.*, Reprogramming of macrophages with macrophage cell membrane-derived nanoghosts. *Nanoscale Adv* **2**, 5254-5262 (2020).
198. C. R. Gault, L. M. Obeid, Y. A. Hannun, An overview of sphingolipid metabolism: from synthesis to breakdown. *Adv Exp Med Biol* **688**, 1-23 (2010).
199. Y. Yan *et al.*, Involvement of early growth response-2 (Egr-2) in lipopolysaccharide-induced neuroinflammation. *J Mol Histol* **44**, 249-257 (2013).
200. B. N. Kang *et al.*, Transcriptional regulation of CD38 expression by tumor necrosis factor-alpha in human airway smooth muscle cells: role of NF-kappaB and sensitivity to glucocorticoids. *FASEB J* **20**, 1000-1002 (2006).
201. S. Zambrano, I. De Toma, A. Piffer, M. E. Bianchi, A. Agresti, NF-kappaB oscillations translate into functionally related patterns of gene expression. *Elife* **5**, e09100 (2016).
202. F. Mercurio *et al.*, IkappaB kinase (IKK)-associated protein 1, a common component of the heterogeneous IKK complex. *Mol Cell Biol* **19**, 1526-1538 (1999).
203. I. Mattioli *et al.*, Transient and selective NF-kappa B p65 serine 536 phosphorylation induced by T cell costimulation is mediated by I kappa B kinase beta and controls the kinetics of p65 nuclear import. *J Immunol* **172**, 6336-6344 (2004).
204. T. Lawrence, M. Bebien, G. Y. Liu, V. Nizet, M. Karin, IKKalpha limits macrophage NF-kappaB activation and contributes to the resolution of inflammation. *Nature* **434**, 1138-1143 (2005).
205. J. P. Pradere *et al.*, Negative regulation of NF-kappaB p65 activity by serine 536 phosphorylation. *Sci Signal* **9**, ra85 (2016).
206. Y. Hu *et al.*, Activation of MTOR in pulmonary epithelium promotes LPS-induced acute lung injury. *Autophagy* **12**, 2286-2299 (2016).
207. T. Lawrence, G. Natoli, Transcriptional regulation of macrophage polarization: enabling diversity with identity. *Nat Rev Immunol* **11**, 750-761 (2011).
208. M. Srivastava *et al.*, The TLR4-NOS1-AP1 signaling axis regulates macrophage polarization. *Inflamm Res* **66**, 323-334 (2017).
209. G. Knittel *et al.*, B-cell-specific conditional expression of Myd88p.L252P leads to the development of diffuse large B-cell lymphoma in mice. *Blood* **127**, 2732-2741 (2016).
210. C. Ouk *et al.*, Continuous MYD88 Activation Is Associated With Expansion and Then Transformation of IgM Differentiating Plasma Cells. *Front Immunol* **12**, 641692 (2021).
211. K. Schmidt *et al.*, B-Cell-Specific Myd88 L252P Expression Causes a Premalignant Gammopathy Resembling IgM MGUS. *Front Immunol* **11**, 602868 (2020).
212. M. H. Laird *et al.*, TLR4/MyD88/PI3K interactions regulate TLR4 signaling. *J Leukoc Biol* **85**, 966-977 (2009).
213. K. Burns *et al.*, MyD88, an adapter protein involved in interleukin-1 signaling. *J Biol Chem* **273**, 12203-12209 (1998).
214. D. I. Udenwobele *et al.*, Myristoylation: An Important Protein Modification in the Immune Response. *Front Immunol* **8**, 751 (2017).
215. B. Wang *et al.*, Protein N-myristoylation: functions and mechanisms in control of innate immunity. *Cell Mol Immunol* **18**, 878-888 (2021).

216. P. Haberkant *et al.*, Protein-sphingolipid interactions within cellular membranes. *J Lipid Res* **49**, 251-262 (2008).
217. S. M. Opal, Endotoxins and other sepsis triggers. *Contrib Nephrol* **167**, 14-24 (2010).
218. A. Liepelt *et al.*, Differential Gene Expression in Circulating CD14(+) Monocytes Indicates the Prognosis of Critically Ill Patients with Sepsis. *J Clin Med* **9**, (2020).
219. J. Liu *et al.*, Screening cytokine/chemokine profiles in serum and organs from an endotoxic shock mouse model by LiquiChip. *Sci China Life Sci* **60**, 1242-1250 (2017).
220. T. Liu, L. Zhang, D. Joo, S. C. Sun, NF-kappaB signaling in inflammation. *Signal Transduct Target Ther* **2**, 17023- (2017).
221. D. A. Zisman *et al.*, Anti-interleukin-12 therapy protects mice in lethal endotoxemia but impairs bacterial clearance in murine Escherichia coli peritoneal sepsis. *Shock* **8**, 349-356 (1997).
222. S. E. Moreno *et al.*, IL-12, but not IL-18, is critical to neutrophil activation and resistance to polymicrobial sepsis induced by cecal ligation and puncture. *J Immunol* **177**, 3218-3224 (2006).
223. C. C. Li, I. Munitic, P. R. Mittelstadt, E. Castro, J. D. Ashwell, Suppression of Dendritic Cell-Derived IL-12 by Endogenous Glucocorticoids Is Protective in LPS-Induced Sepsis. *PLoS Biol* **13**, e1002269 (2015).
224. S. E. Dickinson, G. T. Wondrak, TLR4 in skin cancer: From molecular mechanisms to clinical interventions. *Mol Carcinog* **58**, 1086-1093 (2019).
225. K. Nakamura *et al.*, Characterization of mouse melanoma cell lines by their mortal malignancy using an experimental metastatic model. *Life Sci* **70**, 791-798 (2002).
226. I. Arkhypov *et al.*, HSP90alpha induces immunosuppressive myeloid cells in melanoma via TLR4 signaling. *J Immunother Cancer* **10**, (2022).
227. Y. H. Li *et al.*, Occurrences and Functions of Ly6C(hi) and Ly6C(lo) Macrophages in Health and Disease. *Front Immunol* **13**, 901672 (2022).
228. K. W. Lee, Y. Lee, D. S. Kim, H. J. Kwon, Direct role of NF-kappaB activation in Toll-like receptor-triggered HLA-DRA expression. *Eur J Immunol* **36**, 1254-1266 (2006).
229. C. Wu, Q. Hua, L. Zheng, Generation of Myeloid Cells in Cancer: The Spleen Matters. *Front Immunol* **11**, 1126 (2020).
230. H. Pircher *et al.*, Viral escape by selection of cytotoxic T cell-resistant virus variants in vivo. *Nature* **346**, 629-633 (1990).
231. R. Mercado-Lubo, B. A. McCormick, A unique subset of Peyer's patches express lysozyme. *Gastroenterology* **138**, 36-39 (2010).
232. K. Voss *et al.*, A guide to interrogating immunometabolism. *Nat Rev Immunol* **21**, 637-652 (2021).
233. S. Daemen, J. D. Schilling, The Interplay Between Tissue Niche and Macrophage Cellular Metabolism in Obesity. *Front Immunol* **10**, 3133 (2019).
234. D. G. Ryan, L. A. J. O'Neill, Krebs Cycle Reborn in Macrophage Immunometabolism. *Annu Rev Immunol* **38**, 289-313 (2020).
235. W. C. Chou, E. Rampanelli, X. Li, J. P. Ting, Impact of intracellular innate immune receptors on immunometabolism. *Cell Mol Immunol* **19**, 337-351 (2022).
236. A. G. York *et al.*, Limiting Cholesterol Biosynthetic Flux Spontaneously Engages Type I IFN Signaling. *Cell* **163**, 1716-1729 (2015).
237. L. Berod *et al.*, De novo fatty acid synthesis controls the fate between regulatory T and T helper 17 cells. *Nature Medicine* **20**, 1327-1333 (2014).
238. T. Hla, A. J. Dannenberg, Sphingolipid signaling in metabolic disorders. *Cell Metab* **16**, 420-434 (2012).
239. A. Madi, G. Cui, Regulation of immune cell metabolism by cancer cell oncogenic mutations. *Int J Cancer* **147**, 307-316 (2020).
240. G. Krejcova *et al.*, Drosophila macrophages switch to aerobic glycolysis to mount effective antibacterial defense. *Elife* **8**, (2019).
241. O. M. C *et al.*, The Warburg Effect Occurs Rapidly in Stimulated Human Adult but Not Umbilical Cord Blood Derived Macrophages. *Front Immunol* **12**, 657261 (2021).
242. O. Canli *et al.*, Myeloid Cell-Derived Reactive Oxygen Species Induce Epithelial Mutagenesis. *Cancer Cell* **32**, 869-883 e865 (2017).
243. A. H. Kim *et al.*, Addition of an N-Terminal Poly-Glutamate Fusion Tag Improves Solubility and Production of Recombinant TAT-Cre Recombinase in Escherichia coli. *J Microbiol Biotechnol* **30**, 109-117 (2020).
244. F. M. Goni, Sphingomyelin: What is it good for? *Biochem Biophys Res Commun* **633**, 23-25 (2022).

245. Z. Li *et al.*, Impact of sphingomyelin synthase 1 deficiency on sphingolipid metabolism and atherosclerosis in mice. *Arterioscler Thromb Vasc Biol* **32**, 1577-1584 (2012).
246. M. Akhtari, S. J. Zargar, M. Vojdanian, A. Jamshidi, M. Mahmoudi, Monocyte-derived and M1 macrophages from ankylosing spondylitis patients released higher TNF-alpha and expressed more IL1B in response to BzATP than macrophages from healthy subjects. *Sci Rep* **11**, 17842 (2021).
247. N. Wang, H. Liang, K. Zen, Molecular mechanisms that influence the macrophage m1-m2 polarization balance. *Front Immunol* **5**, 614 (2014).
248. J. Sakai *et al.*, Lipopolysaccharide-induced NF-kappaB nuclear translocation is primarily dependent on MyD88, but TNFalpha expression requires TRIF and MyD88. *Sci Rep* **7**, 1428 (2017).
249. F. Christian, E. L. Smith, R. J. Carmody, The Regulation of NF-kappaB Subunits by Phosphorylation. *Cells* **5**, (2016).
250. J. L. Luo, H. Kamata, M. Karin, IKK/NF-kappaB signaling: balancing life and death--a new approach to cancer therapy. *J Clin Invest* **115**, 2625-2632 (2005).
251. O. Ernst, S. J. Vayttaden, I. D. C. Fraser, Measurement of NF-kappaB Activation in TLR-Activated Macrophages. *Methods Mol Biol* **1714**, 67-78 (2018).
252. S. Przybylski *et al.*, Influence of nanoparticle-mediated transfection on proliferation of primary immune cells in vitro and in vivo. *PLoS One* **12**, e0176517 (2017).
253. S. S. Iyer, D. J. Kusner, Coordinate regulation of sphingosine kinase and actin dynamics. *Methods Mol Biol* **531**, 347-361 (2009).
254. Y. H. Zeidan, R. W. Jenkins, Y. A. Hannun, Remodeling of cellular cytoskeleton by the acid sphingomyelinase/ceramide pathway. *J Cell Biol* **181**, 335-350 (2008).
255. C. S. Technology. (2023), vol. 2023.
256. Proteintech. (2023), vol. 2023.
257. S. Mitra, C. A. Traughber, M. K. Brannon, S. Gomez, D. G. S. Capelluto, Ubiquitin interacts with the Tollip C2 and CUE domains and inhibits binding of Tollip to phosphoinositides. *J Biol Chem* **288**, 25780-25791 (2013).
258. A. Ciarrocchi *et al.*, Tollip is a mediator of protein sumoylation. *PLoS One* **4**, e4404 (2009).
259. H. Zhao, P. Lappalainen, A simple guide to biochemical approaches for analyzing protein-lipid interactions. *Mol Biol Cell* **23**, 2823-2830 (2012).
260. N. Ueda, Ceramide-induced apoptosis in renal tubular cells: a role of mitochondria and sphingosine-1-phoshate. *Int J Mol Sci* **16**, 5076-5124 (2015).
261. X. Wittebole, D. Castanares-Zapatero, P. F. Laterre, Toll-like receptor 4 modulation as a strategy to treat sepsis. *Mediators Inflamm* **2010**, 568396 (2010).
262. B. Schaaf *et al.*, Mortality in human sepsis is associated with downregulation of Toll-like receptor 2 and CD14 expression on blood monocytes. *Diagn Pathol* **4**, 12 (2009).
263. J. Ni *et al.*, Toddalolactone Protects Lipopolysaccharide-Induced Sepsis and Attenuates Lipopolysaccharide-Induced Inflammatory Response by Modulating HMGB1-NF-kappaB Translocation. *Front Pharmacol* **11**, 109 (2020).
264. J. W. Park *et al.*, Comparison of response to LPS-induced sepsis in three DBA/2 stocks derived from different sources. *Lab Anim Res* **37**, 2 (2021).
265. S. Newton *et al.*, Sepsis-induced changes in macrophage co-stimulatory molecule expression: CD86 as a regulator of anti-inflammatory IL-10 response. *Surg Infect (Larchmt)* **5**, 375-383 (2004).
266. M. Haloul *et al.*, mTORC1-mediated polarization of M1 macrophages and their accumulation in the liver correlate with immunopathology in fatal ehrlichiosis. *Sci Rep* **9**, 14050 (2019).
267. M. J. Page, D. B. Kell, E. Pretorius, The Role of Lipopolysaccharide-Induced Cell Signalling in Chronic Inflammation. *Chronic Stress (Thousand Oaks)* **6**, 24705470221076390 (2022).
268. D. A. Nicholas *et al.*, Palmitic acid is a toll-like receptor 4 ligand that induces human dendritic cell secretion of IL-1β. *PLOS ONE* **12**, e0176793 (2017).
269. S. Xu *et al.*, Uptake of oxidized lipids by the scavenger receptor CD36 promotes lipid peroxidation and dysfunction in CD8(+) T cells in tumors. *Immunity* **54**, 1561-1577.e1567 (2021).
270. S. Wang, Y. Zhang, HMGB1 in inflammation and cancer. *J Hematol Oncol* **13**, 116 (2020).
271. A. Deguchi *et al.*, Eritoran inhibits S100A8-mediated TLR4/MD-2 activation and tumor growth by changing the immune microenvironment. *Oncogene* **35**, 1445-1456 (2016).
272. E. Kallberg *et al.*, S100A9 interaction with TLR4 promotes tumor growth. *PLoS One* **7**, e34207 (2012).
273. J. Cummins, M. Tangney, Bacteria and tumours: causative agents or opportunistic inhabitants? *Infect Agent Cancer* **8**, 11 (2013).

274. J. Ma *et al.*, The role of the tumor microbe microenvironment in the tumor immune microenvironment: bystander, activator, or inhibitor? *J Exp Clin Cancer Res* **40**, 327 (2021).
275. J. R. Brocklyn, Regulation of cancer cell migration and invasion by sphingosine-1-phosphate. *World J Biol Chem* **1**, 307-312 (2010).
276. M. E. Venable, J. Y. Lee, M. J. Smyth, A. Bielawska, L. M. Obeid, Role of ceramide in cellular senescence. *J Biol Chem* **270**, 30701-30708 (1995).
277. F. Scarlatti *et al.*, Ceramide-mediated macroautophagy involves inhibition of protein kinase B and up-regulation of beclin 1. *J Biol Chem* **279**, 18384-18391 (2004).
278. J. Wang *et al.*, UV-induced somatic mutations elicit a functional T cell response in the YUMMER1.7 mouse melanoma model. *Pigment Cell Melanoma Res* **30**, 428-435 (2017).
279. J. Zhou, S. Zhang, C. Guo, Crosstalk between macrophages and natural killer cells in the tumor microenvironment. *Int Immunopharmacol* **101**, 108374 (2021).
280. A. Di Lorenzo, E. Bolli, L. Tarone, F. Cavallo, L. Conti, Toll-Like Receptor 2 at the Crossroad between Cancer Cells, the Immune System, and the Microbiota. *Int J Mol Sci* **21**, (2020).
281. W. Zhang, N. Borcherding, R. Kolb, IL-1 Signaling in Tumor Microenvironment. *Adv Exp Med Biol* **1240**, 1-23 (2020).
282. C. A. Dinarello, Overview of the IL-1 family in innate inflammation and acquired immunity. *Immunol Rev* **281**, 8-27 (2018).
283. A. Mackensen, C. Galanos, R. Engelhardt, Treatment of cancer patients with endotoxin induces release of endogenous cytokines. *Pathobiology* **59**, 264-267 (1991).
284. F. Otto *et al.*, Phase II trial of intravenous endotoxin in patients with colorectal and non-small cell lung cancer. *Eur J Cancer* **32A**, 1712-1718 (1996).
285. M. R. Chicoine, E. K. Won, M. C. Zahner, Intratumoral injection of lipopolysaccharide causes regression of subcutaneously implanted mouse glioblastoma multiforme. *Neurosurgery* **48**, 607-614; discussion 614-605 (2001).
286. M. A. Shetab Boushehri, M. M. A. Abdel-Mottaleb, A. Beduneau, Y. Pellequer, A. Lamprecht, A nanoparticle-based approach to improve the outcome of cancer active immunotherapy with lipopolysaccharides. *Drug Deliv* **25**, 1414-1425 (2018).
287. G. J. Vosika, C. Barr, D. Gilbertson, Phase-I study of intravenous modified lipid A. *Cancer Immunol Immunother* **18**, 107-112 (1984).
288. A. Romerio, F. Peri, Increasing the Chemical Variety of Small-Molecule-Based TLR4 Modulators: An Overview. *Front Immunol* **11**, 1210 (2020).
289. Y. K. Kim *et al.*, Airway exposure levels of lipopolysaccharide determine type 1 versus type 2 experimental asthma. *J Immunol* **178**, 5375-5382 (2007).
290. E. J. Park *et al.*, Dietary ganglioside inhibits acute inflammatory signals in intestinal mucosa and blood induced by systemic inflammation of Escherichia coli lipopolysaccharide. *Shock* **28**, 112-117 (2007).
291. S. Ma, Sandhoff, R., Luo, X., Shang, F., Li, Z., Wu, J., Schwarz, F., Ming, Y., Madi, A., Weißhaar, N., Mieg, A., Mohr, K., ten Bosch, N., Li, Z., Hering, M., Poschet, G., Buettner, M., Rodewald, HR., Wang, X., Gao, P., Cui, G., Serine enrichment in tumor promotes regulatory T cell accumulation through sphinganine. *Manuscript submitted for publication*, (2023).
292. Y. S. Lee *et al.*, Myriocin, a serine palmitoyltransferase inhibitor, suppresses tumor growth in a murine melanoma model by inhibiting de novo sphingolipid synthesis. *Cancer Biol Ther* **13**, 92-100 (2012).
293. N. Dana, S. H. Javanmard, G. Vaseghi, Effect of lipopolysaccharide on toll-like receptor-4 signals in mouse cancer cells. *Bratisl Lek Listy* **118**, 598-601 (2017).
294. C. W. t. Shields *et al.*, Cellular backpacks for macrophage immunotherapy. *Sci Adv* **6**, eaaz6579 (2020).
295. G. Raes *et al.*, Arginase-1 and Ym1 are markers for murine, but not human, alternatively activated myeloid cells. *J Immunol* **174**, 6561; author reply 6561-6562 (2005).
296. E. P. McCarron *et al.*, Exploring the translational disconnect between the murine and human inflammatory response: analysis of LPS dose-response relationship in murine versus human cell lines and implications for translation into murine models of sepsis. *J Inflamm Res* **8**, 201-209 (2015).
297. J. Lasselin *et al.*, Comparison of bacterial lipopolysaccharide-induced sickness behavior in rodents and humans: Relevance for symptoms of anxiety and depression. *Neurosci Biobehav Rev* **115**, 15-24 (2020).

298. R. S. Munford, Murine responses to endotoxin: another dirty little secret? *J Infect Dis* **201**, 175-177 (2010).
299. A. F. Suffredini *et al.*, Effects of recombinant dimeric TNF receptor on human inflammatory responses following intravenous endotoxin administration. *J Immunol* **155**, 5038-5045 (1995).